



HAL
open science

Dynamics of neuronal networks

Anirudh Kulkarni

► **To cite this version:**

Anirudh Kulkarni. Dynamics of neuronal networks. Physics [physics]. Université Pierre et Marie Curie - Paris VI, 2017. English. NNT : 2017PA066377 . tel-01745313

HAL Id: tel-01745313

<https://theses.hal.science/tel-01745313v1>

Submitted on 28 Mar 2018

HAL is a multi-disciplinary open access archive for the deposit and dissemination of scientific research documents, whether they are published or not. The documents may come from teaching and research institutions in France or abroad, or from public or private research centers.

L'archive ouverte pluridisciplinaire **HAL**, est destinée au dépôt et à la diffusion de documents scientifiques de niveau recherche, publiés ou non, émanant des établissements d'enseignement et de recherche français ou étrangers, des laboratoires publics ou privés.

**THÈSE DE DOCTORAT
DE L'UNIVERSITÉ PIERRE ET MARIE CURIE**

Spécialité : Physique

École doctorale : "Physique en Île-de-France"

réalisée

à LPS, École Normale Supérieure

présentée par

Anirudh KULKARNI

pour obtenir le grade de :

DOCTEUR DE L'UNIVERSITÉ PIERRE ET MARIE CURIE

Sujet de la thèse :

Dynamics of Neuronal Networks

soutenance prévu le **28/09/2017**

devant le jury composé de :

M.	A. Arrenberg	Rapporteur	Universität Tübingen
M.	A. Torcini	Rapporteur	Université Cergy-Pontoise
Mme	D. Salort	Examinatrice	Université Pierre et Marie Curie
M.	A. Destexhe	Examineur	European Institute for Theoretical Neuroscience
M.	G. Debrégeas	Examineur	Université Pierre et Marie Curie
M.	G. Sumbre	Membre invité	École Normale Supérieure
M.	V. Hakim	Directeur de thèse	École Normale Supérieure

Contents

Introduction	3
I Models of single neurons	5
I.1 Hodgkin Huxley Model of a single neuron	6
I.2 Simplified single neuron models	9
I.2.1 Spike generation dynamics	13
I.2.2 Adaptation currents and spike rate adaptation	13
I.2.3 Refractoriness	13
I.2.4 Subthreshold voltage gated currents	14
I.2.5 Spatial structure of the cell	14
I.3 Synapses	14
I.3.1 Time course of synaptic currents	15
I.3.2 Synaptic plasticity	15
I.4 Dynamics of a single neuron instantaneous firing rate	16
I.4.1 Deriving the static transfer function and the dynamical transfer function for the IF neuron	16
I.5 Numerical implementation of the static transfer function and the dynamical transfer function	18
I.6 Analyzing network dynamics	23
I.6.1 Analyzing network dynamics using numerical simulations . . .	23
I.6.2 Analyzing network dynamics using analytical calculations . . .	25
I.6.3 Dynamics of Fully Connected Excitatory Networks	26
I.7 Conclusion	26
II Rate models - an introduction	29
II.1 Rate Models	29
II.1.1 Single population models	29
II.1.2 Models with adaptation	30
II.1.3 Linear Nonlinear (LN) models	30
II.2 Bridging spiking neuron models and rate models	32
II.3 Autocorrelation of the firing rate	34
II.4 Single population with oscillatory input	42
II.5 Introducing a new timescale to rate model	48
II.6 Conclusion	51
III Oscillations in EI networks	57
III.1 Oscillations in the brain	57

III.2	Dynamics of a single EI network	60
III.2.1	Different dynamical regimes of the EI network	62
III.3	Rate Model with coupling	65
III.4	Comparing the oscillatory phases of the rate model and the network model	73
III.4.1	Computing the limit cycles of the EI dynamical system	73
III.4.2	Comparing the limit cycles of the two Adaptive rate models	77
III.5	Two coupled EI networks	79
III.5.1	Antiphase or finite phase different regime	82
III.5.2	Alternating phase regime	83
III.5.3	Modulating phase regime	83
III.5.4	Finite phase regime	86
III.5.5	Synchronous phase regime	86
III.5.6	Phase diagram for the two coupled EI groups	86
III.6	Analytical derivation of the bifurcation plot	87
III.6.1	Transition from the synchronous regime to the phase difference regime	87
III.6.2	Transition from finite phase difference regime to other regimes	90
III.6.3	Computing the phase difference regime at very low coupling factors	91
III.7	Effects of finite size noise in Adaptive rate model1	94
III.8	Comparing with the network simulations	96
III.9	Comparing with the finite size networks	103
III.10	Finite size networks with finite connectivity	103
III.11	Conclusion	109
IV	Sensory Adaptation	113
IV.1	Adaptation: Marr's three levels of analysis	113
IV.1.1	Computational level	115
IV.1.2	Algorithmic level	116
IV.1.3	Implementation level	117
IV.2	Motion After Effect	118
IV.3	The zebrafish as a vertebrate model for systems neuroscience	121
IV.4	Optokinetic response and Motion After Effect	125
IV.5	Two-photon calcium imaging	125
IV.6	Visual system of zebrafish	130
IV.7	MAE in the zebrafish larva	132
IV.8	Laing Chow model	134
IV.9	MAE model in the zebrafish tectum	136
IV.9.1	Comparator cells	137
IV.10	Conclusion	137
V	Sustained Rhythmic Brain Activity Underlies Visual Motion Perception in Zebrafish	139
VI	Conclusion and Future perspectives	203

Introduction

Neuroscience is a rapidly growing field with collaborations and intersections among many different disciplines. Despite the huge upsurge of obtained data and ever more increasing data from different large scale initiatives such as the Obama Brain initiative or the European Human Brain Project, there is no complete framework yet to understand the brain. Modern statistical physics has undertaken investigation in the rich field of neuroscience and this has contributed to modeling in computational neuroscience. Theoretical neuroscience is on the pursuit of understanding the brain mechanisms by modeling neurons, the interaction between neurons and the emergence of large scale dynamics of neuronal networks and ultimately, comparing the results to those obtained in experimental data [nne, 2016] [neu, 2017].

Neurons are particular cells in the brain that are known to process information. Neurons are special cells in the body which can communicate with each other via electrical signals or chemical molecules called neurotransmitters. When the potential of a neuron reaches a threshold, it emits electrical signals called spikes which activate release of neurotransmitters. These neurotransmitters then diffuse across the synaptic cleft, the space between two neurons, and either activate or suppress the other neuron, thus communicating information.

In chapter 1 of this thesis, we describe a detailed biophysical model of a single neuron, the Hodgkin Huxley model, and then move on to simplified models of single neurons which capture the essential features of neuronal dynamics. After describing synapses, the connections between neurons, we introduce the firing rate of a neuron which is the number of action potentials or spikes emitted by the neuron per second. We will then describe how the dynamics of the firing rate can be computed analytically and numerically. We then connect these simplified neurons via synapses and study the mean population firing rate of a group of neurons in a network. This mean population firing rate can again be analyzed using numerical and analytical calculations.

However, even network models of simplified neurons are computationally very expensive. Therefore, we try to just retain the essential features of these network models to allow us to establish parallel links with experimental observations. This results in rate models, which we discuss in chapter 2. We establish a link between rate models and the network models and describe how the autocorrelation of the population firing rate in the network can be studied via rate models. To quantitatively describe better the effect of sinusoidal input currents into rate models, we introduce a new rate model inspired by Augustin, M., Ladenbauer, J. et al. [Augustin et al., 2016].

The brain is a complex system and eludes, as of yet, description by a single unified model. However, several experimentally observed phenomena in different brain regions

can be described by models (e.g. the olfactory bulb, [Li and Hopfield, 1989], the cerebellum [Bouvier et al., 2016], the hippocampus [Andersen et al., 2006]). Along this line, we use rate model descriptions to describe two phenomena that we observe in the brain: oscillations and sensory adaptation. In chapter 3, we discuss brain oscillations that have been widely reported in areas such as the motor cortex ([Baker et al., 1999] [Rubino et al., 2006] [Murthy and Fetz, 1992]) or in neocortical slices ([Wu et al., 1999] [Bai et al., 2006]). These oscillations in the beta range and the lower gamma range ($\sim 10 - 40$ Hz) are known to be related to motor initiation and attention. We describe Excitatory-Inhibitory (EI) network models and EI rate models in the subsequent sections of this chapter. A single EI network can produce oscillations in this frequency range and when we couple two of them, we observe different dynamical regimes of these coupled oscillators. By coupling more of them, we can study how oscillations synchronize or propagate among these various oscillators, which correspond to different brain regions, as has been observed experimentally.

In chapters 4 and 5, we then focus on adaptation in sensory systems. We describe the phenomenon of adaptation and use the zebrafish larva [Sumbre and de Polavieja, 2014] as an experimental model to study adaptation. More particularly, we focus on the motion after effect illusion in the zebrafish. We record behavioural and neuronal activity in the highest visual center of the larva, the optic tectum and then use rate models to model this phenomenon. Chapter 4 presents the necessary introduction while Chapter 5 describes our work in detail. We end the thesis with a conclusion chapter summarizing our work and discussing the future perspectives that can be undertaken.

PUBLICATIONS

1. Sustained Rhythmic Brain Activity Underlies Visual Motion Perception in Zebrafish: Veronica Perez-Schuster, [Anirudh Kulkarni](#), Morgane Nouvian, Sebastian A. Romano, Konstantinos Lygdas, Adrien Jouary, Mario Dippopa, Thomas Pietri, Mathieu Haudrechy, Virginie Candat, Jonathan Boulanger-Weill, Vincent Hakim and German Sumbre. **Cell Reports** **17**, 1098–1112, 2016

2. Synchronization of oscillatory activity in networks with spatially-structured connectivity: [Anirudh Kulkarni](#), Jonas Ranft and Vincent Hakim (in preparation).

Chapter I

Models of single neurons

The brain is one of the most complex objects in the universe. It continuously processes the sensory stimuli in the environment of the organism and responds to these inputs by making various motor movements. The sensory information is transmitted from the sensory organ through nerves in the form of spike trains to the brainstem and then to the thalamus and the cerebral cortex. The neuron is the fundamental information processing unit of the brain. Information is encoded in the electrical pulses emitted by a neuron (called action potentials), which are voltage spikes and is communicated from neuron to neuron through synapses. Neurons in the cortex receive input not only in a feedforward way but also in a recurrent fashion. It is known that recurrent inputs amount for about 90–95% of the input received by the neurons in the cat visual cortex [Douglas and Martin, 2007]. To understand how information is processed in the brain, we therefore need not only to understand the working of an individual neuron but also how neurons communicate with each other through synapses to form networks and how these networks of neurons dynamically process the information they receive.

In this chapter, we will firstly list out a few of the single neuron models that have been used in network studies. A detailed biophysical model was first developed by Hodgkin and Huxley to describe the dynamics of a neuron [Hodgkin and Huxley, 1952]. To capture the essential dynamics of this model, various simplified neuronal models have also been developed such as integrate-and-fire neuron, exponential integrate-and-fire neuron, etc. These simplified models greatly reduce the computational cost of simulating networks of neurons. However, despite the reduction in terms of the computations performed, these simplified neuronal models are not very helpful to qualitatively understand the dynamics of large networks of neurons as they are not easily tractable analytically. For this purpose, various rate models have been proposed. These rate models provide a dynamical description of the average population activity of the network of neurons.

In this chapter, we detail single neuron models and networks of excitatory neurons. In the next chapter, we will bridge them to rate models. To begin with, we recapitulate the Hodgkin Huxley model of a neuron and describe some of the simpler neuron models [Dayan and Abbott, 2001] [Gerstner and Kistler, 2002] [Brunel, 2011].

I.1 Hodgkin Huxley Model of a single neuron

In 1939, Hodgkin and Huxley set out to understand the laws that govern the movement of ions through nerve cells during an action potential. For this purpose, they used the giant axon of a squid because it is large enough (typically around 0.5 mm in diameter) to manipulate. The giant axon of the squid is involved in the water jet propulsion system. To study the ion movement mechanisms, they used the voltage clamp technique (see figure I.1). This technique consists in measuring the amount of current that flows through the neuronal membrane of a given area of the axon of a giant squid. To do this, they had to keep the voltage through the membrane constant with the help of an operational amplifier (op-amp) and they measured the current passing through the membrane by measuring the current passing through the output of the op-amp.

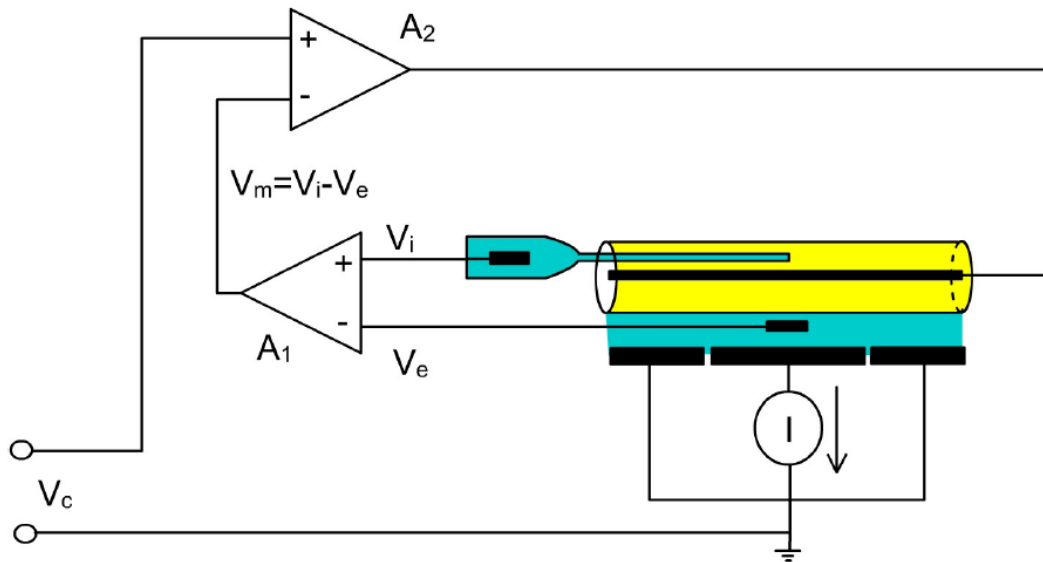


Figure I.1: **Voltage patch clamp technique.** The difference voltage, V_m , between the intracellular voltage V_i and the extracellular voltage V_e is maintained to be at V_c . This results in the injection of a current I , which is measured by an ammeter. Taken from <http://nerve.bsd.uchicago.edu>, Credits: F. Bezanilla.

They performed experiments to elucidate the function of the neuronal membrane under normal conditions. To describe their findings, we need to firstly specify a few points about neurons. The membrane of a neuronal cell separates the interior of the neuron from the extracellular space and a neuron can be described by its intracellular voltage, i.e. the membrane potential V . The extracellular fluid is considered to be at a potential of 0 mV. When there is no external current into a given cell, the membrane potential is steady and is called the rest potential (typically -65 mV). The concentrations of the ions inside the cell is different from the concentration of the ions outside the cell. Ion pumps are proteins on the cell membrane that maintain this concentration difference between the ions inside and outside the cell. Ion channels, on the other hand, are proteins embedded in the cell membrane that allow specific ions to pass through

the membrane. Ion channels belong mainly to three classes: voltage-activated ion channels, ion-activated ion channels (such as Na^+ activated ion channels, Ca^{+2} activated ion channels etc.) and transmitter-activated ion channels i.e. their conductances can change depending on the membrane potential or the intracellular concentration of ions or the extracellular concentration of the transmitters respectively. Electric forces and diffusion are the two mechanisms which drive ions through channels. The electric force is produced by the difference in potential between the interior and the exterior of the cell while diffusion is the result of concentration gradient across the membrane. Due to the thermal fluctuations, the ions are able to move across the membrane. The concentration gradient is maintained by the ion pumps and there is more sodium ions and calcium ions in the extracellular space and more potassium and chloride ions inside the cell. In the a cell with a single ion channel, the membrane potential at which the current flow due to diffusion cancels the current flow due to electric forces is called the equilibrium potential of the ion. This equilibrium potential E characterizes the ratio of the concentration of the ion inside ($[\text{inside}]$) and outside ($[\text{outside}]$) the cell as given by the Nernst equation.

$$E = \frac{V_T}{z} \ln \left(\frac{[\text{outside}]}{[\text{inside}]} \right), \quad (\text{I.1.1})$$

where V_T is the thermal energy at temperature T and z is the charge number of the ion. The equilibrium potentials for Na^+ ion, Ca^{+2} ion, K^+ ion and Cl^- ions are ~ 50 mV, ~ 150 mV, ~ -70 mV and ~ -60 mV respectively. In a cell with multiple ion channels, a steady state is reached for the membrane potential and this “reversal potential” has a value intermediate between the equilibrium potentials of the different ion channels of the cell. This membrane potential is generally called the resting state potential of the neuron.

Hodgkin and Huxley discovered that the ionic current passing through the neuronal membrane can be resolved into three main sources: sodium current, potassium current and leak current, which consists of all the remaining contributions to the membrane current. However, it is now known that the neural membrane contains many more ionic conductances and anatomically detailed neuron models have emerged [Mainen et al., 1995] [Poirazi et al., 2003] [Hay et al., 2011]. They also studied how changes in sodium concentration affected the action potential. By carefully manipulating the sodium concentration, they deduced how the potassium concentration affected the action potential. They studied how sudden potential changes affected the action potential and the ionic conductance. Finally, they also studied how the inactivation of sodium channel reduces sodium permeability. From their experiments, they were able to create a mathematical model for the action potential generation mechanism of the neuron in the squid.

The schematic diagram for the Hodgkin-Huxley (HH) model is given in figure I.2. In the circuit model for a neuron, the ion channels through which the ions move can be modelled as conductances. These conductances are active i.e. the value of the conductance depends on the membrane potential. The membrane of the neuron that separates the extracellular medium from the interior of the cell can be modelled as a capacitor C . There is typically an excess negative charge $-Q$ on the inner surface of the cell membrane and the same amount of positive charge $+Q$ on the outer surface. If the

potential difference across the membrane is V , then the cell membrane is equivalent to a capacitor C , given by $C = Q / V$.

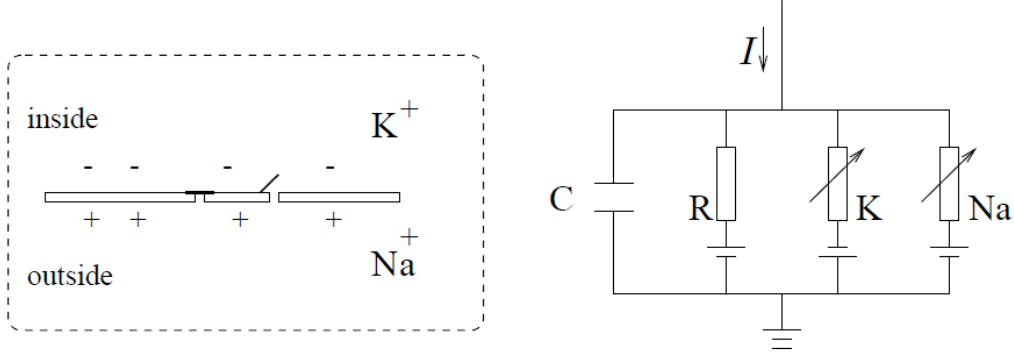


Figure I.2: **A schematic diagram of the Hodgkin-Huxley Model.** On the left is a description of the cell membrane, the ions inside and outside the cell and the ion channels. On the right is a circuit description of the neuron. The capacitance C represents the membrane. The active conductances represent the ion channels and the voltage sources represent the reversal potentials. I is the external current injected into the neuron. Taken from [Gerstner and Kistler, 2002].

We can then write the equations for the membrane dynamics of a neuron as follows:

$$I(t) = I_C(t) + I_{Na}(t) + I_K(t) + I_L(t) + I_{ext}(t), \quad (\text{I.1.2})$$

where

$$I_C(t) = -C \frac{dV}{dt}, \quad (\text{I.1.3})$$

$$I_{Na}(t) = g_{Na} m^3 h (V - E_{Na}), \quad (\text{I.1.4})$$

$$I_K(t) = g_K n^4 (V - E_K), \quad (\text{I.1.5})$$

$$I_L(t) = g_L (V - E_L). \quad (\text{I.1.6})$$

The parameters E_{Na} , E_K , and E_L are the sodium, potassium and leak reversal potentials respectively and I_{ext} is the external injected current. The reversal potentials and conductances are determined empirically.

The three variables m , n , and h are called gating variables and they evolve according to the following differential equations:

$$\tau_m \dot{m} = m_\infty(V) - m, \quad (\text{I.1.7})$$

$$\tau_n \dot{n} = n_\infty(V) - n, \quad (\text{I.1.8})$$

$$\tau_h \dot{h} = h_\infty(V) - h. \quad (\text{I.1.9})$$

The various functions $\tau_m(V)$, $\tau_n(V)$, $\tau_h(V)$, $m_\infty(V)$, $n_\infty(V)$ and $h_\infty(V)$ were empirically determined by Hodgkin and Huxley to fit the data of the giant axon of the squid and are shown in the figure I.3

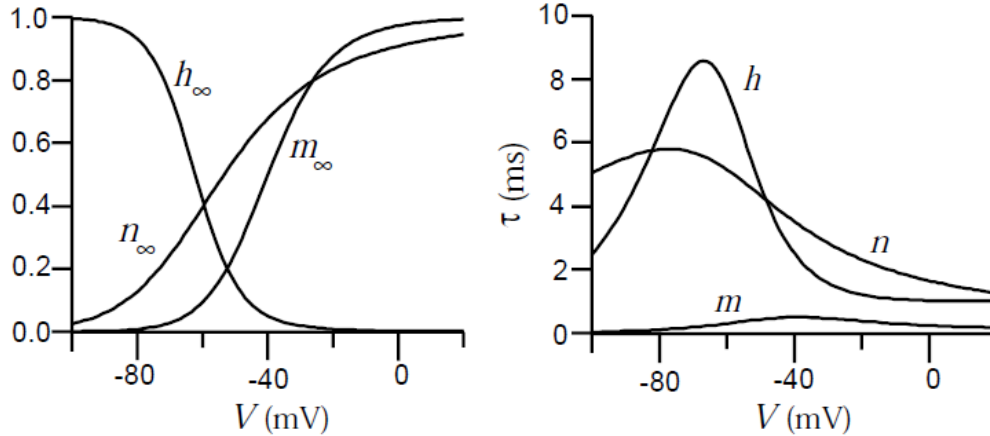


Figure I.3: **The different functions of the Hodgkin-Huxley model.** On the left are the functions $m_\infty(V)$, $n_\infty(V)$ and $h_\infty(V)$, the steady-state levels of activations of Na^+ conductance, K^+ conductance and steady-state level of inactivation of Na^+ conductance. On the right are shown the time constants of the different gating variables as a function of the membrane potential V . Taken from [Dayan and Abbott, 2001].

The dynamics of the membrane potential of a HH neuron are described in figure I.4. In this figure, a single action potential is shown along with the different variables of the HH model. At $t = 5$ ms, a pulse current is injected using an electrode into the cell. When the membrane potential of the cell V reaches about -50 mV, the sodium channel is activated (m is increasing) and since, the sodium inactivation variable h is nonzero, there is a large influx of sodium ions resulting in a sharp influx of inward current as shown in the second subplot. There is a spike in the membrane potential as a result of this and when V reaches about 0 mV (the cell is depolarized), the sodium channel is inactivated i.e. $h \rightarrow 0$ and the potassium channel is activated $n \rightarrow 1$. The rise in potassium current drives the membrane potential back to a negative value i.e. the cell becomes hyperpolarized before going back to its steady state value.

I.2 Simplified single neuron models

The Hodgkin Huxley model can describe the electrophysiological recordings of the squid neuron very accurately and has been successfully used in modeling different types of neurons. However, recent studies have questioned the validity of the extensiveness of applicability of the HH model for all neurons. In particular, the dynamics of the initiation of a spike in a cortical neuron i.e. the rapid initiation of the spike and the

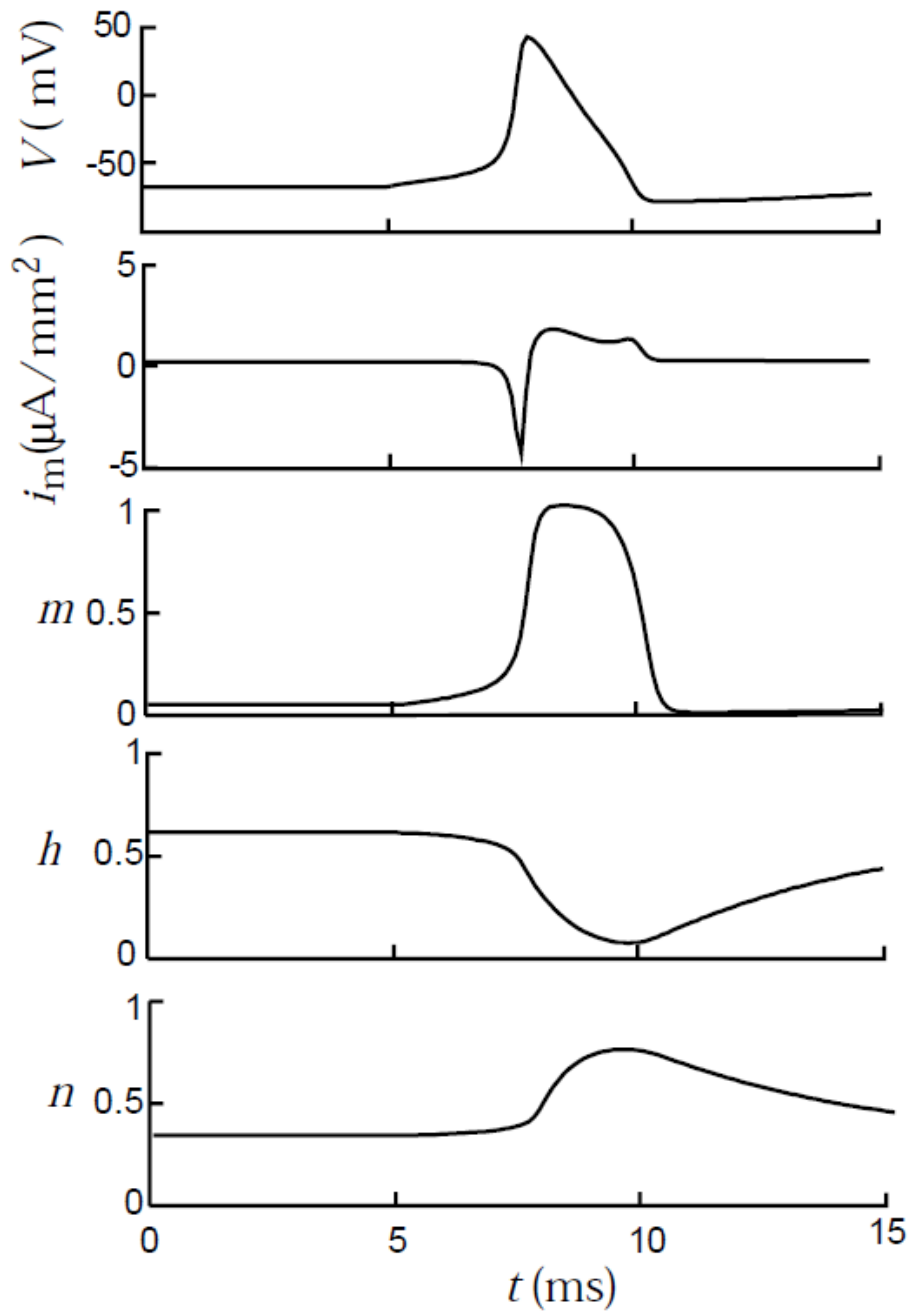


Figure I.4: **The dynamics of the different variables of the Hodgkin-Huxley model.** The dynamics of the membrane potential V , the membrane current i_m , the sodium activation variable m , the sodium inactivation variable h , the potassium activation variable n . A pulse current is injected at 5 ms. Taken from [Dayan and Abbott, 2001].

variable onset potential, cannot be described by the single compartment HH model. One hypothesis that was suggested was that these behaviours can be reproduced by cooperative activation of sodium channels in the cell membrane as opposed to the independent channel opening in the HH model [Naundorf et al., 2006] [Volgushev et al., 2008]. However, there is no experimental evidence to support this hypothesis. Another hypothesis proposes a multi-compartmental HH model where the action potential back-propagates to the soma after being initiated in the axon. During its backpropagation to the soma, the action potential is sharpened by the active conductances in the axon, thus resulting in the kink in the action potential observed in the soma [Yu et al., 2008]. However, there are evidences that indicate that it is not just the action potential in the soma that is sharp but also the initiation of the action potential. To explain this, Brette hypothesized that the kink comes from the specific morphology of the neuron [Brette, 2013]. In particular, he showed using biophysical modelling that the kink can be reproduced by placing the sodium channels in the thin axon. If the distance to the soma exceeds a critical value, then these channels open abruptly as a function of the somatic voltage. Another criticism of the HH model comes from the studies in hippocampal mossy fiber neurons. It was shown that the energy demand per action potential was only 1.3 times the theoretical minimum as opposed to 4 times [Hodgkin, 1975] the theoretical minimum as predicted by the HH model [Alle et al., 2009]. The ionic conductance parameters of Na^+ and K^+ channels in non-myelinated axons are such that the action potentials minimize the metabolic demands. Moreover, the analysis of the underlying dynamics is complicated in the HH model. It is a quite complex model and hence, is not well suited for analytical derivations. For this reason, simple models were explored for modeling the neuron dynamics. These models try to capture the essential features of the neuronal dynamics. For instance, in neocortical slices of rats, when the membrane potential of a neuron reaches about -55 to -50 mV, it typically fires an action potential as shown in Figure I.5. During the action potential, we notice that the voltage increases rapidly in a stereotypical trajectory and then hyperpolarizes rapidly to a value below the baseline level before coming back to baseline level (refractoriness). The mechanism behind the action potential is captured by the dynamics of the Na^+ and the K^+ channels. To simplify the model and accelerate numerical simulations, we can add an action potential artificially each time the neuron reaches a threshold. This is the basis of integrate-and-fire models described next.

The integrate-and-fire models are highly popular for modeling network dynamics. The first usage of such a model dates back to Lapicque [Lapicque, 1907], but the term “integrate-and-fire” first appears in [Knight, 1972]. The simplest example of the integrate-and-fire neuron consists of a capacitor C driven by a current $I(t)$ through a resistor R . Notice that here, we have included only the capacitance of the membrane potential and the resistance offered to the external current. The details of the active conductance of the ion channels are excluded from this description. If the membrane potential of the neuron is denoted as $V(t)$, the capacitive current is given by

$$RI(t) = C \frac{dV}{dt}. \quad (\text{I.2.1})$$

Here $I(t)$ has the dimensions of voltage. By introducing the time constant, $\tau_m = C/R$ (typically in the order of 10 – 20 ms), we have

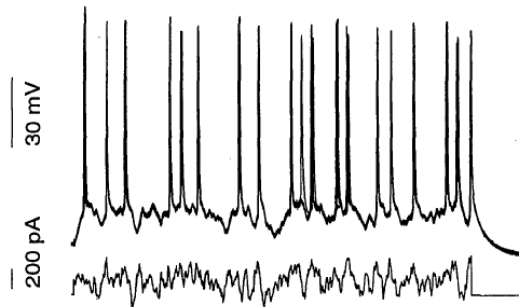


Figure I.5: **Spikes of a neuron in the neocortex.** The membrane potential of a neuron in neocortical slices of rats (shown above) stimulated with a fluctuating current (shown below). Notice the evoked spikes. Taken from [Mainen and Sejnowski, 1995].

$$\tau_m \frac{dV}{dt} = I(t). \quad (\text{I.2.2})$$

In other words, the neuron acts as an integrator of the input current $I(t)$. When the membrane potential of the neuron reaches a certain threshold V_{th} (typically 10–20 mV above the reset potential V_R), the neuron emits a spike and its voltage is reset to V_R . The voltage is clamped to V_R for a certain refractory time period τ_{ref} after which it resumes its evolution according to the above equation.

The simplest model attempting to model the subthreshold dynamics is the leaky integrate-and-fire neuron. The passive or the linear integrate-and-fire is based on two approximations: a) a simplified description of the action potential mechanism itself and b) a linear membrane current. This model includes the leak current and is given by

$$\tau_m \frac{dV}{dt} = -(V - V_L) + I(t). \quad (\text{I.2.3})$$

Here, the resting potential of the cell is given by V_L . As in the case of the IF neuron, when the membrane potential of the LIF neuron reaches V_{th} , the neuron emits a spike and its voltage is reset to V_R and the dynamics continues again. Despite the fact that the LIF has been extensively used in network simulations and analytical studies, it cannot account for the following features of real neurons:

- a) spike generation dynamics
- b) adaptation currents and spike rate adaptation
- c) Refractory effects
- d) subthreshold voltage gated currents
- e) details of the spatial structure of the cell.

In this thesis, the first three features will be of interest to us. We will not consider the last two features, however, we mention them here for the purpose of completeness. The following extensions can, therefore, be added to the above model to overcome the shortcomings.

I.2.1 Spike generation dynamics

To describe the spike generation dynamics of an LIF neuron, a suitable nonlinearity can be added to the voltage dynamics as follows:

$$\tau_m \frac{dV}{dt} = -(V - V_L) + \Psi(V) + I(t), \quad (\text{I.2.4})$$

where $\Psi(V)$ is a nonlinear function of voltage [Fourcaud-Trocmé et al., 2003]. Choices for $\Psi(V)$ include quadratic [Ermentrout and Kopell, 1986] [Ermentrout, 1996] [Gutkin and Ermentrout, 1998] [Latham et al., 2000], quartic [Touboul, 2008], or exponential $\Psi(V) = \Delta_T \exp((V - V_T)/(\Delta_T))$ functions, where Δ_T is the sharpness of the action potential initiation and V_T is the membrane potential threshold. It was found [Fourcaud-Trocmé et al., 2003] that the exponential nonlinearity includes biophysically meaningful parameters and best describes the dynamics of the fast sodium currents in the Hodgkin Huxley model and the f-I (firing rate as a function of input current) curves thus obtained fit very well the ones observed in pyramidal and fast spiking interneurons in the cortex [Badel et al., 2008b]. For this reason, in this thesis, we will use the exponential integrate and fire (EIF) neuron for all our simulations of networks of neurons.

I.2.2 Adaptation currents and spike rate adaptation

Sensory adaptation will be discussed in more detailed in chapter IV. One means of implementation of sensory adaptation is through spike rate adaptation. The firing rate of a neuron, defined as the number of spikes emitted by the neuron in a given time-bin, is known to exhibit adaptation with constant input current in real neurons i.e. the Interspike interval increases over time. This phenomenon is called spike rate adaptation. The LIF neuron fires regularly with constant current and does not exhibit spike rate adaptation. To accommodate the phenomenon of spike rate adaptation in the model, we can introduce an additional variable through which the firing rate steadily decreases upon the injection of a constant current. This is done as follows:

$$\tau_m \frac{dV}{dt} = -(V - V_L) + \gamma W + I(t), \quad (\text{I.2.5})$$

$$\tau_w \frac{dW}{dt} = -W. \quad (\text{I.2.6})$$

The variable W jumps each time a spike is emitted, by a value, say b i.e. $W \rightarrow W + b$. As W increases, the firing rate of the neuron decreases. This model is therefore called “Adaptive LIF” model. This variable W could be the fraction of open channels of an ion-gated conductance ($[\text{Ca}^{+2}]$ ions, for instance).

I.2.3 Refractoriness

To account for the refractoriness of real neurons, when the IF neurons reach v_{th} and are reset to v_R , the voltage can be clamped to v_R for a certain refractory time period τ_{ref} after which it resumes its evolution according to the above equation.

1.2.4 Subthreshold voltage gated currents

To accommodate richer subthreshold dynamics, a simple model can be developed from the Hodgkin Huxley model [Richardson et al., 2003]. The equations derived are

$$\tau_m \frac{dV}{dt} = -(V - V_L) + \gamma W + I(t), \quad (I.2.7)$$

$$\tau_w \frac{dW}{dt} = -W + V. \quad (I.2.8)$$

Unlike the previous case with adaptation, here the W variable is related to the activation or inactivation variable of a current that contributes to subthreshold dynamics. This model is called the “Generalized integrate-and-fire model” and when γ is negative and large enough, it can display subthreshold resonance [Izhikevich, 2001].

1.2.5 Spatial structure of the cell

To accommodate for the spatial structure of the neuron, the simple model can be extended to a multi-compartment model with a membrane potential defined for each introduced compartment.

1.3 Synapses

Neurons communicate with each other through synapses. Synapses can either be electrical or chemical. Electrical synapses are ion channels which connect two cells and allow ions to directly pass between cells. They are bidirectional and conduct nerve impulses much faster than chemical synapses, but the gain of the postsynaptic response is smaller when compared to a chemical synapse. In the case of a chemical synapse, when an action potential is initiated, it travels down the axon and when it reaches the presynaptic terminal, it activates voltage gated Ca^{+2} channels triggering an increase of calcium concentration in the cell. The increase in the Ca^{+2} concentration causes neurotransmitter vesicles within the cell to fuse with the cell membrane and release the neurotransmitters into the synaptic cleft between the presynaptic and the post synaptic neuron. The neurotransmitters then bind to the receptors on the postsynaptic neuron thus opening the transmitter-activated ion channels, which modifies the conductance of the post synaptic neuron. These synaptic currents can be described by

$$I_{syn}(t) = g_{syn}(t)(V - E_{syn}), \quad (I.3.1)$$

where E_{syn} , the reversal potential and g_{syn} , the synaptic conductance characterize the synapse. These synapses can be either excitatory or inhibitory depending on the effect they have on the postsynaptic neuron. Excitatory synapses have E_{syn} greater than the membrane potential of the neuron; for instance, glutamate synapses have an E_{syn} of about 0 mV. Inhibitory synapses can either be shunting or hyperpolarizing depending on the value of E_{syn} . A hyperpolarizing synapse has E_{syn} less than the membrane potential of the neuron and tends to hyperpolarize the neuron whereas a shunting synapse has E_{syn} close to the membrane potential of the neuron, so, its primary impact

is to increase the membrane conductance of the neuron. AMPA receptors and NMDA receptors are the most common types of excitatory receptor channels. AMPA receptors lead to a fast EPSC whereas NMDA receptors lead to a slower EPSC. GABA receptors are the most common inhibitory receptors.

In the above description of synapses, the synaptic current is voltage dependent. This leads to conductance based models. We can simplify the description of the synaptic current by taking them to be voltage independent. This leads to current-based synaptic models. In this section, we will describe the different models that provide approximate description of synapses. These models must specify how a postsynaptic current is generated in response to a presynaptic spike train. A synaptic current can be modelled by specifying its a) time course and b) plasticity.

I.3.1 Time course of synaptic currents

The postsynaptic current elicited by a series of input spikes $\sum_k \delta(t - t_j^k)$ can be written as

$$I(t) \propto \int_{-\infty}^t S(t - u) \sum_k \delta(u - t_j^k) du \propto \sum_k S(t - t_j^k). \quad (\text{I.3.2})$$

The function $S(t)$ is the post synaptic current triggered by a single presynaptic spike. Synaptic currents typically exhibit the three phases described by such a function (latency, rise and decay times). The simplest choices for the function $S(t)$ include:

1) A delta function, $S(t) = \delta(t)$. This results in an instantaneous increase in the postsynaptic membrane potential on the arrival of a presynaptic spike. To account for the delay between the presynaptic spike and the post synaptic jump, a delay D can be included as $S(t) = \delta(t - D)$

2) An instantaneous jump in the postsynaptic current accompanied by an exponential decay: $S(t) \propto \exp(-t/\tau_s)\Theta(t)$. Here τ_s is the synaptic decay time and $\Theta(t)$ is the Heaviside function.

3) Difference of two exponentials $S(t) \propto [\exp(-t/\tau_s) - \exp(-t/\tau_r)]\Theta(t)$ where τ_r is the rise time of the postsynaptic current and τ_s is the decay time. In the limit of $\tau_r = \tau_s$, we obtain the alpha function ($\propto t \exp(-t/\tau_s)$).

I.3.2 Synaptic plasticity

Synaptic plasticity can occur on short time scales (10 – 100 ms) to longer timescales (seconds to minutes) [Sumbre et al., 2008]. Short-term plasticity has been described by simple phenomenological models such as the model by [Tsodyks and Markram, 1997] where the conductivity $g(t)$ is described by a dynamical equation, which drops by some amount at each presynaptic spike, and then recovers exponentially. Short-term facilitation has also been described by some models [Tsodyks et al., 1998]. Other models include [Abbott et al., 1997]. Finally, there exists a large number of models to describe the phenomenon of long-term plasticity [Bi and Poo, 2001] [Shouval et al., 2002] [Mongillo et al., 2005].

I.4 Dynamics of a single neuron instantaneous firing rate

The firing rate of a single neuron is defined as the number of spikes emitted by the neuron in a given time-bin. In order to study the dynamics of networks of neurons, it is helpful to understand the dynamics of the instantaneous firing rate of single neurons in the presence of varying input currents. For this purpose, two quantities in the case of single neuron models are defined: the static transfer function or the f-I curve and the dynamical transfer function of the linear firing rate response. The static transfer function is the average firing frequency in time of a single neuron as a function of a constant input current. The dynamical transfer function or the linear firing rate response is the modulation of the instantaneous firing rate of the neuron when a small input of a particular frequency is injected into it.

To compute the static transfer function for the various neuron models, one needs to inject a constant current, say I_0 into a neuron and calculate the firing rate i.e. the average number of spikes emitted per second. For the LIF model, the firing rate is zero when $I_0 < V_T - V_L$ and then increases monotonically above the threshold $V_T - V_L$. It eventually saturates to $1/\tau_{ref}$ because a neuron cannot fire during the refractory period. The f-I curve can also be calculated when a noisy current is injected into the neuron, in two limiting cases: a) white noise: $I_{ext} = I_0 + \sigma\eta(t)$ where η is a white noise of unit variance and σ is the standard deviation of the noise [Tuckwell, 1988] [Amit and Tsodyks, 1991] [Brunel and Hakim, 1999], and in the presence of b) shot noise: with exponential amplitude distributions [Richardson and Swarbrick, 2010].

Because of the noise, the firing rate is non-zero around V_T . Firing of the neuron in this regime is due to the fluctuations around the mean inputs that occasionally brings the neuron to the threshold resulting in the emission of a spike by the neuron. This results in a firing process that is Poissonian in nature and the inter-spike interval distribution in this case is an exponential. The firing rate of the nonlinear IF neurons can also be computed analytically [Fourcaud-Trocmé et al., 2003].

In the presence of time varying inputs, computing the instantaneous firing rate is difficult. However, one can compute the response to a sinusoidal perturbation of small amplitude at a given frequency and this is called the linear firing rate response. If the external input current is given by $I_{ext} = I_0(1 + \epsilon\cos(\omega t)) + \sigma\sqrt{\tau_m}\eta(t)$, then the firing rate in response to this current is given by $r_0(I_0, \sigma) + \epsilon Re[r_1(I_0, \sigma, \omega) \exp 2\pi\omega t]$ in the limit $\epsilon \rightarrow 0$.

Here r_0 is the static transfer function, r_1 is the dynamical transfer function, I_0 is the amplitude of the input current, ω is the frequency of the input current, τ_m is the membrane time constant of the neuron, σ determines the standard deviation of the input current and $\eta(t)$ is a white Gaussian noise.

I.4.1 Deriving the static transfer function and the dynamical transfer function for the IF neuron

In this section, we will sketch the analytical calculation for the static transfer function of a simplified neuron model in the presence of a fluctuating white noise input $I(t) = I_0 + \sigma\sqrt{\tau_m}\eta(t)$.

To recapitulate, the LIF model is given by:

$$\tau_m \frac{dV}{dt} = -(V - V_L) + I(t). \quad (\text{I.4.1})$$

If we represent V to be difference between the membrane potential and the leak reversal potential, we can rewrite the above equation as:

$$\tau_m \frac{dV}{dt} = -V + I_0 + \sigma \sqrt{\tau_m} \eta(t). \quad (\text{I.4.2})$$

This system can instead be described by transforming it into the Fokker-Planck equation to describe the probability distribution of the membrane potential $P(V, t)$. In general, a Langevin equation of the form:

$$\frac{dx}{dt} = f(x) + \eta(t), \quad (\text{I.4.3})$$

where $\eta(t)$ is a Gaussian white noise with correlations $\langle \eta(t)\eta(t') \rangle = \Delta \delta(t - t')$. The above Langevin equation can be converted to a Fokker-Planck equation, which is the dynamical equation for the probability distribution of the variable x [Van Kampen, 1992]

$$\frac{dP(x, t)}{dt} = -\frac{\partial}{\partial x}(f(x)P(x, t)) + \frac{1}{2}\Delta \frac{\partial^2}{\partial x^2}P(x, t). \quad (\text{I.4.4})$$

Equation I.4.1 can be rewritten as :

$$\tau_m \frac{\partial P(V, t)}{\partial t} + \frac{\partial J(V, t)}{\partial V} = 0, \quad (\text{I.4.5})$$

where $J(V, t)$ is the probability current defined by:

$$J(V, t) = f(V)P(V, t) - \frac{\Delta}{2} \frac{\partial P}{\partial V}. \quad (\text{I.4.6})$$

The two terms on the right correspond to the drift term and the diffusion term respectively. The Fokker-Planck equation for $P(V, t)$ is thus given by

$$\tau_m \frac{dP(V, t)}{dt} = -\frac{\partial}{\partial V}[(V - I_0)P(V, t)] + \frac{\sigma^2(t)}{2} \frac{\partial^2}{\partial V^2}P(V, t). \quad (\text{I.4.7})$$

At $V = V_{th}$, the neuron emits a spike and beyond this value of the membrane potential, the probability of finding the neuron is 0. Therefore, to satisfy continuity of the probability distribution $P(V_{th}) = 0$, the emitted spike contributes to the firing rate of the neuron and the probability current, $J(V = V_{th})$ is proportional to the firing rate of the neuron. This gives the condition:

$$\frac{\partial P}{\partial V}(V_{th}, t) = -\frac{2r(t)\tau}{\sigma^2(t)}. \quad (\text{I.4.8})$$

When the neuron spikes, it is reinitialized to the reset potential V_r and this imposes the condition that the current at V_r^+ is greater than the current at V_r^- by the same amount of current that is emitted at the threshold. This is written as

$$\frac{\partial P}{\partial V}(V_r^+, t) - \frac{\partial P}{\partial V}(V_r^-, t) = -\frac{2r(t)\tau}{\sigma^2(t)}. \quad (\text{I.4.9})$$

Finally, the probability distribution should be normalized to 1.

$$\int_{-\infty}^{\theta} P(V, t) dV = 1. \quad (\text{I.4.10})$$

For the integrability condition to hold, the probability distribution must satisfy two more conditions:

$$\lim_{V \rightarrow -\infty} P(V, t) = 0, \quad (\text{I.4.11})$$

$$\lim_{V \rightarrow -\infty} VP(V, t) = 0. \quad (\text{I.4.12})$$

The stationary solutions of the Fokker-Planck equation can be solved for and this gives for the probability distribution:

$$P_0(V) = 2 \frac{r_0 \tau_m}{\sigma} \exp\left(-\frac{(V - I_0)^2}{\sigma^2}\right) \int_{\frac{V - I_0}{\sigma}}^{\frac{V_{th} - I_0}{\sigma}} \Theta\left(u - \frac{V_r - I_0}{\sigma}\right) e^{u^2} du. \quad (\text{I.4.13})$$

Integrating the above equation to 1 gives the value of the firing rate. In the regime where $V_{th} - I_0 \gg \sigma$, the firing rate is given by

$$r_0 = \frac{(V_{th} - I_0)}{\sigma \sqrt{\pi} \tau_m} \exp\left(-\frac{(V_{th} - I_0)^2}{\sigma^2}\right). \quad (\text{I.4.14})$$

The dynamical response has also been calculated for the LIF model [Brunel and Hakim, 1999]. The static response and the dynamic response for the LIF neuron are shown in figure I.6.

However, for non-linear integrate-and-fire neuronal model and for models with a conductance based synaptic drive, such closed form analytical forms are not available for the static transfer function and the dynamical transfer function. One has to resort to numerical implementation schemes in these cases. Such an implementation for the EIF neuron model is outlined in the next section (See also [Richardson, 2007]).

1.5 Numerical implementation of the static transfer function and the dynamical transfer function

As we have mentioned in the previous section, the static transfer function and the dynamical transfer function are hard to extract analytically in the case of nonlinear integrate-and-fire neurons. In this section, we outline the numerical implementation of these functions for a general nonlinear IF neuron model and then show the results for the EIF neuron model since we will be using it for modeling the neuronal dynamics in this thesis [Richardson, 2007]. To begin with, the Fokker-Planck equation for the probability distribution of the voltage $P(V, t)$ is written as :

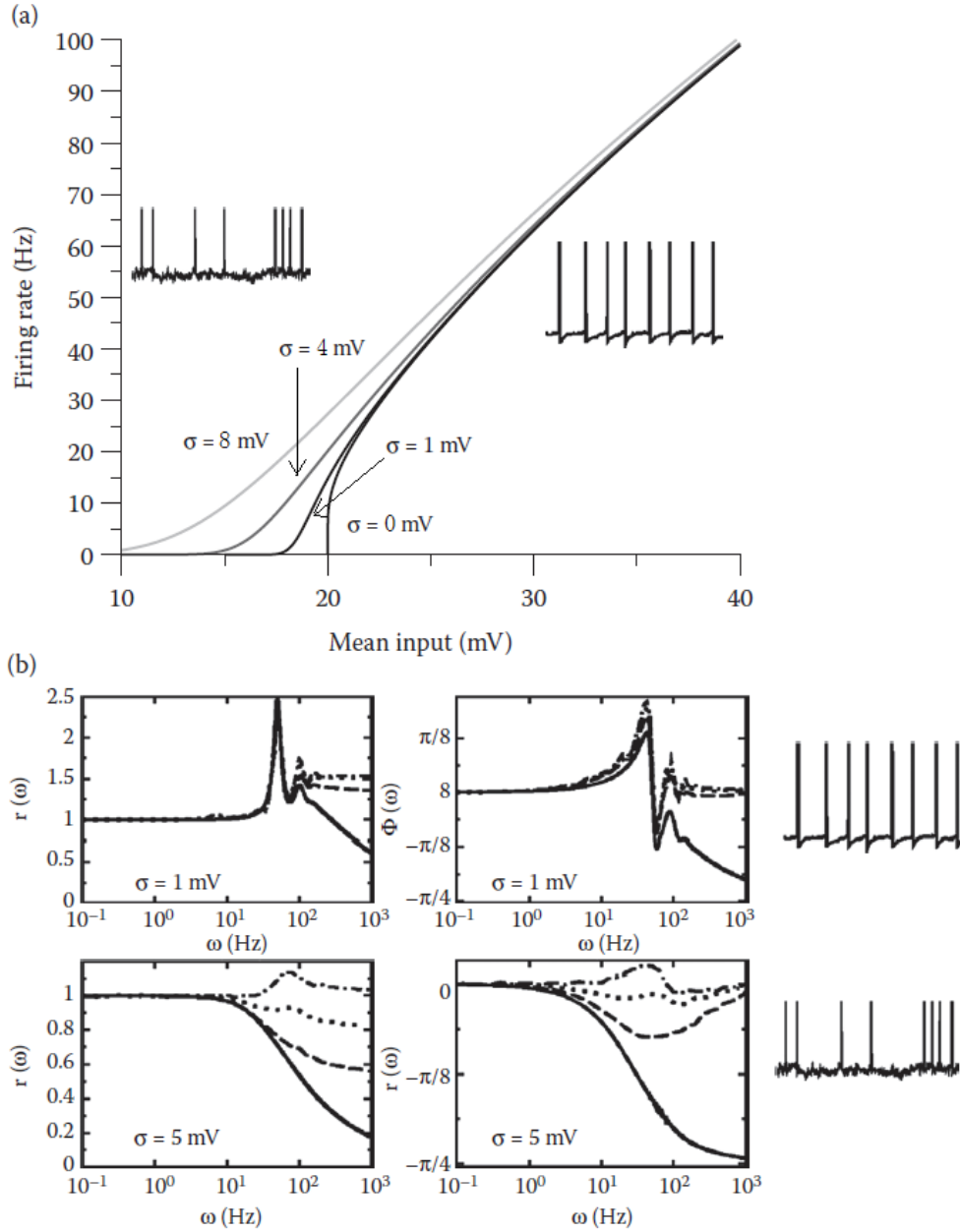


Figure I.6: **Static and dynamical transfer function for LIF neuron.** (a) The static transfer function or the f-I curve for the LIF model for four values of the noise 0mV, 1mV, 4mV and 8mV respectively. For 0mV of noise, we see a sharp increase in the firing rate at a mean input current of 20mV whereas for higher values of noise, the increase is gradual as a function of the mean input current. (b) The dynamical transfer function for the LIF neuron for weak noise on top and strong noise on bottom. The left panels show the amplitude and the right panels show the phase shift of the modulated instantaneous firing rate when a small sinusoidal input current of frequency ω is injected. A schematic spike train on the right shows the irregularity of spike emission. Taken from [Brunel, 2011].

$$\frac{\partial P}{\partial t} = \mathcal{L}P. \quad (\text{I.5.1})$$

The operator \mathcal{L} contains derivatives up to second order in voltage. From the continuity equation, which reads

$$\frac{\partial P}{\partial t} + \frac{\partial J}{\partial V} = 0, \quad (\text{I.5.2})$$

one can identify a current operator \mathcal{J} defined by $\mathcal{J}P = J$.

The spike and reset conditions of the model are taken into account by the boundary conditions as before. In the numerical simulations, a further constraint is added by taking a lower bound for the voltage V_{lb} . However, V_{lb} is chosen to be sufficiently negative so that its precise value does not affect the firing rate and probability density.

For the steady-state distribution

$$\mathcal{L}_0 P_0 = 0 \quad (\text{I.5.3})$$

i.e.

$$-\frac{\partial}{\partial V}[(V - I_0 - \Psi(V))P_0(V, t)] + \frac{\sigma^2(t)}{2} \frac{\partial^2}{\partial V^2} P_0(V, t) = 0, \quad (\text{I.5.4})$$

where $\Psi(V)$ is a nonlinear function of voltage and in the case of the EIF neuron model, it is given by $\Psi(V) = \Delta_T \exp((V - V_T)/(\Delta_T))$, where Δ_T is the sharpness of the action potential initiation and V_T is the membrane potential threshold. Upon integrating equation I.5.4, we get

$$-(V - I_0 - \Psi(V))P_0(V, t) + \frac{\sigma^2(t)}{2} \frac{\partial}{\partial V} P_0(V, t) = J_0(V). \quad (\text{I.5.5})$$

For the steady state current, one can write the following equation by absorbing the boundary conditions:

$$-\frac{\partial J_0}{\partial V} = r_0 [\delta(V - V_{th}) - \delta(V - V_{re})]. \quad (\text{I.5.6})$$

Note that the current J_0 is proportional to r_0 and hence, the stationary probability distribution is also proportional to r_0 . Therefore, we can define $j_0 = J_0/r_0$ and $p_0 = P_0/r_0$. Both the differential equations for the steady state are of the form

$$-\frac{\partial P}{\partial V} = GP + H. \quad (\text{I.5.7})$$

To find the static f-I curve and the dynamic rate response numerically, the voltage can be discretized into $n+1$ bins of size Δ over the range V_{lb} to V_{th} such that the k^{th} bin is given by $V^{(k)} = V_{lb} + k\Delta$ and the last bin $V^{(n)} = V_{th}$. A bin size Δ is chosen such that the k_{re}^{th} bin corresponds to the voltage V_{re} . To have good convergence properties, instead of implementing a straightforward Euler scheme, Richardson proposed the following method. The above equation is firstly integrated to get:

$$P^{(k-1)} = P^{(k)} e^{\int_{V^{(k-1)}}^{V^{(k)}} G(V) dV} + \int_{V^{(k-1)}}^{V^{(k)}} dV H(V) e^{\int_{V^{(k-1)}}^V G(U) dU}. \quad (\text{I.5.8})$$

G and H can be expanded around V^k to zero order in Δ which simplifies the above equation to

$$P^{(k-1)} = P^{(k)} e^{\Delta G^{(k)}} + \Delta H^{(k)} \left(\frac{e^{\Delta G^{(k)}} - 1}{\Delta G^{(k)}} \right), \quad (\text{I.5.9})$$

where $G^{(k)}$ and $H^{(k)}$ are the discretized versions of G and H. Upon defining the following dimensionless quantities,

$$A^{(k)} = e^{\Delta G^{(k)}}, \quad (\text{I.5.10})$$

$$B^{(k)} = \frac{1}{\sigma_0^2} \frac{e^{\Delta G^{(k)}} - 1}{\Delta G^{(k)}}, \quad (\text{I.5.11})$$

we can solve for the steady state probability density and the probability current by integrating the equations backwards from $V^{(n)} = V_{th}$ to $V^{(0)} = V_{lb}$ with initial conditions of $j_0^{(n)} = 1$ and $p_0^{(n)} = 0$. This leads to

$$p_0^{(k-1)} = p_0^{(k)} A^{(k)} + \Delta \tau_m j_0^{(k)} B^{(k)}, \quad (\text{I.5.12})$$

$$j_0^{(k-1)} = j_0^{(k)} - \delta_{k, k_{re}+1}, \quad (\text{I.5.13})$$

where $\delta_{a,b}$ is the Kronecker delta function which is equal to 1 when $a = b$ and it is zero otherwise.

The firing rate of the steady state distribution is then found by inverting the sum of un-normalized probability distribution i.e.

$$r_0 = \frac{1}{\sum_{k=0}^n \Delta p_0^{(k)}}.$$

To compute the dynamical rate response, we vary one of the parameters of the operator \mathcal{L} (say α) weakly in a cosinusoidal manner at an angular frequency velocity ω . The parameter could be the synaptic strength, firing rate of the population, etc. It is written as,

$$\alpha(t) = \alpha_0 + \alpha_1 \cos(\omega t). \quad (\text{I.5.14})$$

As a result, all the state variables can be written as :

$$P(V, t) = P_0(V) + P_\alpha \cos(\omega t + \psi_\alpha(V)), \quad (\text{I.5.15})$$

$$J(V, t) = J_0(V) + J_\alpha(V) \cos(\omega t + \gamma_\alpha(V)), \quad (\text{I.5.16})$$

$$r(t) = r_0 + r_\alpha \cos(\omega t + \rho_\alpha), \quad (\text{I.5.17})$$

where P_α , J_α , r_α are the amplitudes and ψ_α , γ_α , ρ_α are the phases of the probability distribution, probability current and firing rate respectively. The above equations can

also be written in a complex form i.e., for example, $r_\alpha \cos(\omega t + \rho_\alpha) + ir_\alpha \sin(\omega t + \rho_\alpha) = \hat{r}_\alpha e^{i\omega t}$.

Following the above definitions, the continuity equation

$$\frac{\partial P}{\partial t} + \frac{\partial J}{\partial V} = 0, \quad (\text{I.5.18})$$

becomes

$$-i\omega \hat{P}_\alpha = \frac{\partial J_\alpha}{\partial V}. \quad (\text{I.5.19})$$

By absorbing the boundary conditions, we get

$$-\frac{\partial J_\alpha}{\partial V} = i\omega \hat{P}_\alpha + \hat{r}_\alpha [\delta(V - V_{th}) - \delta(V - V_{re})]. \quad (\text{I.5.20})$$

And the Fokker-Planck equation together with the continuity equation gives,

$$\mathcal{J}P = J, \quad (\text{I.5.21})$$

$$(\mathcal{J}_0 + \hat{\mathcal{J}}_\alpha e^{i\omega t})(P_0 + \hat{P}_\alpha e^{i\omega t}) = J_0 + J_\alpha e^{i\omega t}, \quad (\text{I.5.22})$$

with $\mathcal{J}_0 P_0 = J_0$ and

$$\hat{\mathcal{J}}_\alpha P_0 + \mathcal{J}_0 \hat{P}_\alpha = \hat{J}_\alpha. \quad (\text{I.5.23})$$

We have ignored the higher order terms because the variation in the parameter α is weak. Representing $F_\alpha = -\hat{\mathcal{J}}_\alpha P_0$, we get

$$\mathcal{J}_0 \hat{P}_\alpha = \hat{J}_\alpha + F_\alpha. \quad (\text{I.5.24})$$

The solutions \hat{J}_α and \hat{P}_α are separated as:

$$\hat{J}_\alpha = \hat{r}_\alpha \hat{j}_r + \alpha_1 \hat{j}_\alpha, \quad (\text{I.5.25})$$

$$\hat{P}_\alpha = \hat{r}_\alpha \hat{p}_r + \alpha_1 \hat{p}_\alpha. \quad (\text{I.5.26})$$

This can be done because the modulations in \hat{J}_α and \hat{P}_α are due to the modulations in the parameter α and in the firing rate \hat{r}_α respectively. Even though the firing rate \hat{r}_α is being modulated by α , it provides an additional contribution to the current modulation \hat{J}_α and hence, we can study the two terms separately.

Therefore, when we study the above two equations with $\alpha = 0$ i.e. $F_\alpha = 0$, we get two equations for \hat{j}_r and \hat{p}_r with boundary conditions $\hat{j}_r(V_{th}) = 1$ and $\hat{p}_r(V_{th}) = 0$:

$$-\frac{\partial \hat{j}_r}{\partial V} = i\omega \hat{p}_r + \delta(V - V_{th}) - \delta(V - V_{re}), \quad (\text{I.5.27})$$

$$\mathcal{J}_0 \hat{p}_r = \hat{j}_r. \quad (\text{I.5.28})$$

Similarly, after defining $F_\alpha = \alpha_1 f_\alpha$ we get two equations for \hat{j}_α and \hat{p}_α with the boundary conditions $\hat{j}_\alpha(V_{th}) = 0$ and $\hat{p}_\alpha(V_{th}) = 0$:

$$-\frac{\partial \hat{j}_\alpha}{\partial V} = i\omega \hat{p}_\alpha, \quad (\text{I.5.29})$$

$$\mathcal{J}_0 \hat{p}_\alpha = \hat{j}_\alpha + f_\alpha. \quad (\text{I.5.30})$$

Both these pairs of equations can be integrated backwards and the firing rate modulation can be calculated as (from the condition $J(V_{lb}, t) = 0$) :

$$\hat{r}_\alpha = -\alpha_1 \frac{\hat{j}_\alpha(V_{lb})}{\hat{j}_r(V_{lb})}. \quad (\text{I.5.31})$$

When the above algorithm is implemented for the EIF neuron, one obtains the results shown in figure I.7.

I.6 Analyzing network dynamics

Equipped with tools to analyze the firing rate of a single neuron, one can proceed to understand dynamics of networks of neurons. To analyze network dynamics, one can either perform numerical simulations or analytical calculations (in several limiting cases). To perform numerical simulations, we use the package BRIAN2, written in the Python programming language [Goodman and Brette, 2008] [Goodman and Brette, 2009]. To specify a network model, one needs to define (1) the number of neuronal populations in the network, number of neurons per population and the connectivity matrix of the network, (2) the external inputs to the neurons in the network, (3) the dynamics of the single neurons in the network and (4) the dynamics of the synaptic connections.

I.6.1 Analyzing network dynamics using numerical simulations

BRIAN2 can be used to define neuron models by systems of differential equations, which specify the voltage dynamics of populations of neurons. These voltage dynamics are defined using objects called NeuronGroups. These differential equations could correspond to any neuron model that we want to implement, for example LIF neuron, EIF neuron etc. We can also specify the integration method for the differential equations, the threshold of spiking, the reset potential, the refractory period. Brian is a clock-driven simulator as opposed to an event-driven simulator. In a clock-driven simulator, the simulation is performed on an equally spaced time grid, $0, dt, 2*dt, 3*dt, \dots$ and at each time step t , the differential equations are first integrated giving the values for the variables (membrane potentials) at time $t+dt$. If a condition such as $V > V_{th}$ is satisfied, spikes are then generated and spikes can only occur on the time grid. On the other hand, event-driven simulators are more accurate than clock-driven simulators in that the spikes can occur at arbitrary times, but they are computationally more expensive and they are usually more restrictive in terms of the differential equations that can be specified for the neuron models. Clock driven simulators, though faster and efficient for networks with a large size, are susceptible to erroneous results if one does not use the correct time step [Rudolph and Destexhe, 2009]. Therefore,

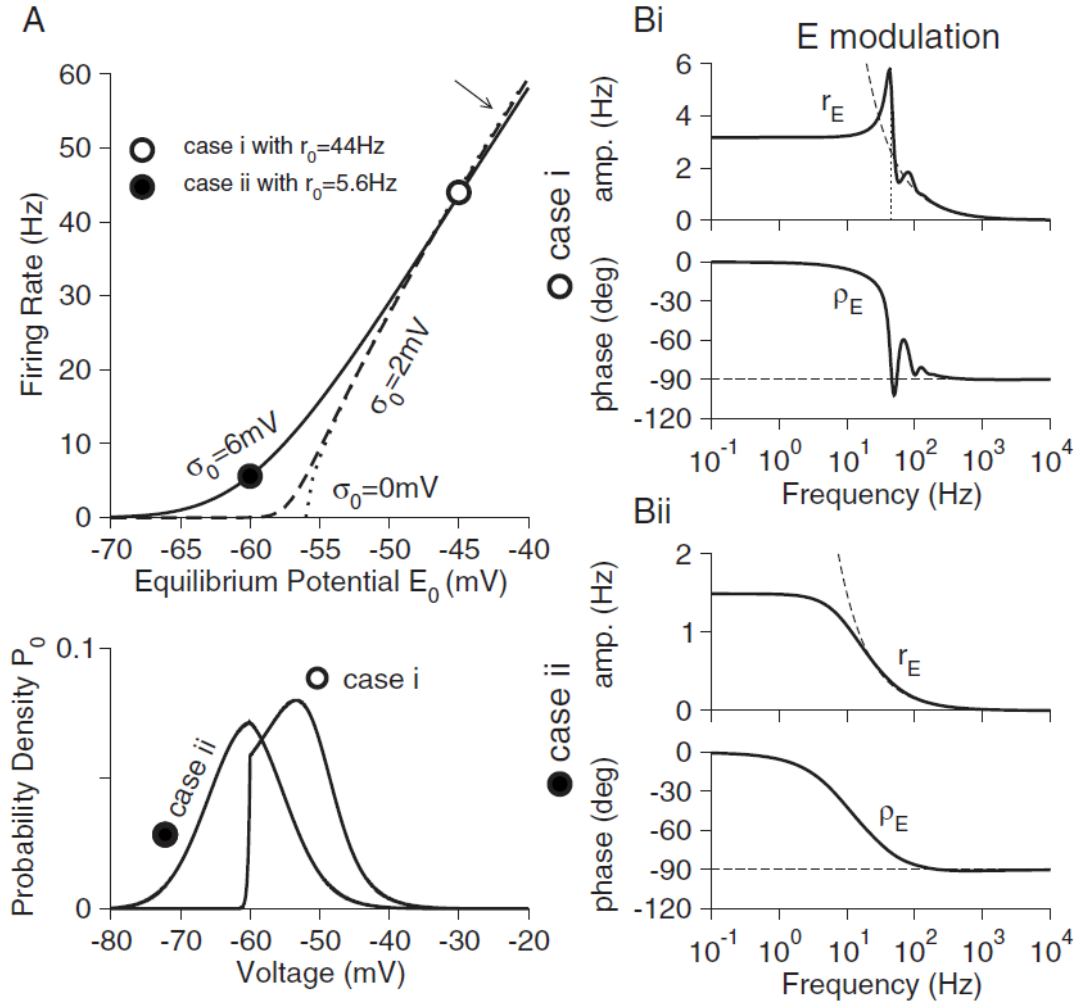


Figure I.7: **Static and dynamic transfer functions of EIF neuron.** A. Top panel: The static transfer function for different noise strengths σ_0 . The lower panel shows the steady-state probability densities for the two cases shown in the top panel. B. The bold lines in the amplitude and phase panels shows the dynamical transfer function and the dashed lines are the high-frequency asymptotics. Bi and Bii are for case i and case ii respectively. Taken from [Richardson, 2007].

in clock-driven simulators such as BRIAN2, one can reduce errors which overestimate synchrony by choosing the appropriate time step dt (see [Brette et al., 2007]).

Using BRIAN2 packages such as StateMonitors and PopulationMonitors, one can obtain the population firing rates and the population raster plots (spikes times of neurons) respectively. The neurons in different neuron groups or across different groups can be connected by synapses using the command Synapses. A connection probability can be specified for finite connectivity instead of all-to-all connectivity. Synapses can be specified by implementing the effect on the post synaptic neuron upon a presynaptic spike. The simplest synapse would be a delta synapse, where the membrane potential of the post synaptic neuron increases by a certain amount because of a presynaptic spike. More complicated postsynaptic functions and synaptic plasticity rules can be added to build more realistic models. Finally, the Network object handles the running of the simulation and consists of a set of BRIAN2 objects such as NeuronGroups, Synapses and the different monitors. The Network object is called using “run” method to run the simulation.

BRIAN2’s user-visible part will therefore have objects such as NeuronGroup, Synapses, Network, etc. all written in Python. BRIAN2 translates these objects into short blocks of code. The order of execution of these code blocks in each time step is specified by the order of the object in the function schedule in the Network object (Network.schedule), which is [‘start’, ‘groups’, ‘thresholds’, ‘synapses’, ‘resets’, ‘end’] by default.

I.6.2 Analyzing network dynamics using analytical calculations

Analytical calculations can be performed in several limiting cases [Brunel and Hakim, 1999] [Brunel, 2000]. If the network is fully connected, and the synapses are weak $\sim O(1/N)$, then in the presence of a white noise, the dynamics of the probability density of the voltage $P(V, t)$, can be described by the Fokker-Planck equation. Note that this is qualitatively similar to the computation in the case of a single neuron. The firing rate of the population in this case is the number of spikes emitted per neuron per time-bin. The difference as opposed to the case of the computation for a single neuron arises from the fact that now, the input to the neuron (drift term in the Fokker-Planck equation) is not only the external input but also the recurrent inputs from the network. The diffusion term corresponds to the injected external noise as before. The firing rate in this case is given by the first passage mean rate over the threshold [Abbott and van Vreeswijk, 1993].

However, real networks are sparsely connected with a probability of connection of about 0.1 [?]. To solve the dynamics of such sparsely connected networks, two approximations have to be made [Amit and Brunel, 1997] [Brunel and Hakim, 1999] [Brunel, 2000]. The first one is approximating the total synaptic inputs to a given neuron by a Gaussian white noise. This is called the diffusion approximation and follows from the central limit theorem. If each neuron is considered Poissonian in its firing rate, then a sum of these inputs to each neuron can be approximated by a Gaussian white noise. However, this is only valid when the temporal correlations in the inputs can be neglected and when the synaptic inputs are weak compared to the threshold. Moreover, the noise terms to each neuron are considered to be uncorrelated. This is true only when the connection probability is small. Neglecting the temporal

correlations in the input to each neuron and the correlations among different neurons, the synaptic inputs to neuron i is given by:

$$I_{syn,i}(t) = \mu(t) + \sigma(t)\sqrt{\tau_m}\eta_i(t) \quad (\text{I.6.1})$$

where the average synaptic input is given by $\mu(t) = CJr(t)\tau_m$ and the variance in the synaptic input is given by $\sigma^2(t) = CJ^2r(t)\tau_m$ and $\eta_i(t)$ is a random normal variable. Here C is the number of excitatory connections any neuron receives, J is the strength of the excitatory synaptic connection, $r(t)$ is the firing rate of the population and τ_m is the membrane time constant of the neuron. The noise terms $\eta_i(t)$ are assumed to be uncorrelated and this is valid only when the connectivity is sparse, so that the fraction of common inputs received by any two neurons can be neglected.

With these two approximations, the dynamics of the network can be described by the Fokker-Planck equation. The difference with the fully connected network or the unconnected network is that the fluctuations in the input comprise of the external fluctuations as well as fluctuations from the network. For constant external inputs, the steady state solutions or the “asynchronous state”, i.e. states with stationary global activity and where individual neurons are not synchronized, can be computed and the firing rates can be obtained numerically [Amit and Brunel, 1997] [Brunel and Hakim, 1999] [Brunel, 2000]. Linear stability analysis can then be used to compute the stability of the asynchronous state [Abbott and van Vreeswijk, 1993] [Brunel and Hakim, 1999]. The phase space can be charted out and the bifurcations can be marked. A typical bifurcation of the inhibitory neuronal networks is the Hopf bifurcation which results in synchronized network oscillations, where the population firing rate oscillates in time. Neurons are therefore correlated through this population oscillation and these oscillatory states can also be characterized using weakly nonlinear analysis in some cases. Using a diffusion approximation of the global network activity, the finite-size effects can also be computed [Brunel and Hakim, 1999]. To compute the effects of time-dependent external inputs on the network, one can use linear response theory to compute the network dynamical transfer function [Ledoux and Brunel, 2011].

1.6.3 Dynamics of Fully Connected Excitatory Networks

We can fix the firing rate of a purely excitatory network to be 10Hz and vary the noise level σ and the coupling strength J . This determines the external current that needs to be injected into the neurons of the network. We can then determine the stability of this asynchronous state. The stability diagram is shown in figure I.8. The asynchronous stable state can become unstable in two ways: via a saddle-node bifurcation leading to a rate instability or a Hopf bifurcation leading to synchronized oscillations where the whole network exhibits periodic bursting activity. All the neurons spike synchronously in each burst and hence, the state is also termed as “spike-to-spike” synchrony.

1.7 Conclusion

In this chapter, we showed simple models to single neural activity, starting with the HH model. Later, we outlined the shortcomings of this model and looked at other

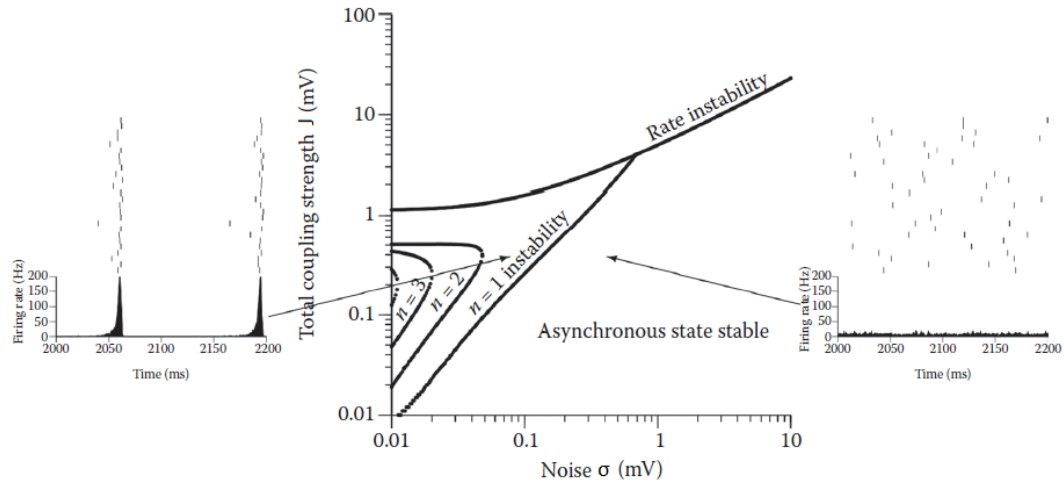


Figure I.8: **Dynamics of fully connected excitatory networks.** The central panel shows the phase diagram in the σ - J plane. The asynchronous stable state undergoes a Hopf bifurcation for weak noise leading to synchronized oscillations and for larger values of the noise, the asynchronous state destabilizes due to a rate instability. Taken from [Brunel, 2011].

simple single neuron models which implement the essential features of neurons such as spike generation and refractory effects that we are interested in this thesis. We looked at the firing rate of a single neuron and introduced two quantities that help us understand the dynamics of the firing rate: the static transfer function and the dynamical transfer function. We looked at how these quantities can be computed analytically and numerically. Finally, we looked at how these quantities help us analyze the dynamics of a network of neurons.

Chapter II

Rate models - an introduction

II.1 Rate Models

As we have seen in the previous chapter, one quantity that can be used to describe the dynamics of networks of neurons is the firing rate of the network. To recapitulate, the firing rate of the network is defined as the number of spikes per neuron in a given time-bin. There is some evidence that it is the population firing rate of a network that encodes properties about the stimulus [Shadlen and Newsome, 1998]. For this reason, several phenomenological models have emerged to give a qualitative description of the dynamics of the firing rate. The first approach in this direction was based on methods from statistical mechanics and are known under various names, ‘neural field models’, ‘neural mass models’ and ‘rate models’ [Beurle, 1956] [Griffith, 1963] [Griffith, 1965] [Wilson and Cowan, 1972] [Wilson and Cowan, 1973] [Amari, 1977]. In this section, we will introduce these models and relate them to the networks of spiking neurons in the next section.

II.1.1 Single population models

In the single population rate model, the time evolution of the firing rate r is given by the following equation:

$$\tau \frac{dr}{dt} = -r + \Phi(I_{ext} + Jr). \quad (\text{II.1.1})$$

where τ is the time constant of the firing rate dynamics, I_{ext} is the input current to the population and J is the self-coupling strength of the population. If $J > 0$, the population is described as excitatory and if $J < 0$, it is inhibitory. The function Φ is the static transfer function or the f-I (firing rate-current) curve that gives the steady state firing rate of the population when subjected to a fixed external current. The function Φ must be a non-negative number since the firing rate is only non-negative and must saturate for high values of the input current.

Different choices for the static transfer function include the sigmoid function $\Phi(I) = r_0(1+\tanh(I-I_0))/2$, the threshold linear transfer function $\Phi(I) = \begin{cases} I - T, & \text{if } I \geq T \\ 0, & \text{otherwise} \end{cases}$, the f-I curve of single-neuron models.

The rate model for a single population can also be written in terms of the dynamics of the current as follows:

$$\tau \frac{dI}{dt} = -I + I_{ext} + Jr, \quad (\text{II.1.2})$$

where the firing rate, $r = \Phi(I)$. The above two models are equivalent and this is clear when we make the substitution $I = I_{ext} + Jr$ in the first model. We obtain:

$$\tau \frac{dI}{dt} = J\tau \frac{dr}{dt} = -Jr + J\Phi(I), \quad (\text{II.1.3})$$

$$= -I + I_{ext} + J\Phi(I) = -I + I_{ext} + Jr. \quad (\text{II.1.4})$$

In this manuscript, we will be mostly describing the dynamics of the neuronal populations in terms of the dynamics of the currents. For a one-population network and constant inputs, the firing rate equation has at least one fixed point that can be obtained by solving

$$r = \Phi(I_{ext} + Jr). \quad (\text{II.1.5})$$

For an inhibitory network, only a single fixed point exists whereas for an excitatory network, either one stable state or two stable states are possible depending on the value of J (see figure II.1). For the case with two stable points, the network can exhibit bistability, between a low and a high activity state.

II.1.2 Models with adaptation

Models with adaptation will be discussed in more detail in chapter IV. Various types of adaptation currents are present in neurons. Since these currents vary on much slower timescales than synaptic currents, they can be added to firing rate models by introducing variables which are proportional to the firing rate of the population. The dynamics of these variables are slower than that of the rate variables [Tsodyks et al., 1998] [Tsodyks et al., 2000] [Tabak et al., 2000] [Fuhrmann et al., 2002] [Laing and Chow, 2002].

II.1.3 Linear Nonlinear (LN) models

The Linear Nonlinear cascade model is another kind of model that determines the firing rate response of a neuron to a given stimulus [Chichilnisky, 2001] [Truccolo et al., 2004] [Pillow et al., 2008]. The model consists of a linear filter followed by a nonlinearity. In this model, the firing rate, r , of a network is determined by applying a nonlinear function, F , to the result of the convolution of the input stimulus, $I(t)$ with a linear filter, $D(t)$, see equation II.1.6. The linear filter consists of the neuron's space time receptive field and describe the feature selectivity of the neuron. The linear filter is convolved with the stimulus at this stage. The nonlinearity then describes how this filtered stimulus is converted to the instantaneous spike rate. The nonlinearity function also accounts for effects such as thresholding, rectification and saturation [Pillow, 2007].

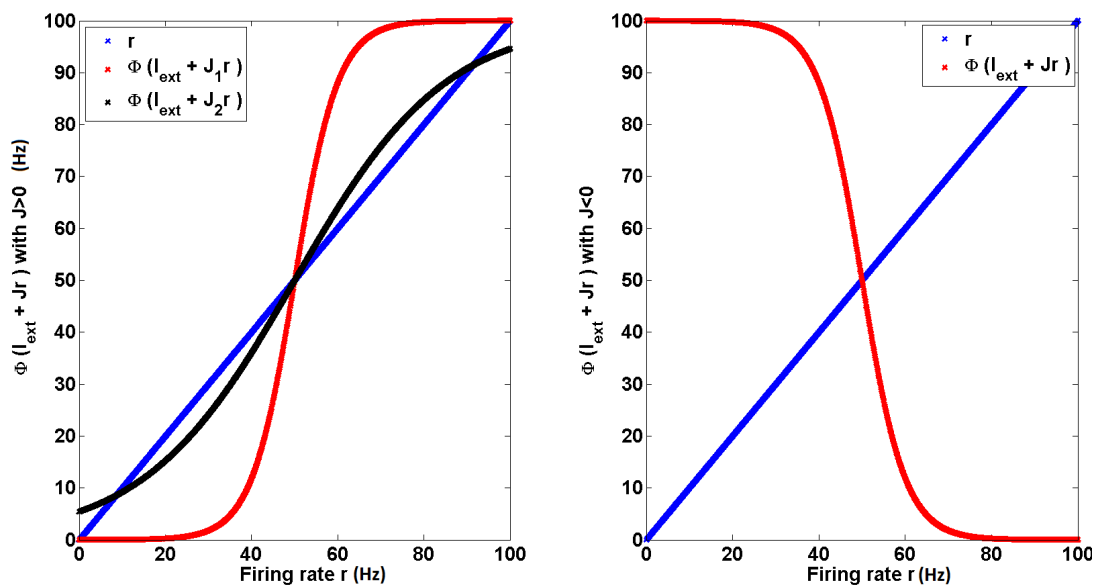


Figure II.1: **The fixed points of firing rate equation for one population.** The left panel shows the fixed points in the case of excitatory coupling. The firing rate r is plotted in blue and the function on the right $\Phi(I_{ext} + Jr)$ is plotted in red and black for two values of J . Note that depending on the value of J , the model can exhibit either one fixed point (red curve) or three fixed points (black curve), of which two are stable and one is unstable. The panel on the right shows the fixed point in the case of inhibitory coupling. The firing rate r is plotted in blue and the function on the right $\Phi(I_{ext} + Jr)$ is plotted in red. Note that in the case of inhibitory coupling, we will have only one fixed point.

$$r(t) = F(D * I(t)) \quad (\text{II.1.6})$$

The linear cascade model is not biophysically realistic but it provides a reasonable estimate of the firing rate in many early sensory areas. The linear filter is estimated using the spike triggered average or the reverse correlation [Bryant and Segundo, 1976] and the nonlinear function is estimated using a simple histogram procedure [Bryant and Segundo, 1976] [Chichilnisky, 2001].

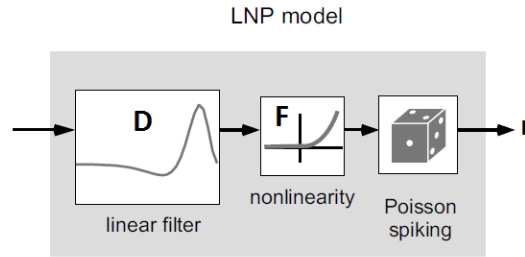


Figure II.2: **Schematic description of a linear nonlinear Poisson model.** The input stimulus is filtered through a linear filter and then passed through a nonlinearity to give the firing rate. The firing rate is used to generate spikes with a Poisson distribution. Taken from [Pillow, 2007].

II.2 Bridging spiking neuron models and rate models

Spiking neuron models offer insight into dynamics of local networks whereas neural rate models provide an insight into the global activity of networks. Both types of models exhibit qualitatively similar population dynamics such as multistability properties and the emergence of global oscillations. The rate models cannot be derived by averaging the slow variables in the network of spiking neurons [Ermentrout, 1994]. Recently, Ostojic and Brunel (2011) have shown that the decay in $1/f$ of the linear firing rate response of the EIF model makes it particularly suitable to perform an approximate reduction to a rate model. This is because the linear filter then resembles the Fourier transform of a decaying exponential function for high frequencies. To outline their derivation, let us consider a network of neurons that is stimulated with an input current $I(t) = I_0 + \sigma\eta(t) + I_s n(t)$. Here, $n(t)$ is a Gaussian process with zero mean, unit variance and correlation time τ_s , I_s is the standard deviation of the temporally correlated Gaussian noise, σ is the standard deviation of the temporally uncorrelated Gaussian noise, I_0 is the static input current into the neurons and $\eta(t)$ is a white (no temporal correlations) Gaussian process with zero mean and unit variance i.e. $\langle \eta(t)\eta(t') \rangle = \delta(t - t')$.

The different realizations of the correlated Gaussian noise $n(t)$ are generated through the equation:

$$\tau_s \frac{dn(t)}{dt} = -n(t) + \zeta(t),$$

where $\zeta(t)$ is a zero-mean, unit variance temporally uncorrelated Gaussian process, with zero mean, unit variance i.e.

$$\langle \zeta(t)\zeta(t') \rangle = \delta(t - t').$$

For simplicity, let us consider a network of unconnected neurons. In this case, since all the neurons in the network are stimulated with the same input current, the firing rate of the network is equivalent to the firing rate of a single neuron over different trials of stimulation with the same input current. This firing rate can be derived in two different ways. One way is to employ a generalized linear nonlinear model, wherein the input current is firstly filtered through a linear filter and then passed through a nonlinearity to determine the firing rate. The LN model, though enabling us to perform the mapping between sensory inputs and output firing rate, lacks a direct one to one correspondence with the underlying biophysics of single neurons. Spiking neuron models, on the other hand, capture the details of the membrane potential dynamics. However, simulations of networks of spiking neurons are computationally more expensive and analytically less tractable. Ostojic and Brunel showed that these spiking neuron models can be mapped onto a linear-nonlinear cascade [Ostojic and Brunel, 2011] as follows:

$$r(t) = F(D \star I_s n(t)), \quad (\text{II.2.1})$$

where $s(t)$ is the signal input, D is the temporal linear filter and F is the static non-linearity and $D \star I_s n(t)$ is the convolution between D and $s(t)$ i.e.

$$D \star I_s n(t) = \int_0^\infty d\tau D(\tau) I_s n(t - \tau). \quad (\text{II.2.2})$$

They derived the corresponding LN models for the case of LIF neurons, EIF neurons and conductance based Wang-Buzsaki models [Wang and Buzsaki, 1996]. The approximation of the firing rate dynamics of the spiking neuron model by the LN model becomes exact in two limiting cases:

(1) when the amplitude of the signal goes to zero i.e. $I_s \rightarrow 0$. This is because in this case, we can perform Taylor expansion of $r(t)$ around r_0 and we get

$$r(t) = F(0) + F'(0) I_s D \star n(t). \quad (\text{II.2.3})$$

We can identify the dynamical rate response function of a neuron $R_n(t)$ in the above equation:

$$r(t) = r_0 + I_s R_n(t) \star n(t) \quad (\text{II.2.4})$$

Thus, in this limit, the two models are exactly equal to each other as can be seen by looking at equations II.2.3 and II.2.4. $R_n(t)$ depends on I_0 and σ ,

(2) when the correlation time $\tau_s \rightarrow \infty$. This means that the variation in input signal is very long compared to the timescale of the linear filter and so, we can write $D \star n(t) = D_0 n(t)$, with $D_0 = \int_0^\infty d\tau D(\tau)$ and this gives

$$r(t) = F(D_0 I_s n(t)). \quad (\text{II.2.5})$$

The above equation resembles the equation for the f-I curve where the input current is a white noise of mean $I_0 + I_s n(t)$ and variance σ and the f-I curve Φ reads as $\Phi(I_0 + L/D_0) = F(L)$. These values for $F(L)$ and $D(t)$ are then extended to the whole parameter space.

In the case of the EIF model, the rate response function and hence, the linear filter can be approximated by an exponential with a single effective timescale τ_{eff} as

$$D_{eff}(t) = A \exp(-t/\tau_{eff}). \quad (\text{II.2.6})$$

To derive the effective timescale τ_{eff} , Ostojic and Brunel [Ostojic and Brunel, 2011] consider the amplitude of the higher frequencies of the Fourier transform of $D(t)$. This amplitude decays as $r_0/(\Delta_T 2\pi \tau_m f)$, whereas for low frequencies, the amplitude reaches a finite value equal to the slope of the f-I curve evaluated at the I_0 . They match these observations with the Fourier transform of D_{eff} i.e. $(\tau_{eff} A)/(1 + i2\pi f \tau_{eff})$, to obtain:

$$\tau_{eff} = \tau_m \Delta_T \frac{\Phi'(I_0)}{r_0}, \quad (\text{II.2.7})$$

$$A = \frac{\Phi'(I_0)}{\tau_{eff}}. \quad (\text{II.2.8})$$

With such a filter, the linear nonlinear cascade for this model can be rewritten in the form of a dynamical system

$$r(t) = \Phi(I), \quad (\text{II.2.9})$$

$$\tau_{eff} \frac{dI}{dt} = -I + I_0 + s(t). \quad (\text{II.2.10})$$

Ostojic and Brunel [Ostojic and Brunel, 2011] then introduce the adaptive timescale rate model, where the timescale is a function of the instantaneous firing rate. They found that this model provides a better estimate of the Peristimulus time histogram (PSTH) of the neuron when compared to the LN model or the non-adaptive time scale rate model for the exponential-integrate-and-fire neuron (see figure II.3). The Peri-Stimulus Time Histogram or the PSTH i.e. is the time dependent firing rate of the neuron and is obtained by averaging the spike rate over trials.

The timescale in this model is given as:

$$\tau_{eff}(t) = \tau_m \Delta_T \frac{\Phi'(I(t))}{r(t)}. \quad (\text{II.2.11})$$

We will refer to this model as adaptive rate 0 (AR0) model in the following.

II.3 Autocorrelation of the firing rate

In this section, we will look at the autocorrelation function of the population firing rate of a single excitatory population and analyze it using the adaptive timescale rate model that was described in the previous section. The autocorrelation $A(\tau)$ of the population firing rate $r(t)$ is defined as follows:

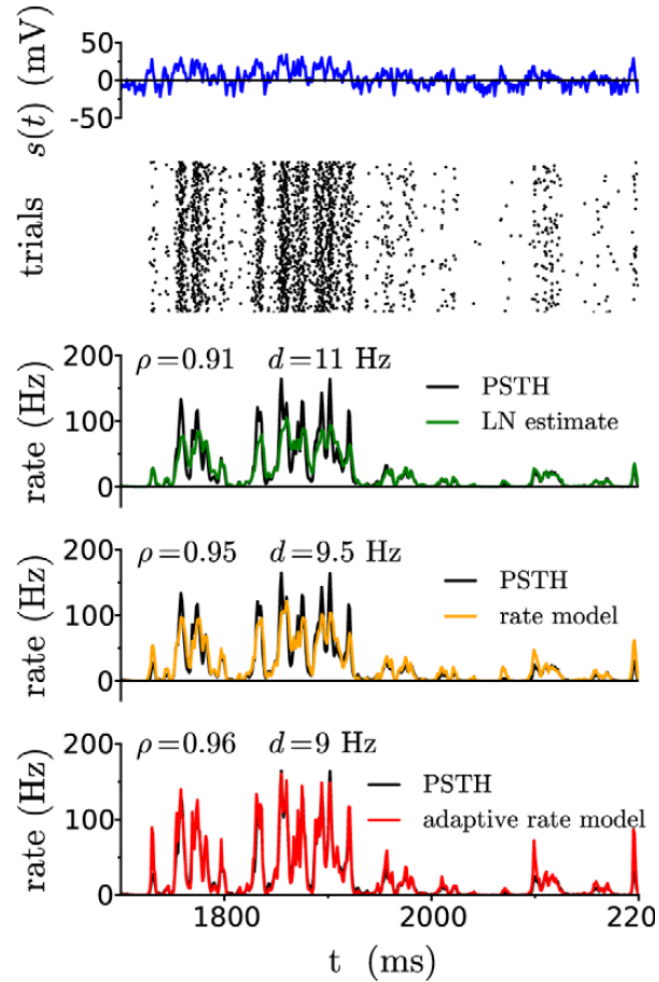


Figure II.3: **The different estimates of the rate models for firing rate of network of EIF neurons.** The input current is shown in the top panel trace and the raster plot of the neurons is shown in the second panel for 200 trials. The next three panels compare the firing rate of the network of independent neurons (PSTH-Peristimulus time histogram) with the LN estimate, the rate model and the adaptive timescale rate model. ρ is the correlation coefficient between the two signals and d is the root-mean-square-difference between the two signals. Taken from [Ostojic and Brunel, 2011].

τ_m	10ms	v_L	-65mV
ΔT	3.5mV	v_T	-59.9mV
v_R	-68mV	v_{th}	-30mV
σ	10mV	N_e	1000
J	0.1 mV	C	200

Table II.1: Parameters used in the network simulation for studying the autocorrelation of the firing rate.

$$A(\tau) = \lim_{T \rightarrow \infty} \frac{1}{T} \int_{t=0}^{t=T} dt (r(t) - r_0)(r(t + \tau) - r_0), \quad (\text{II.3.1})$$

where r_0 is the mean of the population firing rate. For the discretized version, we have

$$A_j = \frac{1}{N-j} \sum_{i=1}^{N-j} \delta r_i \delta r_{i+j}, \quad (\text{II.3.2})$$

where N is the number of samples and $\delta r_i = r_i - \frac{1}{N} \sum_{k=1}^N (r_k)$.

For the network simulations, we use a network of $N_e = 1000$ EIF neurons connected via delta synapses with an incoming connectivity of $C = 200$ per neuron. The neuronal membrane potentials v obeys the following equations:

$$\frac{dv}{dt} = \frac{-v + v_L + F_v + I_{ext}}{\tau_m} + \frac{\sigma}{\sqrt{\tau}} \eta_i(t), \quad (\text{II.3.3})$$

$$F_v = \Delta_T \exp\left(\frac{v - v_T}{\Delta_T}\right), \quad (\text{II.3.4})$$

where v_L is the leak voltage, I_{ext} is the external current that is injected into the neuron, σ^2 is the variance of the white noise inserted into the neuron, η_i is a random normal variable associated with neuron i , τ_m is the membrane time constant, Δ_T is the sharpness of the action potential initiation v_T is the membrane potential threshold, N_e is the number of neurons in the network, C is the number of excitatory connections to each neuron. Moreover, whenever there is a presynaptic spike, there is an increase in the membrane voltage of the postsynaptic neuron by an amount J on the next time step (delta synapse). When the membrane potential of any neuron crosses v_T , it diverges to infinity in finite time. Therefore, when the membrane potential reaches the threshold potential v_{th} , we insert a spike for the neuron and the membrane potential of the neuron is reset to v_R . For a duration of t_{ref} , the refractory time period, the neuron is clamped to the voltage v_R , before it resumes its dynamics again according to the above equations. We run the simulation for a time duration of 1000 s and use the following parameters for the neurons.

The network of neurons has an input current I_{ext} apart from a white Gaussian noise of zero mean and standard deviation 10 mV. We insert a mean current of $I_{ext} = I_0 = -6.29$ mV such that the network has a steady state time-averaged firing rate of 5 Hz. The dynamics of this network corresponds to the asynchronous stable state shown in figure I.8.

The autocorrelation for a single excitatory population is shown in figure II.4. The value of the autocorrelation at $t=0$ corresponds to the variance of the firing rate. We notice that the population has a variance much larger compared to the autocorrelation at non zero time and that the autocorrelation for $t>0$ decays exponentially as can be seen from the fit with an exponential.

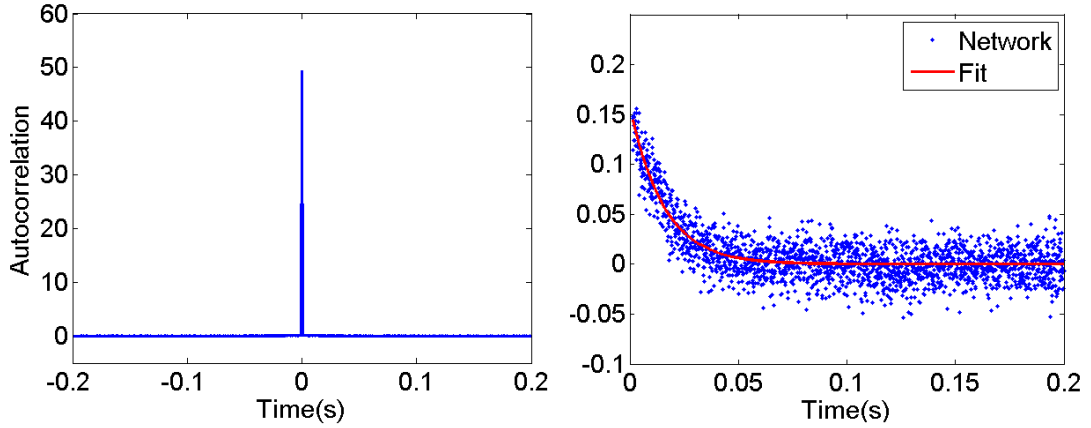


Figure II.4: **Autocorrelation of the population firing rate of a single excitatory population.** The left panel shows the autocorrelation of the population firing rate of a single excitatory population. Notice that the autocorrelation at time $t=0$ i.e. the variance of the firing rate is much larger than the autocorrelation for non-zero time t . The panel on the right zooms in on the autocorrelation function for time $t>0$. The autocorrelation function can be fitted with a single exponential function.

We want to compare these results to the one we obtain in the case of an adaptive timescale rate model. We will derive the autocorrelation of the population firing rate for the rate model of a single excitatory population. To recapitulate, the dynamics of an adaptive timescale rate model (equations II.2.9 - II.2.11) is listed below:

$$r(t) = \Phi(I(t)), \quad (\text{II.3.5})$$

$$\tau_{eff}(I(t)) \frac{dI(t)}{dt} = -I(t) + I_{ext}(t), \quad (\text{II.3.6})$$

with τ_{eff} given by

$$\tau_{eff}(I(t)) = \tau_m \Delta_T \frac{\Phi'(I(t))}{\Phi(I(t))}. \quad (\text{II.3.7})$$

The above equations do not account for the finite size of the network ($N_e = 1000$). To include the finite size effects, we add a noise term to the rate equation which can be estimated as follows. Consider a neuron which fires a spike with a probability of $\nu \Delta t$ in a time-bin Δt when a current I_0 is inserted into it. When the network of N_e neurons is inserted with this current, then the firing rate per neuron in this time-bin is

$$r = \frac{\sum_j s_j}{N_e \Delta t}, \quad (\text{II.3.8})$$

where $s_j = 1$ if the j th neuron spikes and 0 otherwise. $s_j = 1$ with a firing probability of $\nu \Delta t$. We can consider all the variables s_j to be independent because all the neurons receive uncorrelated inputs. Though there is connectivity between the neurons, when the synaptic inputs to the neurons are low, the correlations between synaptic inputs to different neurons can be neglected in favour of the external noise injected to each neuron. However, for high excitatory synaptic strengths and high firing rates, the above assumption may no longer hold. With this assumption, the mean firing rate is given by

$$\langle r \rangle = \frac{\langle \sum_j s_j \rangle}{N_e \Delta t} = \nu. \quad (\text{II.3.9})$$

And the variance in the firing rate per neuron in a time-bin Δt is given by

$$\langle r^2 \rangle - \langle r \rangle^2 = \frac{\langle (\sum_j s_j)^2 \rangle}{N_e^2 \Delta t^2} - \nu^2 \quad (\text{II.3.10})$$

$$= \frac{\langle \sum_j s_j^2 \rangle + 2 \sum_{i>j} \langle s_i s_j \rangle}{N_e^2 \Delta t^2} - \nu^2 \quad (\text{II.3.11})$$

(making the independence assumption)

$$= \frac{N_e \nu \Delta t - N_e (N_e - 1) \nu^2 \Delta t^2}{N_e^2 \Delta t^2} - \nu^2 \quad (\text{II.3.12})$$

$$= \frac{N_e \nu \Delta t - N_e \nu^2 \Delta t^2}{N_e^2 \Delta t^2} \quad (\text{II.3.13})$$

$$\approx \frac{\nu}{N_e \Delta t} \quad (\text{II.3.14})$$

$$= \frac{\langle r \rangle}{N_e \Delta t}. \quad (\text{II.3.15})$$

We see that the variance goes as $1/N_e$. The higher order cumulants can therefore be neglected and we can approximate the firing rate process by a Gaussian process with a mean $\Phi(I(t))$ and a variance $\Phi(I(t))/N_e$. We can include this variance in firing rate, due to finite size of the population, in the adaptive time scale rate model as follows:

$$r(t) = \Phi(I(t)) + \sqrt{\frac{\Phi(I(t))}{N_e}} \eta(t), \quad (\text{II.3.16})$$

$$\tau_{eff}(I(t)) \frac{dI(t)}{dt} = -I(t) + I_{ext}(t), \quad (\text{II.3.17})$$

where $\eta(t)$ is a Gaussian white noise with mean 0 and variance 1 and τ_{eff} is given by

$$\tau_{eff}(I(t)) = \tau_m \Delta T \frac{\Phi'(I(t))}{r(t)}. \quad (\text{II.3.18})$$

Consider the firing rate model including the excitatory synaptic input:

$$r(t) = \Phi(I(t)) + x(t), \quad (\text{II.3.19})$$

$$\tau_{eff}(I(t)) \frac{dI(t)}{dt} = -I(t) + I_{ext}(t) + wr(t), \quad (\text{II.3.20})$$

where $x(t) = \sqrt{\Phi(I(t))/N_e} \eta(t)$ is the noise term due to the finite size effects and w is the strength of the excitatory synaptic connection. The synaptic currents in the network are delta functions and hence the net synaptic input to a neuron at any given instant t^k is given by $\tau_m \sum_j J_j \sum_k \delta(t - t_j^k)$ where the sum over j is over all the incoming neurons and t_j^k is the spike emission time of the j 'th neuron [Brunel and Hakim, 1999]. For our network with uniform synaptic strengths i.e. $J_j = J$ for all neurons and $\sum_j \delta(t - t_j^k) \approx C \tau_m r(t^k)$. This translates to a value of $w = CJ\tau_m$ in the firing rate model.

We want to linearize the above equation around the fixed point (r^*, I^*) , $r(t) = r^* + \tilde{r}(t)$, $I(t) = I^* + \tilde{I}(t)$ where $\tilde{r}(t) = \phi' \tilde{I}(t) + x(t)$ with

$$\phi' = \left. \frac{\partial \phi}{\partial I} \right|_{I=I^*}. \quad (\text{II.3.21})$$

Taking the Fourier transform of the linearized equation with the definitions,

$$F(\omega) = \int_{-\infty}^{\infty} f(t) e^{-i\omega t} dt, \quad (\text{II.3.22})$$

$$f(t) = \frac{1}{2\pi} \int_{-\infty}^{\infty} F(\omega) e^{i\omega t} d\omega, \quad (\text{II.3.23})$$

we get (where \tilde{I} and X are functions of ω):

$$i\tau_{eff}\omega \tilde{I}(\omega) = -\tilde{I}(\omega) + w\phi' \tilde{I}(\omega) + wX(\omega), \quad (\text{II.3.24})$$

$$\tilde{I}(\omega) = \frac{wX(\omega)}{g + i\omega\tau_{eff}}, \quad (\text{II.3.25})$$

where

$$g = 1 - w\phi', \quad (\text{II.3.26})$$

$$\tilde{r}(\omega) = \phi' \tilde{I}(\omega) + X(\omega). \quad (\text{II.3.27})$$

The correlation function of the population firing rate is given by

$$A(\tau, t) = \langle \tilde{r}(t + \tau) \tilde{r}(t) \rangle \quad (\text{II.3.28})$$

$$= \frac{1}{(2\pi)^2} \int_{-\infty}^{\infty} d\omega_1 \int_{-\infty}^{\infty} d\omega_2 \langle \tilde{r}(\omega_1) \tilde{r}(\omega_2) \rangle e^{i\omega_1(t+\tau)} e^{i\omega_2 t} \quad (\text{II.3.29})$$

$$= \frac{1}{2\pi} \int_{-\infty}^{\infty} A(\omega_1; t) e^{i\omega_1 t} d\omega_1. \quad (\text{II.3.30})$$

$$\therefore A(\omega_1, t) = \frac{1}{2\pi} \int_{-\infty}^{\infty} \langle \tilde{r}(\omega_1) \tilde{r}(\omega_2) \rangle e^{i(\omega_1 + \omega_2)t} d\omega_2, \quad (\text{II.3.31})$$

$$\langle \tilde{r}(\omega_1) \tilde{r}(\omega_2) \rangle = \langle (\phi' \tilde{I}(\omega_1) + X(\omega_1)) (\phi' \tilde{I}(\omega_2) + X(\omega_2)) \rangle. \quad (\text{II.3.32})$$

$$\implies \langle \tilde{r}(\omega_1) \tilde{r}(\omega_2) \rangle = \langle \phi'^2 \tilde{I}(\omega_1) \tilde{I}(\omega_2) + \phi' \tilde{I}(\omega_1) X(\omega_2) + \phi' \tilde{I}(\omega_2) X(\omega_1) + X(\omega_1) X(\omega_2) \rangle. \quad (\text{II.3.33})$$

We can write the correlation of the noise due to finite size, $x(t)$, as:

$$\langle x(t_1) x(t_2) \rangle = \rho^2 \delta(t_1 - t_2). \quad (\text{II.3.34})$$

Then, we have for its Fourier transform

$$\langle X(\omega_1) X(\omega_2) \rangle = \int_{-\infty}^{\infty} dt_1 \int_{-\infty}^{\infty} dt_2 e^{-i\omega_1 t_1} e^{-i\omega_2 t_2} \rho^2 \delta(t_1 - t_2) \quad (\text{II.3.35})$$

$$= \int_{-\infty}^{\infty} dt e^{-i(\omega_1 + \omega_2)t} \rho^2 \quad (\text{II.3.36})$$

$$= 2\pi \delta(\omega_1 + \omega_2) \rho^2. \quad (\text{II.3.37})$$

where we used the Fourier transform of delta function:

$$\delta(\omega) = \int_{-\infty}^{\infty} e^{-i\omega t} \delta(t) dt = 1, \quad (\text{II.3.38})$$

$$\delta(t) = \frac{1}{2\pi} \int_{-\infty}^{\infty} e^{i\omega t} d\omega. \quad (\text{II.3.39})$$

This gives us, for the autocorrelation of the population firing rate:

$$\langle \tilde{r}(\omega_1) \tilde{r}(\omega_2) \rangle = \left(\frac{\phi'^2 w^2}{(g + i\omega_1 \tau_{eff})(g + i\omega_2 \tau_{eff})} + \frac{\phi' w}{g + i\omega_1 \tau_{eff}} + \frac{\phi' w}{g + i\omega_2 \tau_{eff}} + 1 \right) \langle X(\omega_1) X(\omega_2) \rangle \quad (\text{II.3.40})$$

$$= 2\pi \rho^2 \left(\frac{\phi'^2 w^2}{g^2 + \omega^2 \tau_{eff}^2} + \frac{2\phi' w g}{g^2 + \omega^2 \tau_{eff}^2} + 1 \right) \delta(\omega_1 + \omega_2). \quad (\text{II.3.41})$$

$$\therefore A(\omega_1, t) = \rho^2 \left(1 + \frac{1 - g^2}{g^2 + \omega^2 \tau_{eff}^2} \right). \quad (\text{II.3.42})$$

We observe that there is no dependence on t in the above equation. Taking the inverse Fourier transform of the above expression, we can obtain the autocorrelation $A(\tau)$ as a function of time,

$$A(\tau) = \frac{1}{2\pi} \int_{-\infty}^{\infty} d\omega_1 A(\omega_1, t) e^{i\omega_1 \tau} \quad (\text{II.3.43})$$

$$= \frac{\rho^2}{2\pi} \int_{-\infty}^{\infty} d\omega_1 \left(1 + \frac{1 - g^2}{g^2 + \omega_1^2 \tau_{eff}^2} \right) \quad (\text{II.3.44})$$

$$= \rho^2 \delta(\tau) + \frac{\rho^2(1 - g^2)}{2g\tau_{eff}} \exp\left(-\frac{\tau g}{\tau_{eff}}\right) \quad (\text{II.3.45})$$

$$= \rho^2 \delta(\tau) + \rho_a \exp\left(-\frac{\tau}{\tau_a}\right). \quad (\text{II.3.46})$$

The first term, at $\tau = 0$, corresponds to the variance of the firing rate. For the firing rate that's discrete in time with a time-bin Δt , we have the variance $\rho^2/\Delta t = \langle r \rangle / (N_e \Delta t)$. The maximum of the autocorrelation (for $\tau > 0$) is then given by $\rho_a = \rho^2(1 - g^2)/(2g\tau_{eff})$ and the autocorrelation decays exponentially with a time constant of $\tau_a = \tau_{eff}/g$. If we assume $\tau_{eff}/g = 15$ ms, then after a time of about 0.1 s, the exponential factor is about 0.0013 sec^{-1} . We can then compute the mean and the standard deviation of the autocorrelation function from 0.1 s to 0.2 s. intuitively, we expect the mean of the autocorrelation to be zero. We can show that this is the case below. For a discrete firing rate r_j , the autocorrelation at a timeshift of j is given by:

$$A_j = \frac{1}{N-j} \sum_{i=1}^{N-j} \delta r_i \delta r_{i+j}. \quad (\text{II.3.47})$$

We want to compute the mean and the variance of the autocorrelation when $j \gg 1$ but $j \ll N$. We have

$$\langle A_j \rangle = \frac{1}{N-j} \sum_{i=1}^{N-j} \langle \delta r_i \delta r_{i+j} \rangle = 0, \quad (\text{II.3.48})$$

$$\langle A_j^2 \rangle = \frac{1}{(N-j)^2} \sum_{i=1}^{N-j} \sum_{k=1}^{N-j} \langle \delta r_i \delta r_{i+j} \delta r_k \delta r_{k+j} \rangle. \quad (\text{II.3.49})$$

The term in equation II.3.48 is zero because the firing rate is not correlated over long timescales. For the term in equation II.3.49, one can consider three cases a) $i = k \implies i + j = k + j$, b) $i = k + j \implies i + j = k + 2j$ and c) $i + j = k \implies i + 2j = k + j$. Using symmetry arguments, we can simplify this term as follows:

$$\langle A_j^2 \rangle = \frac{1}{(N-j)^2} \sum_{i=1}^{N-j} \langle \delta r_i \delta r_i \delta r_{i+j} \delta r_{i+j} \rangle + 2 \frac{1}{(N-j)^2} \sum_{i=1}^{N-j} \langle \delta r_i \delta r_i \delta r_{i+j} \delta r_{i+2j} \rangle \quad (\text{II.3.50})$$

The second term above can be written as

$$2 \frac{1}{(N-j)^2} \sum_{i=1}^{N-j} \langle \delta r_i \delta r_i \rangle \langle \delta r_{i+j} \rangle \langle \delta r_{i+2j} \rangle = 0 \quad (\text{II.3.51})$$

Thus, we have

$$\langle A_j^2 \rangle = \frac{1}{(N-j)^2} \sum_{i=1}^{N-j} \langle \delta r_i^2 \rangle \langle \delta r_{i+j}^2 \rangle \quad (\text{II.3.52})$$

$$= \frac{1}{N^2} N \left(\frac{r_0}{N_e dt} \right)^2 \quad (\text{II.3.53})$$

$$= \frac{r_0^2}{N N_e^2 dt^2} \quad (\text{II.3.54})$$

We can compare the four different analytical quantities obtained above 1) maximum of the autocorrelation function, ρ_a , 2) variance of the population firing rate, ρ^2 , 3) decay timescale of the autocorrelation function, τ_a and 4) variance of the autocorrelation function, $\langle A_j^2 \rangle$, after it has decayed down with their corresponding values obtained in the network simulations for a) different network sizes, b) different excitatory strengths J , c) different connectivity C and d) different firing rates. This is shown in the figure II.5. Each of the quantities obtained in the network is rescaled by dividing it with the corresponding analytic quantity. We observe that all the quantities are close to 1. For higher values of J and r , the correlations in input synaptic currents might be significant to account for the slight discrepancies away from unity.

Therefore, we notice that the adaptive rate 0 model is effective in capturing the firing rate dynamics of a single population of EIF neurons in the presence of a noisy input current $I(t) = I_0 + \sigma\eta(t) + I_s n(t)$. In the next section, we will explore the limitations of the adaptive rate 0 model by stimulating the recurrent excitatory network of EIF neurons with a mean input current that varies sinusoidally in time.

II.4 Single population with oscillatory input

We have seen in the previous section (see section II.3) that the adaptive rate 0 model reproduces very well the firing rate dynamics of a single population of EIF neurons in the presence of a noisy input current $I(t) = I_0 + \sigma\eta(t) + I_s n(t)$. It also reproduces well the autocorrelation of the population firing rates for a recurrent excitatory network (see figure II.5). Here, $\eta(t)$ is a white (no temporal correlations) Gaussian process with zero mean and unit variance, and $n(t)$ is a Gaussian process with zero mean, unit variance and correlation time τ_s . Note that the mean input current in both the cases was constant in time. In this section, will explore the limitations of this model by stimulating the recurrent excitatory network of EIF neurons with a mean input current that varies sinusoidally in time. We will consider the case of a network with zero coupling or finite excitatory coupling (as shown in figures II.6, II.7, II.8). We observe that the adaptive timescale rate model falls short of explaining the network activity in the presence of a varying sinusoidal current. We then define a new time scale to capture this behaviour (corresponding to figures II.9, II.10, II.11, II.12).

As explained before, for the network simulations, we use a network of N_e EIF neurons connected via delta synapses, whose membrane potential obeys the following equations:

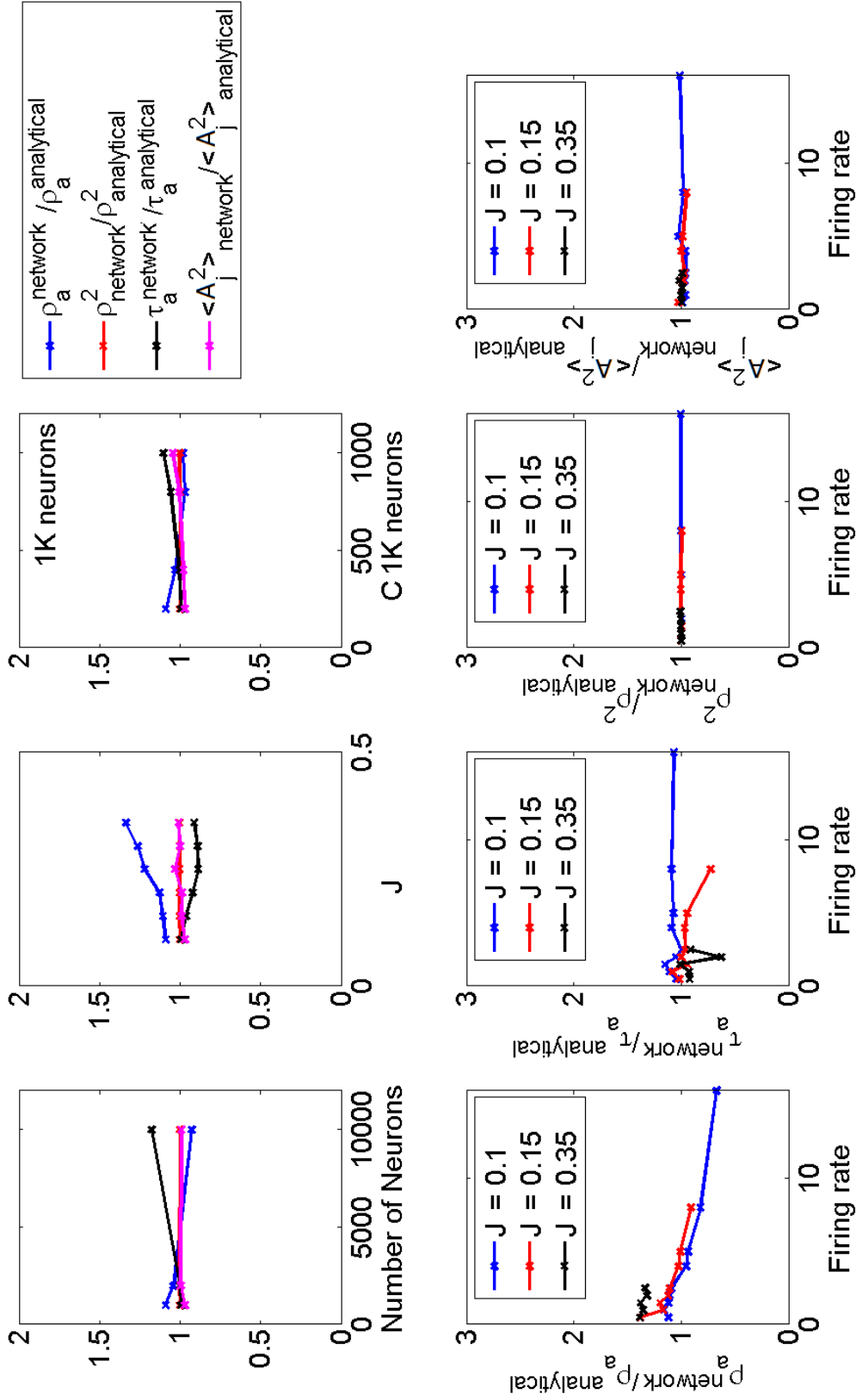


Figure II.5: Comparing the quantities obtained in the network to the analytical simulations. The top three panels show the network to analytical ratios of the 1) fit of the maximum of the network correlation for $t > 0$, $\rho_a^{\text{network}} / \rho_a^{\text{analytical}}$ 2) variance, ρ_a^2 / ρ_a^2 3) fit of the timescale, $\tau_a^{\text{network}} / \tau_a^{\text{analytical}}$ 4) variance of the correlation of the network population firing rate, $\langle A_j^2 \rangle_{\text{network}} / \langle A_j^2 \rangle_{\text{analytical}}$. The firing rate in the three panels correspond to 2.5 Hz and $J = 0.1$ mV, $N = 1000$ and $C = 200$ wherever unspecified. The four bottom panels show the rescaled quantities for different values of excitatory coupling strength J (legend) and steady state firing rates r (xaxis).

τ_m	10ms	v_L	-65mV
ΔT	3.5mV	v_T	-59.9mV
v_R	-68mV	v_{th}	-30mV
σ	10mV	N_e	5000
J	0.1mV	C	0

Table II.2: Parameters used in the network simulation for studying the response to an oscillatory input.

$$\frac{dv}{dt} = \frac{-v + v_L + F_v + I_{ext}(t)}{\tau} + \frac{\sigma}{\sqrt{\tau}}\eta_i(t), \quad (\text{II.4.1})$$

$$F_v = \Delta_T \exp\left(\frac{v - v_T}{\Delta_T}\right), \quad (\text{II.4.2})$$

with the neurons parameters as defined below:

To begin with, we will consider a network of neurons that are not connected (this is equivalent to repeated trials on a single neuron). Apart from the white noise of standard deviation 10 mV, we insert a mean current of $I_{ext}(t) = I_0 + A \sin(\omega t)$. I_0 is set equal to -6.29 mV such that the network gives a steady state firing rate of 5 Hz in the absence of any other mean input currents. The time period of the sinusoidal input current is taken as 60 ms and the amplitude of the current is varied from 0.5 mV to 19 mV. We will then compute the cycle-averaged population firing rate of the network using two averaging procedures: Firstly, we will compute the mean firing rate of the network across neurons. We will then take another mean over the different cycles of the input sinusoidal current. This final quantity is the cycle-averaged population firing rate.

We want to compare these results to the one obtained in the adaptive timescale rate model with finite-size noise described in the previous section (see equation II.3.16, which we list here again):

$$r(t) = \Phi(I(t)) + \sqrt{\frac{\Phi(I(t))}{N_e}}\eta(t) \quad (\text{II.4.3})$$

$$\tau_{eff}(r)\frac{dI(t)}{dt} = -I(t) + I_{ext}(t) + CJr(t)\tau_m \quad (\text{II.4.4})$$

To study the network with different C , we scale the synaptic strength J such that the product CJ remains constant.

In figures II.6 and II.7, we compare the cycle-averaged population firing rates for the network model (in solid lines) and the adaptive timescale rate model (in dashed lines) for zero and finite connectivity respectively. The different curves correspond to the different amplitudes used. The population firing rate is averaged over all the cycles of the input sinusoidal current. For both the network and the adaptive rate model, we obtain the same curves for different finite connectivities C . For high amplitudes in the case of finite connectivity, we notice that the population firing rate in the network shows two peaks whereas the rate model shows only a single peak. For instance, for

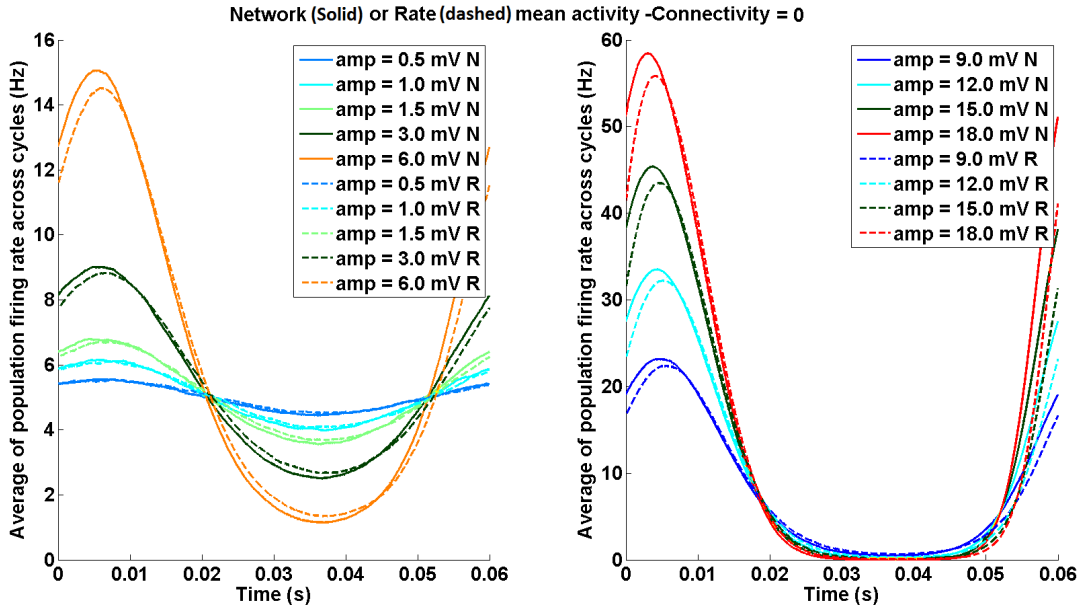


Figure II.6: **Comparing firing rates for Network and Rate Models with zero connectivity.** The average of the population firing rates of the adaptive rate model (R) and the EIF-network (N_e) across 1666 cycles (corresponds to 100 seconds) of the output current for different amplitudes of input current (0.5 mV, 1 mV, 1.5 mV, 3 mV and 6 mV in the left panel; 9 mV, 12 mV, 15 mV and 18 mV in the right panel). The x-axis is the time period of one oscillation of the input current. The curves for the adaptive rate model are shown in dashed lines whereas the curves for the network model are shown in solid lines. The standard deviation at firing rate r goes as $\sqrt{r/(N_e \Delta t)}$ for all curves shown. To give an estimate, at a firing rate of 60 Hz, the standard error of the mean is 0.85 Hz.

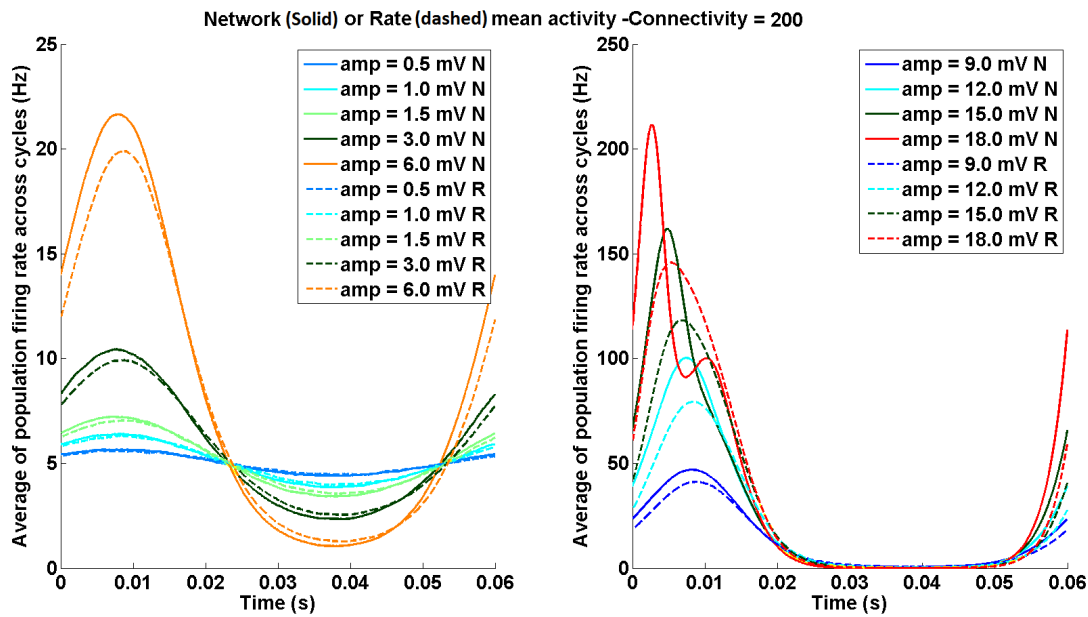


Figure II.7: **Comparing firing rates for Network and Rate Models with finite connectivity** The average of the population firing rates of the adaptive rate model (R) and the EIF-network (N) across 1666 cycles (corresponds to 100 seconds) of the output current for different amplitudes of input current (0.5 mV, 1 mV, 1.5 mV, 3 mV and 6 mV in the left panel; 9 mV, 12 mV, 15 mV and 18 mV in the right panel). The x-axis is the time period of one oscillation of the input current. The curves for the adaptive rate model (R) are shown in dashed lines whereas the curves for the network model (N) are shown in solid lines. The connectivity of the network $C = 200$ and the connection strength $J = 0.1$ mV in this case though any C and J with the same product CJ gives the same results.

an excitatory population with connection strength $J = 0.1$ mV, connectivity $C = 200$ and when subjected to an input sinusoidal current of amplitude 20 mV, the neurons in the network are in bursting mode as shown in the figure II.8. This nonlinear behaviour cannot be accounted for by our rate model since our dynamical equations have a linear input current.

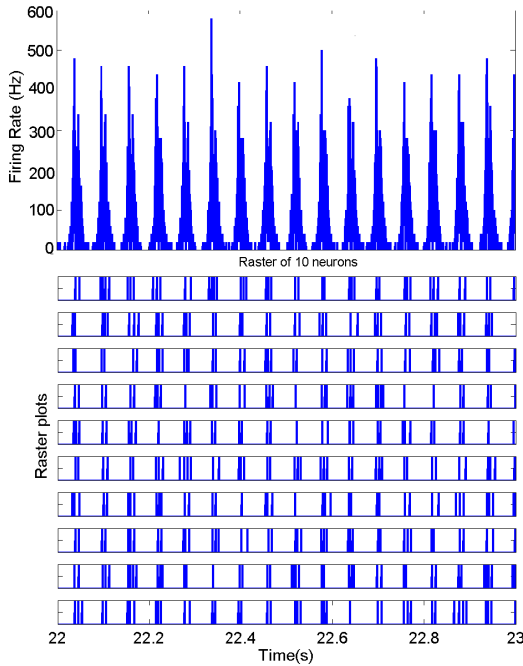


Figure II.8: **Population firing rate and raster plot of 10 neurons** for an excitatory network of $J = 0.1$ mV, $C = 200$ when subjected to an input sinusoidal current of amplitude 20 mV. The neurons enter a bursting mode and this behaviour cannot be accounted by the rate model which is linear in its input current.

To compute how well the adaptive rate model describes the results of the network simulations, we calculate the correlation coefficient between the two curves r and \hat{r} as defined in [Ostojic and Brunel, 2011].

$$\rho(r, \hat{r}) = 1 - \frac{\langle (r - \hat{r})^2 \rangle}{2\text{var}(r)} \quad (\text{II.4.5})$$

where $\langle \dots \rangle$ denotes the time averaged mean and $\text{var}(r)$ is the variance of the signal r . The correlation coefficient between the two models is shown by the red curves with crosses in figures II.13 and II.14 for zero and finite connectivity respectively. We observe that the correlation coefficient drops below 0.99 for amplitudes of about 11 mV and 4 mV for zero and finite connectivity respectively. The correlation coefficient between the two models for sinusoidal input currents of other time periods (15 ms shown with red circles; 30 ms shown with red double dashes and 120 ms shown with red diamonds) are also shown in figures II.13 and II.14 for zero and finite connectivity respectively. In the next section, we will try to improve the performance of the rate model by using a new timescale. For the rest of the thesis, the first model will be referred to as the ‘‘Adaptive rate’’ (AR0) model and the second model will be referred to as the ‘‘Adaptive rate’’ (AR1) model.

II.5 Introducing a new timescale to rate model

To try and improve the estimate of the rate model as compared to the network model in the presence of a sinusoidal current of larger finite amplitudes, we introduce a new time constant to the rate model. The time constant is derived based on Augustin et al. [Augustin et al., 2016]. They derive the reduced LN_{exp} model from the Fokker-Planck equation that describes the population activity of a network of sparsely coupled adaptive nonlinear integrate-and-fire neurons when exposed to a noisy synaptic input. They used a different method from the one described in section II.2, where the LN model used to approximate the Fokker-Planck equation has the linear filter which is the dynamic response of the firing rate. This linear filter $D(t)$ was approximated with a single exponential of effective timescale τ_{eff} which was derived from the amplitude decay at high frequencies of the Fourier transform of $D(t)$. Instead, Augustin et al. derived the timescale by approximating $D(t)$ with a fitted exponential (minimum least squared error between the fit and the original) for all frequencies. We compute the response rate function for the EIF neuron for all frequencies from 1 Hz to 1000 Hz with a linear spacing of 1Hz. This amounts to computing the Fourier transform of $D(t)$. To fit it with an exponential, we approximate the Fourier transform with $\frac{\tau_{eff}A}{1+i2\pi f\tau_{eff}}$ for each value of input current I_0 and compute the parameters of the fit which give the minimum squared error between the original data and the fit (see figure II.9). This gives a time constant that is a function of the input current as shown in blue in the figure II.10.

The time constant in figure II.10 can be fit with a function

$$\tau_{eff}(I) = A \frac{1 - \exp(B(I - I_0))}{1 + C \exp(D(I - I_0)) + E \exp(F(I - I_0))} \quad (\text{II.5.1})$$

Using minimum least squares, the parameters of the above fit obtained are $A = 0.1748$ s, $B = -0.3218$ mV⁻¹, $C = -0.114$, $D = -0.3211$ mV⁻¹, $E = -0.9866$, $F = -0.0051$ mV⁻¹, $I_0 = -0.6854$ mV. Note that at the value of $I_0 = -0.6854$ mV, the numerator and denominator of the above fit are both zero and hence the ratio is undefined. However, in the limit of $I \rightarrow I_0$, the value of the fit converges to the expected value in the data. With this new time constant, we can re-compute the cycle-averaged population firing rates for the rate model of a single-excitatory population. We call this model in the following as the ‘‘adaptive rate’’ or the AR1 model. In figures II.11 and II.12, we compare the cycle-averaged population firing rates for the network model and the adaptive rate 1 model for zero and finite connectivity respectively. The different curves correspond to the different amplitudes used. The population firing rate is averaged over all the cycles of the input sinusoidal current. For both the network and the adaptive rate 1 model, we obtain the same curves for different finite connectivities C used as before. The variance of the population firing rate across different cycles is linear to the mean across different cycles in the case of zero connectivity in both the rate model and the network as before (Poissonian spiking of neurons). We can compute the correlation coefficient between the two models, the network and the adaptive rate 1 model and this is shown by the blue curves with the crosses in figures II.13 and II.14 for zero and finite connectivity respectively. We observe that the correlation coefficient is always greater than 0.99 for zero connectivity and drops below 0.99 for

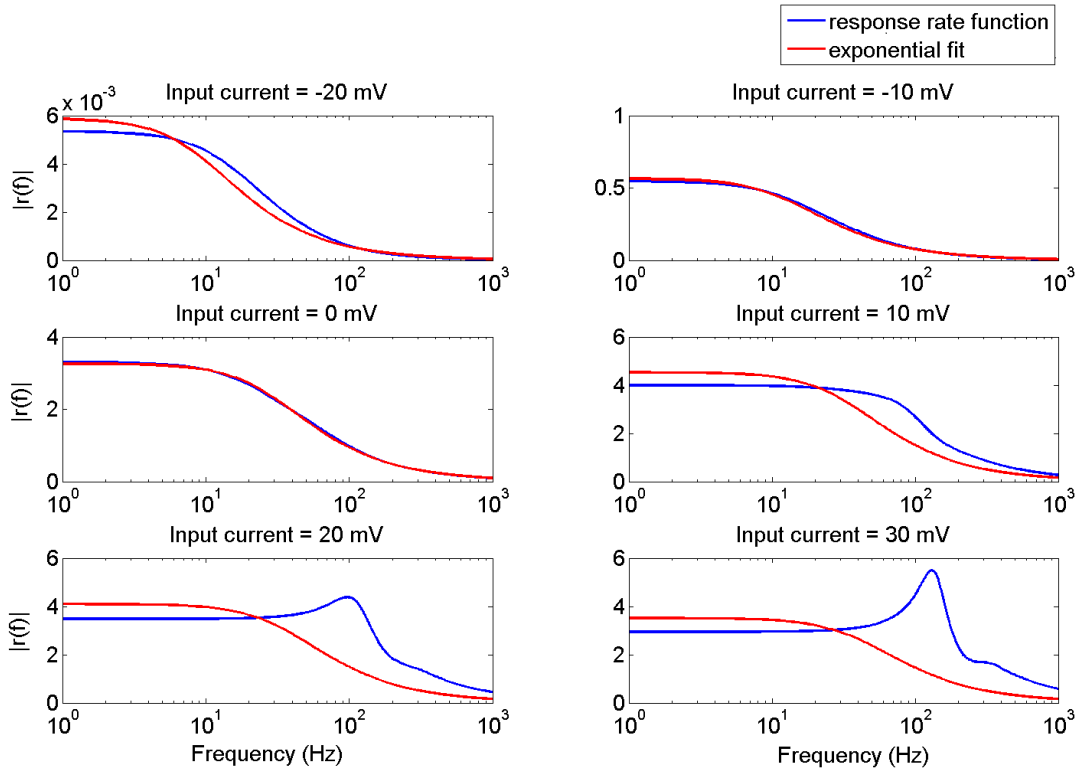


Figure II.9: **Computing the new time constant by approximating $D(t)$ with a fitted exponential.** The six panels correspond to six different value of input current into the network of EIF neurons. The response rate function of the network (shown in blue) is computed from 1 to 1000 Hz with a linear spacing of 1 Hz and the resulting curve is fit with an exponential (shown in red) whose parameters give the minimum least squared error between the fit and the data. The parameters for the simulations correspond to the standard network parameters listed in Table II.2.

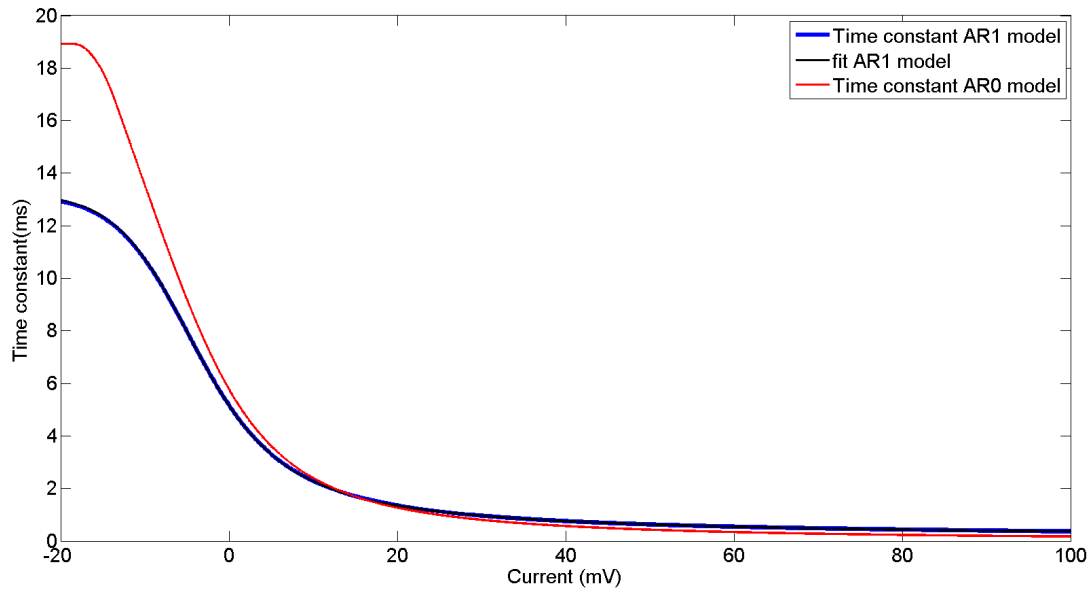


Figure II.10: **The time constant obtained by approximating $D(t)$ and the corresponding fit as a function of input current in mV.** The new time constant (blue) is computed by approximating $D(t)$ with a fitted exponential. The time constant of the AR0 model is shown in red and the AR1 model in blue. The time constant can be fit for the AR1 model (shown in black) with the function as defined in equation II.5.1. The parameters used for the fit of this function are $A = 0.1748$ s, $B = -0.3218$ mV⁻¹, $C = -0.114$, $D = -0.3211$ mV⁻¹, $E = -0.9866$, $F = -0.0051$ mV⁻¹, $I_0 = -0.6854$ mV. The parameters for the network simulations correspond to the standard parameters listed in Table II.2.

an amplitude 13 mV for finite connectivity. The correlation coefficient for the AR1 model with the network simulations for sinusoidal input currents of other time periods (15 ms shown with blue circles; 30 ms shown with blue double dashes and 120 ms shown with blue diamonds) are also shown in figures II.13 and II.14 for zero and finite connectivity respectively. We observe that the correlation coefficient between the network simulation and the AR1 model is always greater than the correlation coefficient between the network simulation and the AR0 model. Thus, we see that the adaptive rate 1 model is better than adaptive rate 0 model at predicting the firing rate of the network for higher amplitudes of sinusoidal input currents.

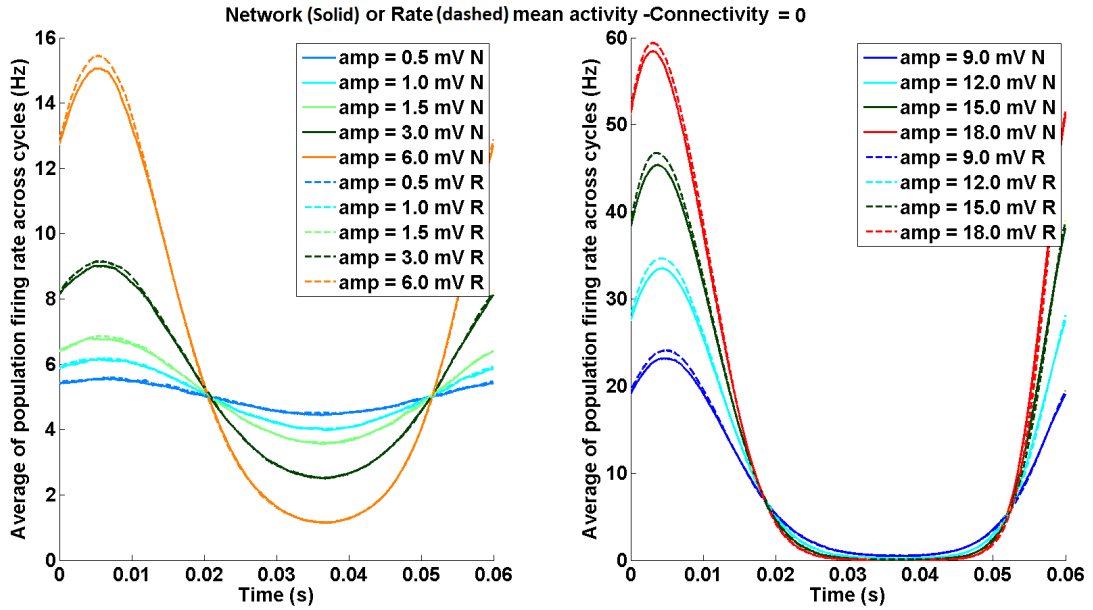


Figure II.11: **Comparing firing rates for Network and Rate Models with no connectivity.** The average of the population firing rates of the adaptive rate 1 model (R) and the EIF-network (N) across 1666 cycles (corresponds to 100 seconds) of the output current for different amplitudes of input current (0.5 mV, 1 mV, 1.5 mV, 3 mV and 6 mV in the left panel; 9 mV, 12 mV, 15 mV and 18 mV in the right panel). The x-axis is the time period of one oscillation. The curves for the adaptive rate 1 model (R) are shown in dashed lines whereas the curves for the network model (N) are shown in solid lines. The standard deviation at firing rate r goes as $\sqrt{r/(N_e \Delta t)}$ for all curves shown. To give an estimate, at a firing rate of 60 Hz, the standard error of the mean is 0.85 Hz.

II.6 Conclusion

In this chapter, we began with phenomenological rate models that described dynamics of the population firing rate of a network. We then showed how the EIF spiking neuron model can be described by the adaptive rate 0 model for stationary firing rates. Later, we compared the autocorrelation of the firing rate of a population of the rate model

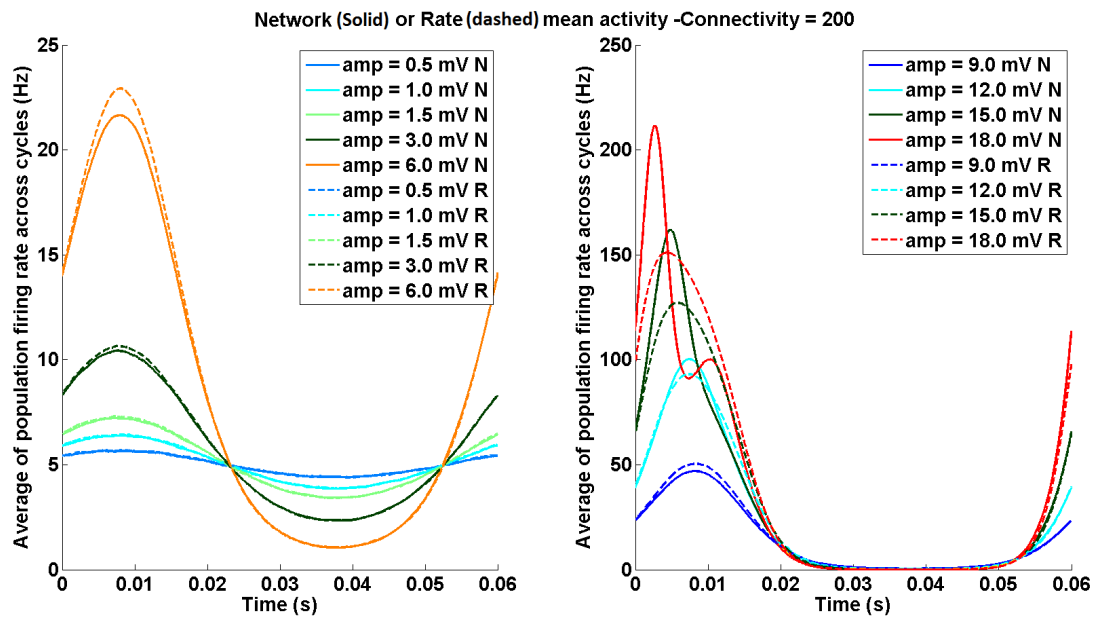


Figure II.12: **Comparing firing rates for Network and Rate Models with finite connectivity.** The average of the population firing rates of the adaptive rate 1 model (R) and the EIF-network (N) across 1666 cycles (corresponds to 100 seconds) of the output current for different amplitudes of input current (0.5 mV, 1 mV, 1.5 mV, 3 mV and 6 mV in the left panel; 9 mV, 12 mV, 15 mV and 18 mV in the right panel). The x-axis is the time period of one oscillation. The curves for the adaptive rate 1 model (R) are shown in dashed lines whereas the curves for the network model (N) are shown in solid lines. The connectivity of the network $C = 200$ and the connection strength $J = 0.1$ mV in this case though any C and J with the same product CJ gives the same results.

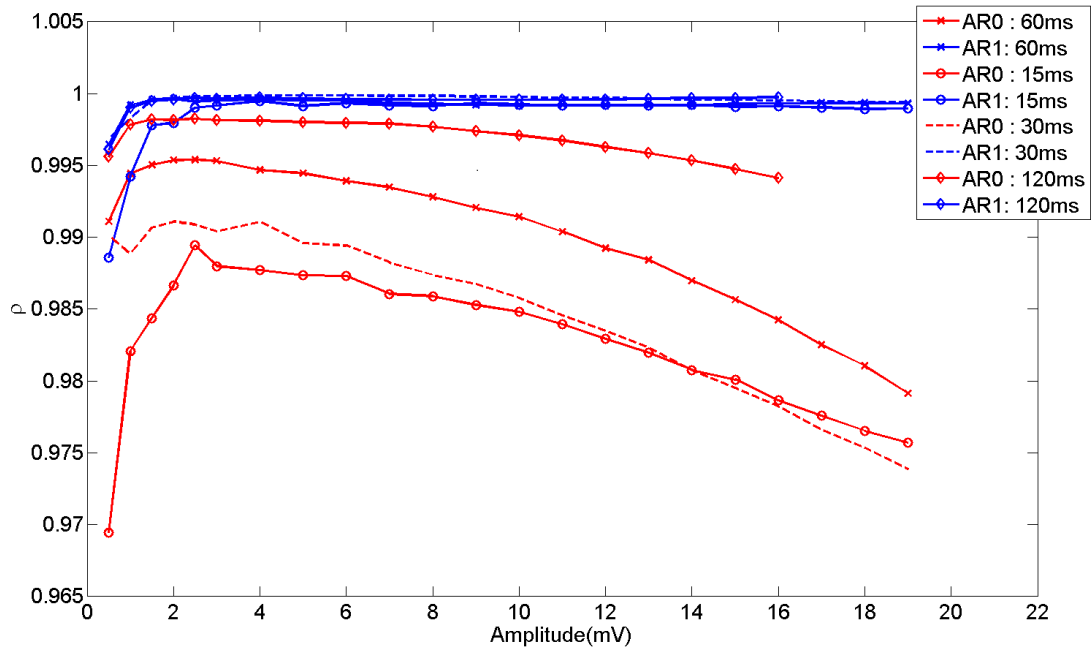


Figure II.13: **Correlation coefficient between the cycle averaged population rates of two rate models and the unconnected network with zero connectivity.** Correlation coefficient between the cycle averaged population rates of the EIF unconnected network and adaptive rate 0 model (in red) and adaptive rate 1 model (in blue) as a function of the amplitude of the input current (mV). The different curves correspond to the different time periods of the input sinusoidal current used: the 'x' to 60 ms, the 'o' to 15 ms, the '-' to 30 ms and the 'o' to 120 ms.

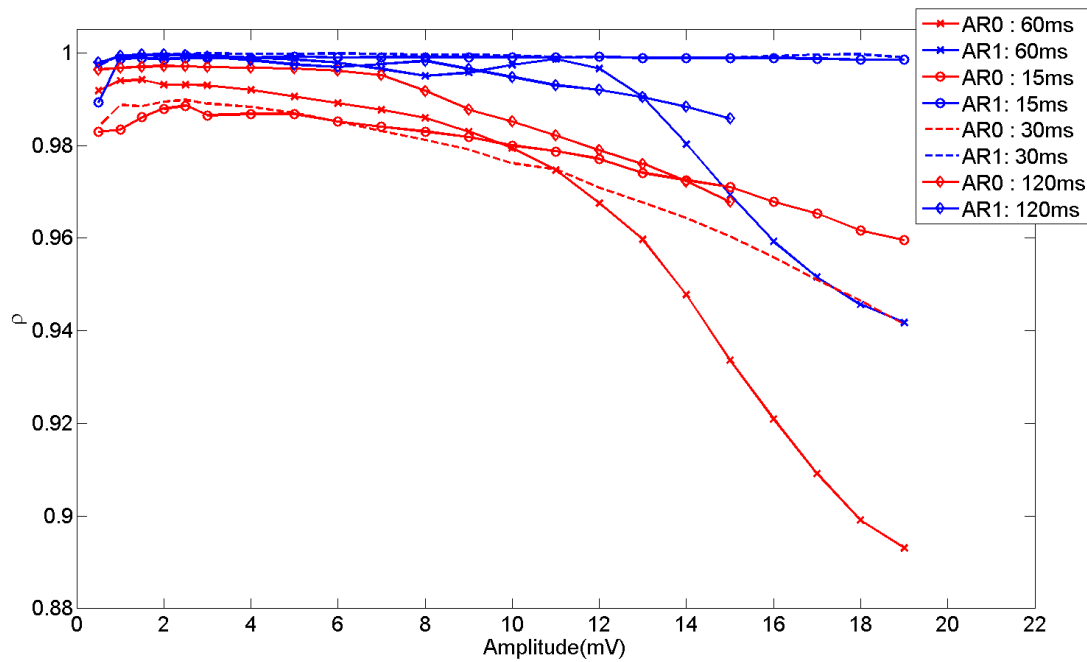


Figure II.14: **Correlation coefficient between the cycle averaged population rates of two rate models and the network with finite connectivity.** Correlation coefficient between the cycle averaged population rates of the EIF network with finite excitatory connectivity and adaptive rate 0 model (in red) and adaptive rate 1 model (in blue) as a function of the amplitude of the input current (mV). The different curves correspond to the different time periods of the input sinusoidal current used: the 'x' to 60 ms, the 'o' to 15 ms, the '-.-' to 30 ms and the '◇' to 120 ms.

and an excitatory network of EIF neurons. We then introduced the adaptive rate 1 model and we saw that it describes better the firing rate response of the network of EIF neurons to a sinusoidally varying current as compared to the adaptive rate 0 model. In the next chapter, we will discuss oscillations in the brain and use the adaptive rate 1 model to describe the oscillations generated in the Excitatory-Inhibitory (EI) network. We will then study the different dynamical regimes when we couple EI oscillators together.

Chapter III

Oscillations in EI networks

III.1 Oscillations in the brain

Understanding cortical rhythms is one of the major topics of neuroscience [Buzsaki, 2006] [Buzsaki and Draguhn, 2004]. Cortical rhythms can be understood at different levels: the biophysical mechanisms at the cellular level, neuronal interaction dynamics at the network level, the interactions between different brain regions at the systems level and correlation with behaviour and cognitive processes at the behavioural level [Wang, 2010]. To measure the cortical rhythms one can perform either scalp electroencephalogram (EEG) recordings or magnetoencephalogram (MEG) recordings or subdural electrocorticogram (ECoG), where the electrodes are placed on the cortical surface after removing the scalp or mesoscopic local field potential (LFP), where the electrodes are inserted deep into the brain. The different brain rhythms can be classified according to their frequency and are listed below,

a) **Infraslow oscillations** (0.02– 0.2 Hz) have been observed in the cortex and their amplitude and frequency can be changed by external influences such as poisoning, asphyxia, afferent stimulation of retina, anesthesia among others [Aladjalova, 1957]. The phase of these oscillations correlate with the slow dynamics observed in human behavioural tasks [Monto et al., 2008] and they are also phase locked with interictal events and K complexes during non-SWS sleep. The instantaneous ISO voltage is also correlated with the amplitude envelope of the >1Hz band. They have been suggested to modulate cortical excitability and contribute to increase in epileptic episodes during sleep [Vanhatalo et al., 2004].

b) **Slow oscillations** (< 1 Hz) are observed during non-REM (slow-wave) sleep [Steriade, 2006] [Achermann and Borbely, 1997]. During the slow wave, almost all the cells in the cerebral cortex switch repetitively between an up state (where neurons are at about -65 mV) and a down state (where neurons are at about -80 to -85 mV). This slow wave might be responsible for memory consolidation [Huber et al., 2004].

c) **Theta rhythm** (4–8 Hz) is observed in the hippocampus and other limbic structures during exploratory movements [Bland, 1986], retrieval and formation of spatial and episodic memory [Hasselmo, 2005]. The spatial information during movements may be encoded by the spike timings of the cells with respect to the theta rhythm [Geisler et al., 2007]. This kind of “phase coding” might have a role in communication

between different brain areas [Buzsaki and Chrobak, 1995] [Fries et al., 2007] [Quiroga and Panzeri, 2009] [Schneider et al., 2009] [Tiesinga et al., 2008] [Tognoli and Kelso, 2009].

d) **Alpha rhythms** (~ 10 Hz) are large-amplitude EEG sinusoidal oscillations when the subject is awake and relaxed [Andersen and Andersson, 1968]. They were first observed by Hans Berger [Berger, 1929] around the 1920s and are also called “Berger’s wave”. They are also observed in the neocortex and is enhanced during working memory tasks [Canolty et al., 2006] [Meltzer et al., 2008].

e) **Beta rhythm** (15 – 30 Hz) was also first observed by Hans Berger around the 1920s in the primary motor cortex [Berger, 1929]. It occurs during “readiness” of a movement but ceases at its initiation. It also increases if a response is withheld [Jasper and Penfield, 1949]. Beta rhythms are also known to be involved in sensorimotor integration and top-down signaling.

f) **Gamma rhythms** (30 – 80 Hz) are seen in the olfactory bulb in the presence of a sensory stimulus [Adrian, 1942]. In the hippocampus, gamma and theta rhythms overlap [Bragin et al., 1995]. In the neocortex, gamma rhythms are associated with states of attentiveness [Bouyer et al., 1981]. It was also observed in the primary visual cortex in anesthetized as well as alert animals [Eckhorn et al., 1988]. Synchronization of gamma waves between neural assemblies might play a role in sensory integration [Gray, 1994].

g) **Ultrafast oscillations** (~ 100 Hz) can be found in the cerebellum [Adrian, 1935] as well as the hippocampus during awake immobility, consummatory behaviors and non-REM sleep, when theta rhythm is absent [Buzsaki et al., 1983] [Buzsaki et al., 1992]. It can also be found transiently in the neocortex [Canolty et al., 2006].

In terms of the functionality, apart from being involved in phase coding, memory consolidation, working memory tasks, attentiveness [Deco and Thiele, 2009] and sensory integration [Ghazanfar et al., 2008], neuronal temporal correlations resulting from synchronous oscillations can also be useful for Spike-timing dependent plasticity (STDP) [Harris et al., 2003]. They also play an important role in circuit pattern formation of the developing brain [Blankenship and Feller, 2010]. They are believed to increase the efficiency of information transfer in the brain [Baker et al., 1999].

In a network of neurons, three types of synchronization mechanisms by chemical synapses are possible: 1) due to excitatory neurons only, 2) due to inhibitory neurons only [Traub et al., 1996] [Wang and Buzsaki, 1996] [Whittington et al., 1995], and 3) due to the coupling of excitatory and inhibitory neuronal populations. Electrical synapses by gap junctions have also been proposed to contribute to neural synchrony. In this thesis, we focus on the oscillations generated by the excitatory-inhibitory interactions because we are interested in modeling oscillations in the beta and low gamma range as recorded, for example, in the motor cortex region during preparation of motor movements. In excitatory-inhibitory networks, the oscillations are generated by slower feedback inhibition following fast recurrent excitations [Andersen and Eccles, 1962] [Freeman, 1975] [Frolov and Medvedev, 1986] [Wilson and Cowan, 1972] [Wilson and Cowan, 1973]. Wilson and Cowan analyzed this phenomena by means of a firing rate model for the excitatory-inhibitory populations [Destexhe and Sejnowski, 2009]. The oscillations generated by this mechanism can be used to model the gamma oscillations in the olfactory bulb [Freeman, 1968], [Freeman, 1975] and in the hippocampus

[Horowitz, 1972] [Leung, 1982]. To understand how the interaction between the excitatory and the inhibitory population generates the oscillation, consider the beginning of the oscillatory cycle. Here, the excitatory input increases and the firing rate of the excitatory population increases due to a positive feedback, until the inhibition catches up and brings the population activity down again. As the excitatory population activity and then the inhibitory population activity goes down, the network recovers from inhibition and the excitatory firing rate increases again. This results in a rhythmic behaviour [Hansel and Mato, 2003] [Paik et al., 2009] [Tsodyks et al., 1997] [Wang, 1999]. This is also called the pyramidal-interneuron gamma mechanism or the PING mechanism [Borgers and Kopell, 2003]. The other mechanism of generation of oscillations is the ING mechanism or the interneuron gamma mechanism which comprises of a network solely made of inhibitory neurons where the timescale of oscillations is on the order of the synaptic delay between neurons [Whittington et al., 2000]. However, since we are interested in oscillations which have a time period of about 50ms, they cannot be explained by slow synapses as it is not biologically realistic to have a synaptic delay of that timescale.

Finally, we wish to analyze waves of oscillatory activity among the different neural populations in the brain. We should distinguish propagatory waves of activity and phase waves. The former simply corresponds to propagation of activity from one region to another (for instance, like the outward flow of ripples on a surface of water when something hits the surface). The latter, on the other hand, corresponds to oscillations in different spatial regions with a fixed phase difference between them. As a result, the maximum of one oscillation is reached a little time after the maximum of another oscillation and this creates the impression of a wave. Cognitive processes such as sensory perception, motor actions and decision making engage selective neural populations. The neural activities in these populations can either be spatially confined in time or can propagate as waves among the different populations. For instance, gamma waves have been observed in the frontal cortex [Llinas and Ribary, 1993] [Ribary et al., 1991], slow sleep oscillations have been observed in the frontal cortex [Massimini et al., 2004] [Massimini et al., 2007] [Murphy et al., 2009]. LFP beta oscillatory episodes have been observed in the motor and premotor cortical areas of a monkey and they contain information about the visual target that the alert monkey needs to reach [Rubino et al., 2006]. Stimulus-induced waves have been observed in vivo using EEG recordings or voltage-sensitive dye in the olfactory bulb [Eeckman and Freeman, 1990] [Eeckman and Freeman, 1978] [Orbach and Cohen, 1983], turtle visual cortex [Prechtl et al., 1997], and rat somatosensory cortex [Petersen and Sakmann, 2001]. In vitro studies have also demonstrated wave propagation of evoked responses in cortical slices [Contreras and Llinas, 2001] [Tanifuji et al., 1994] [Wu et al., 2008] [Xu et al., 2007].

To model both kinds of waves, we can use the fact that in the cortex, the probability of synaptic connection decreases with the physical distance for both excitatory pyramidal cells and inhibitory interneurons [Gilbert, 1993] [Sik et al., 1995] [Stepanyants et al., 2007]. This enables the spiking activity to spread from one group of neurons to the next in the form of a propagating wave or the different oscillating regions to synchronize.

III.2 Dynamics of a single EI network

In this section, we first describe the dynamics of a network of two populations of neurons, excitatory (E) and inhibitory (I) neurons. We will look at the different dynamical regimes of this system and in the next section, we will make a connection to the two population rate model. We compare the dynamics of the EI network in different regimes with the corresponding adaptive rate model for the two populations. We will then focus on the regime where this network displays oscillations. After we have identified this regime, we will spatially extend our EI network to two EI networks and study the different dynamical regimes in this extended model.

In the single EI network, the two populations i.e. the excitatory and inhibitory populations are connected to each other. In addition, the excitatory population is recurrently connected to itself (see figure III.1).

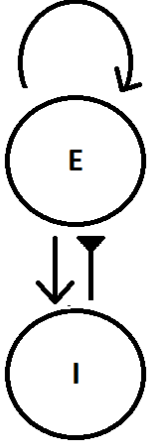


Figure III.1: **The Excitatory-Inhibitory network.** The excitatory and the inhibitory populations are synaptically connected to each other and the excitatory population is recurrently connected in itself. We do not include the I-I synaptic connections because we wish to study the oscillations mediated by E-I coupling and not the fast oscillations at the timescale of synaptic coupling that are elicited due to recurrent inhibition.

For the single EI network of neurons, each neuron in the network model is modelled by an exponential integrate and fire neuron. An excitatory neuron obeys the following equation for its membrane potential v_e :

$$\frac{dv_e}{dt} = \frac{-v_e + v_L + F_v + I_{ext}}{\tau} + \frac{\sigma}{\sqrt{\tau}}\eta_i + \sum_{j=1}^{C_e} \sum_k J_{EE}\delta(t - t_j^k) - \sum_{j=1}^{C_i} \sum_k J_{IE}\delta(t - t_j^k), \quad (\text{III.2.1})$$

$$F_v = \Delta_T \exp\left(\frac{v_e - v_T}{\Delta_T}\right), \quad (\text{III.2.2})$$

whereas an inhibitory neuron obeys the following equation for its membrane potential v_i :

$$\frac{dv_i}{dt} = \frac{-v_i + v_L + F_v + I_{ext}}{\tau} + \frac{\sigma}{\sqrt{\tau}}\eta_i + \sum_{j=1}^{C_e} \sum_k J_{EI}\delta(t - t_j^k), \quad (\text{III.2.3})$$

$$F_v = \Delta_T \exp\left(\frac{v_i - v_T}{\Delta_T}\right), \quad (\text{III.2.4})$$

where v_L is the leak voltage, I_{ext} is the external current that is injected into the neuron, σ^2 is the variance of the white noise inserted into the neuron, η_i is a random normal

variable associated with neuron i , τ is the membrane time constant, Δ_T is the sharpness of the action potential initiation, v_T is the membrane potential threshold, N_e is the number of excitatory neurons, N_i is the number of inhibitory neurons, C_e is the number of excitatory connections that each neuron (both excitatory and inhibitory) receives, C_i is the number of inhibitory connections received by each excitatory neuron, t_j^k is the time of the k -th spike of the j -th neuron. Whenever there is a presynaptic spike in an excitatory neuron, there is an increase in the membrane voltage of the postsynaptic neuron by an amount J_{EE} if it is an excitatory neuron and J_{EI} if it is an inhibitory neuron on the next time step (delta synapse). Whenever there is a presynaptic spike in an inhibitory neuron, there is a decrease in the membrane voltage of the postsynaptic excitatory neuron by an amount J_{IE} in the next time step (delta synapse). Note that the convention we use for J_{EI} and J_{IE} is different from the convention regularly used in literature. Usually, in literature, J_{EI} refers to the decrease in postsynaptic membrane potential of the excitatory neuron when there is an action potential in the presynaptic inhibitory neuron and J_{IE} refers to the increase in postsynaptic membrane potential of the inhibitory neuron when there is an action potential in the presynaptic excitatory neuron. However, in this manuscript, we use J_{EI} to refer to the increase in postsynaptic membrane potential of the inhibitory neuron when there is an action potential in the presynaptic excitatory neuron and J_{IE} to refer to the decrease in postsynaptic membrane potential of the excitatory neuron when there is an action potential in the presynaptic inhibitory neuron.

We do not include the I-I synaptic connections for simplicity and also because we wish to study the oscillations mediated by E-I coupling and not the fast oscillations at the timescale of synaptic coupling that are elicited due to recurrent inhibition. When the membrane potential of any neuron crosses v_T , it diverges to infinity in finite time. Therefore, when the membrane potential reaches the threshold potential v_{th} , we insert a spike for the neuron and the membrane potential of the neuron is reset to v_R . For a duration of t_{ref} , the refractory time period, the neuron is clamped to the voltage v_R , before it resumes its dynamics again according to the above equations. All the network simulations are performed in BRIAN2 [Goodman and Brette, 2009]. For the network simulations, we use a time step of 0.01 ms. We fix the desired firing rates of the excitatory population and the inhibitory population to be $r_E^0 = 5$ Hz and $r_I^0 = 10$ Hz respectively. To obtain these firing rates in the two populations, we firstly compute the necessary currents I_E^0 and I_I^0 that needs to be injected into each of the neurons. This can be done by inverting the f-I curve of the EIF neuron at the values corresponding to 5 Hz and 10 Hz. However, these currents are the total currents that need to be injected into the neurons and they include the contributions due to the synaptic connectivity of the neurons. Hence, to find out the external current that needs to be injected into the neurons, we should subtract the contribution to the mean input current due to synaptic connectivity. The contribution to the mean input current due to synaptic connectivity to the excitatory neurons is given by $C_e J_{EE} r_E \tau_m - C_i J_{IE} r_E \tau_m$ and the contribution to the mean input current due to synaptic connectivity to the inhibitory neurons is given by $C_e J_{EI} r_E \tau_m$. Subtracting the values of the mean input current due to synaptic connectivity from I_E^0 and I_I^0 gives the necessary external currents I_E^{ext} and I_I^{ext} that need to be injected in neurons to give a firing rate of 5 Hz and 10 Hz. Similarly, the standard deviation of the inserted noise σ is chosen to be 10 mV, which

τ	10 ms	v_L	-65 mV
ΔT	3.5 mV	v_T	-59.9 mV
v_R	-68 mV	$v_{T^{thresh}}$	-30 mV
r_E^0	5 Hz	r_I^0	10 Hz
I_E^0	-6.283 mV	I_I^0	-3.621 mV
I_E^{ext}	-10.283 mV	I_I^{ext}	-11.621 mV
σ_E	10 mV	σ_I	10 mV
σ_E^{ext}	9.994 mV	σ_I^{ext}	9.996 mV
N_E	4000	N_I	1000
C_E	800	C_I	200
J_{EE}	0.2 mV	J_{IE}	0.2 mV
J_{EI}	0.2 mV	J_{II}	0.0 mV

Table III.1: Parameters used in the E-I network simulation.

is high enough so as to reproduce a Coefficient of Variation (CV) of around 1.0 in the neurons. In order to maintain the standard deviation of the total input noise to the neurons to be equal to 10 mV in the presence of connectivity, we subtract the corresponding contributions due to synaptic connectivity. The contribution to the variance of the inserted noise due to synaptic connectivity to the excitatory neurons is given by $C_e J_{EE}^2 r_E \tau_m + C_i J_{IE}^2 r_E \tau_m$ while the contribution to the variance of the inserted noise due to synaptic connectivity to the inhibitory neurons is given by $C_e J_{EI}^2 r_E \tau_m$. Subtracting these values from the variance of a noise standard deviation 10 mV gives us the variance of the external noises σ_E^{ext} and σ_I^{ext} that needs to be inserted into the neurons. The following table shows the values used for one such simulation and the corresponding result is shown in figure III.4.

III.2.1 Different dynamical regimes of the EI network

Using different values of the synaptic connectivity strengths, we can run the network simulations. If the network indeed converges to the firing rates that we have specified, then these firing rates are a stable point of the network for the corresponding connectivity strengths. If, on the other hand, the network does not converge to the stationary state of the specified firing rates: 5 Hz and 10 Hz for the excitatory population and the inhibitory population, respectively, in our case, then the fixed point is not stable for the corresponding parameters of the connectivity strengths. Indeed, in the network simulations, we find a range of parameters where the fixed point is stable (see figure III.2) and other points in the phase space of connectivity strengths where the network population firing rates either oscillate in time (see figure III.4) or converge to another fixed point (see figure III.3) or exhibit synchronous spikes of activity (see figure III.5). Due to the Poissonian spiking of neurons, the population firing rate is not exactly 5 Hz but it fluctuates around it. To explain the different regimes on the phase diagram, we can turn to the corresponding adaptive rate models.

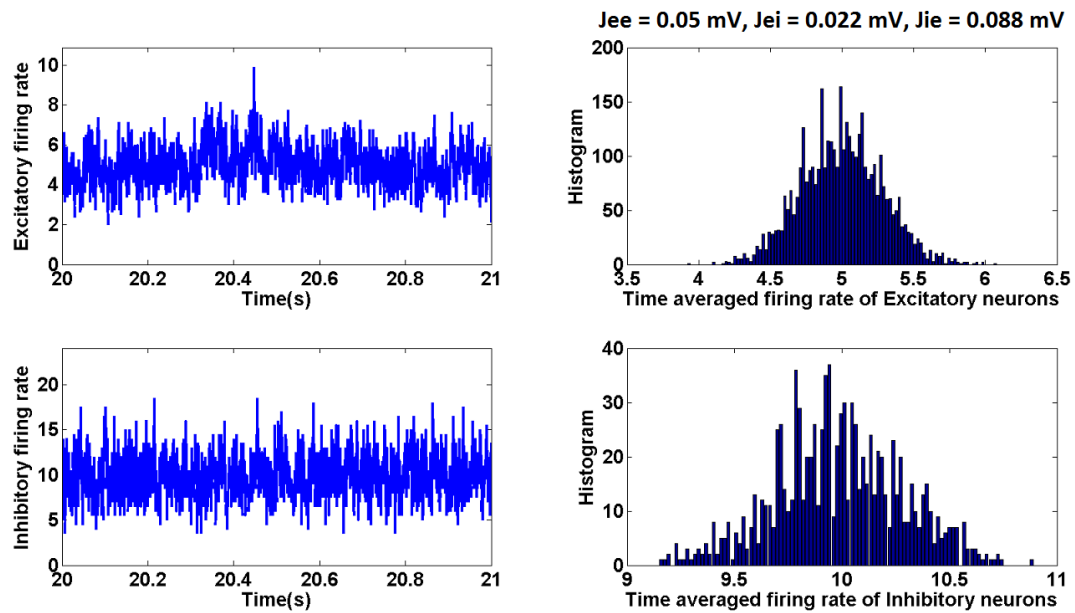


Figure III.2: Network firing rates converge to the stable fixed point for the corresponding synaptic strengths. The left panels show the excitatory and inhibitory population firing rate as a function of time. The right panels show the histogram of the excitatory and inhibitory population firing rates.

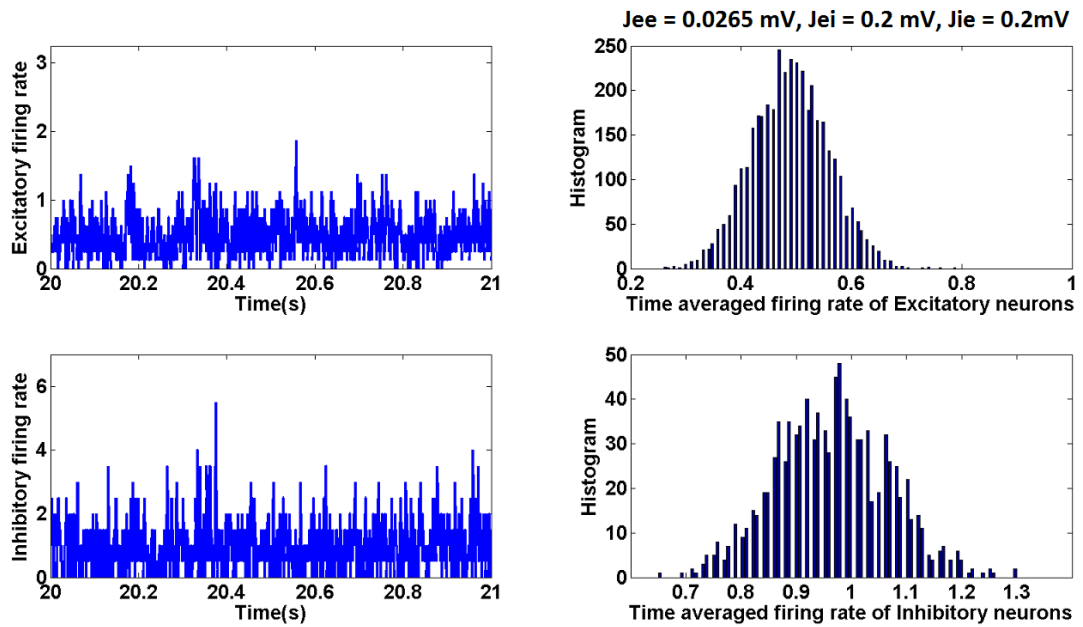


Figure III.3: Network firing rates reach another fixed point for the corresponding synaptic strengths. The left panels show the excitatory and inhibitory population firing rate as a function of time. The right panels show the histogram of the excitatory and inhibitory population firing rates.

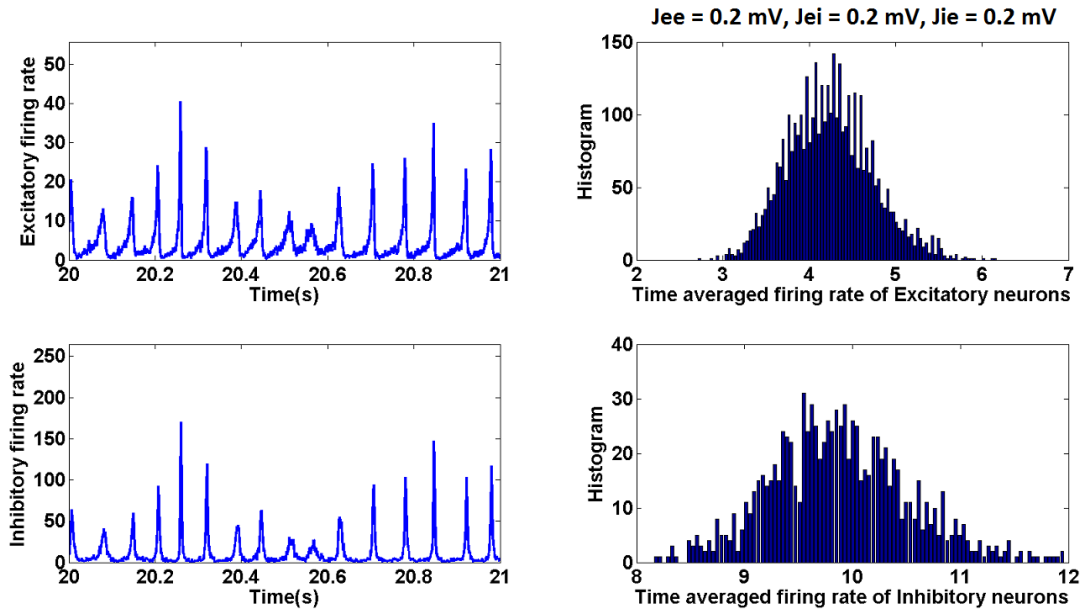


Figure III.4: **Network firing rates oscillate in time for the corresponding synaptic strengths.** The left panels show the excitatory and inhibitory population firing rate as a function of time. The right panels show the histogram of the excitatory and inhibitory population firing rates.

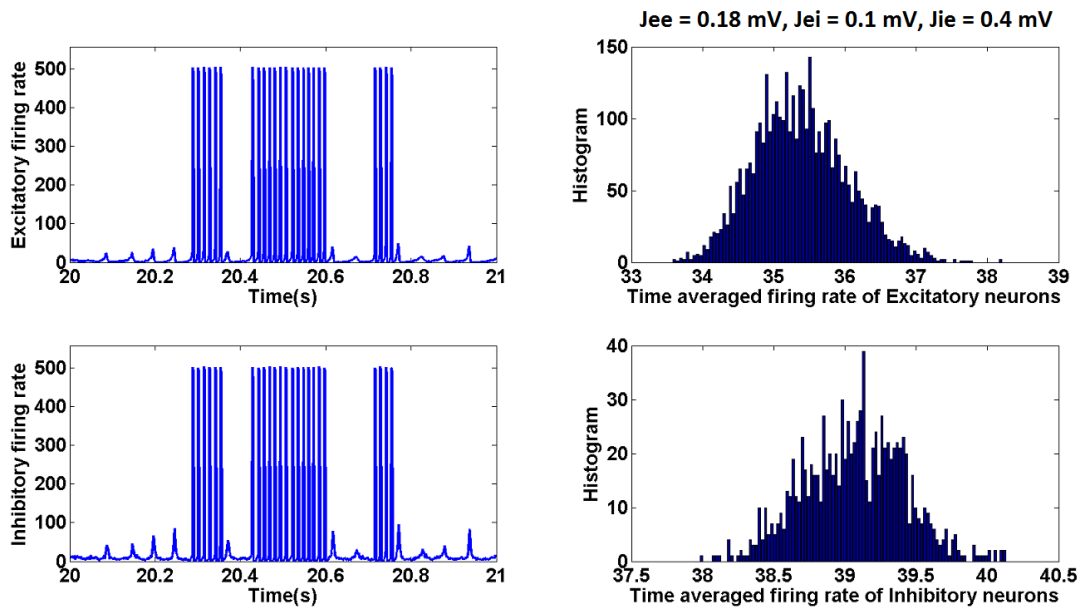


Figure III.5: **Network firing rates exhibit synchronous spikes of activity for the corresponding synaptic strengths.** The left panels show the excitatory and inhibitory population firing rate as a function of time. The right panels show the histogram of the excitatory and inhibitory population firing rates.

III.3 Rate Model with coupling

In this section, we describe the dynamics of the adaptive rate 0 model for two population of neurons, excitatory and inhibitory neurons. The two populations i.e. the excitatory and inhibitory populations are connected to each other. In addition, the excitatory population is recurrently connected to itself. For the sake of simplicity, we first consider a rate model without any finite size effects due to the limited size of the network. Hence, we neglect the noise due to finite network size. The dynamics of the corresponding adaptive rate model for two populations are given by the following equations:

$$r_E = \Phi_E(I_E), \quad (\text{III.3.1})$$

$$r_I = \Phi_I(I_I), \quad (\text{III.3.2})$$

$$\tau_E \frac{dI_E}{dt} = -I_E + I_E^{ext} + w_{EE}r_E - w_{IE}r_I, \quad (\text{III.3.3})$$

$$\tau_I \frac{dI_I}{dt} = -I_I + I_I^{ext} + w_{EI}r_E, \quad (\text{III.3.4})$$

where r_E and r_I represent the firing rates of the excitatory and inhibitory populations respectively, I_E and I_I represent the input currents to the two populations, $\Phi_E(\cdot)$ and $\Phi_I(\cdot)$ are the f-I curves of the exponential-integrate and fire neuron, I_E^{ext} and I_I^{ext} are the external currents injected into the excitatory and inhibitory populations respectively, w_{EE} and w_{EI} are the coupling strengths from the excitatory population to the excitatory and the inhibitory populations respectively, w_{IE} is the coupling strength from the inhibitory population to the excitatory population. The correspondence to the EI network simulations with connectivity strengths J_{EE} , J_{EI} and J_{IE} can therefore be made by taking $w_{EE} = C_e J_{EE} \tau_m$, $w_{EI} = C_e J_{EI} \tau_m$ and $w_{IE} = C_i J_{IE} \tau_m$. The time constants of the two populations, τ_E and τ_I are functions of the currents I_E and I_I as prescribed by Ostojic and Brunel (see section II.5 for AR0 model) or as explained in section II.5 (AR1 model).

We look for the regions in the w space where we have the steady state (r_E^0, r_I^0) or equivalently (I_E^0, I_I^0) :

$$I_E^0 = I_E^{ext} + w_{EE}r_E^0 - w_{IE}r_I^0, \quad (\text{III.3.5})$$

$$I_I^0 = I_I^{ext} + w_{EI}r_E^0. \quad (\text{III.3.6})$$

This can be done by assuming small perturbations (linearization) around this state and looking at the eigenvalues to determine how the perturbations grow or diminish in time.

$$I_E = I_E^0 + i_E, \quad (\text{III.3.7})$$

$$I_I = I_I^0 + i_I, \quad (\text{III.3.8})$$

This gives us the following equations for the dynamics of the perturbations:

$$\tau_E \frac{di_E}{dt} = -I_E + I_E^{ext} + w_{EE}r_E - w_{IE}r_I, \quad (\text{III.3.9})$$

$$\tau_I \frac{di_I}{dt} = -I_I + I_I^{ext} + w_{EI}r_E, \quad (\text{III.3.10})$$

where

$$r_E = \Phi(I_E^0 + i_E) = r_E^0 + \Phi'(I_E^0)i_E, \quad (\text{III.3.11})$$

$$r_I = \Phi(I_I^0 + i_I) = r_I^0 + \Phi'(I_I^0)i_I, \quad (\text{III.3.12})$$

Substituting this in the above equations, we can rewrite the 2x2 dynamical system as follows:

$$\frac{d}{dt} \begin{pmatrix} i_E \\ i_I \end{pmatrix} = \begin{pmatrix} \frac{-1+w_{EE}\Phi'(I_E^0)}{\tau_E} & \frac{-w_{IE}\Phi'(I_I^0)}{\tau_E} \\ \frac{w_{EI}\Phi'(I_E^0)}{\tau_I} & \frac{-1}{\tau_I} \end{pmatrix} \begin{pmatrix} i_E \\ i_I \end{pmatrix} \quad (\text{III.3.13})$$

To determine the stability of the above dynamical system, we compute its eigenvalues. The eigenvalues of the above matrix are the solutions of the polynomial equation:

$$1 - w_{EE}\Phi'(I_E^0) + w_{EI}w_{IE}\Phi'(I_E^0)\Phi'(I_I^0) + \lambda(\tau_E + \tau_I - \tau_I w_{EE}\Phi'(I_E^0)) + \lambda^2\tau_E\tau_I = 0, \quad (\text{III.3.14})$$

where λ denotes the eigenvalues. Let us write $\Phi'(I_E^0)$ as Φ'_E and $\Phi'(I_I^0)$ as Φ'_I for simplicity. The solutions of the polynomial equation are:

$$\lambda_{1,2} = -\left(\frac{\tau_E + \tau_I - \tau_I w_{EE}\Phi'_E}{2\tau_E\tau_I}\right) \pm \frac{\sqrt{(\tau_E - \tau_I + \tau_I w_{EE}\Phi'_E)^2 - 4\tau_E\tau_I w_{EI}w_{IE}\Phi'_E\Phi'_I}}{2\tau_E\tau_I}. \quad (\text{III.3.15})$$

The sum and product of the eigenvalues are given as:

$$\lambda_1 + \lambda_2 = -\frac{\tau_E + \tau_I - \tau_I w_{EE}\Phi'_E}{\tau_E\tau_I}, \quad (\text{III.3.16})$$

$$\lambda_1\lambda_2 = \frac{1 - w_{EE}\Phi'_E + w_{EI}w_{IE}\Phi'_E\Phi'_I}{\tau_E\tau_I}. \quad (\text{III.3.17})$$

The eigenvalues have an imaginary component when:

$$(\tau_E + \tau_I - \tau_I w_{EE}\Phi'_E)^2 < 4\tau_E\tau_I(1 - w_{EE}\Phi'_E + w_{EI}w_{IE}\Phi'_E\Phi'_I), \quad (\text{III.3.18})$$

i.e.,

$$(\tau_E - \tau_I + \tau_I w_{EE}\Phi'_E)^2 < 4\tau_E\tau_I w_{EI}w_{IE}\Phi'_E\Phi'_I. \quad (\text{III.3.19})$$

If $\tau_E + \tau_I - \tau_I w_{EE}\Phi'_E > 0$ i.e. $w_{EE} < \frac{\tau_E + \tau_I}{\tau_I\Phi'_E}$, we have the condition to get oscillatory eigenmodes to be,

$$w_{EE} < \frac{2\sqrt{\tau_E\tau_I\Phi'_E\Phi'_I w_{EI}w_{IE} - \tau_E + \tau_I}}{\Phi'_E\tau_I}. \quad (\text{III.3.20})$$

While if $\tau_E + \tau_I - \tau_I w_{EE}\Phi'_E < 0$ i.e. $w_{EE} > \frac{\tau_E + \tau_I}{\tau_I\Phi'_E}$, we get the condition,

$$w_{EE} > \frac{-2\sqrt{\tau_E\tau_I\Phi'_E\Phi'_I w_{EI}w_{IE} - \tau_E + \tau_I}}{\Phi'_E\tau_I}. \quad (\text{III.3.21})$$

We will look at the 2D phase space with the following parameters as variables: w_{EE} and $\sqrt{w_{IE}w_{EI}}$. There are four regimes that we can consider: stable fixed point regime, stable oscillations regime, unstable fixed point regime and unstable oscillations regime. 1) Stable regime: In this regime, the fixed point is stable and any perturbations around the fixed point will eventually vanish away. For this to be the case, the real part of the two eigenvalues should be negative or equivalently the sum of eigenvalues must be negative and the product must be positive. The fact that the timescale is adaptive or not does not matter for these conditions and they only depend on the timescale at the fixed point.

A stable fixed point regime is, therefore, given by the following conditions for the sum and product of eigenvalues (from equations III.3.16 and III.3.17),

$$\tau_E + \tau_I - \tau_I w_{EE} \Phi'_E > 0, \quad (\text{III.3.22})$$

and

$$1 - w_{EE} \Phi'_E + w_{EI} w_{IE} \Phi'_E \Phi'_I > 0. \quad (\text{III.3.23})$$

$$\Rightarrow w_{EE} < \frac{\tau_E + \tau_I}{\Phi'_E \tau_I}, \quad (\text{III.3.24})$$

and

$$\Rightarrow w_{EE} < \frac{1 + w_{EI} w_{IE} \Phi'_E \Phi'_I}{\Phi'_E}. \quad (\text{III.3.25})$$

The perturbations away from the fixed point can vanish in two ways: either, it can decay exponentially to the fixed point or it can oscillate around the fixed point with the amplitude of the oscillations decaying in time. This corresponds to whether or not the eigenvalue has an imaginary component or not. For the eigenvalues to not have an imaginary component, we need

$$w_{EE} > \frac{2\sqrt{\tau_E \tau_I \Phi'_E \Phi'_I w_{EI} w_{IE}} - \tau_E + \tau_I}{\Phi'_E \tau_I}. \quad (\text{III.3.26})$$

An example of the dynamics of the two populations of the model obtained when this condition is satisfied is shown in figure III.6. Here, $(r_E^0, r_I^0) = (5, 10)$ Hz, $w_{EE} = 0.4$ mV.s, $w_{EI} = 0.1$ mV.s and $w_{IE} = 0.1$ mV.s. For the corresponding network of EIF neurons, these parameters correspond to $J_{EE} = 0.05$ mV, $J_{EI} = 0.0125$ mV and $J_{IE} = 0.05$ mV for network connectivity of $C_e = 800$, $C_i = 200$ and neuronal membrane time constant of $\tau_m = 10$ ms. For these parameters, any small perturbation around the fixed point decays and the firing rates converge to the fixed point.

For the eigenvalues to have an imaginary component, we need

$$w_{EE} < \frac{2\sqrt{\tau_E \tau_I \Phi'_E \Phi'_I w_{EI} w_{IE}} - \tau_E + \tau_I}{\Phi'_E \tau_I}. \quad (\text{III.3.27})$$

Therefore, at $w_{EE} = \frac{2\sqrt{\tau_E \tau_I \Phi'_E \Phi'_I w_{EI} w_{IE}} - \tau_E + \tau_I}{\Phi'_E \tau_I}$, we have a transition from a “stable fixed point regime”, where the perturbations decay exponentially to the fixed point, to a “damped oscillations regime” where the perturbations oscillate towards the fixed

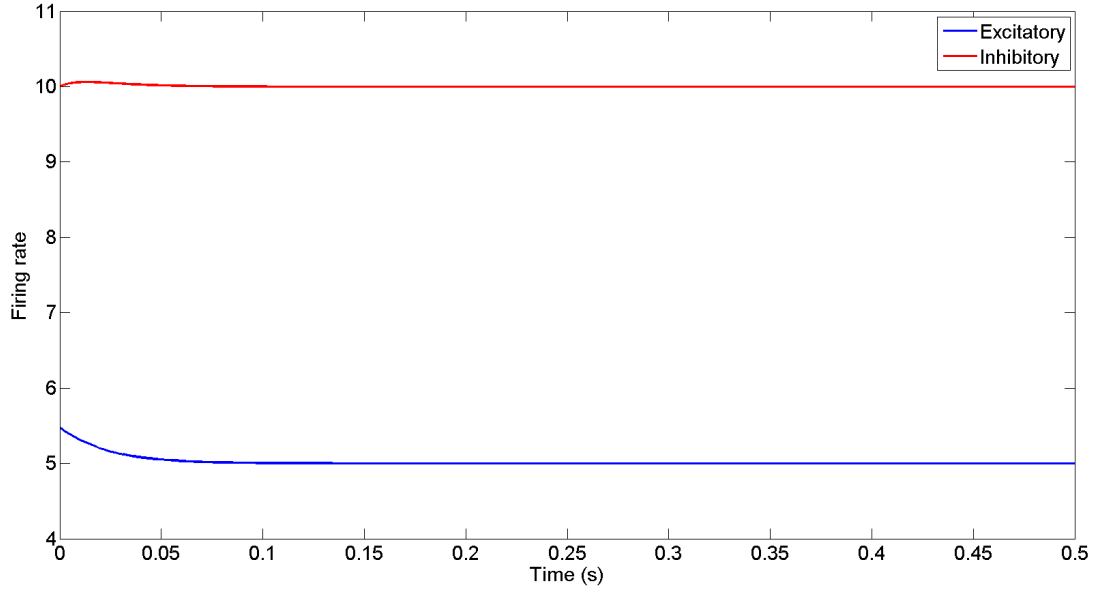


Figure III.6: **Firing rates of the ARO model converge to the stable fixed point.** The excitatory firing rate (in blue) and the inhibitory firing rate (in red) of the adaptive rate 0 model when the fixed point is stable and the dynamics does not have an imaginary component in its eigenvalues. Any small perturbation in the firing rates decays back to the stable fixed point.

point decaying in time. An example of such a dynamics of the two populations obtained when this condition is satisfied is shown in figure III.7. Here, $(r_E^0, r_I^0) = (5, 10)$ Hz, $w_{EE} = 1.4$ mV.s, $w_{EI} = 1.6$ mV.s and $w_{IE} = 0.4$ mV.s. For the corresponding network of EIF neurons, these parameters correspond to $J_{EE} = 0.175$ mV, $J_{EI} = 0.2$ mV and $J_{IE} = 0.2$ mV for network connectivity of $C_e = 800$, $C_i = 200$ and neuronal membrane time constant of $\tau_m = 10$ ms. For these parameters, any small perturbation around the fixed point causes the firing rates to oscillate towards the stable fixed point before converging to it.

2) Unstable regime: In this regime, the fixed point is not stable and any small perturbations drives the system away to either a new fixed point or it causes the system to oscillate forever, if there is an input energy source. For the fixed point to be unstable, at least one eigenvalue must be positive. For this to happen, we need the product as well as the sum of the eigenvalues to be negative. This leads to the following condition,

$$w_{EE} > \frac{\tau_E + \tau_I}{\Phi'_E \tau_I} \quad (\text{III.3.28})$$

or

$$w_{EE} > \frac{1 + w_{EI} w_{IE} \Phi'_E \Phi'_I}{\Phi'_E} \quad (\text{III.3.29})$$

An example of such a dynamics of the two populations obtained when the fixed point is unstable is shown in figure III.8. Here, $(r_E^0, r_I^0) = (5, 10)$ Hz, $w_{EE} = 2.0$ mV.s,

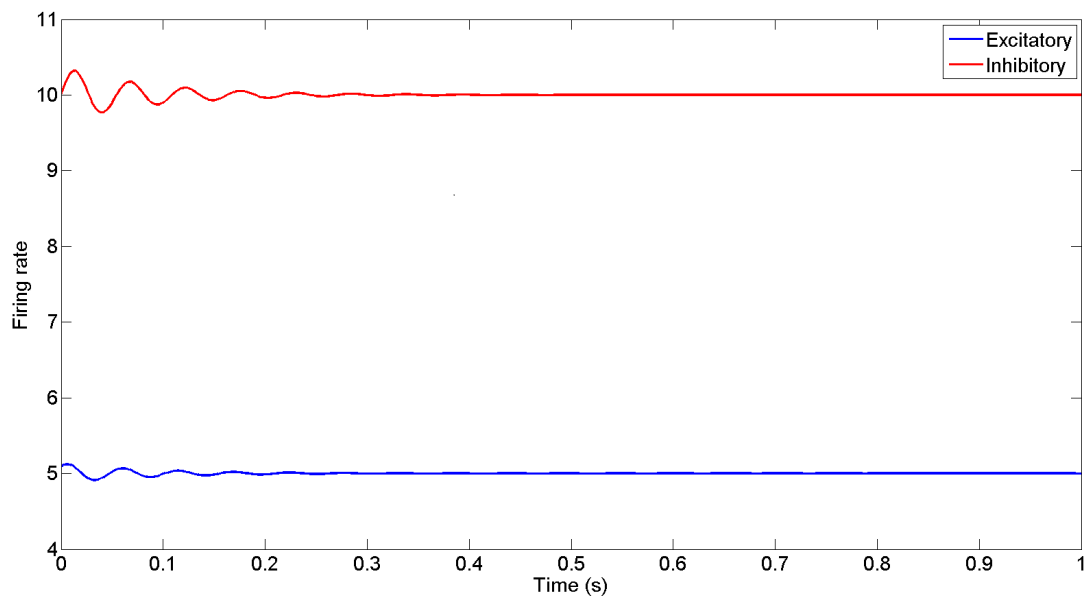


Figure III.7: **Firing rates of the AR0 model oscillate and converge to the stable fixed point.** The excitatory firing rate (in blue) and the inhibitory firing rate (in red) of the adaptive rate 0 model when the fixed point is stable and the dynamics has an imaginary component in its eigenvalues. Any small perturbation in the firing rates oscillates around the fixed point before the firing rates converge to the stable fixed point.

$w_{EI} = 1.6$ mV.s and $w_{IE} = 0.4$ mV.s. For the corresponding network of EIF neurons, these parameters correspond to $J_{EE} = 0.25$ mV, $J_{EI} = 0.2$ mV and $J_{IE} = 0.2$ mV for network connectivity of $C_e = 800$, $C_i = 200$ and neuronal membrane time constant of $\tau_m = 10$ ms. For these parameters, for any small perturbation around the fixed point will drive the firing rates away to another fixed point.

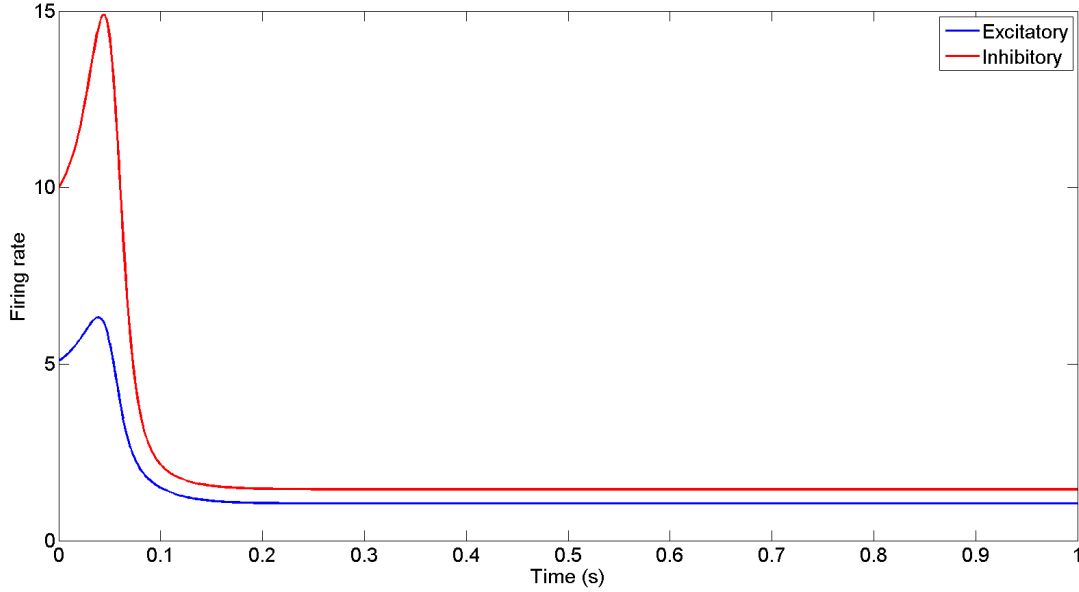


Figure III.8: **Firing rates of the AR0 model reach another fixed point because the initial fixed point is unstable for the corresponding coupling strength parameters.** The excitatory firing rate (in blue) and the inhibitory firing rate (in red) of the adaptive rate 0 model when the fixed point is unstable and the dynamics does not have an imaginary component in its eigenvalues. Any small perturbation in the firing rates around the original fixed point $(r_E, r_I) = (5, 10)$ Hz takes the system away to the other fixed point.

Here again, there is a transition from this regime i.e. “unstable fixed point” to a regime where we find oscillations depending on whether the eigenvalue has an imaginary component or not. This occurs when,

$$(\tau_E - \tau_I + \tau_I w_{EE} \Phi'_E)^2 = 4\tau_E \tau_I w_{EI} w_{IE} \Phi'_E \Phi'_I \quad (\text{III.3.30})$$

$$\Rightarrow w_{EE} = \frac{-2\sqrt{\tau_E \tau_I \Phi'_E \Phi'_I w_{EI} w_{IE} - \tau_E + \tau_I}}{\Phi'_E \tau_I}. \quad (\text{III.3.31})$$

The transition from stable to unstable oscillations is given by $\text{Re}(\lambda)=0$ i.e. (from equation III.3.15)

$$\tau_E + \tau_I - \tau_I w_{EE} \Phi'_E = 0 \quad (\text{III.3.32})$$

$$\Rightarrow w_{EE} = \frac{\tau_E + \tau_I}{\tau_I \Phi'_E} \quad (\text{III.3.33})$$

The frequency of the oscillation can be calculated by inverting the imaginary component of the eigenvalue and is given by:

$$\omega = \frac{\sqrt{(\tau_E - \tau_I + \tau_I w_{EE} \Phi'_E)^2 - 4\tau_E \tau_I \Phi'_E \Phi'_I w_{EI} w_{IE}}}{2\tau_E \tau_I} \quad (\text{III.3.34})$$

An example of such a dynamics of the two populations obtained when the fixed point is unstable and the eigenvalues of the dynamics have an imaginary component is shown in figure III.9. Here, $(r_E^0, r_I^0) = (5, 10)$ Hz, $w_{EE} = 1.6$ mV.s, $w_{EI} = 1.6$ mV.s and $w_{IE} = 0.4$ mV.s. For the corresponding network of EIF neurons, these parameters correspond to $J_{EE} = 0.2$ mV, $J_{EI} = 0.2$ mV and $J_{IE} = 0.2$ mV for network connectivity of $C_e = 800$, $C_i = 200$ and neuronal membrane time constant of $\tau_m = 10$ ms. For these parameters, any small perturbation around the fixed point will cause the system to become unstable and oscillate. The oscillations saturate because of the nonlinearity in the system. The oscillations observed here, indeed correspond to a PING mechanism, with the peaks of the inhibitory firing rate following the peaks of the firing rate of the excitatory population.

To recapitulate all of the above information, we can plot the corresponding phase diagram for the EI model as shown in figure III.10. To plot the phase diagram, we consider the parameters w_{EE} on one axis and $\sqrt{w_{IE} w_{EI}}$ on the other axis. The phase diagram demarcates the various dynamical regimes and the different lines of bifurcations in the EI system.

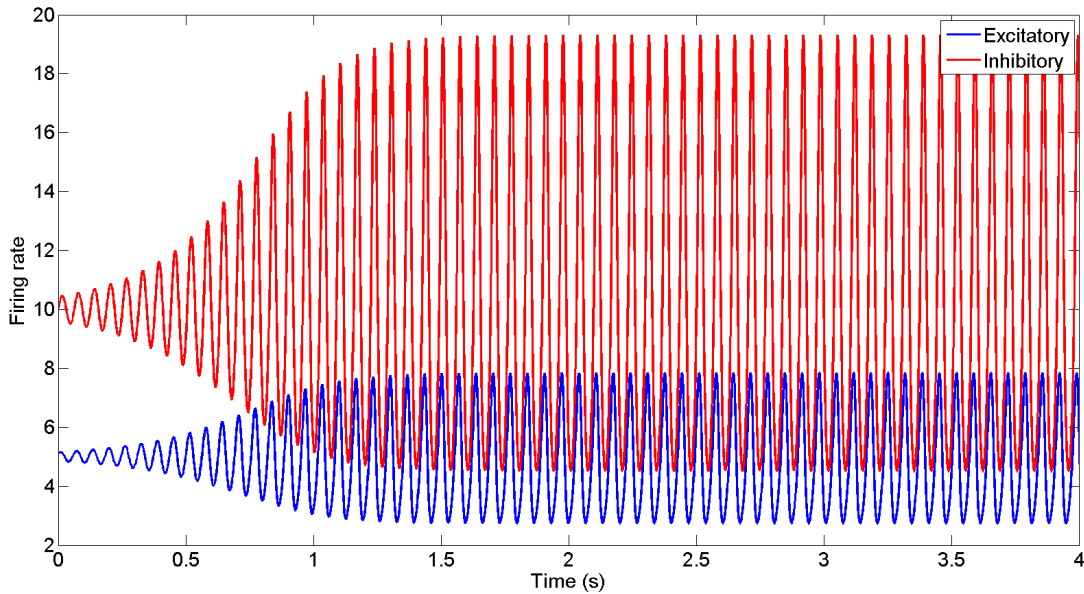


Figure III.9: **Firing rates of the AR0 model oscillate in time.** The excitatory firing rate (in blue) and the inhibitory firing rate (in red) of the adaptive rate 0 model when the fixed point is unstable and the dynamics has an imaginary component in its eigenvalues.

Since we want to model the oscillations of the EI network, we will confine ourselves to the oscillatory regime in the phase diagram. However, from figure III.4, we observe

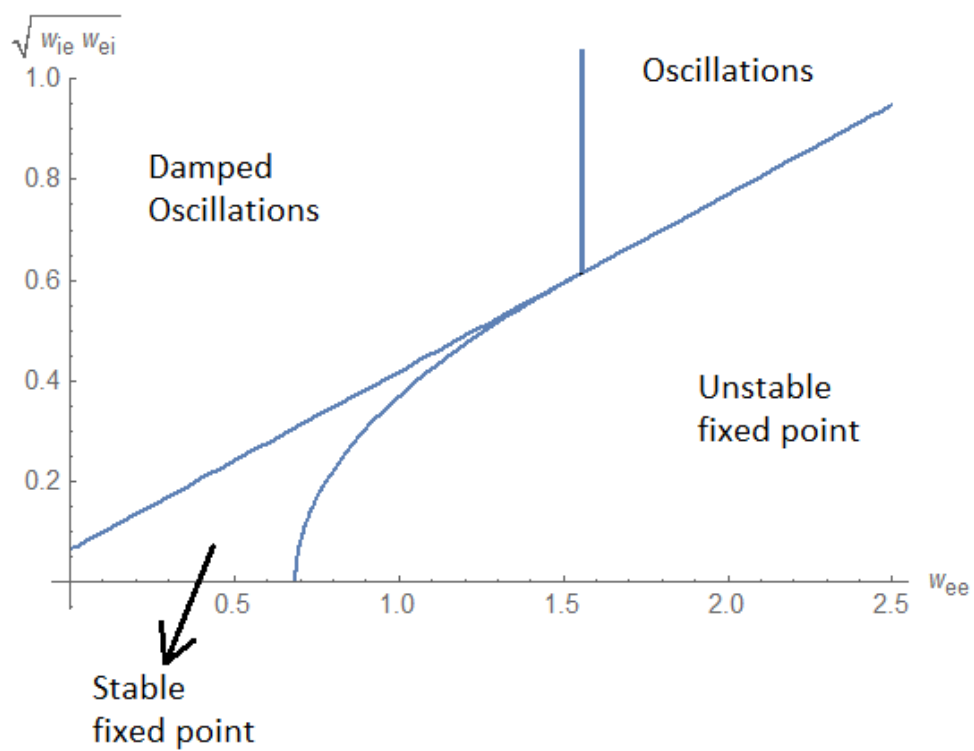


Figure III.10: The phase diagram of the EI rate model displaying the bifurcation lines and the four regimes.

that the oscillations in the spiking network are noisy. We also do not observe a sharp transition to the oscillatory regime from the damped oscillations regime because of the finite size noise. In the next section, we will compare the oscillations observed in the network with the oscillations observed in the two adaptive rate models with finite size noise. We will see that the AR1 model performs better than the AR0 model in the oscillatory regime. We will then try to reproduce the oscillations in the network using the AR1 model.

III.4 Comparing the oscillatory phases of the rate model and the network model

We begin by comparing the two adaptive rate models for the case of the EI network of EIF neurons. To do this, we simulate the network of 5000 neurons (4000 excitatory and 1000 inhibitory) and 20000 neurons (16000 excitatory and 4000 inhibitory) for a time duration of 200 seconds each. We extract the average over neurons of the synaptic input into each excitatory neuron and each inhibitory neuron from each excitatory and each inhibitory neuron. We thus obtain three quantities as a function of time: the mean synaptic excitatory input to an excitatory neuron, the mean synaptic inhibitory input to an excitatory neuron and the mean synaptic excitatory input to an inhibitory neuron. We inject these quantities into the rate models with no connectivity i.e. $w_{EE} = w_{EI} = w_{IE} = w_{II} = 0$. We run the rate model simulations 1000 times accounting for the finite size effects as presented in equation II.3.16 (for network sizes of 5000 and 20000 neurons respectively). We compute the mean firing rate over the different trials in both cases for the Adaptive Rate 0 and the Adaptive Rate 1 models and compute the correlation coefficient with the original firing rates of the network. The cross correlation coefficients between the network of 5000 neurons and adaptive rate 0 model are 0.9721 and 0.9780 for the excitatory and inhibitory firing rates respectively whereas the cross correlation coefficients between the network of 5000 neurons and adaptive rate 1 model are 0.9802 and 0.9814 respectively. Similarly, the cross correlation coefficients between the network of 20000 neurons and adaptive rate 0 model are 0.9864 and 0.9910 for the excitatory and inhibitory firing rates respectively whereas the cross correlation coefficients between the network of 20000 neurons and adaptive rate 1 model are 0.9921 and 0.9922 respectively. Shown in figures III.11, III.12, III.13 and III.14 are the comparisons between the firing rates of the network and the Adaptive Rate 0 model and the Adaptive Rate 1 model respectively. Even though the correlation coefficients do not change significantly, we observe that the adaptive rate 1 model better fits the peaks of the network activity than the adaptive rate 0 model.

III.4.1 Computing the limit cycles of the EI dynamical system

We simulate the dynamics of the firing rates for the case of a fully connected EI network of 5000 and 20000 EIF neurons (with 4:1 as ratio of number of excitatory neurons and inhibitory neurons) and the two corresponding adaptive rate models for the case of $w_{EE} = w_{EI} = 1.6$ mV.s and $w_{IE} = 0.4$ mV.s for 100 seconds each. Firstly, to compare the firing rates obtained, we can plot the 2D histograms of the firing rates. For purposes of visualization, we plot instead the log of the histogram as shown in figures III.15 and

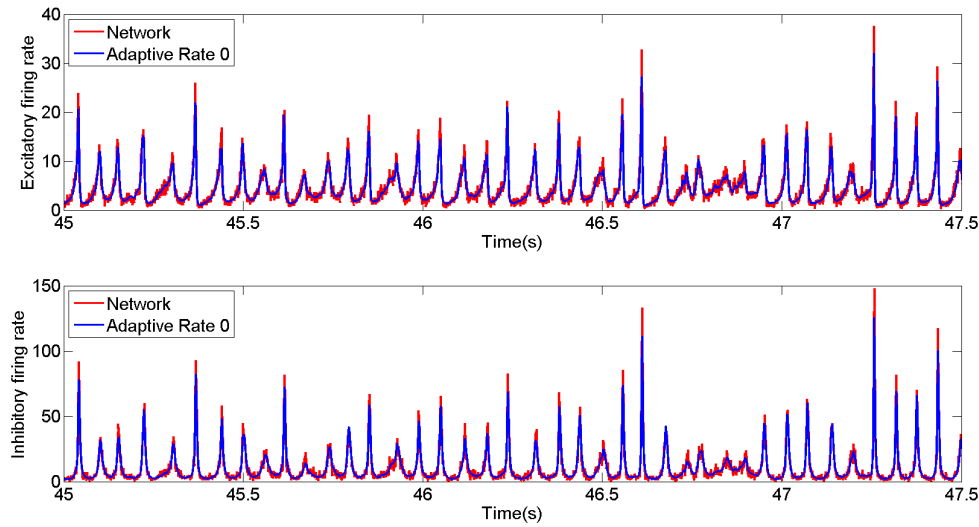


Figure III.11: **Comparing the firing rates of the AR0 model and Network of 5000 EI neurons.** For this plot, the mean synaptic input received by the neurons in the network of 5000 neurons is injected into the adaptive rate 0 model with no connectivity and the firing rates of the two are then compared. The top panel shows the excitatory firing rates of the network (in red) and the adaptive rate 0 model (in blue) and the bottom panel shows the inhibitory firing rates of the network (in red) and the adaptive rate 0 model (in blue).

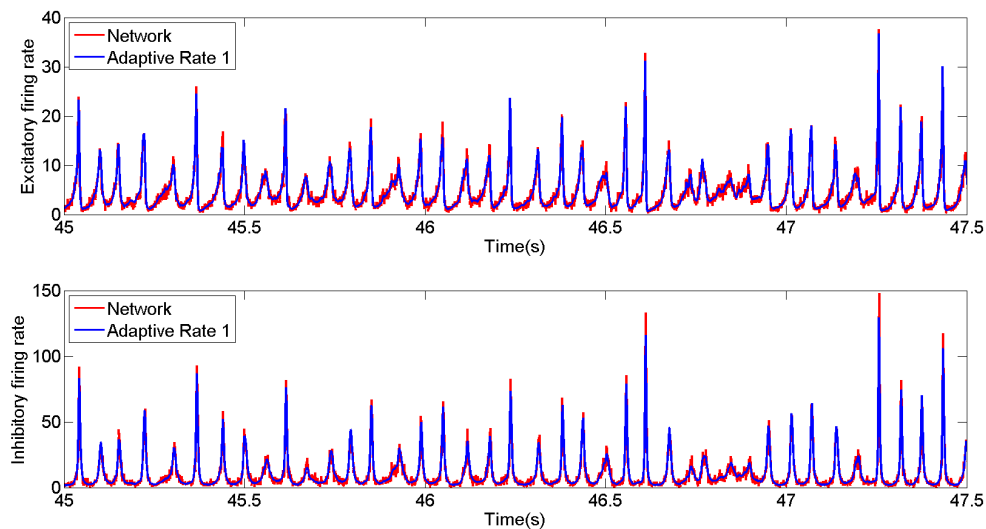


Figure III.12: **Comparing the firing rates of the AR1 model and Network of 5000 EI neurons.** For this plot, the mean synaptic input received by the neurons in the network of 5000 neurons is injected into the adaptive rate 1 model with no connectivity and the firing rates of the two are then compared. The top panel shows the excitatory firing rates of the network (in red) and the adaptive rate 1 model (in blue) and the bottom panel shows the inhibitory firing rates of the network (in red) and the adaptive rate 1 model (in blue).

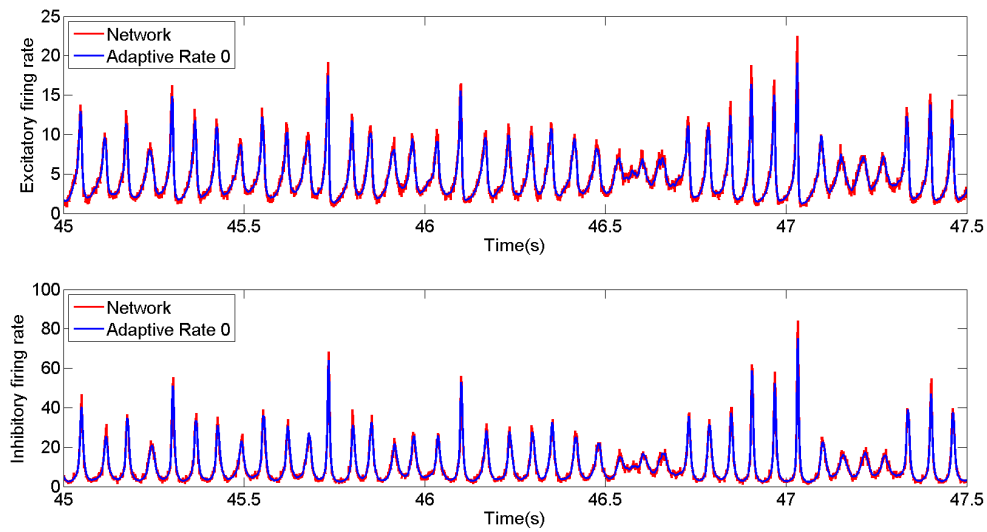


Figure III.13: **Comparing the firing rates of the AR0 model and Network of 20000 EI neurons.** For this plot, the mean synaptic input received by the neurons in the network of 20000 neurons is injected into the adaptive rate 0 model with no connectivity and the firing rates of the two are then compared. The top panel shows the excitatory firing rates of the network (in red) and the adaptive rate 0 model (in blue) and the bottom panel shows the inhibitory firing rates of the network (in red) and the adaptive rate 0 model (in blue).

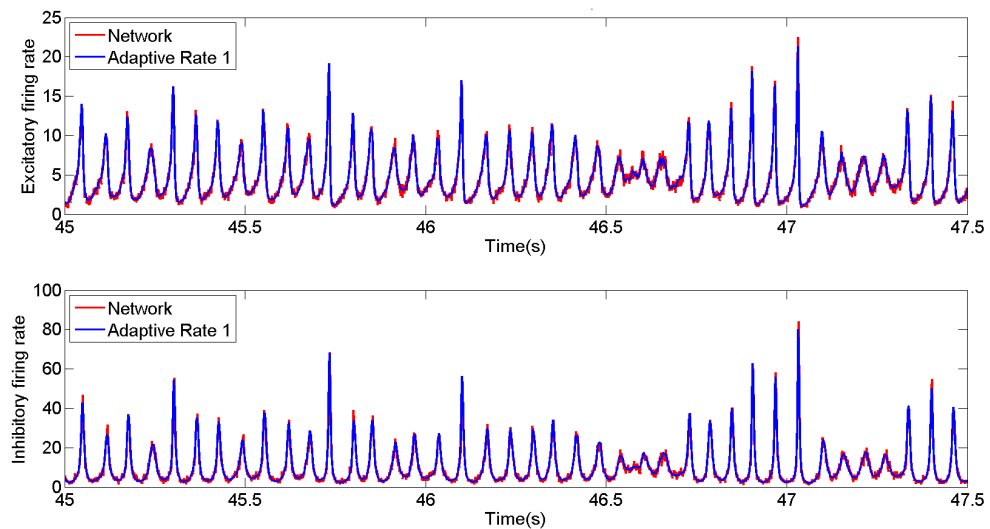


Figure III.14: **Comparing the firing rates of the AR1 model and Network of 20000 EI neurons.** For this plot, the mean synaptic input received by the neurons in the network of 20000 neurons is injected into the adaptive rate 0 model with no connectivity and the firing rates of the two are then compared. The top panel shows the excitatory firing rates of the network (in red) and the adaptive rate 1 model (in blue) and the bottom panel shows the inhibitory firing rates of the network (in red) and the adaptive rate 1 model (in blue).

	AR0 and network	AR1 and network
5k FullC	0.0123	0.0013
20k FullC	0.0714	0.0021

Table III.2: Table comparing the KL divergences of the fully connected EI network of 5000 and 20000 EIF neurons and the corresponding AR0/AR1 model simulations for.

III.16. We can normalize the histograms to obtain the probability distributions of firing rates and compute the Kullback-Leibler (KL) divergence between the AR0 distribution and the network distribution and AR1 distribution and the network distribution. The KL divergence or the relative entropy is a measure of the divergence between two probability distributions $P(x)$ and $Q(x)$, of variable x [Cover and Thomas, 2005] and is given by:

$$D_{KL}(P||Q) = \int_{-\infty}^{\infty} P(x) \log \frac{P(x)}{Q(x)} dx. \quad (\text{III.4.1})$$

Two identical probability distributions have a KL divergence of zero. We obtain the values shown in the following table. We notice that the KL divergence for the AR1 model and the network is ten times smaller than that for the AR0 model and the network.

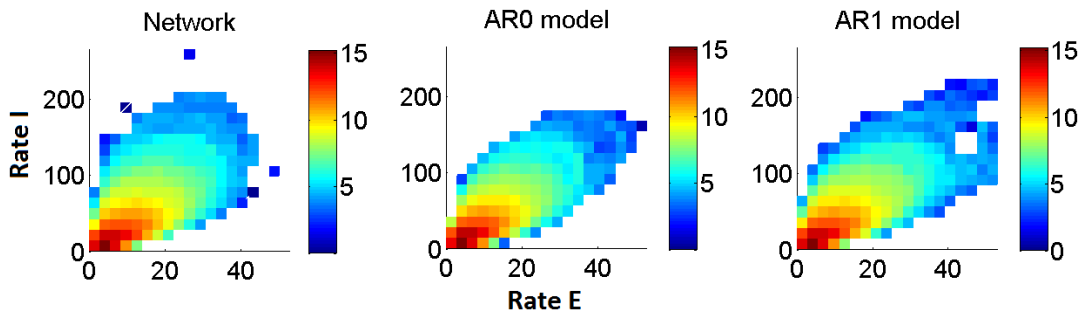


Figure III.15: **Histogram of the firing rates for a 5k network. Values refer to the log of the bin count.** The excitatory (E) firing rate is shown on the X axis and the inhibitory (I) firing rate is shown on the Y axis. The firing rates on both the axes are divided into 20 bins. The left panel corresponds to the network, the middle panel to the AR0 model and the right panel to the AR1 model.

We also want to compute the limit cycle of the dynamics from the firing rates for the case of a fully connected EI network and the two corresponding adaptive rate models. Since the dynamics of the network is not entirely periodic, we compute the limit cycle as follows.

1) We smooth the raw data of the firing rates of the two populations with a rectangular averaging window of 20 ms. 2) We use the smoothed firing rates of one of the populations, say the excitatory population, and extract the peaks of the signal, as shown in figure III.17. 3) We then compute the mean time difference between the

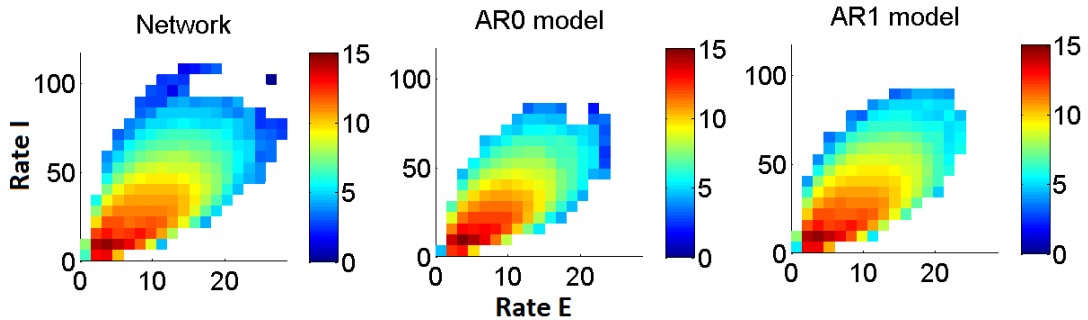


Figure III.16: **Histogram of the firing rates for a 20k network. Values refer to the log of the bin count.** The firing rates on both the axes are divided into 20 bins. The left panel corresponds to the network, the middle panel to the AR0 model and the right panel to the AR1 model.

peaks. 4) Next, we use the raw firing rates of the excitatory and inhibitory populations again and smooth it this time using a rectangular averaging window of 2 ms. The peaks extracted for the 20ms smoothed data extend over to the 2ms smoothed data. 5) We consider the 2ms smoothed data signal between any two consecutive peaks and stretch or contract this data, of both the excitatory and the inhibitory populations, to this mean time difference between the peaks. 6) With this, we then have signals of the same length for each cycle. 7) We then compute the average excitatory population firing rate and the average inhibitory population firing rate over the different cycles. 8) This helps us determine the average limit cycle of the network activity.

The same method is applied for the adaptive rate models. The limit cycles for the case of $w_{EE} = w_{EI} = 1.6$ mV.s and $w_{IE} = 0.4$ mV.s for the case of fully connected EI network of 5000 and 20000 EIF neurons (with 4:1 as ratio of number of excitatory neurons and inhibitory neurons) is shown in figures III.18 and III.19 respectively.

III.4.2 Comparing the limit cycles of the two Adaptive rate models

We observe that the limit cycle of the adaptive rate 1 model corresponds more closely to the network limit cycle. To compare the limit cycles in the three cases for $w_{EI} = 1.6$ mV.s, $w_{IE} = 0.4$ mV.s and different values of w_{EE} , we can compare a few quantities characterizing the limit cycles obtained in the case of the network simulations as well as the adaptive rate 0 model and adaptive rate 1 model for a network size of 20000 neurons (16000 E and 4000 I neurons). In figures III.20 and III.21, we compare six quantities in the three limit cycles as a function of w_{EE} : 1) the area of the averaged limit cycle, 2) the maximum excitatory amplitude in the averaged limit cycle, 3) the minimum excitatory amplitude in the averaged limit cycle, 4) the average time period, 5) the maximum inhibitory amplitude in the averaged limit cycle and 6) the minimum inhibitory amplitude in the averaged limit cycle. We observe that the quantities obtained in the adaptive rate 1 model match more closely with the network than with the adaptive rate 0 model.

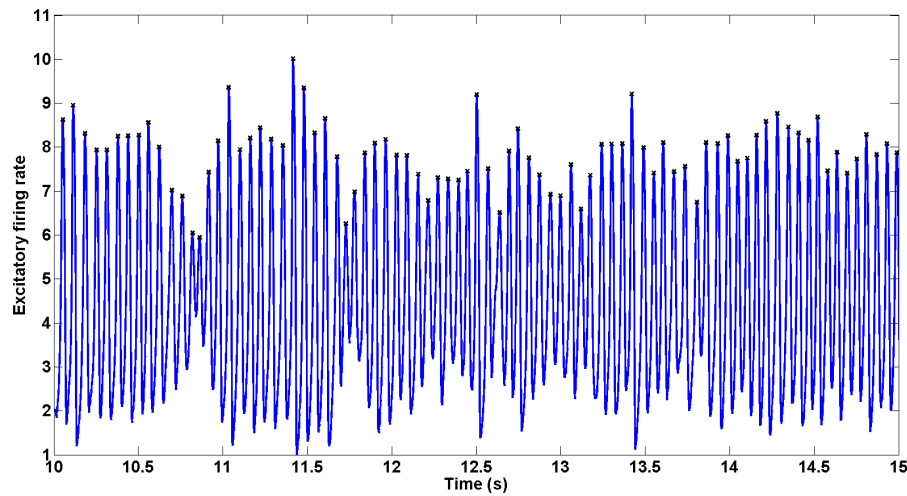


Figure III.17: **Extracting the peaks of the firing rate signal.** An example of the excitatory population firing rate and its identified peaks, represented by the black dots.

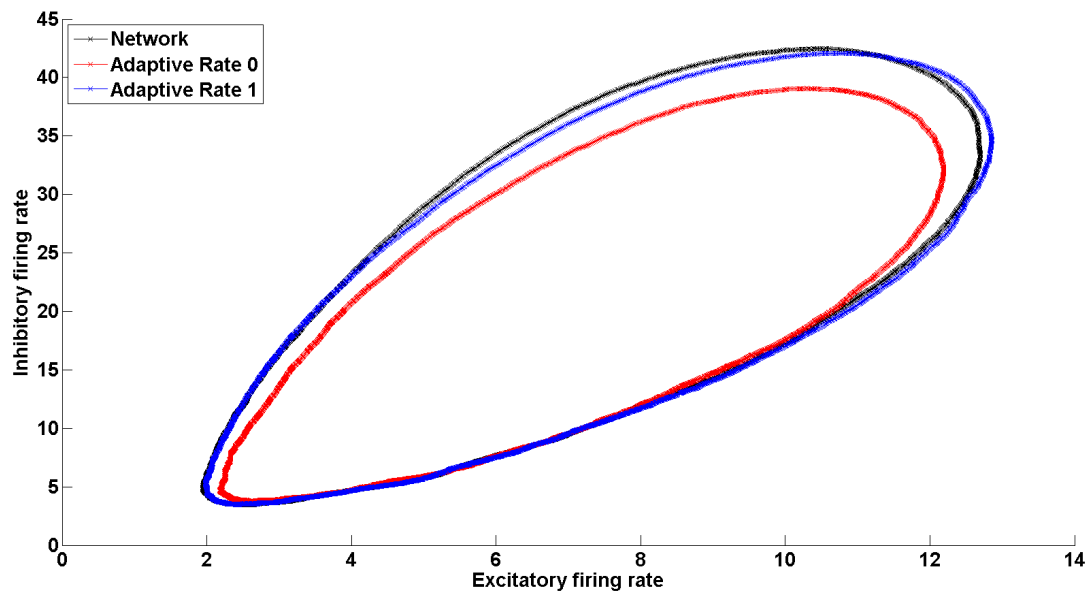


Figure III.18: **Comparing the three limit cycles for a network size of 5000 neurons.** The three limit cycles for a fully connected network of 5000 neurons for $w_{EE} = w_{EI} = 1.6 \text{ mV}\cdot\text{s}$ and $w_{IE} = 0.4 \text{ mV}\cdot\text{s}$ (in black) and the corresponding adaptive rate 0 model (in red) and adaptive rate 1 model (in blue).

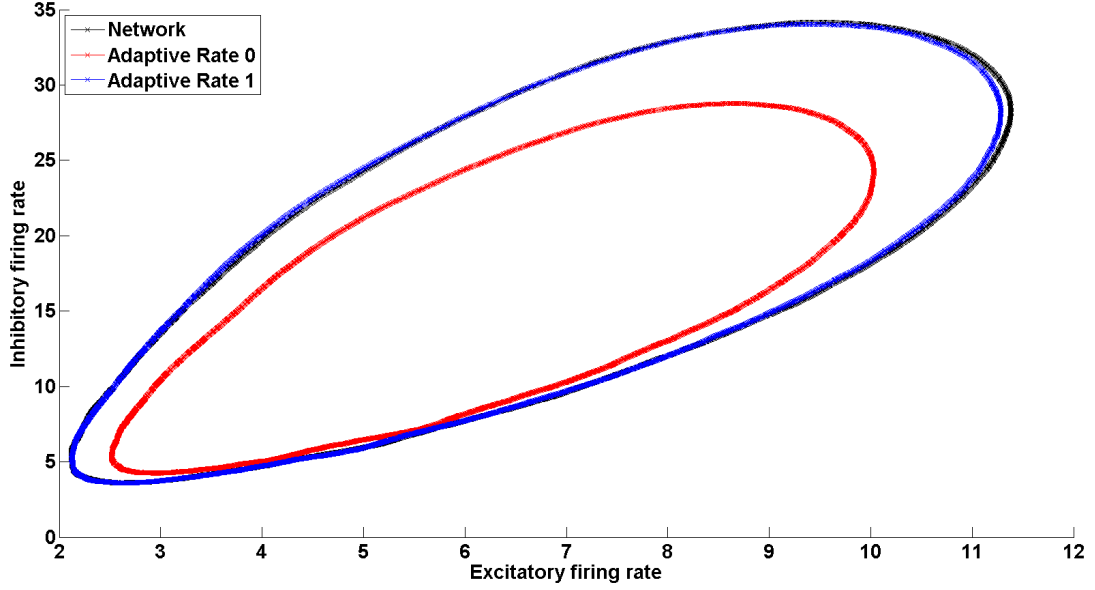


Figure III.19: **Comparing the three limit cycles for a network size of 20000 neurons.** The three limit cycles for a fully connected network of 20000 neurons for $w_{EE} = w_{EI} = 1.6$ mV.s and $w_{IE} = 0.4$ mV.s (in black) and the corresponding AR0 model (in red) and AR1 model (in blue).

III.5 Two coupled EI networks

In order to study oscillations and synchrony among networks, we need to introduce inter-excitatory coupling between different groups of EI neuronal populations. In this section, we begin by coupling two EI networks via inter-excitatory coupling. From the data in the cortex, we know that the probability of synaptic connection decreases with the physical distance for the excitatory pyramidal cells. Hence, we can consider two EI networks with inter-excitatory coupling that is a fraction of the net excitatory input received by each excitatory population (see figure III.22).

We will use the adaptive rate 1 model for this purpose, because it fits the limit cycles of the network better quantitatively. For simplicity, we begin with the case where there are no finite size effects due to the network size. The dynamics of the two coupled EI populations can be described by the following equations:

$$r_{E1} = \Phi_E(I_{E1}), \quad (\text{III.5.1})$$

$$r_{I1} = \Phi_I(I_{I1}), \quad (\text{III.5.2})$$

$$r_{E2} = \Phi_E(I_{E2}), \quad (\text{III.5.3})$$

$$r_{I2} = \Phi_I(I_{I2}), \quad (\text{III.5.4})$$

$$\tau_{E1} \frac{dI_{E1}}{dt} = -I_{E1} + I_E^{ext} + w_{EE} \frac{1}{1+f} r_{E1} + w_{EE} \frac{f}{1+f} r_{E2} - w_{IE} r_{I1}, \quad (\text{III.5.5})$$

$$\tau_{I1} \frac{dI_{I1}}{dt} = -I_{I1} + I_I^{ext} + w_{EI} r_{E1}, \quad (\text{III.5.6})$$

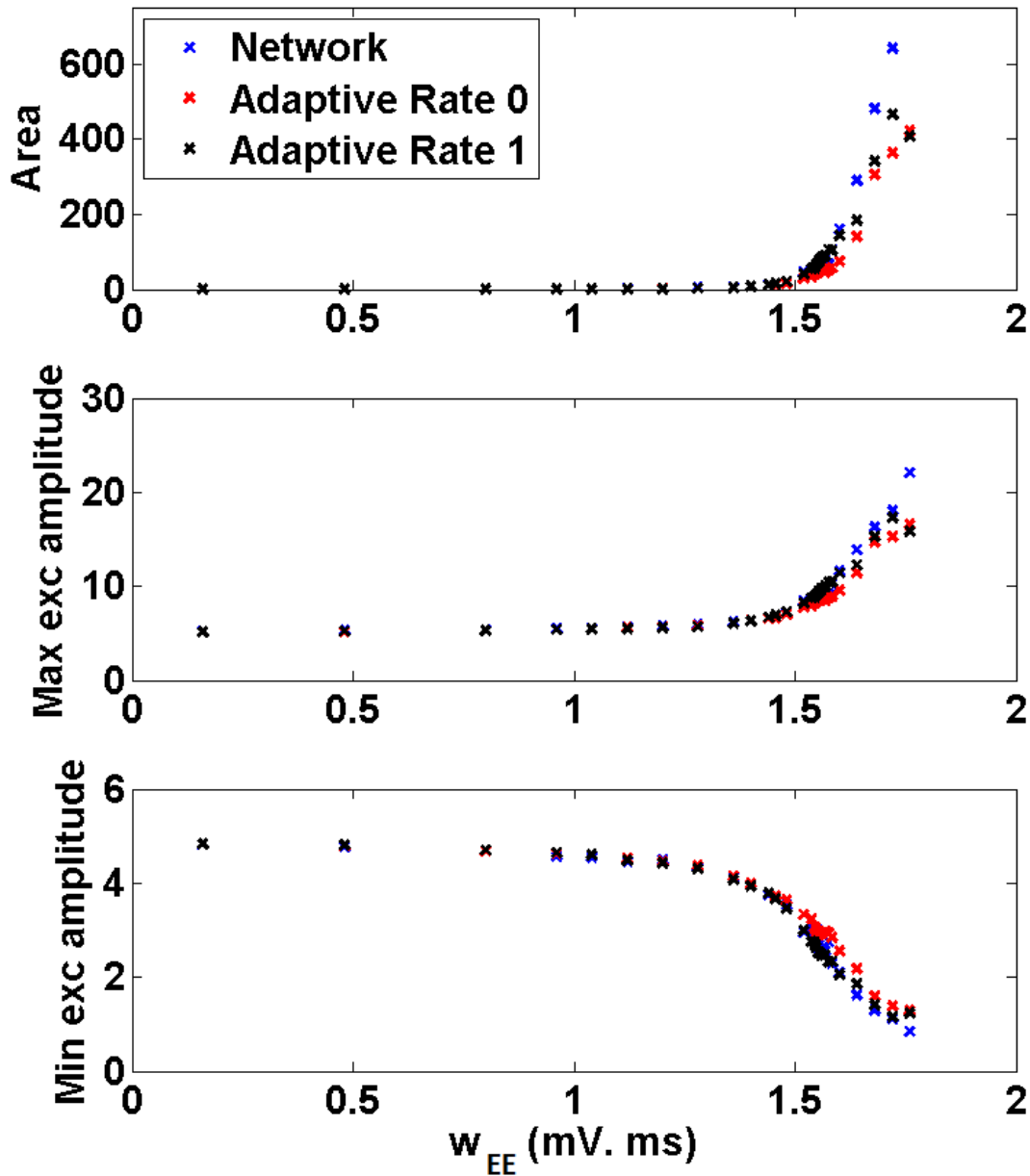


Figure III.20: **Comparing the limit cycles-I.** The top panel compares the area under the limit cycles of the EI network (in blue), AR0 model (in red) and AR1 model (in black) for $w_{EI} = 1.6$ mV.s, $w_{IE} = 0.4$ mV.s and different values of w_{EE} . The middle panel and the bottom panel compares the maximum and minimum of the excitatory amplitude of the limit cycles of the EI network, AR0 model and AR1 model for different values of w_{EE} . The E population has 16000 neurons and the I population has 4000 neurons.

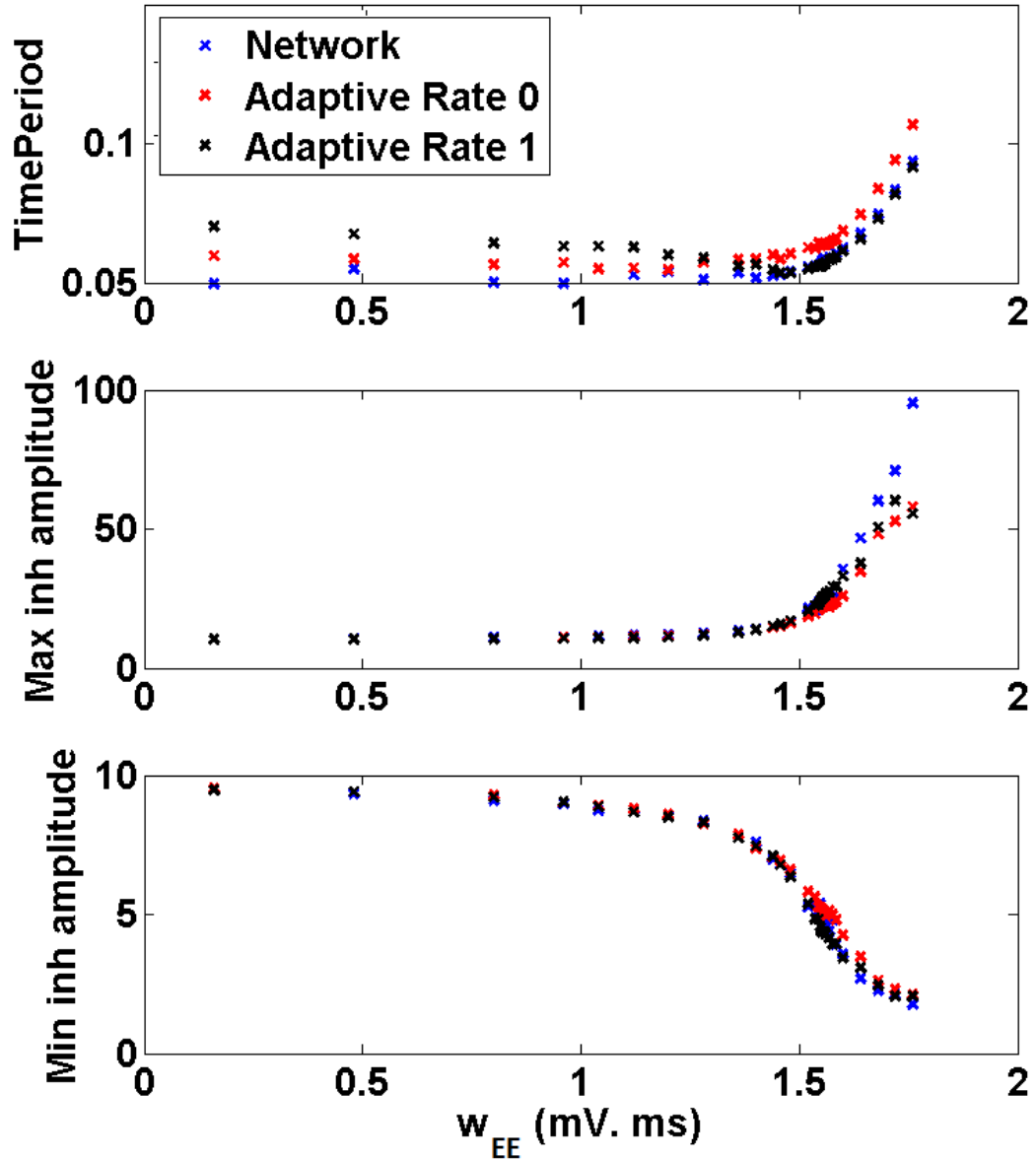


Figure III.21: **Comparing the limit cycles-II.** The top panel compares the time period of the limit cycles of the EI network (in blue), AR0 model (in red) and AR1 model (in black) for $w_{EI} = 1.6$ mV.s, $w_{IE} = 0.4$ mV.s and different values of w_{EE} . The middle panel and the bottom panel compares the maximum and minimum of the inhibitory amplitude of the limit cycles of the EI network, AR0 model and AR1 model for different values of w_{EE} . The E population has 16000 neurons and the I population has 4000 neurons.

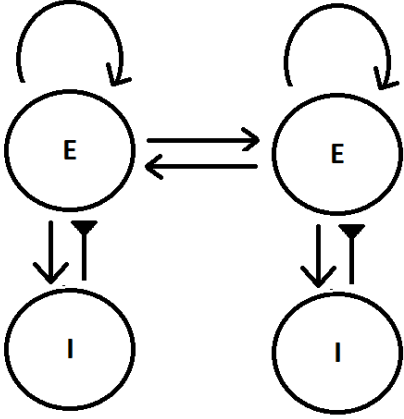


Figure III.22: **Two coupled EI networks.** In each EI group, the excitatory and the inhibitory populations are synaptically connected to each other and the excitatory population is recurrently connected in itself. The two EI groups are coupled to each other through inter-excitatory coupling.

$$\tau_{E2} \frac{dI_{E2}}{dt} = -I_{E2} + I_E^{ext} + w_{EE} \frac{f}{1+f} r_{E1} + w_{EE} \frac{1}{1+f} r_{E2} - w_{IE} r_{I2}, \quad (\text{III.5.7})$$

$$\tau_{I2} \frac{dI_{I2}}{dt} = -I_{I2} + I_I^{ext} + w_{EI} r_{E2}, \quad (\text{III.5.8})$$

where r_{E1} , r_{E2} , r_{I1} and r_{I2} represent the firing rates of the two excitatory and inhibitory populations respectively, I_{E1} , I_{E2} , I_{I1} and I_{I2} represent the input currents to the two populations, $\Phi_E(\cdot)$ and $\Phi_I(\cdot)$ are the f-I curves of the exponential-integrate and fire neuron, I_E^{ext} and I_I^{ext} are the external currents injected into the excitatory and inhibitory populations respectively, w_{EE} and w_{EI} are the strengths of the synaptic connections from the excitatory population to the excitatory and the inhibitory populations respectively, w_{IE} is the synaptic strength from the inhibitory population to the excitatory population and f is the measure of coupling between the two excitatory populations. It is the ratio of the inter-population excitatory coupling to the intra-population excitatory coupling. The time constants of the two populations τ_{E1} , τ_{I1} , τ_{E2} , τ_{I2} depend on the instantaneous firing rates of the two populations and are based on the adaptive rate 1 model.

We begin by fixing w_{EE} and the product $w_{EI}w_{IE}$ to put ourselves on a point in the oscillatory regime of the phase diagram of a single EI network shown in figure III.10. If we select $w_{EE} = w_{EI} = 1.6$ mV.s and $w_{IE} = 0.4$ mV.s and we insert currents into each population corresponding to $(r_E^0, r_I^0) = (5, 10)$ Hz, then we expect the two EI groups to exhibit oscillations. By varying the coupling between the excitatory populations of these groups, we can study the different dynamical regimes that we find these oscillations in. Although the results we describe here are for excitatory populations, the same results hold for the inhibitory populations of the two EI groups because they are excited by the corresponding excitatory populations. In the following subsections, we describe the different dynamical regimes of the two oscillators.

III.5.1 Antiphase or finite phase different regime

For very low coupling, we find that the firing rates of the two excitatory populations are in antiphase to each other (see figure III.23 for coupling factor of $f=0.011$). We call this the antiphase regime. For very low coupling, the two excitatory populations could also have a finite phase difference (Finite Phase difference regime) rather than

being in antiphase; we will discuss that in the next section. Figure III.24 shows the inhibitory firing rate and the excitatory firing rate of the two modules. In accordance with the PING mechanism, the peaks of inhibitory firing rates follow the peaks of the excitatory populations in each module. Therefore, it can be deduced that the firing rates of the two inhibitory populations are also in antiphase.

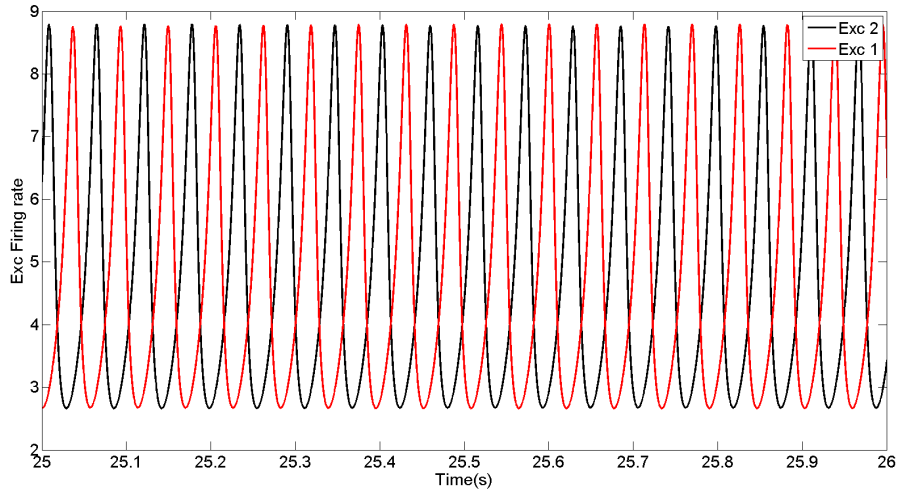


Figure III.23: **The population firing rates of the two excitatory populations in the antiphase regime.** For this simulation, each EI network is a point in the oscillatory regime of the phase diagram, shown in figure III.10, corresponding to the parameters $w_{EE} = w_{EI} = 1.6$ mV.s and $w_{IE} = 0.4$ mV.s and we insert currents into each population corresponding to $(r_E^0, r_I^0) = (5, 10)$ Hz. The coupling factor between the two excitatory populations is $f = 0.011$. For these parameters, the two excitatory populations are in antiphase.

III.5.2 Alternating phase regime

As the coupling is increased, we notice a transition to an oscillating envelope on the firing rates of the two excitatory populations. This is the alternating regime because the two excitatory populations alternate in time. For a coupling factor of $f = 0.012 - 0.014$, shown in figures III.25 and III.26, we observe the envelope on top of the firing rates of the two excitatory populations and the two excitatory populations are alternating with respect to time.

III.5.3 Modulating phase regime

As the coupling is further increased, we still have the oscillating envelope on the firing rates of the two excitatory populations. However, the two excitatory populations no longer alternate. Instead, the firing rate of one excitatory population is always lower than the firing rate of the other excitatory population. (See figure III.27 for a coupling factors of $f = 0.016$). We call this the modulating phase.

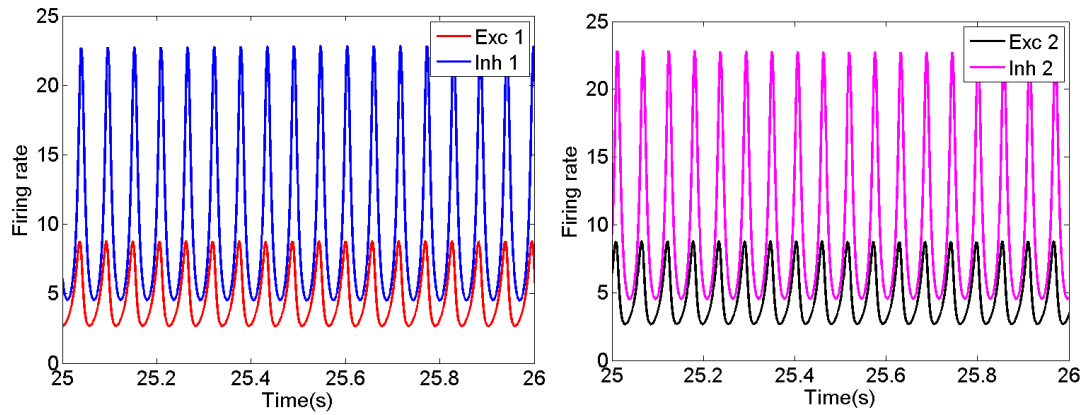


Figure III.24: **The population firing rates of the excitatory and inhibitory populations of the two modules in the antiphase regime.** The population firing rates of the excitatory and inhibitory populations for the same parameters as mentioned in figure III.23). The left panel shows the firing rates of the first module and the right panel shows the firing rates of the second module. The peaks of the inhibitory populations follow those of the excitatory populations as in the PING mechanism.

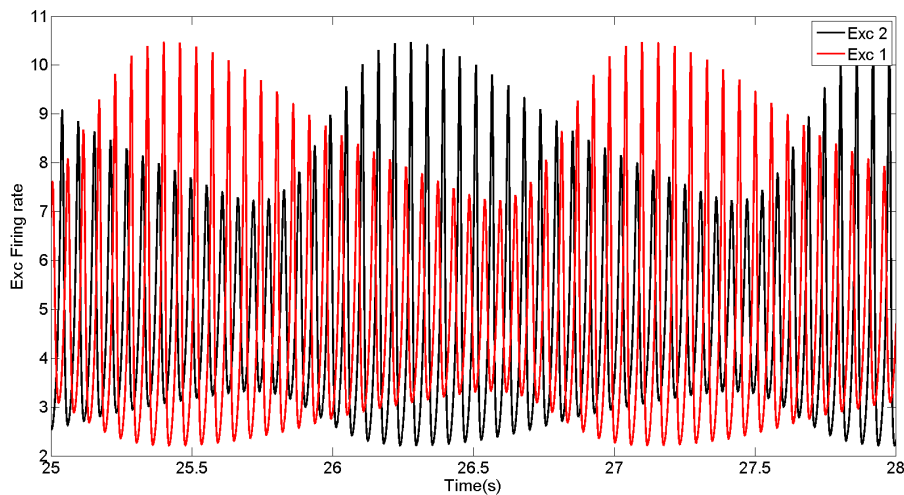


Figure III.25: **The population firing rates of the two excitatory populations in the alternating phase regime.** For a coupling factor of $f=0.012$ (other parameters as mentioned in figure III.23), the two excitatory populations alternatively win over the other population.

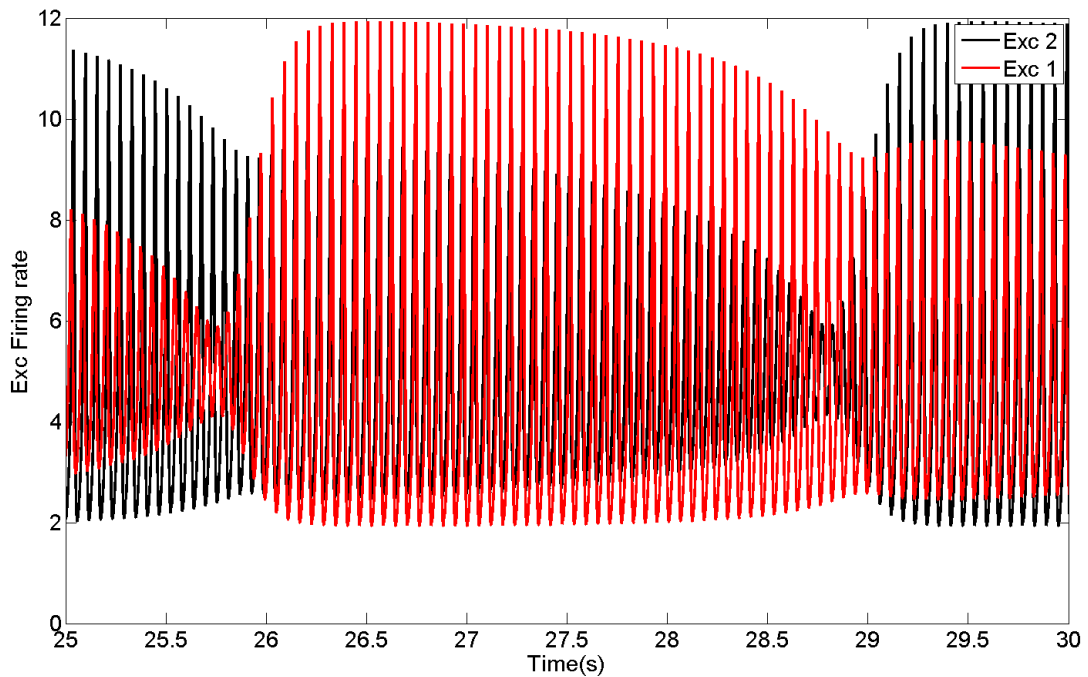


Figure III.26: **The population firing rates of the two excitatory populations in the alternating phase regime.** For a coupling factor of $f=0.014$ (other parameters as mentioned in figure III.23), the two excitatory populations alternatively win over the other population.

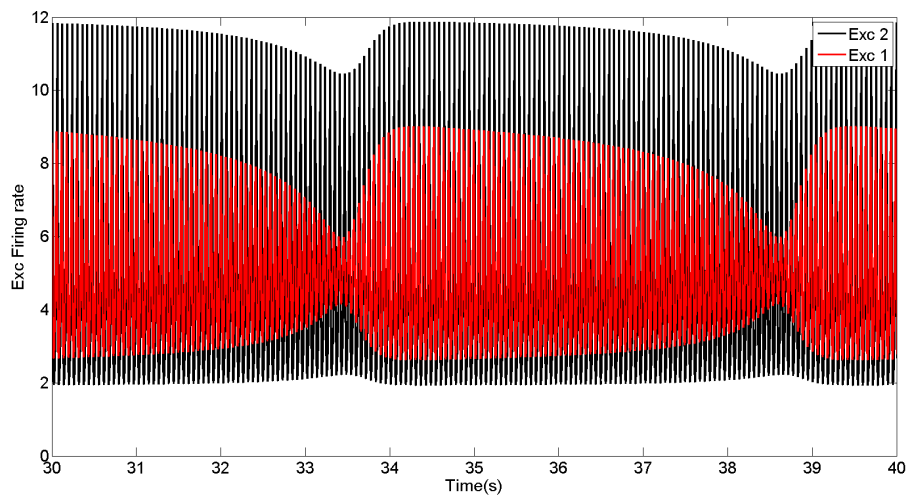


Figure III.27: **The population firing rates of the two excitatory populations in the modulating phase regime.** For a coupling factor of $f=0.016$ (other parameters as mentioned in figure III.23), the firing rates of one excitatory population is always below the firing rates of the other excitatory population.

III.5.4 Finite phase regime

Upon further increasing the coupling, the oscillating envelope vanishes and the two excitatory populations exhibit a finite phase difference. (See figures III.28 for coupling factor of $f=0.017$).

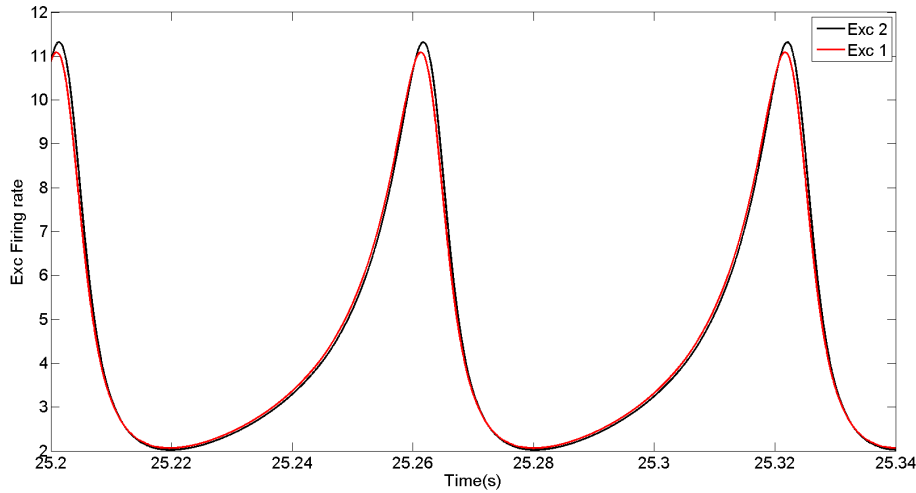


Figure III.28: **The population firing rates of the two excitatory populations in the finite phase difference regime.** For a coupling factor of $f=0.017$ (other parameters as mentioned in figure III.23), the firing rates of the two excitatory populations have a phase difference.

III.5.5 Synchronous phase regime

On increasing the coupling even more, the system synchronizes and oscillates in phase. The two excitatory populations behave as one big excitatory population. (See figures III.29 for coupling factor of $f=0.018$).

III.5.6 Phase diagram for the two coupled EI groups

We can generalize the above description to the entire range of J_{EI} , the magnitude of the strength of the coupling from the excitatory population to the inhibitory population, and plot the corresponding phase diagram for the adaptive rate 1 simulations with no finite size effects as seen in figure III.30. For this plot, we have used steps of 0.01 mV on the X-axis for the different J_{EI} and we have used steps of 0.0025 for the coupling factor on the Y-axis. For this plot, we select $J_{EE} = 0.2$ mV, $C_e = 800$, $C_i = 200$ and $J_{IE} = 0.04/J_{EI}$ mV and we insert currents into each population corresponding to $(r_E^0, r_I^0) = (5, 10)$ Hz. We observe that for J_{EI} less than 0.21, we have a finite phase difference regime for low coupling rather than antiphase regime. Generally, as we increase the coupling, the system goes from the finite phase difference or antiphase regime to the alternating regime to the modulating regime and to a finite phase regime before reaching synchrony.

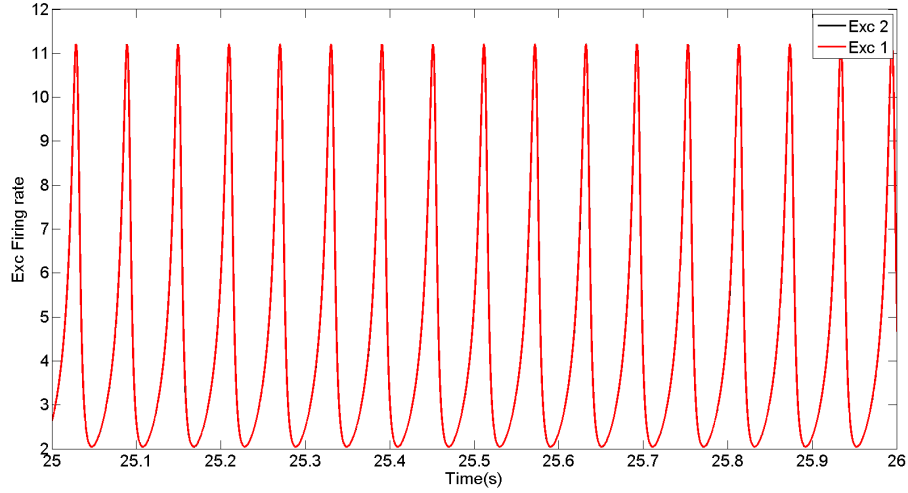


Figure III.29: **The population firing rates of the two excitatory populations in the synchronous phase regime.** For a coupling factor of $f=0.018$ (other parameters as mentioned in figure III.23), the firing rates of the two excitatory populations are synchronized. The two curves lie on top of each other.

III.6 Analytical derivation of the bifurcation plot

In this section, we detail how we can analytically compute the three bifurcation lines: synchronous regime to the finite phase difference regime (green curve in figure III.30), the finite phase difference regime to the modulating phase regime (red curve in figure III.30) and the alternating regime to the antiphase difference regime (blue curve in figure III.30). In the next section, we also detail how we can compute the phase difference between the two excitatory populations for very low coupling.

III.6.1 Transition from the synchronous regime to the phase difference regime

At the transition from the synchronous regime to the finite phase difference regime, the single limit cycle solution in the synchronous regime for the dynamical system must become unstable. We can thus find out the coupling factor at which the single limit cycle solution becomes unstable. For that, consider the dynamical equations for the two EI groups again (see equations III.5.1-III.5.8). One solution of this system is the limit cycle that one obtains for high coupling. If both the oscillators are in phase on the limit cycle and there is no noise, then they will continue to be in phase. If the system is in the synchronous regime, a slight perturbation in the dynamics of the two oscillators will bring the system back to the stable limit cycle. If, however, the system is not in synchronous regime, then a slight perturbation will take the system away from the unstable initial limit cycle. Let the stable limit cycle be denoted by $(I_e^*(t), I_i^*(t))$. By introducing a slight perturbation in the excitatory currents of the two limit cycles, one can write $I_{E1}(t) = I_e^*(t) + i_{e1}(t)$, $I_{E2}(t) = I_e^*(t) + i_{e2}(t)$, $I_{I1}(t) = I_i^*(t) + i_{i1}(t)$ and

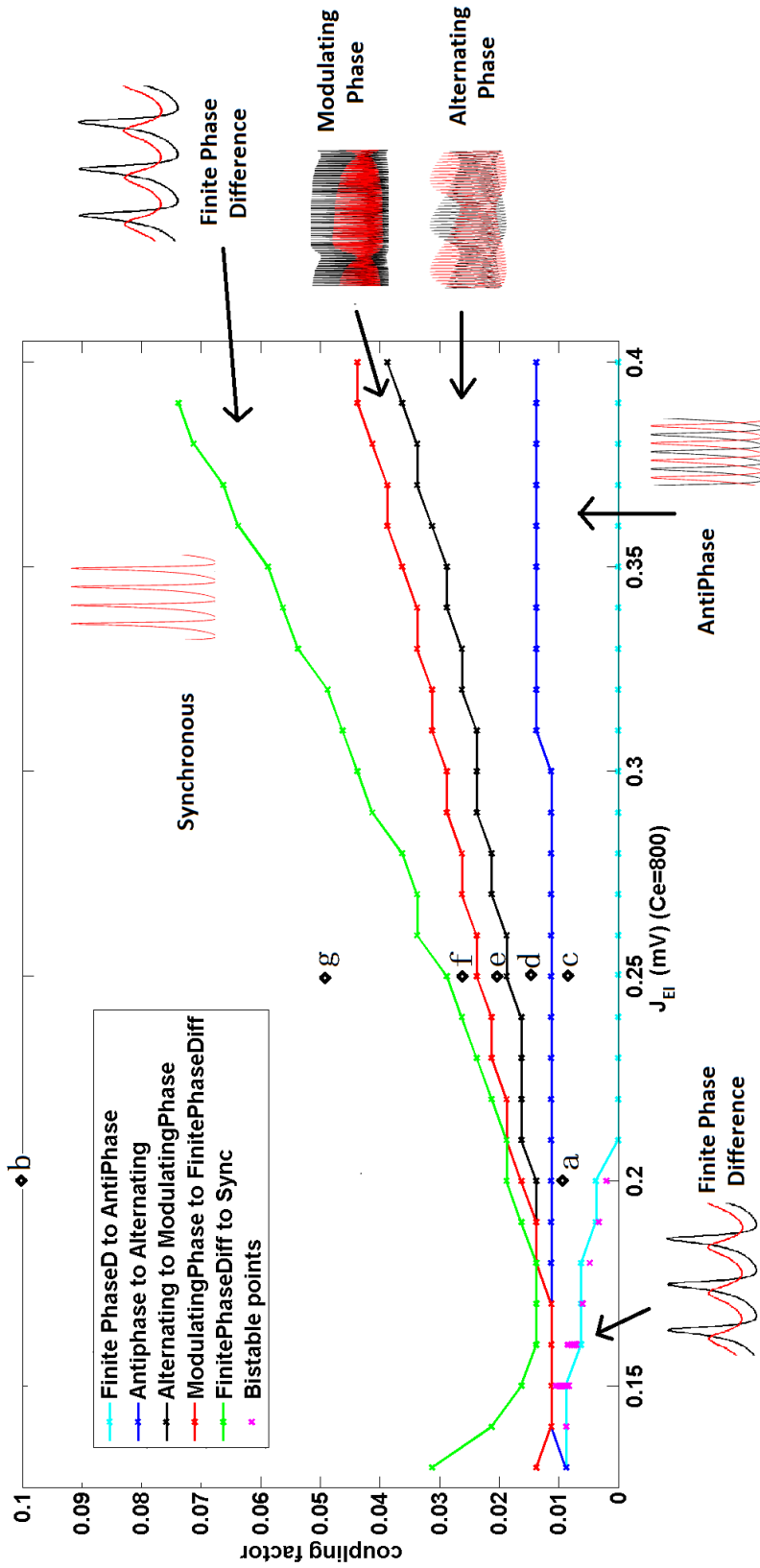


Figure III.30: The phase diagram for the two adaptive 1 rate EI groups that are coupled via inter-excitatory coupling. For very low coupling, the system can either be in finite phase difference regime or antiphase regime. As the coupling factor is increased, the system generally passes to the alternating, modulating, finite phase difference and the synchronous regimes. The different diamonds correspond to the different points we use for our simulations.

$I_{I2}(t) = I_i^*(t) + i_{i2}(t)$. Defining

$$i_e(t) = i_{e1}(t) - i_{e2}(t), \quad (\text{III.6.1})$$

$$i_i(t) = i_{i1}(t) - i_{i2}(t), \quad (\text{III.6.2})$$

$$\tau_e^0(t) = \tau_{I_e^*}(t), \quad (\text{III.6.3})$$

$$\tau_i^0(t) = \tau_{I_i^*}(t), \quad (\text{III.6.4})$$

$$\Phi'(I_e^*(t)) = d\Phi_E(I_e^*(t))/dt, \quad (\text{III.6.5})$$

$$\Phi'(I_i^*(t)) = d\Phi_I(I_i^*(t))/dt, \quad (\text{III.6.6})$$

and keeping terms only up to order $i_e(t)$ and $i_i(t)$ after subtracting $\tau_{E1}dI_{E1}/dt$ from $\tau_{E2}dI_{E2}/dt$, we get

$$\tau_e^0(t) \frac{di_e}{dt} = -i_e + w_{EE} \frac{1-f}{1+f} \Phi'(I_e^*(t))i_e - w_{IE} \Phi'(I_i^*(t))i_i, \quad (\text{III.6.7})$$

$$\tau_i^0(t) \frac{di_i}{dt} = -i_i + w_{EI} \Phi'(I_e^*(t))i_e. \quad (\text{III.6.8})$$

We can rewrite the above equations as:

$$\frac{d}{dt} \begin{pmatrix} i_e \\ i_i \end{pmatrix} = \mathcal{L} \begin{pmatrix} i_e \\ i_i \end{pmatrix} \quad (\text{III.6.9})$$

The matrix $\mathcal{L}(t)$ is periodic with the same periodicity as the limit cycle, say T . According to the Floquet theory, we can compute the eigen vectors and eigenvalues of the above system. Consider the matrix solutions of:

$$\frac{d}{dt} M(t) = \mathcal{L}M(t), \quad (\text{III.6.10})$$

with the initial condition $M(0) = I_d$, the identity matrix. The solution of the above equation $M(t)$ then describes the linear evolution of the perturbation around the limit cycle. After one complete period T , $M(T)$ represents the evolution of the perturbation around the complete limit cycle. We can compute the eigenvalues of $M(T)$. If the synchronous limit cycle is a stable state of the system for a given coupling factor, then one of the eigenvalues of $M(T)$ must be zero and the other one must be negative. The zero eigenvalue corresponds to the perturbation in the direction of the limit cycle and the other eigenvalue corresponds to the perturbation away from the limit cycle. If, on the other hand, the synchronous limit cycle is not a stable state of the system for a given coupling factor, then either $M(T)$ has no zero eigenvalues or $M(T)$ has a positive eigenvalue. By varying the coupling factor from very high values to lower values and studying when the system develops a positive eigenvalue or two non-zero eigenvalues, one can demarcate the transition from the synchronous regime to the finite phase difference regime.

III.6.2 Transition from finite phase difference regime to other regimes

In the finite phase difference regime, the synchronous limit cycle is no longer stable. However, there exists a four-dimensional limit cycle that is a solution of the above four dimension system. After a time period T , the system returns to the original point in phase space. We can perturb the system around this four dimensional limit cycle and look at the eigenvalues of the 4×4 matrix $M(t)$ after one complete time period i.e. $M(T)$. If the four dimensional solution is stable, then one of the eigenvalues must be zero and the other three eigenvalues must be negative. As we vary the coupling factor below from the “synchronous to the finite phase difference transition”, we reach a point where one of the eigenvalues becomes positive or there exists no longer a zero eigenvalue. This marks the finite phase difference to the modulated phase regime transition. Similarly, one can start from very low coupling, where the system is either in the finite phase difference regime or the antiphase regime and compute the eigenvalues of $M(T)$ for each increasing value of coupling factor. The coupling factor where either one of the eigenvalues becomes positive or all the eigenvalues are nonzero then marks the transition from either the finite phase difference regime or the Antiphase regime to the alternating phase regime.

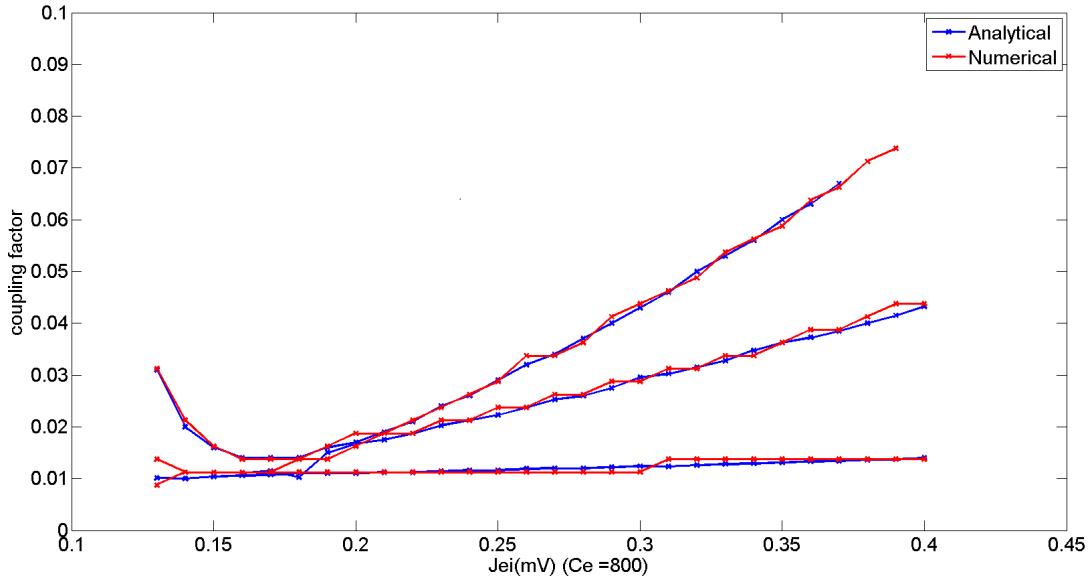


Figure III.31: **Comparing the analytical and numerical bifurcation curves.**

We can also compute the time period of the modulation or the alternation of the firing rates at the transition by looking at the imaginary component of the eigenvalues at the point of the transition. More specifically, at the transition, we have

$$\lambda_1 + i\lambda_2 = e^{i\omega_{mod}T_{LC}}$$

where λ_1 is the real part of the eigenvalue, λ_2 is the imaginary part of the eigenvalue, $\omega_{mod} = 2\pi T_{mod}$ is the angular frequency of either the modulation or the alternation (depending on the regime) at the point of transition and T_{LC} is the timeperiod of one oscillation of the limit cycle.

W_{EI} (mV.s)	Finite Phase to Modulating Phase		Finite Phase to Alternating Phase	
	$T_{analytical}$ (s)	$T_{numerical}$ (s)	$T_{analytical}$ (s)	$T_{numerical}$ (s)
184	1.247	1.252	1.141	1.108
272	0.517	0.513	0.674	0.670
320	0.410	0.369	0.516	0.553

Table III.3: Table comparing the analytical values of the time period of the modulation or alternation to the ones observed numerically.

This gives us

$$T_{mod} = \frac{2\pi T_{LC}}{\arctan(\lambda_2/\lambda_1)}.$$

The above obtained analytical value of the time period of the modulation or alternation does indeed correspond to the one observed numerically as shown in the table below.

III.6.3 Computing the phase difference regime at very low coupling factors

One can also compute the value of the phase difference for very low coupling factor of the system. We outline the procedure in this section. In the absence of any coupling, the dynamics of the two excitatory populations follow:

$$\frac{dI_{E1}}{dt} = \frac{1}{\tau(I_{E1}(t))} \{I_{E,ext} - I_{E1}(t) + w_{EE}\Phi(I_{E1}(t)) - w_{IE}\Phi(I_{I1}(t))\} = F(I_{E1}(t), I_{I1}(t)), \quad (\text{III.6.11})$$

$$\frac{dI_{E2}}{dt} = \frac{1}{\tau(I_{E2}(t))} \{I_{E,ext} - I_{E2}(t) + w_{EE}\Phi(I_{E2}(t)) - w_{IE}\Phi(I_{I2}(t))\} = F(I_{E2}(t), I_{I2}(t)). \quad (\text{III.6.12})$$

The limit cycle solution to the above equations can be denoted by $(I_E^0(t), I_I^0(t))$. If the initial conditions of the two oscillators are the same, they will oscillate in phase. In the presence of coupling, the dynamical equations for the two oscillators become:

$$\frac{dI_{E1}}{dt} = \frac{1}{\tau(I_{E1}(t))} \{I_{E,ext} - I_{E1}(t) + w_{EE}(1-\alpha)\Phi(I_{E1}(t)) + \alpha w_{EE}\Phi(I_{E2}(t)) - w_{IE}\Phi(I_{I1}(t))\}, \quad (\text{III.6.13})$$

$$\frac{dI_{E2}}{dt} = \frac{1}{\tau(I_{E2}(t))} \{I_{E,ext} - I_{E2}(t) + w_{EE}(1-\alpha)\Phi(I_{E2}(t)) + \alpha w_{EE}\Phi(I_{E1}(t)) - w_{IE}\Phi(I_{I2}(t))\}, \quad (\text{III.6.14})$$

where α is related to the coupling factor f by

$$\alpha = \frac{f}{1+f}. \quad (\text{III.6.15})$$

Defining the phases of the two oscillators as ϕ_1 and ϕ_2 , we can write $I_{E1}(t) = I_E^0(t + \phi_1)$ and $I_{E2}(t) = I_E^0(t + \phi_2)$. In the presence of weak coupling, one can use perturbation theory [Kuramoto, 1984] and the dynamical equations for the phases ϕ_1 and ϕ_2 are then given by:

$$\frac{d\phi_1}{dt} = \frac{d\phi_1}{dI_{E1}} \frac{dI_{E1}}{dt} = \omega + \left. \frac{d\phi}{dI_{E1}} \right|_{\phi=t+\phi_1} \frac{\alpha w_{EE}}{\tau(I_E^0(t+\phi_1))} [\Phi(I_E^0(t+\phi_2)) - \Phi(I_E^0(t+\phi_1))], \quad (\text{III.6.16})$$

$$\frac{d\phi_2}{dt} = \frac{d\phi_2}{dI_{E2}} \frac{dI_{E2}}{dt} = \omega + \left. \frac{d\phi}{dI_{E2}} \right|_{\phi=t+\phi_2} \frac{\alpha w_{EE}}{\tau(I_E^0(t+\phi_2))} [\Phi(I_E^0(t+\phi_1)) - \Phi(I_E^0(t+\phi_2))]. \quad (\text{III.6.17})$$

Writing $\phi_2 = \phi_1 + \Delta\phi$ and subtracting the above two equations, we can write

$$\frac{d\Delta\phi}{dt} = \left. \frac{d\phi}{dI_E} \right|_{I_E^0(t)} \frac{\alpha w_{EE}}{\tau(I_E^0(t))} [\Phi(I_E^0(t-\Delta\phi)) - \Phi(I_E^0(t+\Delta\phi))]. \quad (\text{III.6.18})$$

Because the coupling is weak, we can assume that the phase difference between the two oscillators stays the same throughout the limit cycle and average the above equation over one complete time period of the limit cycle. We get the following:

$$\frac{d\Delta\phi}{dt} = \int_{LC} \left. \frac{d\phi}{dI_E} \right|_{I_E^0(t)} \frac{\alpha w_{EE}}{\tau(I_E^0(t))} [\Phi(I_E^0(t-\Delta\phi)) - \Phi(I_E^0(t+\Delta\phi))] dt. \quad (\text{III.6.19})$$

where \int_{LC} denotes the integral over the limit cycle. We can simplify the above equation as :

$$\frac{d\Delta\phi}{dt} = S(\Delta\phi). \quad (\text{III.6.20})$$

To compute $d\phi/dI_E|_{I_E^0(t)}$, we need to compute the unit vector tangential to the limit cycle. If the vector tangential to the limit cycle at each time step is denoted by $\vec{g}_1(t) = \begin{pmatrix} g_{1,E}(t) \\ g_{1,I}(t) \end{pmatrix}$, then $d\phi/dI_E$ is given by the product of magnitude of $d\phi/d\vec{I}$ with $g_{1,E}(t)$, where $\vec{I} = \begin{pmatrix} I_E \\ I_I \end{pmatrix}$. $d\phi/d\vec{I}$ is a constant along the limit cycle and integrates to 2π over the limit cycle. Therefore, we need to compute $g_{1,E}(t)$. To do this, consider the dynamics of the unperturbed limit cycle for a single oscillator

$$\frac{dI_E}{dt} = \frac{1}{\tau(I_E(t))} \{I_{E,ext} - I_E(t) + w_{EE}\Phi(I_E(t)) - w_{IE}\Phi(I_I(t))\} \quad (\text{III.6.21})$$

$$\frac{dI_I}{dt} = \frac{1}{\tau(I_I(t))} \{I_{I,ext} - I_I(t) + w_{EI}\Phi(I_E(t))\} \quad (\text{III.6.22})$$

whose excitatory and inhibitory currents in the steady state of the limit cycle are given by I_E^0 and I_I^0 respectively. By adding a small perturbation to the currents $I_E(t) = I_E^0 + i_e(t)$ and $I_I(t) = I_I^0 + i_i(t)$, we can write the dynamics of $i_e(t)$ and $i_i(t)$ in the form

$$\frac{d}{dt} \begin{pmatrix} i_e \\ i_i \end{pmatrix} = \mathcal{L} \begin{pmatrix} i_e \\ i_i \end{pmatrix} \quad (\text{III.6.23})$$

The matrix $\mathcal{L}(t)$ is periodic with the same periodicity as the limit cycle, say T . As in the previous section, we can compute the eigenvectors and eigenvalues of the above system. If we consider the matrix solutions of:

$$\frac{d}{dt}M(t) = \mathcal{L}M(t) \quad (\text{III.6.24})$$

with the initial condition $M(0) = I_d$, the identity matrix, then the solution of the above equation $M(t)$ describes the linear evolution of the perturbation around the limit cycle and $M(T)$ represents the evolution of the perturbation around the complete limit cycle. We can compute the eigenvalues of $M(T)$. The vector tangent to the limit cycle $e_1 = (I_E^{0'}(0), I_I^{0'}(0))$ is an eigenvector of $M(T)$ with an eigenvalue 1. Since the limit cycle is stable, the other eigenvalue is less than 1 and the other eigenvector can be represented by $e_2(t)$. To compute then $g_1(t)$, the unit vector parallel to the limit cycle, we can use $g_1(t).e_1(t) = 1$ and $g_1(t).e_2(t) = 0$. Knowing $g_1(t)$ and hence $g_{1,E}(t)$, we can write the dynamical equation for the phase difference of the two oscillators for very low coupling and integrate it over the limit cycle. For different values of w_{EE} with $w_{EI} = 1.6\text{mV.s}$ and $w_{IE} = 0.4\text{ mV.s}$, the dynamics of the phase is shown in figure III.32. The value of Φ where $d\Phi/dt$ has a zero value and the slope of the curve is negative is a stable fixed point of the system. That value determines the phase difference observed between the two excitatory populations for very low coupling. Comparing with simulations of the adaptive rate 1 model, we find that it is indeed the case. Similarly, the dynamics of the phase difference for different values of w_{EI} with $w_{EE} = 1.6\text{mV.s}$ and $w_{IE} = 6.4/w_{EI}\text{ mV.s}$ are shown in figure III.33.

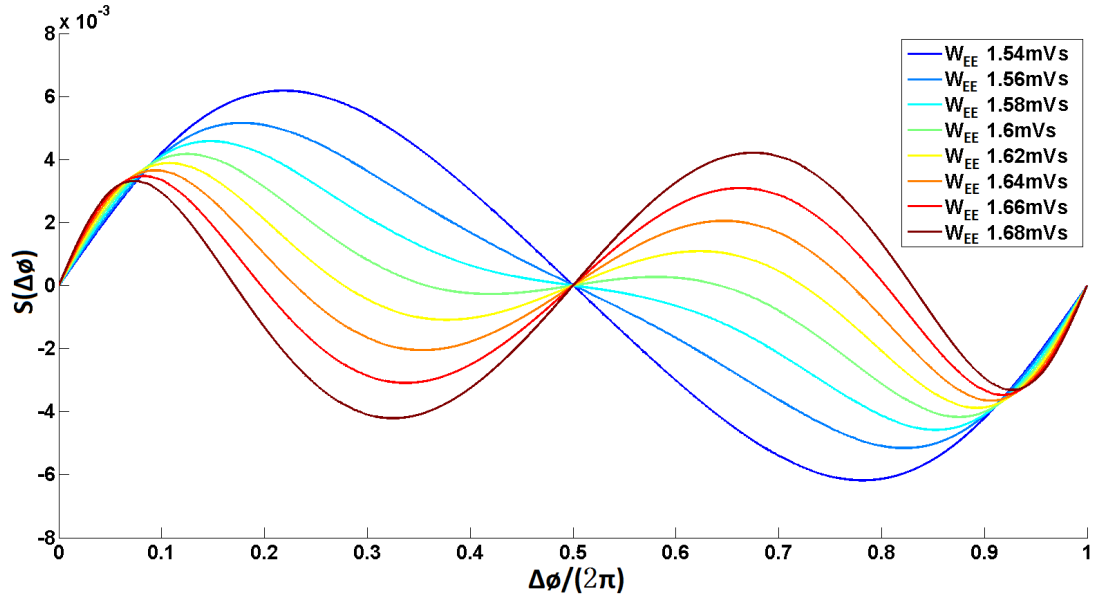


Figure III.32: **Dynamics of the phase difference for weak coupling factor for different values of w_{EE} .** The dynamics of phase difference $d\Delta\phi/dt = S(\Delta\phi)$ for different values of w_{EE} with $w_{EI} = 1.6\text{mV.s}$ and $w_{IE} = 0.4\text{ mV.s}$ and weak coupling factor.

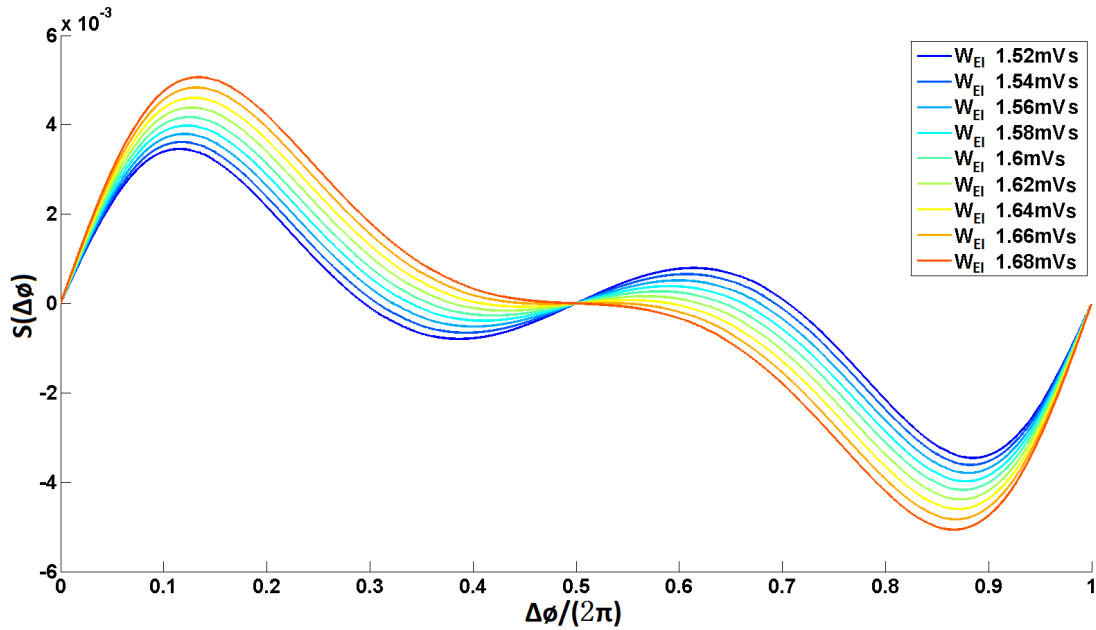


Figure III.33: **Dynamics of the phase difference for weak coupling factor for different values of w_{EI} .** The dynamics of phase difference $d\Delta\phi/dt = S(\Delta\phi)$ for different values of w_{EI} with $w_{EE} = 1.6\text{mV.s}$ and $w_{IE} = 6.4/w_{EI} \text{ mV.s}$ and weak coupling factor.

III.7 Effects of finite size noise in Adaptive rate model1

The previous sections explored the phase diagram of the regimes of two different EI oscillators in the absence of any finite size effects due to the limited size of the network or connectivity. In this section, we add the noise due to the finite network size for the adaptive rate 1 model for two cases: Antiphase regime and synchronous regime and we compare the effects due to the finite size noise. For the simulations, we use the parameters of $w_{EE} = w_{EI} = 1.6 \text{ mV.s}$ and $w_{IE} = 0.4 \text{ mV.s}$. For a coupling factor of $f = 0.01$ (point a in figure III.30), we expect an antiphase regime and for a coupling of $f = 0.1$ (point b in figure III.30), we expect synchrony between the two excitatory populations. For the antiphase regime, we observe that as the network size is reduced, the peak of the cross correlation function of the firing rates of the two excitatory populations shifts towards zero and has a lower magnitude than the peak of the autocorrelation of the firing rate of either excitatory population (see figure III.34). For a coupling factor of $f = 0.1$, we observe that for networks of smaller sizes, the peak of the cross correlation function is still near zero with almost the same amplitude as either of the autocorrelation functions (see figure III.35).

We can also plot the phase difference between the firing rates of the two excitatory populations for each oscillatory cycle. To do this, we can find out the timings of the peaks of the firing rates of the two excitatory populations in every oscillatory cycle. We can then calculate the timing of the peak of the second excitatory population within the cycle with respect to the first. The first excitatory population has a peak either at

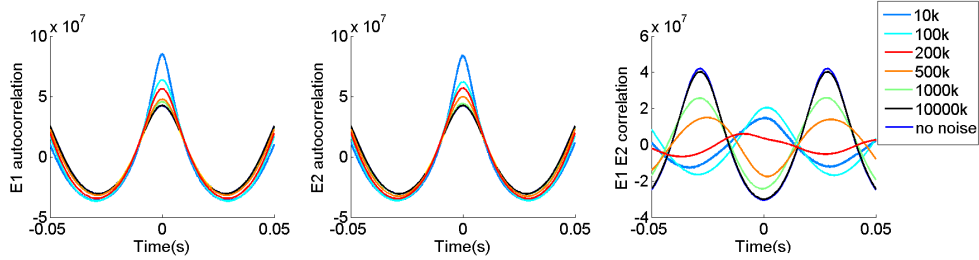


Figure III.34: **Influence of noise due to finite size in adaptive rate 1 model in the antiphase regime.** For the simulations, we use a coupling factor of $f = 0.01$ and keep the other parameters as in figure III.23. For a coupling factor of $f = 0.01$ (point a in figure III.30), we expect an antiphase regime in the case of no noise. The left and the middle panels show the autocorrelation functions of the firing rate of the first excitatory population and the second excitatory populations respectively. The right panel shows the cross correlation between the two. For networks of smaller sizes, the peak of the cross correlation function is shifted towards zero but has a lower magnitude compared to the peak of either autocorrelation function.

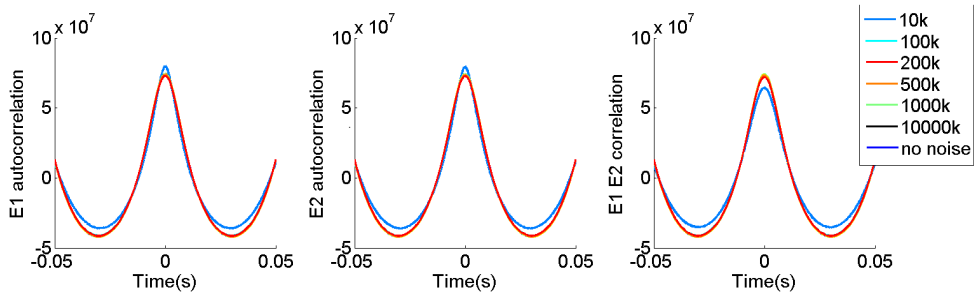


Figure III.35: **Influence of noise due to finite size in adaptive rate 1 model in the synchronous regime.** For the simulations, we use a coupling factor of $f = 0.1$ and keep the other parameters as in figure III.23. For a coupling factor of $f = 0.1$ (point b in figure III.30), we expect a synchronous regime in the case of no noise. The left and the middle panels show the autocorrelation functions of the firing rate of the first excitatory population and the second excitatory populations respectively. The right panel shows the cross correlation between the two. For networks of smaller sizes, the peak of the cross correlation function is still near zero with almost the same amplitude as either autocorrelation function.

time $t = 0$ or at time $t = T$, the time period of that particular cycle, and the second population has a peak within $t = 0$ to $t = T$. In figure III.36, we see that in the presence of no noise or for a very large network size ($\sim 10000k$ neurons), the peaks of the second population show a definite phase shift with respect to the first population (the two populations are antiphase to each other). As the network size is gradually decreased, the noise due to finite size increases, and the peaks of the second population is distributed throughout the time period $0 - T$.

For the case of the coupling factor $f = 0.1$, the firing rates of the two excitatory populations are synchronized in the absence of noise and hence, the two peaks align in every cycle as shown in figure III.37. As the network size is reduced, we still see the alignment of the timing of the peaks and for very low network size $\sim 10k$ neurons, the peaks of the second population are more distributed, however, they are vastly aligned with peaks of the first population.

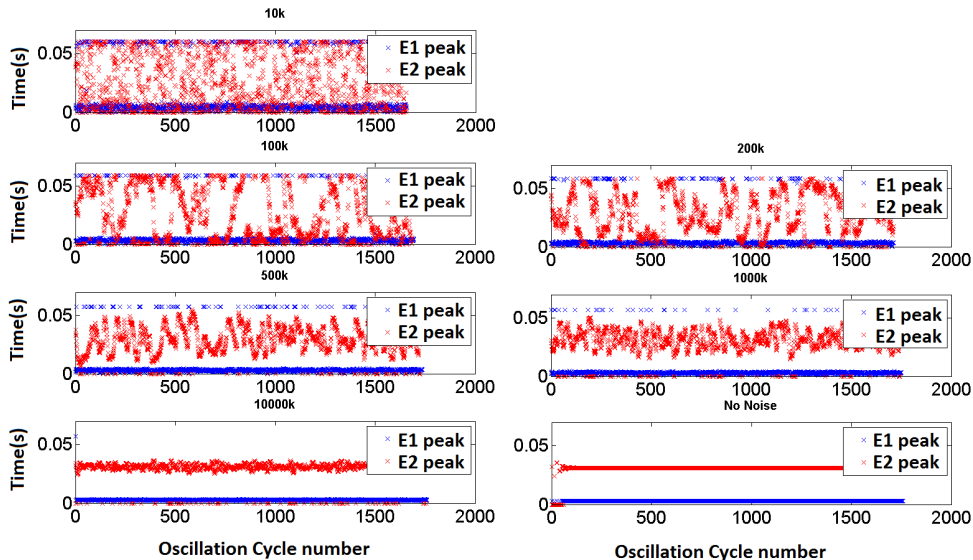


Figure III.36: **Influence of noise due to finite size in adaptive rate 1 model in the antiphase regime for different network sizes.** We extract the timings of the peaks of the firing rates of the two excitatory populations in each oscillatory cycle. The first excitatory population has a peak either at time $t = 0$ or at time $t = T$, the time period of that particular cycle, and the second population has a peak within $t = 0$ to $t = T$. We see that for a very large network size ($\sim 10000k$ neurons), the peaks of the second population are in Antiphase with respect to the first population but as the network size is gradually decreased, the phase difference between the two populations is distributed throughout the time period $0 - T$.

III.8 Comparing with the network simulations

In this section, we will compare the firing rates of the two excitatory populations for the adaptive rate 1 model and the EIF-network simulations in the different regimes of the phase diagram. To do this, we begin with a network of a very large size ($\sim 1600k$

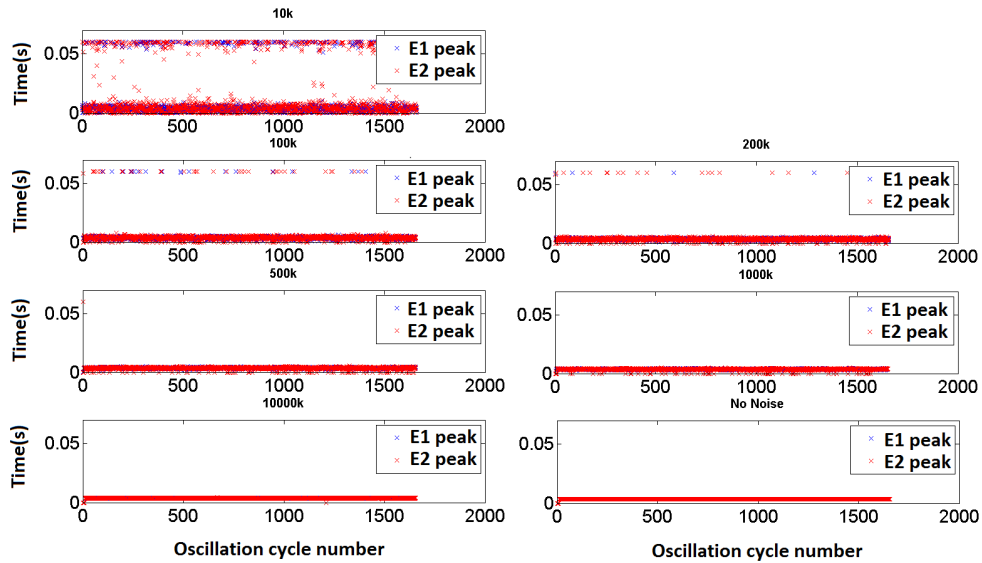


Figure III.37: **Influence of noise due to finite size in adaptive rate 1 model in the synchronous regime for different network sizes.** For a coupling factor of $f = 0.1$, the firing rates of the two excitatory populations are synchronized and the timings of the peaks of two firing rates are mostly aligned even for small network sizes such as $10k$ neurons.

neurons per EI population: $1280k$ neurons in each E population and $320k$ neurons in each I population) with full connectivity so that we can observe the different regimes clearly. Each of the neurons in this network is an EIF neuron. To do this, we will have two EI populations as described in section III.2. The two EI populations are coupled to each other via excitatory coupling: i.e. all the excitatory neurons of the first population are connected to all the excitatory neurons of the second population with a coupling strength of $J_{e_1e_2} = J_{e_2e_1} = J_{EE}f/(1+f)$ where f is the coupling factor. The coupling in each excitatory population is given by $J_{e_1e_1} = J_{e_2e_2} = J_{EE}1/(1+f)$. For the simulations, we use $J_{EE} = 0.2$ mV, $J_{EI} = 0.25$ mV and $J_{IE} = 0.16$ mV. We use different coupling factors corresponding to different regimes in the phase diagram of the two oscillators and compare the network simulations and the simulations of the adaptive rate 1 model. Figures III.38 and III.39 show the two models for a coupling factor of $f = 0.01$ (point c in figure III.30), where the two populations are in Antiphase regime. Figures III.40 and III.41 show the two models for a coupling factor of $f = 0.015$ (point d in figure III.30), where the two populations are in alternating regime. Figures III.42 and III.43 show the two models for a coupling factor of $f = 0.02$ (point e in figure III.30), where the two populations are in the modulating regime. Figures III.44 and III.45 show the two models for a coupling factor of $f = 0.025$ (point f in figure III.30), where the two populations are in finite phase difference regime. Figures III.46 and III.47 show the two models for a coupling factor of $f = 0.05$ (point g in figure III.30), where the two populations are in synchronous regime. In all the cases, we observe that the network simulations match closely to that of the adaptive rate 1 description of the two populations.

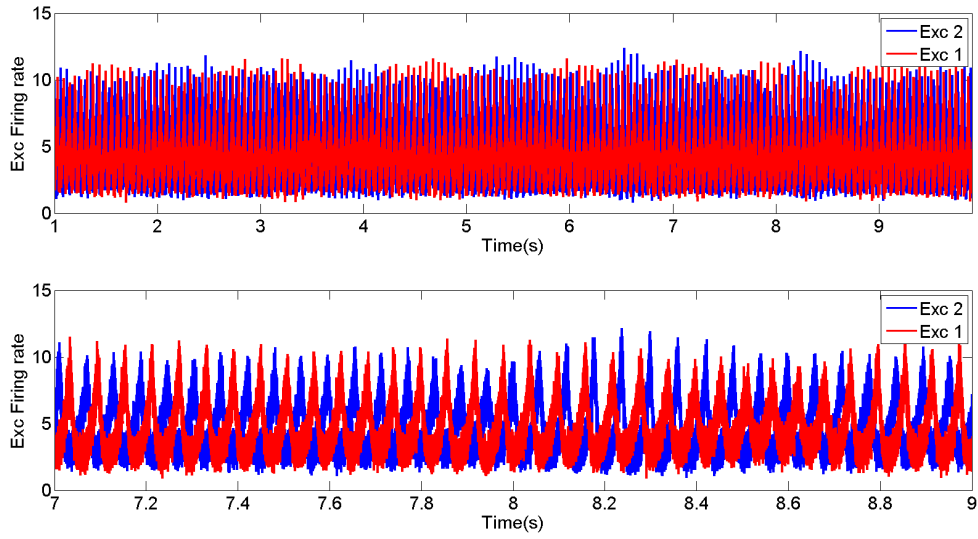


Figure III.38: **The adaptive rate 1 firing rates of the two excitatory populations for a coupling factor of 0.01.** The top panel shows the adaptive rate 1 firing rates of the two excitatory populations that are coupled to each other with a coupling factor of 0.01 (point c in figure III.30) and a finite size noise corresponding to $N_e = 1280k$ and $N_i = 320k$. For these simulations, we use $J_{EE} = 0.2$ mV, $J_{EI} = 0.25$ mV and $J_{IE} = 0.16$ mV and we insert currents into each population corresponding to $(r_E^0, r_I^0) = (5, 10)$ Hz. The bottom panel shows a zoomed in view of the above plot. The two firing rates are in antiphase with each other.

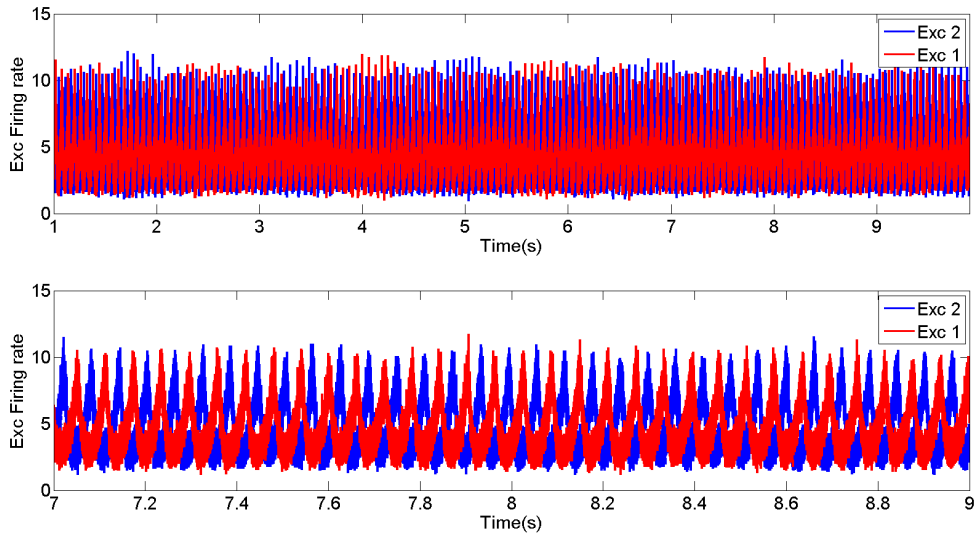


Figure III.39: **The network population firing rates of the two excitatory populations for a coupling factor of 0.01.** We use same parameters as used in figure III.38 (point c in figure III.30). The top panel shows the network population firing rates of the two excitatory populations. The bottom panel shows a zoomed in view of the above plot. The two firing rates are in antiphase with each other.

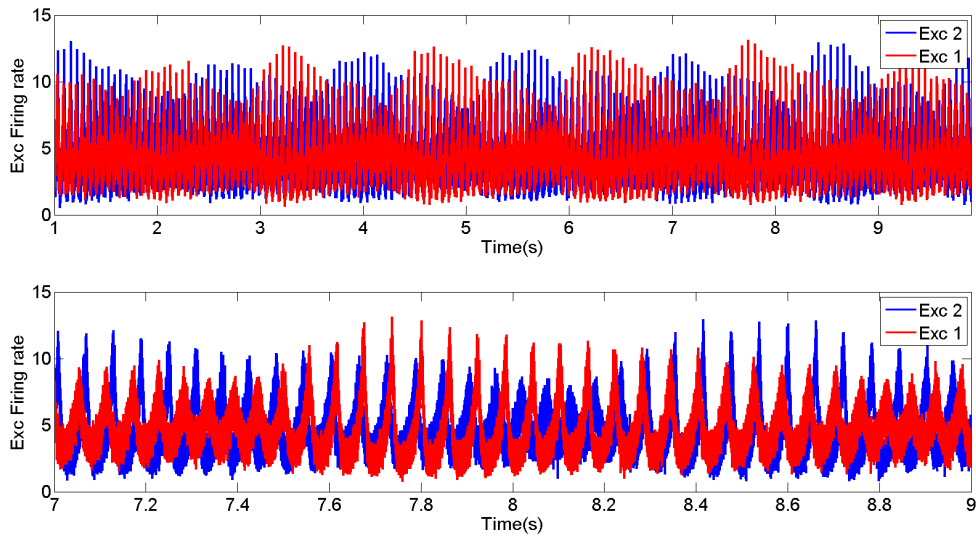


Figure III.40: **The adaptive rate 1 firing rates of the two excitatory populations for a coupling factor of 0.015.** We use same parameters as used in figure III.38 except for the coupling factor for which we take $f= 0.015$ (point d in figure III.30). The top panel shows the adaptive rate 1 firing rates of the two excitatory populations. The bottom panel shows a zoomed in view of the above plot. The two firing rates are in the alternation phase.

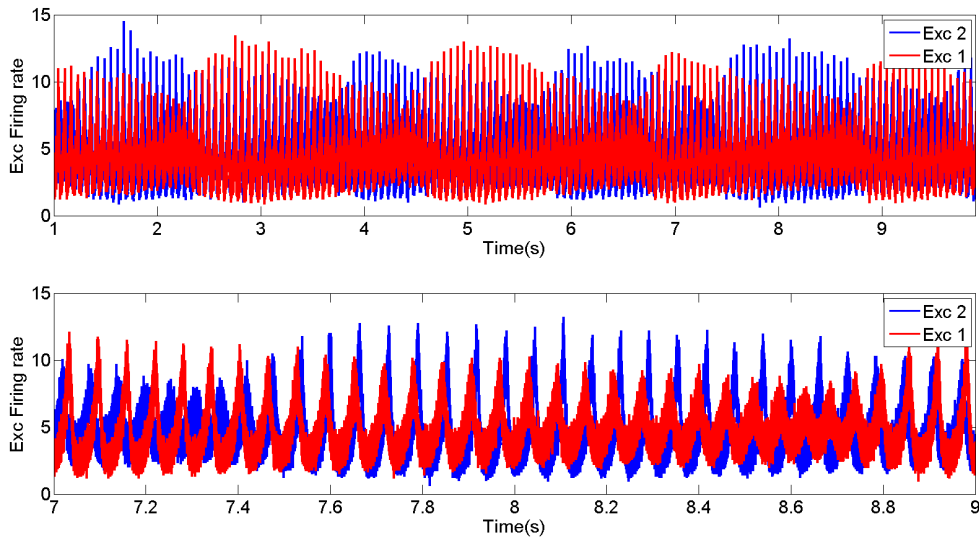


Figure III.41: **The network population firing rates of the two excitatory populations for a coupling factor of 0.015.** We use same parameters as used in figure III.38 except for the coupling factor for which we take $f= 0.015$ (point d in figure III.30). The top panel shows the network population firing rates of the two excitatory populations. The bottom panel shows a zoomed in view of the above plot. The two firing rates are in the alternation phase.

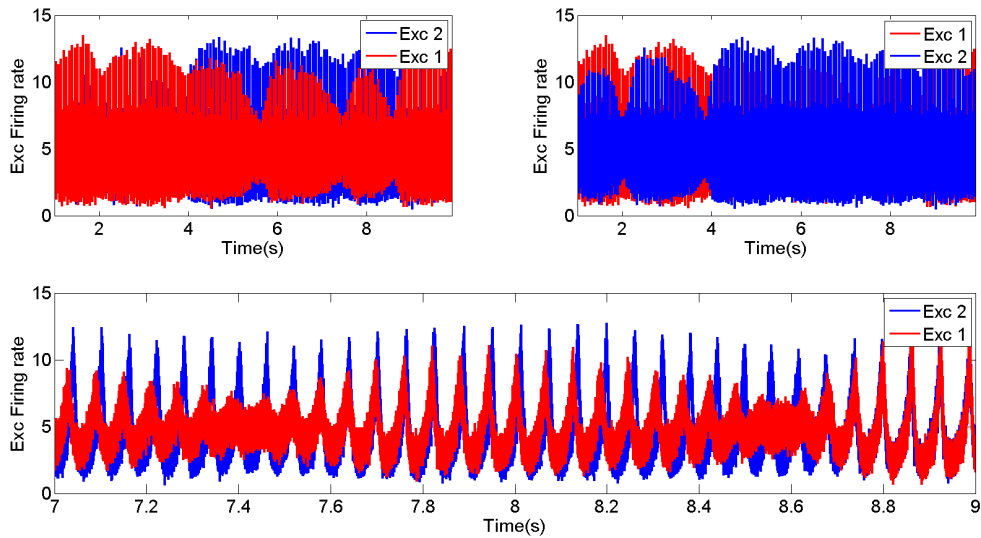


Figure III.42: **The adaptive rate 1 firing rates of the two excitatory populations for a coupling factor of 0.02.** We use same parameters as used in figure III.38 except for the coupling factor for which we take $f=0.02$ (point e in figure III.30). The top panel shows the adaptive rate 1 firing rates of the two excitatory populations and the bottom panel shows a zoomed in view of the above plot. The two firing rates are in the modulation phase. Because of the noise, the higher firing rate could switch from population 1 to population 2.

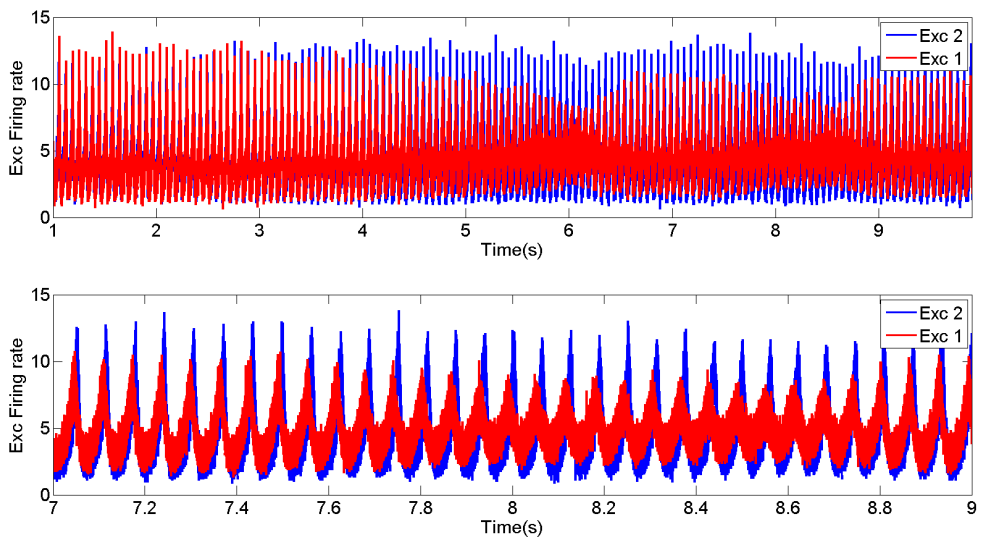


Figure III.43: **The network population firing rates of the two excitatory populations for a coupling factor of 0.02.** We use same parameters as used in figure III.38 except for the coupling factor for which we take $f=0.02$ (point e in figure III.30). The top panel shows the adaptive rate 1 firing rates of the two excitatory populations and the bottom panel shows a zoomed in view of the above plot. The two firing rates are in the modulation phase.

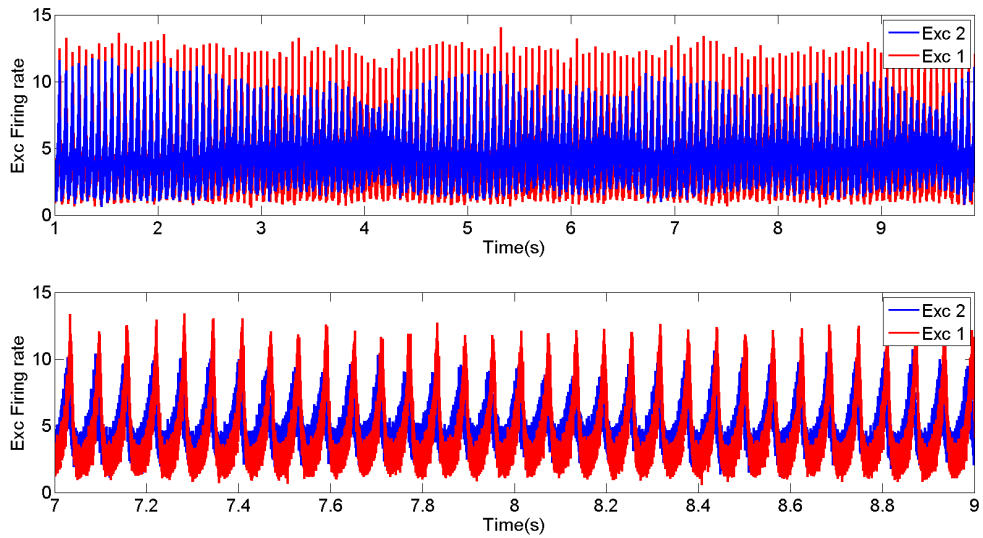


Figure III.44: **The adaptive rate 1 firing rates of the two excitatory populations for a coupling factor of 0.025.** We use same parameters as used in figure III.38 except for the coupling factor for which we take $f= 0.025$ (point f in figure III.30). The top panel shows the adaptive rate 1 firing rates of the two excitatory populations and the bottom panel shows a zoomed in view of the above plot. The two firing rates exhibit a finite phase difference.

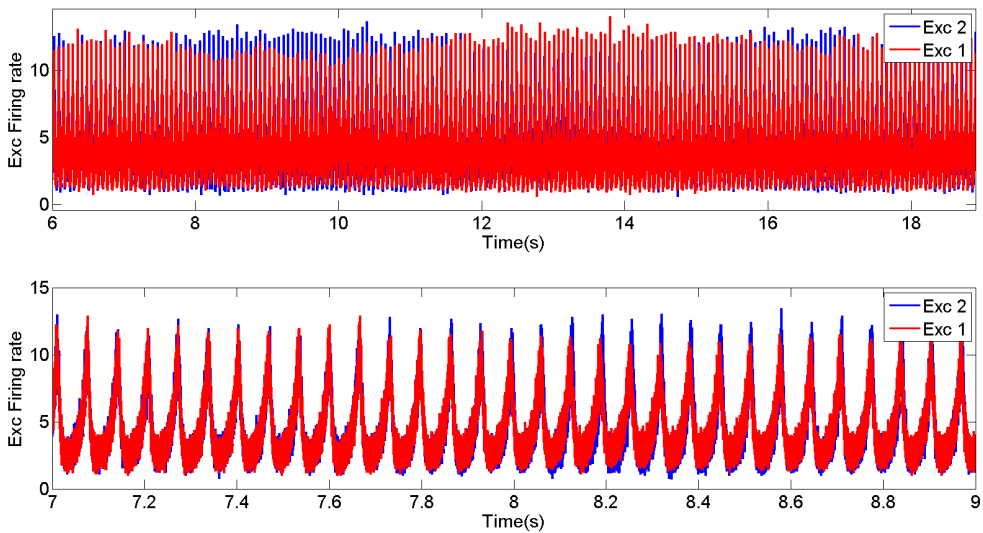


Figure III.45: **The network population firing rates of the two excitatory populations for a coupling factor of 0.025.** We use same parameters as used in figure III.38 except for the coupling factor for which we take $f= 0.025$ (point f in figure III.30). The top panel shows the adaptive rate 1 firing rates of the two excitatory populations and the bottom panel shows a zoomed in view of the above plot. The two firing rates exhibit a finite phase difference.

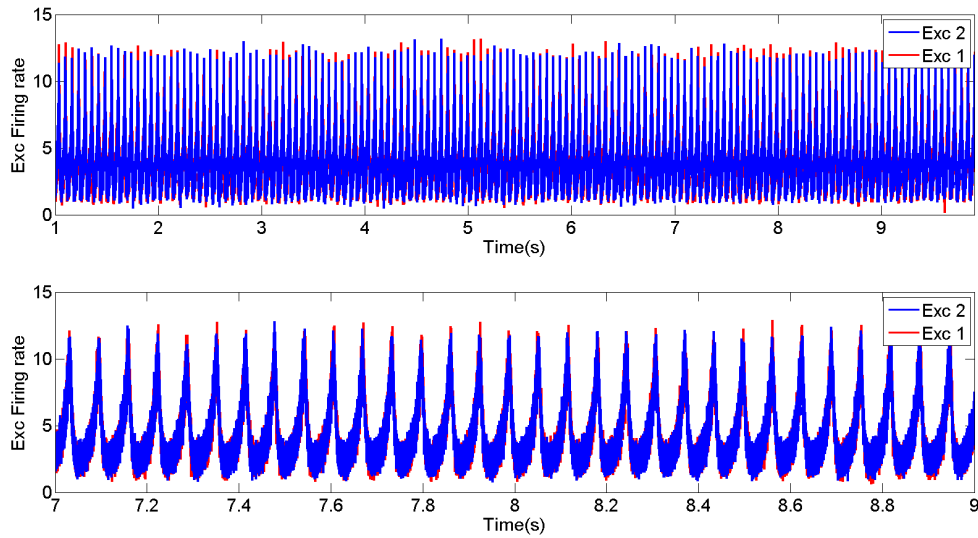


Figure III.46: **The adaptive rate 1 firing rates of the two excitatory populations for a coupling factor of 0.05.** We use same parameters as used in figure III.38 except for the coupling factor for which we take $f= 0.05$ (point g in figure III.30). The top panel shows the adaptive rate 1 firing rates of the two excitatory populations and the bottom panel shows a zoomed in view of the above plot. The two firing rates are synchronized to each other.

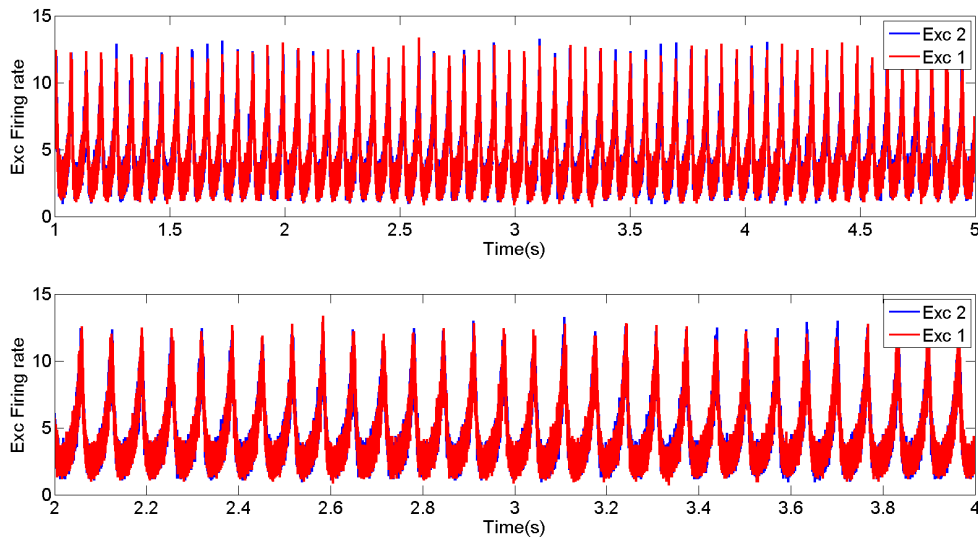


Figure III.47: **The network population firing rates of the two excitatory populations for a coupling factor of 0.05.** We use same parameters as used in figure III.38 except for the coupling factor for which we take $f= 0.05$ (point g in figure III.30). The top panel shows the adaptive rate 1 firing rates of the two excitatory populations and the bottom panel shows a zoomed in view of the above plot. The two firing rates are synchronized to each other.

III.9 Comparing with the finite size networks

In this section, we reduce the size of each EI population in the network to $5k$ neurons ($4k$ excitatory neurons and $1k$ inhibitory neurons) and redo the simulations for the same parameters and coupling factors in the previous section. We show the results in figures III.48-III.52. In each figure, the two panels on the left show the network population firing rates of the two excitatory populations. The two panels differ only with respect to whether the population 1 or population 2 excitatory firing rate is shown on top of the other. This was done for the sake of better visualization. The two right panels show the autocorrelation and the cross correlation of the excitatory firing rates of the two populations, marked as $Re1$, $Re2$ for the autocorrelations and $Re1,2$ for the cross correlation. The bottom right panel shows the zoomed in view of the top panel. We observe that it is difficult to distinguish between the different phases due to noise. However, we see a steady increase in the cross correlation compared to the autocorrelation as the coupling factor is increased. Since, we are interested in ultimately distinguishing synchronous activity from non-synchronous activity, we can use this quantity: the ratio of cross-correlation between the two populations to the autocorrelation of either of the populations as an indicator of the amount of synchrony in the two populations.

We can also compute the phase difference between the firing rates of the two excitatory populations. To do this, we can find out the timings of the peaks of the firing rates of the two excitatory populations in every oscillatory cycle. We can then calculate the timing of the peak of the second excitatory population within the cycle with respect to the first and divide this time difference by the mean timing between the peaks of a single population i.e. the mean time period of oscillation. After multiplying this value by 2π , we get the value of the phase difference of the two populations to be between 0 and 2π . We can then plot the histogram of this phase difference for the different coupling factors as shown in figure III.53. We observe from the figure that as the coupling factor is increased, the phase difference tends to concentrate more around 0, indicating that the two populations have more synchrony for higher coupling factors. For lower coupling factors, even though the peak of the histogram count for the phase difference at 0, we cannot distinguish the different regimes from this curve yet. Further analysis needs to be done to see if one can distinguish the various non-synchronous regimes in two group EI-network in the presence of finite size noise.

III.10 Finite size networks with finite connectivity

In the previous section, we looked at coupled EI networks of 5000 EIF neurons each. All the excitatory neurons in each EI group were coupled to all the excitatory and inhibitory neurons of the corresponding EI group and to all the excitatory neurons of the other EI group; all the inhibitory neurons in each EI group were coupled to all the excitatory neurons in the same EI group. In this section, we will consider two cases: 1) finite connectivity with $C_{e1,e2} = 800$ between the two excitatory populations and full connectivity with $C_e = 4000$ and $C_i = 1000$ within each EI group and 2) finite connectivity with $C_{e1,e2} = 800$ between the two excitatory populations as well as $C_e = 800$ and $C_i = 200$ within each EI group for the same parameters as in figure

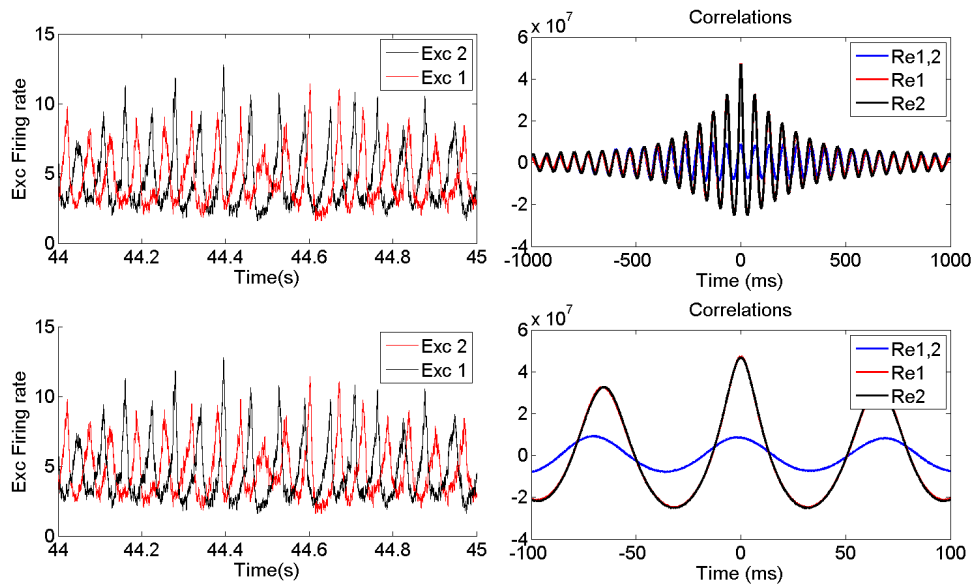


Figure III.48: **The network population firing rates and correlations of the two excitatory populations of 5k neurons each for a coupling factor of 0.01.** The two left panels show the network population firing rates of the two excitatory populations that are coupled to each other with a coupling factor of 0.01 (point c in figure III.30, corresponding to the antiphase regime) for a network size of $N_e = 4k$ and $N_i = 1k$. The two panels differ only with respect to whether the population 1 (red signal) or population 2 excitatory firing rate (black signal) is plotted on top of the other. The two right panels show the autocorrelation and the cross correlation of the excitatory firing rates of the two populations, marked as $Re1$, $Re2$ for the autocorrelations and $Re1,2$ for the cross correlation. The bottom right panel shows the zoomed in view of the above plot. Other parameters are same as in figure III.38.

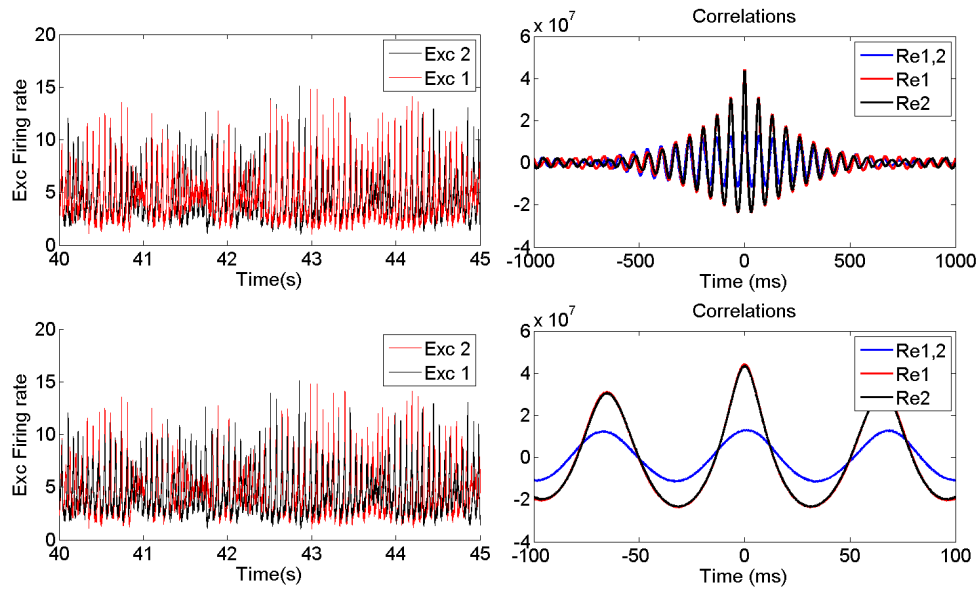


Figure III.49: **The network population firing rates and correlations of the two excitatory populations of 5k neurons each for a coupling factor of 0.015.** The two left panels show the network population firing rates of the two excitatory populations that are coupled to each other with a coupling factor of 0.015 (point d in figure III.30, corresponding to the alternating regime) for a network size of $N_e = 4k$ and $N_i = 1k$. The two panels differ only with respect to whether the population 1 (red signal) or population 2 excitatory firing rate (black signal) is plotted on top of the other. The two right panels show the autocorrelation and the cross correlation of the excitatory firing rates of the two populations, marked as $Re1$, $Re2$ for the autocorrelations and $Re1,2$ for the cross correlation. The bottom right panel shows the zoomed in view of the above plot. Other parameters are same as in figure III.38.

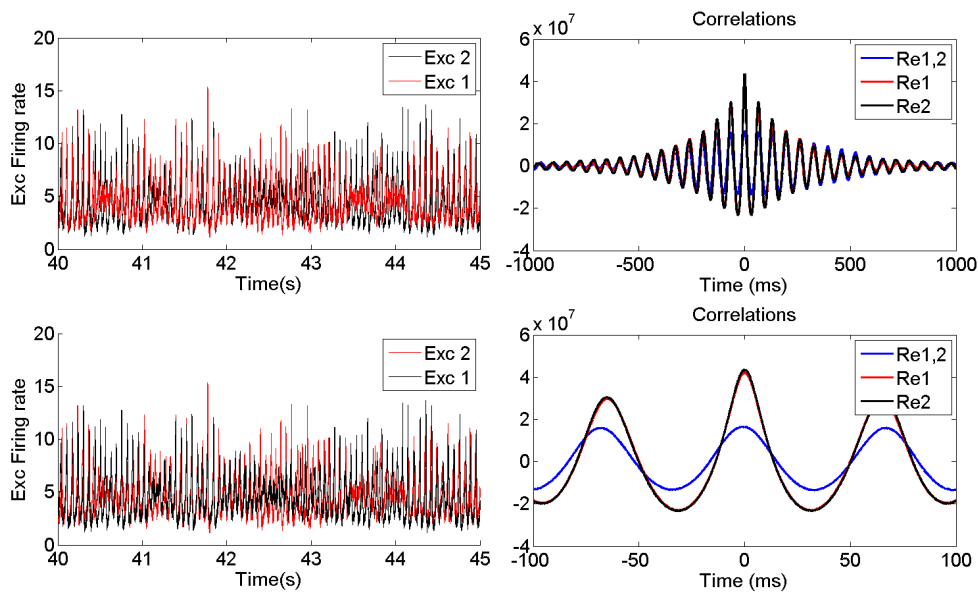


Figure III.50: **The network population firing rates and correlations of the two excitatory populations of 5k neurons each for a coupling factor of 0.02.** The two left panels show the network population firing rates of the two excitatory populations that are coupled to each other with a coupling factor of 0.02 (point e in figure III.30, corresponding to the modulating regime) for a network size of $N_e = 4k$ and $N_i = 1k$. The two panels differ only with respect to whether the population 1 (red signal) or population 2 excitatory firing rate (black signal) is plotted on top of the other. The two right panels show the autocorrelation and the cross correlation of the excitatory firing rates of the two populations, marked as $Re1$, $Re2$ for the autocorrelations and $Re1,2$ for the cross correlation. The bottom right panel shows the zoomed in view of the above plot. Other parameters are same as in figure III.38.

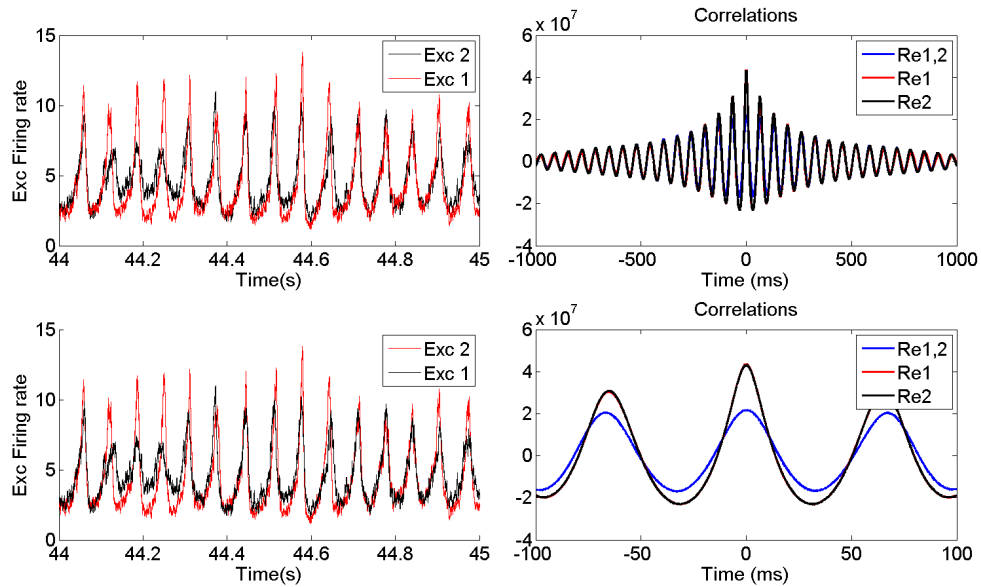


Figure III.51: **The network population firing rates and correlations of the two excitatory populations of 5k neurons each for a coupling factor of 0.025.** The two left panels show the network population firing rates of the two excitatory populations that are coupled to each other with a coupling factor of 0.025 (point f in figure III.30, corresponding to finite phase regime) for a network size of $N_e = 4k$ and $N_i = 1k$. The two panels differ only with respect to whether the population 1 (red signal) or population 2 excitatory firing rate (black signal) is plotted on top of the other. The two right panels show the autocorrelation and the cross correlation of the excitatory firing rates of the two populations, marked as $Re1$, $Re2$ for the autocorrelations and $Re1,2$ for the cross correlation. The bottom right panel shows the zoomed in view of the above plot. Other parameters are same as in figure III.38.

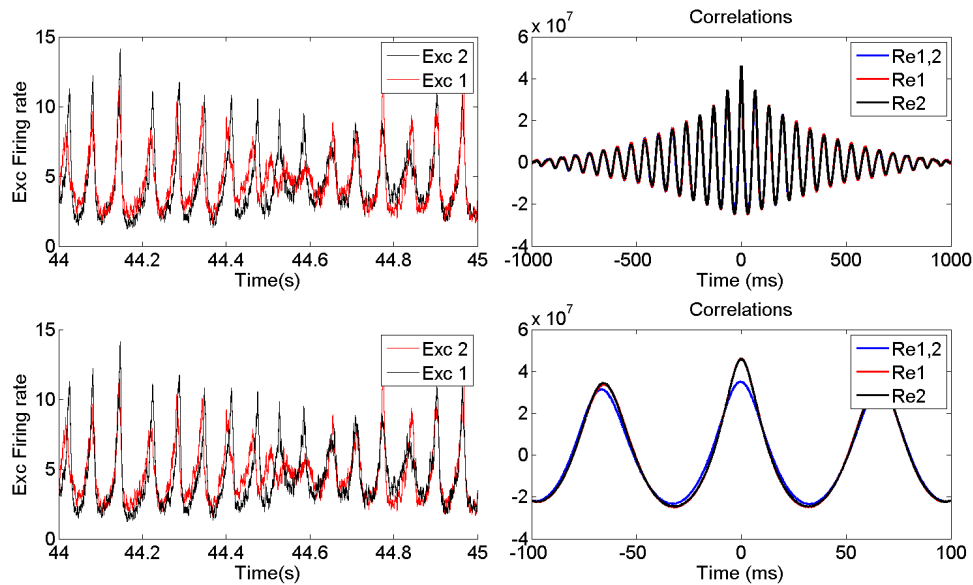


Figure III.52: **The network population firing rates and correlations of the two excitatory populations of 5k neurons each for a coupling factor of 0.05.** The two left panels show the network population firing rates of the two excitatory populations that are coupled to each other with a coupling factor of 0.05 (point g in figure III.30, corresponding to the synchronous regime) for a network size of $N_e = 4k$ and $N_i = 1k$. The two panels differ only with respect to whether the population 1 (red signal) or population 2 excitatory firing rate (black signal) is plotted on top of the other. The two right panels show the autocorrelation and the cross correlation of the excitatory firing rates of the two populations, marked as $Re1$, $Re2$ for the autocorrelations and $Re1,2$ for the cross correlation. The bottom right panel shows the zoomed in view of the above plot. Other parameters are same as in figure III.38.

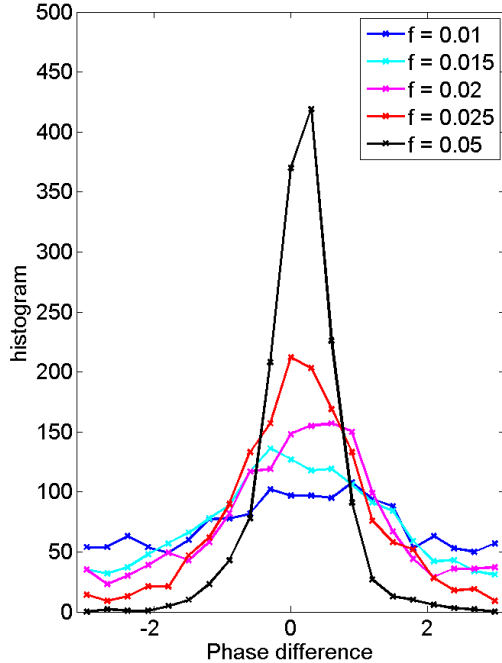


Figure III.53: **The histogram of the phase difference between the two excitatory populations for different coupling factors.** The different curves show the histogram of the phase difference (between 0 and 2π) for different coupling factors. As the coupling is increased, we notice that the phase difference peaks around 0 indicating synchrony. The network has a size of $N_e = 4k$ and $N_i = 1k$ while other parameters are same as in figure III.38.

III.23 (i.e. $w_{EE} = w_{EI} = 1.6$ mV.s and $w_{IE} = 0.4$ mV.s and we insert currents into each population corresponding to $(r_E^0, r_I^0) = (5, 10)$ Hz). We will plot the normalized cross correlation which is the ratio of the cross correlation between the two excitatory populations and the autocorrelation of either of the excitatory population as a function of the coupling factor between the two excitatory populations. The results are shown in figure III.54. We notice that as the coupling factor is increased, this normalized cross correlation increases indicating more synchrony between the two populations.

III.11 Conclusion

In this chapter, we have seen how EI networks generate oscillations in the beta and low-gamma range and how two groups of EI networks can exhibit different regimes depending on the amount of excitatory coupling between the populations. For a large coupling factor between the two excitatory populations, we observe synchronization between the two groups of populations whereas for smaller coupling factors, the system can be in different regimes such as finite phase difference, antiphase regime, alternating regime or modulating regime depending on the coupling factor. The alternating and modulating regimes, reported here for the EI networks, have not been described before in the literature to the best of our knowledge. We can extend this description to more groups of EI networks. Indeed, the description of the different regimes for the case of 2 populations is helpful to understand the regimes for a chain of spatially extended EI networks that are coupled. Such an extension could help us understand the propagation of beta waves that was observed in the motor cortex of the monkey during motor preparation [Rubino et al., 2006]. These waves travelled at a wavelength of around 1cm while the long range connections in the cortex are only around 2mm.

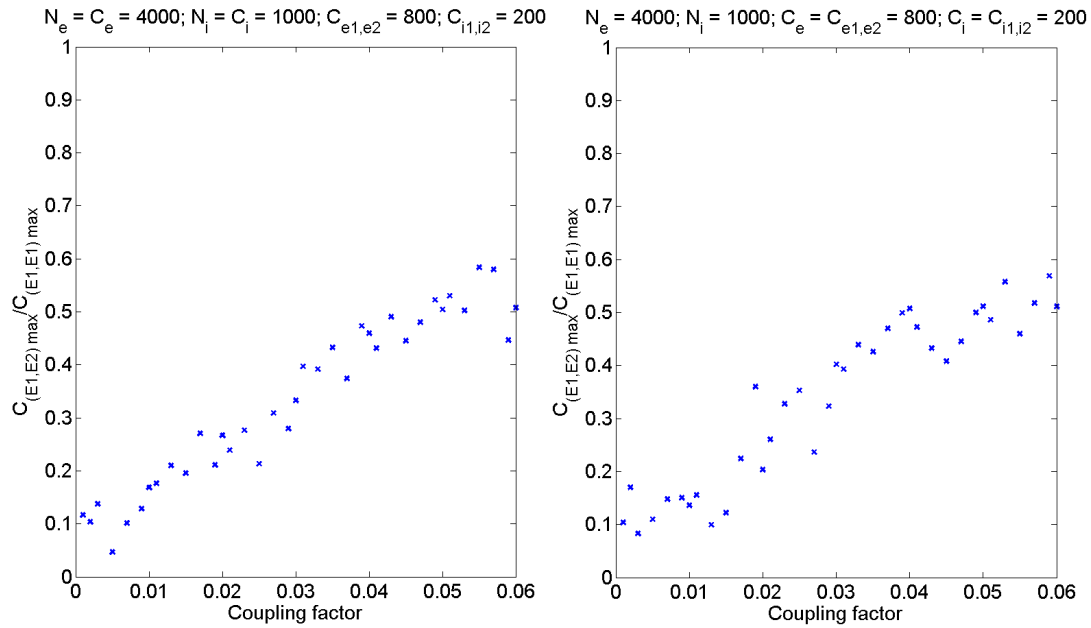


Figure III.54: **The ratio of the cross correlation to the autocorrelation for the case of finite connectivity.** The left panel shows the normalized cross correlation (which is the ratio of the cross correlation between the two excitatory populations and the autocorrelation of either of the excitatory population) as a function of the coupling factor between the two excitatory populations for the case of finite connectivity $C_{e1,e2} = 800$ within the two excitatory populations. The right panel shows the same for the case of finite connectivity within the two populations $C_{e1,e2} = 800$ as well as finite connectivity $C_e = 800$ and $C_i = 200$ within each population. The network has a size of $N_e = 4k$ and $N_i = 1k$ while other parameters are same as in figure III.23.

These results are compatible with our results of the extended chain of EI networks. For the low coupling factor in the case of the 2 coupled groups of EI networks, we observe a finite phase difference or antiphase regime. This desynchronization among the two groups manifests itself as a phase gradient for an extended chain of EI networks. The spontaneous appearance of the phase gradient for low coupling factor could help explain the beta waves observed in the motor cortex. Furthermore, it was recently shown in mice visual cortex that somatostatin (SOM) interneurons are required for long-distance coherence of gamma waves [Veit et al., 2017]. The influence of distance excitatory interaction on interneurons can be studied in our model by introducing long-distance E-I coupling in our model and studying the effects of these interactions. A manuscript, describing these results, titled "Synchronization of oscillatory activity in networks with spatially-structured connectivity" authored by "Anirudh Kulkarni, Jonas Ranft and Vincent Hakim" is in preparation and will be submitted to PLOS Computational Biology. The abstract of this manuscript is provided after this section. In the next chapter, we look at rate models with sensory adaptation and model the results of the motion after effect in the zebrafish larva using these models.

Synchronization and waves in neuronal networks with spatially structured connectivity

Anirudh Kulkarni^{1,3}, Jonas Ranft^{1,2,3}, Vincent Hakim^{1,*},

1 Laboratoire Physique Statistique, CNRS, Ecole Normale Supérieure, PSL Research University, Université Pierre et Marie Curie, Paris, France

2 IBENS, Ecole Normale Supérieure, PSL Research University, CNRS, INSERM, Paris, France

 These authors contributed equally to this work.

* vincent.hakim@ens.fr

Abstract

Oscillations in the beta/low gamma range (10-45Hz) are recorded in diverse neural structures. They have successfully been modeled in several previous works as arising from reciprocal interactions between randomly connected excitatory (E) pyramidal cells and local interneurons (I). The synchronization properties of spatially distant E-I modules have been less studied although this knowledge would help to properly interpret recording data. Here, we analyze the dynamical regimes of two oscillatory E-I modules connected by excitatory interactions as well as those of a chain of such modules. When distant excitation only targets excitatory neurons, we find that it fully synchronizes the oscillations of the two modules when the coupling excitation is sufficiently strong but that it gives rise to a variety of dynamical regimes for two weakly coupled E-I modules. This generally results in the spontaneous appearance of phase gradients in a sufficiently long chain of oscillatory E-I modules, as well as in allied phase waves travelling along the chain. When distant excitation equally targets excitatory and inhibitory interneurons, it always tends to synchronize E-I modules irrespective of its strength. However, stochastic variations in the spike emission of E-I modules comprising finite number of neurons tend to disrupt synchronization. This also gives rise to the appearance of phase gradients and phase waves in a spatially extended network. We characterize these different phenomena and discuss their relations to experimental observations, with particular attention to previously reported waves of beta oscillations during movement preparation.

Author summary

Interactions between local groups of excitatory and inhibitory neurones can produce oscillatory neural activity, as recorded in electro-encephalograms. Distant neuron groups are sometimes observed to oscillate in unisson or with a time lag that depends on the distance between the groups. Distant groups of neurons are also known to be coupled by excitatory interaction rather than inhibitory ones. We study here this excitatory coupling between distant groups of neurons govern their relative oscillatory properties. In particular, we find that it seems to account quite naturally for the occurrence of waves of activity that have been recorded in previous experiments.

Chapter IV

Sensory Adaptation

In this chapter, we will look at another phenomenon seen in neural systems, that of sensory adaptation. We will introduce adaptation and focus particularly on the motion after effect (MAE) in the zebrafish larva. We will discuss how the neuronal activity corresponding to this phenomenon can be recorded with the help of 2 photon calcium imaging in the optic tectum, the highest visual center of the larva. We will then introduce rate models of adaptation and model the neuronal activity underlying the MAE phenomenon in the optic tectum. The next chapter includes the manuscript of our work in detail, while this chapter serves as an introduction to the manuscript.

My contributions to the manuscript include the modeling of the experimental data of the Motion after effect. I developed the model and extracted the different parameters required for the model from the experimental data. Comparison with the experimental results guided me to develop a model where the MAE index and the MAE duration curves agreed with that observed in the experiment (Figure 7 and S5 in the manuscript in the next chapter). On the experimental side, I have performed ablation experiments which show that the optic tectum is indeed important for the generation of the MAE (Figure 3 and Figure S1C). I have performed cross correlation analysis on the neuronal data and the behavioral data (Figure 5 and Figure S3A) and also showed that OKR habituation index is correlated with the length of MAE (Figure S1). Finally, I also performed experiments on paralyzed larvae to show that the rhythmicity of MAE-activity is generated through a neuro-muscular loop (Figure S4).

IV.1 Adaptation: Marr's three levels of analysis

Sensory systems dynamically construct representations of the environment and sensory adaptation is the phenomenon of recalibration of responses of sensory neurons in order to adjust to either the changing environment (e.g. in temperature or lighting) or the changing observer (either due to diseases or aging) (see Figure IV.1). For example, when one steps into a bright room from a dim room, the eye-lids tend to close because of the bright light. However, within minutes, one gradually feels comfortable with the level of light in the room. Even though the level of light has not changed, the person feels more comfortable after a while. This can only be partly explained by the adjustment in the size of the pupil. More importantly, the photoreceptors of the

retina have adjusted their sensitivity to accommodate themselves to the surroundings. The responses of the neurons, therefore, do not depend only on the current value of the stimulus parameter but also on the history of stimulation [Adrian and Zotterman, 1926a] [Webster, 2012] [Maravall, 2011].



Figure IV.1: **An example of color adaptation.** An example of a perceptual after-effect because of adaptation. A photograph of a dancer is shown on the right and the corresponding pseudo-negative image is shown on the left. Staring at the black dot in the left image for 30 seconds or more and then switching your gaze to the dot in the right image makes the grayscale image appear colored briefly. Moreover, the perceived illusory colors are opposite to the adapting colors implying a “negative aftereffect”, which is typical in adaptation. This can be explained by a reduction in sensitivity to the local adapting color, thus, biasing perception towards the complementary color. Picture reproduced from [Webster, 2012].

David Marr described three levels at which any information processing task of a machine can be understood: a) computational level, b) algorithmic level and c) implementation level (see Figure IV.2). The computational theory serves to explain the problem and the goal of the computation. It describes why the problem is appropriate and the logic of the strategy by which it can be carried out. The algorithmic level describes how the computational theory can be implemented. It specifies the representation for the input and the output and the algorithm for the transformation of the input to the output. The implementation level tries to identify the biophysical substrate that is used to perform the computation and the implementation. Each level can be viewed as a realization of the level before it.

Marr’s three levels applies to an information processing task carried out by any machine and we could try to extend it to understand adaptation.

Adaptation is found in all sensory systems including visual (color and motion) [Kohn, 2007] [Clifford et al., 2007], auditory [King et al., 2011], whisker system [Petersen et al., 2009], proprioceptive (adapting to the texture of clothing on skin), olfactory (to prolonged smells such as perfume) and gustatory. All sensory neurons except for nociceptors (the neurons involved in the sensation of pain) exhibit the phenomenon of sensory adaptation.

On a computational level, we would need to explain the function served by having sensory adaptation instead of a constant neuronal response to a constant input.

Computational theory	Representation and algorithm	Hardware implementation
What is the goal of the computation, why is it appropriate, and what is the logic of the strategy by which it can be carried out?	How can this computational theory be implemented? In particular, what is the representation for the input and output, and what is the algorithm for the transformation?	How can the representation and algorithm be realized physically?

Figure IV.2: **Marr's three levels of analysis.** Three levels at which any information processing task can be understood. Picture reproduced from [Marr, 1982].

On a representational level, one would need to provide a phenomenological model of adaptation. And finally, on the level of hardware implementation, one would need to specify the exact biophysical processes which contribute to adaptation.

IV.1.1 Computational level

The goal served by adaptation is, as of yet, not very clear [Webster, 2012]. In the visual system, its potential applications are still being discussed [Chopin and Mammassian, 2012]. Some of the suggested applications include enhancing discrimination during post adaptation [Greenlee and Heitger, 1988], highlighting new stimuli (i.e. acting as a novelty detector) [Ranganath and Rainer, 2003], maintaining perceptual constancy (i.e. invariant percepts despite varying viewing contexts) [Foster, 2011]. Yet demonstrations that we can better distinguish among simple patterns, like gratings [Barlow et al., 1976] or complex images like faces [Webster, 2012], after we adapt to them are meager in comparison to the striking changes that adaptation induces in their appearance. Since our sensory systems are exposed to stimuli over a dynamic range of about 10^9 [Frazor and Geisler, 2006], adaptation could also serve to provide neurons with most information in a limited dynamical range that it is exposed to at a given moment (Efficient coding) [Attneave, 1954] [Laughlin, 1981] [Barlow, 1990] [Wark et al., 2007]. Moreover, nearby stimuli are highly correlated, so the range of local fluctuations of stimuli is much smaller than the global range. Thus, efficient coding posits the maximization of information transmitted about the stimulus. Gain control at each stage of transmission in a sensory system could optimize the efficiency of coding in the system as a whole. Accordingly, there should be many sites of adaptation in the sensory system [Petersen et al., 2009] [Lundstrom et al., 2010]. The idea of efficient coding has found evidence across several sensory modalities in different species: luminance and contrast adaptation in the visual system [Chander and Chichilnisky, 2001] [Mante et al., 2005] [Gollisch and Meister, 2010], fly visual system [Petersen et al.,

1997] [Fairhall et al., 2001] [Brenner et al., 2000], midbrain of guinea pigs [Dean et al., 2005], inferior colliculus of cats [Kvale and Schreiner, 2004], songbird auditory fore-brain [Nagel and Doupe, 2006] [Dahmen et al., 2010], and rat barrel cortex [Maravall et al., 2007]. Adaptation with dynamics that change over many timescales also allow the neurons to track changes in statistics of stimuli over an appropriate amount of time.

Theories of predictive coding suggest that maximizing information and metabolic efficiency could be achieved through adaptation [Srinivasan et al., 1982] by using resources only on the unexpected features of the stimulus. This is because the natural stimuli in the immediate sensory environment have highly structured spatial and temporal correlations and as result, there is a lot of redundancy in the stimulus. The adaptive behaviour, in this case, could help to increase sensitivity to novel stimuli and reduce responsiveness to predictable stimuli. This theory, though it powerfully predicts responses in early sensory neurons [Hosoya et al., 2005], is unclear on whether same constraints work for higher perceptual attributes where the range of environmental variation may be much less, and where the goal of sensory coding itself might change [Simoncelli and Olshausen, 2001].

Adaptation has also been proposed to aid in Bayesian inference by either affecting the prior distribution or the Likelihood model [Stocker and Simoncelli, 2006] though it is not yet clear how cortical circuits might implement Bayesian inference [Doya et al., 2007].

Finally, adaptation can lead to ambiguity in the representation of the sensory stimulus because the same stimulus can evoke different responses under different contexts. The ambiguity can either be resolved by including multiple information channels across different neurons [Nagel and Doupe, 2006] or multiple information channels in the same neuron [Lundstrom and Fairhall, 2006]. In some cases, the ambiguity need not be resolved and could lead to harmless illusions, such as visual illusions of contrast or brightness.

IV.1.2 Algorithmic level

Modeling of adaptation in photoreceptors was initially inspired by modeling the biochemical phototransduction cascade, which converts light into neural activity [Fain et al., 2001]. More recent models are phenomenological in nature, such as the ones by Carpenter and Grossberg [Carpenter and Grossberg, 1981] or the Dynamical adaptation (DA) model [Clark et al., 2013]. These models use a series of a succession of linear filters followed by a nonlinearity. The nonlinearity is feedback driven or purely feedforward (with the parameters such as the integration time constant depending on the input history) depending on the model. In the framework of the LNP model (see section II.1.3), which describes the response of a neuron to a given stimulus, adaptation can be modeled as changes in either the linear filter or the nonlinearity function. The adaptive changes affecting the neuronal feature selectivity can be modeled by changes in linear filter whereas the sensitivity to the filtered stimulus can be modeled by adjusting the nonlinearity [Chander and Chichilnisky, 2001] [Rieke, 2001]. Adaptation to mean luminance, for instance, can be interpreted as a shift in the threshold of the nonlinearity of the neuronal tuning curve [Rieke, 2001].

Section I.2.2 discusses rate models of spike rate adaptation. In this chapter, we will focus on the Motion After Effect in the zebrafish and implement adaptation in a rate model description (see section IV.9).

IV.1.3 Implementation level

Adaptation is really a blanket term for a wide range of phenomena with similar functional effects [Maravall, 2011]. Different schemes of implementation of adaptation have been proposed and adaptation could be caused by multiple biophysical phenomena. In the visual system, contrast adaptation is explained by the hyperpolarization of individual neurons due to the activation of intrinsic channels [Baccus and Meister, 2002] [Sanchez-Vives et al., 2000][Carandini and Ferster, 1997]. In the olfactory system, activation of Ca^{+2} channels in second messenger pathways results in adaptation due to feedback mechanisms such as Ca^{+2} -calmodulin interactions and Ca^{+2} -calmodulin-kinase interactions [Dougherty et al., 2005]. In mechanosensory systems, calcium inflow could be used to move proteins to close or open channels. Due to sustained stimulation, the neuron's firing rate is reduced due to spike-frequency adaptation. Another potential mechanism, in the case of orientation adaptation in the early visual system [Dragoi et al., 2000] and in the rat barrel cortex [Chung et al., 2002] [Katz et al., 2006] is suggested to be short-term synaptic depression [Abbott et al., 1997] [Tsodyks and Markram, 1997]. More generally, the ability of the synaptic strength to change either due to modifications in presynaptic neurotransmitter release or postsynaptic sensitivity over timescales from milliseconds to tens of seconds [Fioravante and Regehr, 2011] [Zucker and Regehr, 2002] create a wide variety of adaptive effects [Markram et al., 1998] [Abbott and Regehr, 2004] [Buonomano and Maass, 2009]. Another mechanism for contrast gain control in primary visual cortex, V1, is the divisive normalization, in which the output of a given neuron is modulated by feedback from the responses of neurons with similar receptive field. Adaptation can occur at different levels in the brain and could be the effect of multiple processes acting at different sites. For instance, intrinsic and synaptic mechanisms at several sites in the visual system produce contrast adaptation [Kim and Rieke, 2001][Baccus and Meister, 2002]. In rat barrel cortex, it was shown that a subthreshold component of adaptation is whisker-specific [Katz et al., 2006], while responses in barrel cortex are multi-whisker, implying that the adaptation occurs in intracortical or thalamocortical connections as opposed to via intrinsic mechanisms in the barrel cortical neurons.

The intrinsic dynamics of single neurons evolved over multiple timescales [La Camera et al., 2006] and the apparent time constant of adaptation, more particularly the slow gain change, varies as a function of the period of the stimulus [Marom, 2010] [Wark et al., 2009]. This could be a result of power-law dynamics [Drew and Abbott, 2006] although few studies provide direct evidence for the biophysical mechanisms underlying multiple timescale dynamics. Power-law and fractional differentiation behaviour was shown in cortical slices [Lundstrom et al., 2008] as well as for thalamic and cortical neurons in the whisker somatosensory pathway [Lundstrom et al., 2010]. However, as power-law dynamics can be approximated by a cascade of many exponential processes [Friedlander and Brenner, 2009] [Gray-Keller and Detwiler, 1994] [Cilluffo et al., 2004], a leading hypothesis is that multiple timescale dynamics are the result of a cascade of

exponential processes in a cell or network.

IV.2 Motion After Effect

The Motion After Effect (MAE) is a phenomenon in which continuous exposure to a coherent moving stimulus in a large field of view in one direction results in the perception of illusory motion in the opposite direction at the end of the stimulation. First recorded by Aristotle (Aristotle, c350BC), it was rediscovered by Purkinje (1820), see [Mather et al., 1988] and [Addams, 1834]. Subsequently, a wide range of test stimuli and adapting stimuli were used to explore the effect [Wohlgemuth, 1911]. As Addams noticed the effect when observing the waterfall of Foyers at Loch Ness, it is also known as the waterfall illusion. This illusion has been observed in many vertebrate and invertebrate organisms [Purkinje 1820, [Wohlgemuth, 1911] [Barlow and Hill, 1963] [Petersen et al., 1985] [Niu et al., 2006] [Watamaniuk and Heinen, 2007] [Nordström and O'Carroll, 2009]. An illustration of the illusion is shown in the figure IV.3

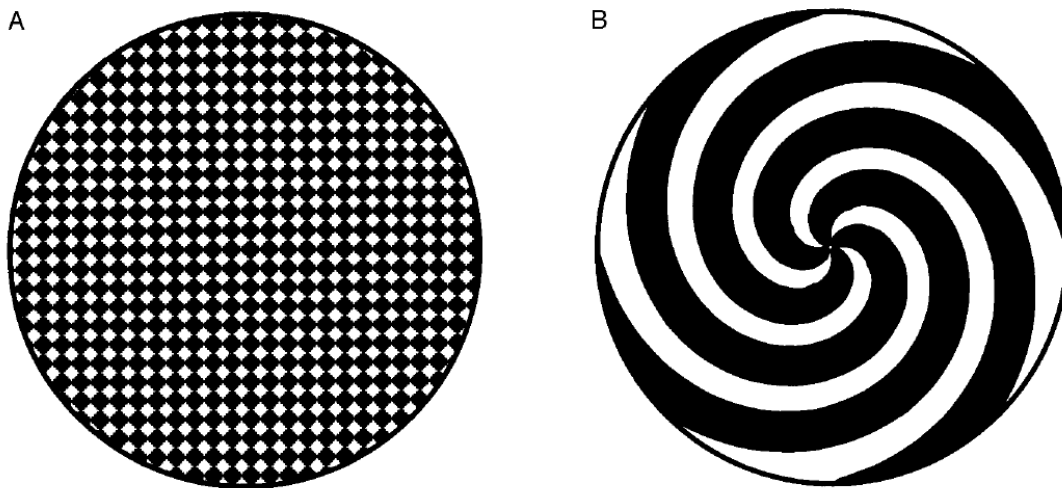


Figure IV.3: **Motion After Effect.** Cut out an enlarged version of either A or B and rotate it on a turntable at a suitable speed for 30s while gazing at the center of the disc. When the disc stops, we perceive the dots rotating backwards in the case of A and a previously contracting spiral appearing expanding in the case of B. Taken from [Anstis et al., 1998].

Adaptation of the motion sensitive neurons in the brain is believed to be the underlying cause of the illusion. Reduced activity in directionally selective cells in the rabbit retina during prolonged exposure to motion in their preferred direction was observed by Barlow and Hill [Barlow and Hill, 1963]. To explain this, they proposed an opponent system of two direction selective cell populations, where the difference in the activity of the two populations encodes for the perceived direction of motion. Following adaptation to a moving stimulus in one direction, the population activity of the cells corresponding to that direction will have its activity lower than the baseline activity

while the other population will remain at its baseline activity. There will, thus, be a bias towards the population which codes for motion in the opposite direction. Similar reductions in responses of the population selective to one direction, upon exposure to a moving stimulus in the preferred direction, were observed in medial temporal visual area in owl monkeys (MT, a brain region encoding for visual motion) [Petersen et al., 1985], area 17 (V1) of anesthetized cats [Giaschi et al., 1993], nucleus lentiformis mesencephali (nLM) in the pigeons [Niu et al., 2006]

For the population coding for the opposite direction, in some cases an enhancement in responses was observed such as in temporal visual area in owl monkeys (MT, a brain region encoding for visual motion), nucleus lentiformis mesencephali (nLM) in the pigeons whereas in some cases, a reduced response was found, such as in the area 17 (V1) of anesthetized cats. However, this reduction was less than the reduction found in the population coding for the stimulus direction. This result is consistent with the original imbalance theory proposed by Barlow and Hill [Barlow and Hill, 1963].

In humans subjects, during and after exposure to expanding or contracting patterns, enhanced fMRI responses were found in MT, and to a smaller extent in areas V2 and V3a but not in V1 [Tootell et al., 1995]. This suggested that the MAE illusion is generated in higher visual brain regions.

There are two potential advantages of the MAE in visual information processing: error correction or/and coding optimization. To keep the perceiver's internal representation of motion fixed, the visual system could have developed an error correction mechanism in the visual system. Upon prolonged viewing of motion in one direction, the corresponding cells which respond to the motion stimulus, show more activity than the baseline activity and this is corrected by a gain-reset mechanism during the viewing of the stimulus. As a result, upon the termination of the stimulus, an erroneous reduction in their output compared to their baseline output would be produced. This reduction would then generate motion perception in the opposite direction (MAE).

In the framework of coding optimization, upon the presentation of a continuous moving stimulus, many neurons will be active simultaneously and will inhibit each other's activities. This inhibition will be sustained for a while following the end of the conditioning stimulus and thus a reversed motion will be perceived.

A schematic diagram of the model explaining these results is outlined in Figure IV.4. On the left, there is no motion stimulus and therefore, the baseline responses of neurons coding for the different directions of motion are the same and as a result, no motion is perceived. Following stimulation in one direction, the north-west direction, the corresponding synapses between the motion detectors (leftward and the upward detectors in this case) and MT habituate. As a result, following the end of the stimulus, the baseline responses of these two populations are lower than the baseline responses of the rightward and downward populations in the MT. As a result, a different direction of motion (south-east) is then perceived.

Another theory by Horace Barlow [Barlow, 1990] proposes that MAE reflects a neural mechanism that removes temporal correlations in incoming data in order to create a sparse neuronal representation to focus on novel items and changes. Accordingly, aftereffects may arise from the same decorrelating processes that are responsible for the original emergence of long-term development feature selectivity [Ball, 2005] [Bednar and Miikkulainen, 2000] [Ciroux, 2005].

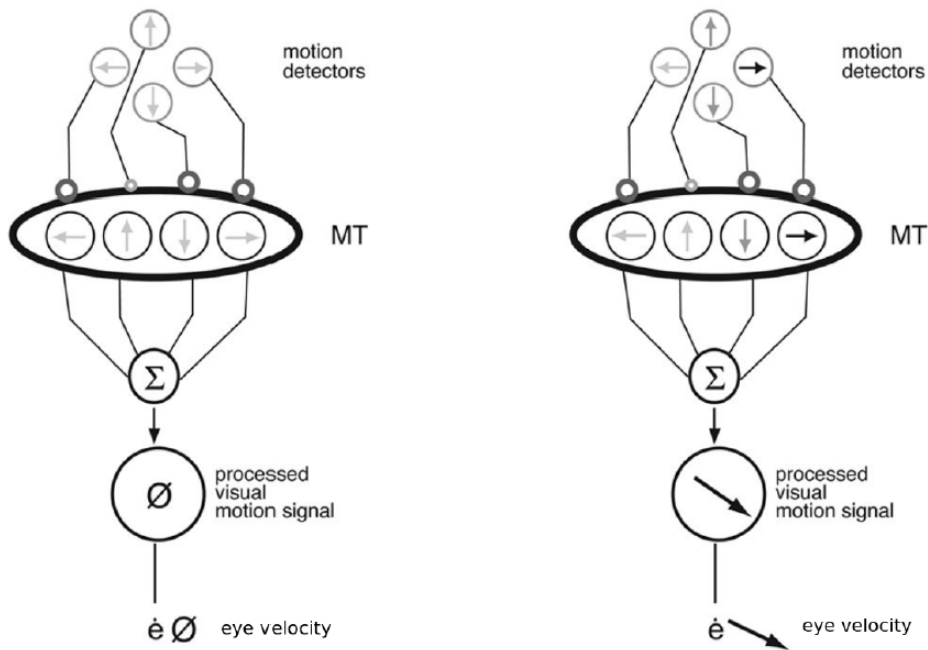


Figure IV.4: **A schematic model explaining MAE proposed by Watamiuk et al.** Motion direction detectors are represented by circles with the corresponding motion direction arrows. These detectors synapse to the area MT whose output is then summed and sent to the eyes. a) After conditioning in the upward direction, habituation is induced in the corresponding synapse between the motion detectors. However, because the subjects' eyes are closed MAE cannot be perceived. b) Following the end of the stimulus for (a) but in the presence of a rightward moving visual input generates MAE perception in the bottom-rightwards direction. Adapted from [Watamaniuk and Heinen, 2007].

Another mechanism was developed by Van de Grind et al. [Van de Grind et al., 2003a] [Van de Grind et al., 2003b] that uses divisive feedforward inhibition as the gain control mechanism. According to this theory, during adaptation, a leaky integrator in the active cells charges up, and following adaptation, the charge dissipates causing an imbalance in output between adapted and unadapted units. Psychophysical [Morgan et al., 2006] and electrophysiological [Kohn and Movshon, 2003] results are consistent with this kind of gain control mechanism.

Here, we will use the zebrafish larva to study the neuronal mechanisms underlying MAE and we will model the results obtained. Since we can monitor the dynamics of large neuronal networks with single-neuron resolution in an intact, non-anaesthetized behaving vertebrate, we will be able to correlate the MAE behaviour with the neuronal activities and shed light on the mechanisms of the brain by the means of a mathematical rate model. We provide a brief introduction to the zebrafish model in the next section.

IV.3 The zebrafish as a vertebrate model for systems neuroscience

As already stated, the human brain is highly complex with over a hundred billion neurons and a thousand times more number of synapses. The ultimate aim of neuroscience is to understand this complexity at various levels: from genes that encode membrane proteins to single neuron dynamics to networks of neurons to behaviour. However, we are still in the nascent stages of understanding the human brain with respect to our current technology but nevertheless, we can make progress by restricting ourselves to animal models. These models must be easy to maintain and breed in a laboratory setting and must have particular experimental advantages. At the present day, a number of animal models are in use in neuroscience research as illustrated in the figure IV.5.


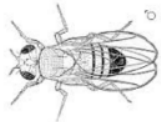



	Caenorhabditis Elegans	Drosophila Melanogaster	Zebrafish larva	Mouse	Rhesus macaque
					
Number of neurons	302	~135,000	~100,000	~71,000,000	~480,000,000

Figure IV.5: **Animal models used in neuroscience.** The number of neurons is indicated in the last row. For Rhesus macaque, only the cortical neurons are indicated.

The zebrafish larva is an excellent animal model to study neuroscience [Sumbre and de Polavieja, 2014]. Zebrafish (*Danio rerio*) is a tropical omnivorous teleost fish originating from the south of Asia (Figure IV.6A-C). They are commonly found in shoals and belong to the family of stomachless fish with toothless jaws of the Cyprinidae

family. They have a relatively fast reproduction cycle and are very easy to breed. This ensures a ready supply of animals for research. When compared to rodents, which have 5-10 offspring per pairing, zebrafish offer about 200-300 eggs each time. The larvae also grow and develop very quickly. Adults grow up to ~ 2.5 to 4cm in length and become sexually mature at ~ 3 months. They can thrive in a wide range of habitat including shallow waters with low currents, pristine waters, man-made canals, streams and ponds (Figure IV.6D-F). Owing to this reason and the fact that they are small, it is easier to keep zebrafish in what appear to be more natural conditions than it is possible to simulate for mammals.

The zebrafish embryo is very popular in developmental and genetic studies because of its transparency. The embryos are able to absorb chemicals that have been added to their water and this makes it easy to introduce genetic modifications using chemical mutagens. It is possible to induce more mutations in their genome as compared to the rodents because they can withstand much higher levels of chemical mutagens than can be tolerated by rodents. Having first been selected as a genetic model about 35 years ago by George Streisinger and colleagues [Streisinger et al., 1981], it became very popular in developmental biology and resulted in a large library of transgenic and mutant fish, enabling one to target specific cell types. The zebrafish genome has been entirely sequenced and shares 70 per cent of its genes with the human genome [Howe et al., 2013]. Because the cell biological and developmental processes are widely conserved across all vertebrates, studies in fish can give insight into human diseases. In fact, 84 percent of the genes known to be associated with human disease have a zebrafish counterpart. Mutations in about 14000 genes of the fish have been created and various vertebrate models of neurodevelopmental, neurological and neurodegenerative diseases have thus been possible [Deo and MacRae, 2011] and numerous models for human diseases such as Melanoma [White et al., 2011], Alzheimer's disease [Paquet et al., 2009] and Rett syndrome [Pietri et al., 2013] have been proposed. MCT8-deficient zebrafish exhibit anatomical impairment and behavioral phenotypes and same genetic defect is also known to be responsible for a significant fraction of the undiagnosed neurological disorders in humans [Zada et al., 2014]. Their muscles, blood, kidneys and eyes share many features with human systems. With their unique ability to repair heart muscle, they could help us to develop ways of repairing hearts of humans with heart failure.

In recent years, the zebrafish larva has become an excellent vertebrate model for neuroscience research as well. It is an ideal model organism for studying early development as the larvae grow in an extra-uterine environment. As old as 5 days post fertilization (dpf), larvae need to avoid predators and capture prey in order to survive. This strong evolutionary pressure is responsible for a rapid development of the sensory-motor systems, vision in particular, and a large repertoire of motor behaviors such as the Optokinetic response (OKR), Optomotor response (OMR) and prey-capture. (Friedrich et al., 2010; Portugues and Engert, 2009).

Due to its small size (the brain is 500 μm thick and 3mm long) and transparency even at the larval stage, the larval brain activity is ideally accessible to the state of the art optical tools such as two-Photon Scanning Microscopy (Figure IV.7B), Selective Plane Illumination Microscopy, and Light-Field Microscopy. Using two-Photon Scanning Microscopy, the activities of large brain regions of the fish can be monitored simultaneously to a spatial resolution of a single neuron and a temporal resolution of



Figure IV.6: **Zebrafish and its habitat.** (A-B) Zebrafish from northeastern India. The upper two fish are males and the lower two fish are females. Males are usually slender and torpedo-shaped with a yellow ventral cast whereas females tend to be fatter due to the eggs they carry. Scale bar given in (A): 5 mm (C) A shoal of zebrafish (a single fish is highlighted with the arrow) in a stream-side pool in Meghalaya, India, north of Bangladesh. (D-F) Zebrafish can be found in diverse habitat: pristine pools, ephemeral pools (B, D) man made canals (E) and rice paddies (F). All pictures reproduced from Parichy (2015).

about 3.91 Hz (Figure IV.7). This is achieved using a genetically encoded calcium indicator such as GCaMP which can be expressed in selected populations of neurons. The idea behind the functioning of GCaMP is that GCaMP changes its fluorescence properties in response to the binding of Ca^{2+} . The firing of neurons causes an opening of calcium channels and this results in an increase in the intracellular calcium concentration. These calcium ions bind to the GCaMP indicators resulting in increase and decrease in the fluorescence of GCaMP sensors, which can be measured using various light microscopies.

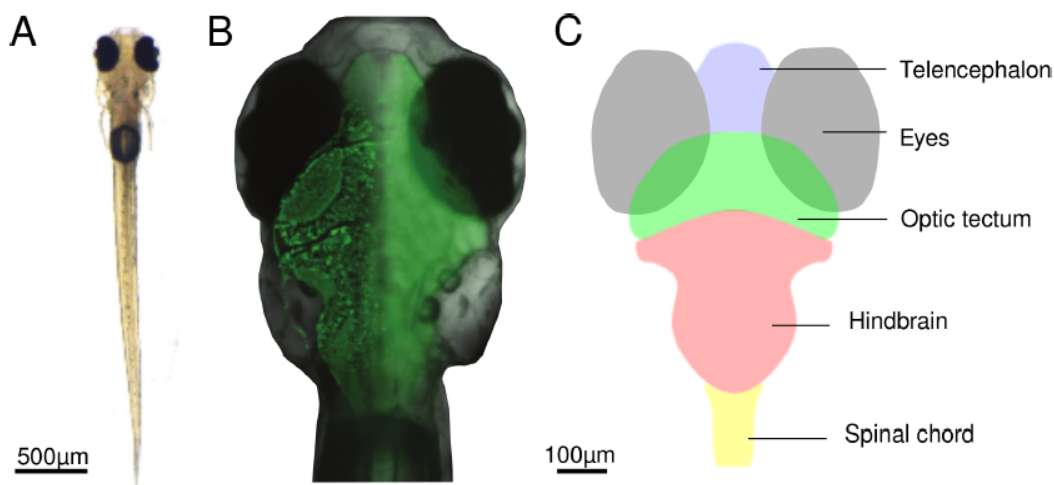


Figure IV.7: **Brain anatomy of the zebrafish larva at 6 dpf.** (A). Bright-field image of a zebrafish larva. (B) Overlay of a bright-field image of the larva head and the images of its brain acquired using two-photon microscopy (left part of the brain) and fluorescent imaging (right part of the brain). Note the spatial resolution on the left part obtained with two-photon microscopy. Neurons are labeled with the green fluorescent calcium indicator GCaMP5G. Image reproduced from Fetcho (2012). (C) Schematic drawing of the larval zebrafish brain showed in (B) representing the main parts of the brain (telencephalon, Optic Tectum, hindbrain and spinal cord) and the eyes. Scale bar is common for B and C.

Additionally, the zebrafish larva also allows the usage of optogenetic actuators, light activated ion channels, such as halorhodopsin or channelrhodopsin [Douglass et al., 2008] [Schoonheim et al., 2010]. These channels when activated can induce or suppress neuronal activity. Manipulation of the neuronal activity can be used to study changes in behaviour and this can shed light on the role of the specific population of neurons involved. All these manipulations are performed in a non-invasive, non-paralyzed and non-anesthetized manner requiring only that the larva be restrained in agarose. The ability to monitor the activity of the entire brain in a behaving, non-paralyzed and non-anesthetized vertebrate make zebrafish an ideal model [Ahrens and Engert, 2015] [Zhu et al., 2012].

IV.4 Optokinetic response and Motion After Effect

At around 80 hours post fertilization (~ 3.3 dpf), the zebrafish larva develops the optokinetic response (OKR). The optokinetic response (Figure IV.8A) is a series of alternating slow-phase and fast-phase movement of an animal's eyes in response to a coherently moving external large field of view. In the presence of a water current, when the larva is moved passively, a compensating movement is generated because of OKR. Thus the OKR serves to stabilize the visual image on the retina and thus a stable position with respect to their visual environment. Due to this evolutionary advantage, all vertebrates display this basic behavior. In the zebrafish, it is the earliest visual behavior requiring pattern vision and directionality [Easter and Nicola, 1996] [Easter and Nicola, 1997]. To study the OKR in the laboratory, the orientation of the eye is extracted by fitting the eyes with an ellipse in an image processing software like MATLAB. The angle between the long axis of the ellipse and the external horizontal axis is then taken as the orientation angle of the eye (see Figure IV.8B). Slightly after the development of the OKR, the optomotor response (OMR) develops. Similar to the OKR, the OMR (Figure IV.8C) serves to maintain the position of the fish stable in a current by generating tail-flip movements in the direction of perceived motion. As both these behaviors are very robust and develop at a very early stage, they are used to screen mutations with defects in their neuronal visual circuits [Rick et al., 2000] [Neuhauss et al., 1999].

In order to record and analyze OKR, larvae are usually immobilized in methylcellulose or in low-melting agarose and the agarose is selectively removed around the eyes. Then, following the presentation of a coherent-motion visual stimulus, such as a rotating drum painted with black stripes, in a large portion of the field of view of the larva, OKR can be observed [Neuhauss et al., 1999] [Qian et al., 2005].

Following a study in 2012 [Ahrens et al., 2012], it was shown that the inferior olive and the cerebellum contained many neurons correlating with the motor adaptation in the optomotor response. Furthermore, lesioning the inferior olive post-training eliminated the motor adaptation [Ahrens et al., 2012].

IV.5 Two-photon calcium imaging

To record neural activities in the brain of the zebrafish larva, we use two-photon imaging of calcium activity in the optic tectum. In this section, we will discuss calcium imaging in neurons [Grienberger and Konnerth, 2012] and two-photon imaging very briefly [Murphy and Davidson, 2013]. And, in the next section, we will discuss the visual system of the larva.

Calcium ions are found in almost every cell type in biological organisms [Berridge et al., 2000] and regulate a number of functions [Dulhunty, 2006] [Lu and Means, 1993] [Orrenius et al., 2003]. In neurons, calcium acts on a wide range of timescales [Berridge et al., 2003]. On the microsecond level, following an action potential, an influx of extracellular calcium ions into a cell through its voltage-gated calcium channels triggers the release of neurotransmitter molecules [Neher and Sakaba, 2008]. On the second to hour level, calcium ions are involved in synaptic plasticity in dendritic spines

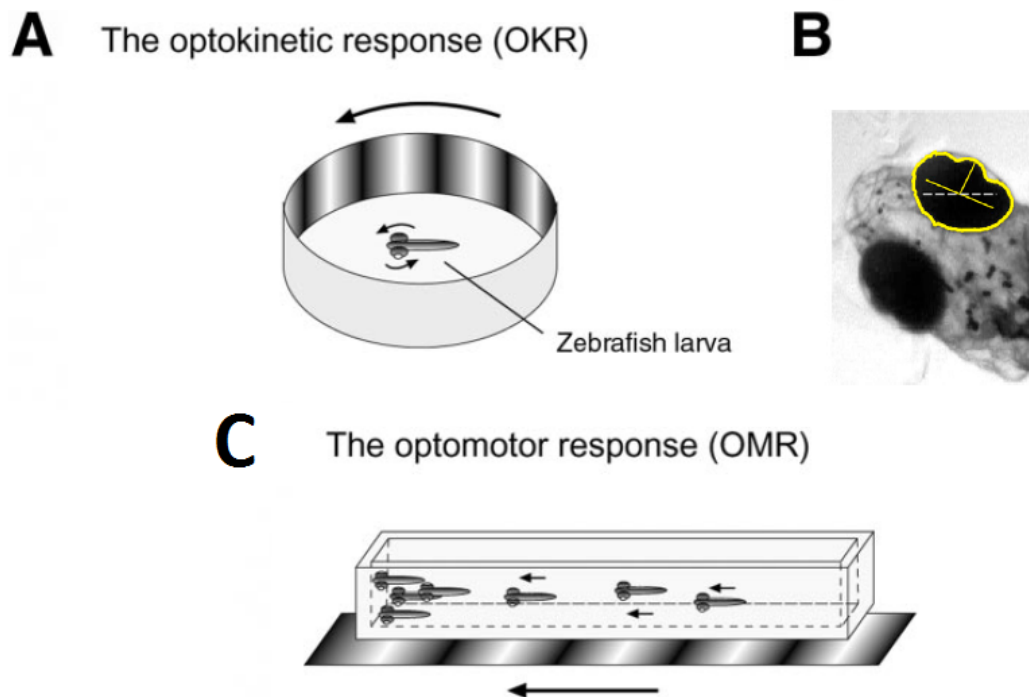


Figure IV.8: **OKR** and **OMR** responses in larva zebrafish. A. OKR: immobilized fish respond with eye movements to a large coherent moving visual stimulus (rotating drum with a sinusoidal painted pattern). B. Detection of eye orientation: The orientation of the eye is calculated by fitting it with an ellipse and extracting the angle between the long axis of the ellipse with respect to the external horizontal axis. C. During the OMR, larvae swim to follow a moving stimulus displayed on the bottom of their tank. The direction of motion is indicated by arrows. Images A. and C. taken from [Roeser and Baier, 2003a].

[Zucker, 1999] and in gene transcription inside the nucleus [Lyons and West, 2011]. Therefore, to study these various processes, calcium imaging has been a useful tool. Calcium imaging involves the usage of a calcium sensor, and the appropriate imaging instrumentation. Historically, various calcium sensors such as bioluminescent calcium-binding photoproteins [Shimomura et al., 1962] and absorbance dyes that change their absorption spectrum as a function of bound calcium [Brown et al., 1975] have been used. Over the years, calcium indicators have been improved to accommodate a wide range of excitation spectra with large signal-to-noise ratios [Paredes et al., 2008].

Protein-based Genetically Encoded Calcium Indicators (GECIs) [Looger and Griesbeck, 2011] were first introduced by Miyawaki et al. [Miyawaki et al., 1997]. The GCaMP family of GECI's are popularly used for in-vivo calcium imaging today [Chalasanani et al., 2007] [Dombeck et al., 2010] [Fletcher et al., 2009] [Wang et al., 2003]. GCaMPs work by increase in emitted fluorescence of the enhanced green fluorescent protein (EGFP) due to a conformational change caused by calmodulin-calcium interactions in the presence of calcium (see figure IV.9) [Nakai et al., 2001] [Tian et al., 2009]. GCaMP3 and GCaMP5, developed by protein engineering, have a higher signal-to-noise ratio, dynamic range, and response kinetics as compared to GCaMP. GCaMP5 measures neuronal activity more reliably than GCaMP3 [Akerboom et al., 2012].

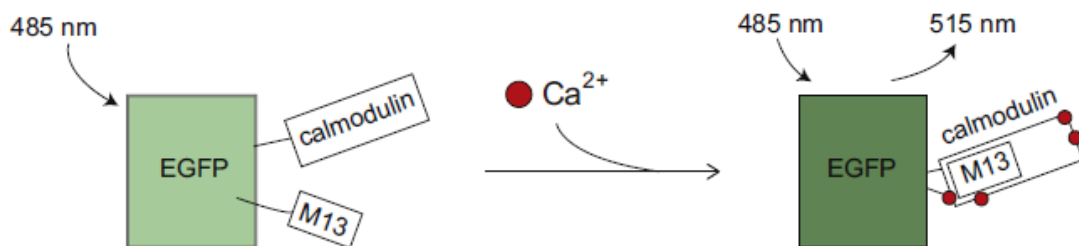


Figure IV.9: **A schematic of the operational mechanism of GCaMP.** GCaMP, a single-fluorophore GECI, emits increased fluorescence at 515 nm in the presence of calcium. Taken from [Grienberger and Konnerth, 2012].

Different methods of imaging the brain have been used: intrinsic imaging (measure of reflectance on brain) [Kalatsky and Stryker, 2003], voltage sensitive dye imaging [Grinvald and Hildesheim, 2004], confocal imaging [Eilers et al., 1995], two-photon imaging [Denk et al., 1990] and SPIM [Panier et al., 2013] [Ahrens et al., 2013]. Fluorescence microscopy is used to image molecules in cells and tissues with great specificity and sensitivity. The limitations of the fluorescence imaging techniques are the absorption and scattering of the beam used to image the specimen, photobleaching of a protein (the photochemical alteration of a molecule such that it is unable to fluoresce anymore) and phototoxicity of cells (cells get damaged due to both the low- and high-wavelength light that is used to excite fluorophores). To avoid photobleaching and phototoxicity, one can use lower intensity of the input beam. However, due to scattering and absorption, the number of photons reaching the detector is reduced. In biological tissues, the scattering length is much smaller when compared to the absorption length; hence scattering is the main source of photon loss. Cell bodies and the

components of the cell are larger than the wavelength of visible light and this is the reason for large scattering of light in biological media. This phenomena is called Mie scattering and it increases exponentially with the thickness of the sample. For this reason, confocal microscopy with visible light requires the sample to be of a thickness $10 - 50\mu\text{m}$. To solve these problems, we can use two-photon microscopy with near-IR illumination and pulsed laser light (see figure IV.10). This can be used to image neural tissues of a thickness of over 1 mm. Neural tissue is relatively transparent to near IR light [Oheim et al., 2001] such that only half of the incident photons are scattered for every $50 - 100\mu\text{m}$ of tissue thickness [Helmchen and Denk, 2005].

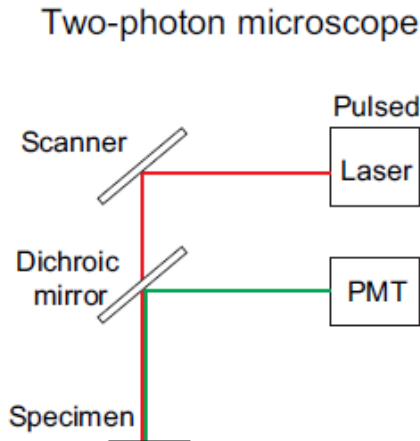


Figure IV.10: **2-Photon microscopy.** Two-photon microscopy setup: a pulsed near-IR laser is scanned over the tissue. The fluorescence emitted by the tissue is detected by a photomultiplier tube (PMT). Taken from [Grienberger and Konnerth, 2012].

The theory of two-photon absorption by atoms is rooted in quantum mechanics and was first described by Maria Goeppert-Mayer [Goeppert-Mayer, 1931]. In one-photon microscopy, a molecule such as GCaMP is excited and the GCaMP then emits a photon of a longer wavelength. The rate of excitation is, therefore, proportional to the intensity of the input beam. In a two-photon excitation, the molecular excitation needs two photons of twice the wavelength and half the frequency (hence, half the energy). The rate of excitation is, therefore, proportional to the square of the intensity of the input beam. The two-photon excitation is, therefore, a nonlinear process and doubling the intensity of the input beam increases the rate of excitation by four. In nature, the two-photon excitation happens at a rate of about 1 in ten million years while a one-photon excitation happens about 1 per second. To obtain two-photon excitation in the laboratory, we can use a pulsed laser as shown in figure IV.11. The pulsed laser has a pulse width τ of 100 fs and a pulse rate of 100 MHz ie. a pulse interval of $T = 1/R = 10$ ns. For a pulse power of $I_p = 1\text{W}$ at 920 nm, the mean intensity is given by

$$\langle I \rangle = \frac{\tau}{T} I_p = 10\text{mW} \quad (\text{IV.5.1})$$

Because of the high-pulse power, it is possible to make two-photon excitation even though the average power is only 10 mW. For a linear system, this does not make a difference but for a nonlinear system like I^2 , it gives us more absorption rate, and hence, fluorescence F as can be seen with the equations below:

$$F_{1p}(\text{1pulse}) \propto I_p \quad (\text{IV.5.2})$$

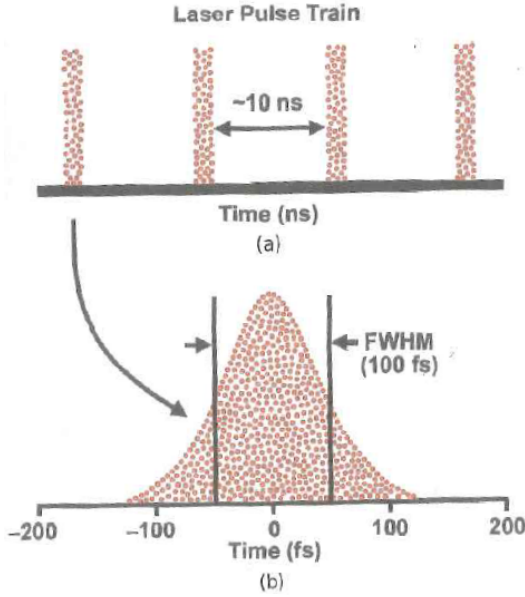


Figure IV.11: **Pulsed IR laser used for two-photon imaging.** A pulsed Titanium:sapphire laser with a) a pulse interval of ~ 10 ns and b) pulse width of ~ 100 fs. Taken from [Murphy and Davidson, 2013].

$$\langle F_{1p} \rangle = \frac{\tau}{T} F_{1p}(1pulse) = \langle I \rangle \quad (\text{IV.5.3})$$

$$F_{2p}(1pulse) \propto I_p^2 \quad (\text{IV.5.4})$$

$$\langle F_{2p} \rangle = \frac{\tau}{T} F_{2p}(1pulse) \propto I_p \langle I \rangle \quad (\text{IV.5.5})$$

Thus, the pulsed laser excites the molecules using both 1-photon and 2-photon excitations. However, the mean fluorescence due to 2-photon is much higher than the one we obtain due to 1-photon excitation. If we use a laser of wavelengths corresponding exclusively to the two-photon excitation, we get only two-photon excitation. 700-1000 nm and femtosecond pulsed lasers are now being provided by Mai Tai, Spectra-Physics for this purpose.

For femtosecond pulses, due to the fundamental Heisenberg's uncertainty principle, we have $\Delta\nu\Delta t \approx 0.3$. Since Δt is small, we have $\Delta\nu \approx 10 - 15$ nm. Thus the pulse is polychromatic. Due to dispersion, longer wavelengths travel faster in materials (positive dispersion) and shorter wavelengths travel faster distances through air (negative dispersion). Therefore, a pair of prisms are used to compensate for the dispersion.

The major advantage of using 2-photon microscopy is that the excitation is localized to a tiny volume around the focal plane [Denk et al., 1990]. Due to this, it can be used for deep tissue imaging. This can be seen as follows: The intensity at any height at a distance z away from the focal plane is given by $I(z) = P/A(z)$ where P is the power of the incoming beam and $A(z)$ is the area of the beam at height z .

For 1-photon microscopy, $F_{1p}(z) \propto I(z)A(z) = P = \text{constant}$ with z , whereas for 2-photon microscopy, $F_{2p}(z) \propto I(z)^2 A(z) = P^2/A(z) \propto (P/z)^2$. Thus, as one moves away from the focal plane, the fluorescence decreases as the square of the distance z from the focal plane. This localizes the fluorescence to the focal plane (see figure IV.12)

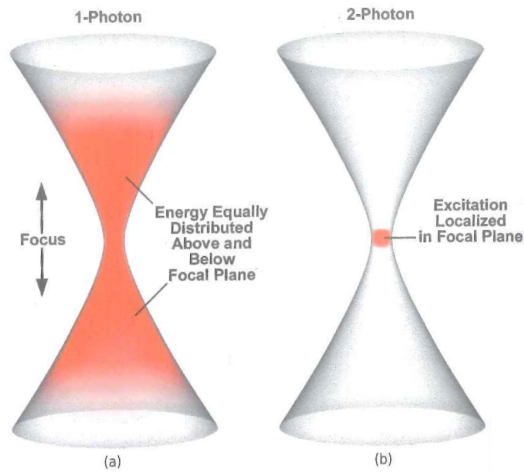


Figure IV.12: **Localization of excitation in two-photon imaging.** a) In one-photon imaging, the fluorescence occupies all the planes whereas in two-photon imaging (b), the fluorescence is constricted to a small volume around the focal plane. Taken from [Murphy and Davidson, 2013].

Therefore, two-photon microscopy enables us to monitor cell activities from the focal plane and also avoid phototoxicity and photobleaching. Though 3 photon could be a better means, there are no commercial laser sources available at 3 photon wavelengths.

IV.6 Visual system of zebrafish

In this section, we will discuss, in brief, the neuroanatomy of the visual center of the larva zebrafish and explain why we are interested in looking at the neuronal activity in the optic tectum during MAE. The zebrafish, being a teleost, has a brain organization similar to that of vertebrates [Friedrich et al., 2010b]. However, owing to the evolutionary pressure of extrauterine development, visual regions of the zebrafish larva such as the Optic Tectum (OT) and the retina are relatively enlarged.

The zebrafish retina consists of three nuclear layers, separated by two plexiform (synaptic) layers. Zebrafish are tetrachromats because the outer retina consists of four types of cone cells, including UV- sensitive cones apart from rod cells. These photoreceptors synapse onto the bipolar, horizontal, and amacrine interneurons of the inner layer in the outerplexiform layer. These cells, in turn, are synaptically connected to the ganglion cells in the outer plexiform layer. The axons of the RGCs, which form the optic nerve, project to 10 arborization fields (AF) of the larva's brain.

All but the first AF are contralateral. AF1, present in the hypothalamus, also received ipsilateral projections [Burrill and SS Easter, 1994]. In terms of their function, different AFs seem to be implied in generating behavioural responses to specialized external stimuli. AF-6 and AF-8, for instance, respond robustly to looming stimuli (an approaching predator or an obstacle) [Temizer et al., 2015]. AF-7 responds to the optimal prey stimulus (3 angular degrees or 3°) and ablation of AF-7 has been shown to reduce prey-capture behaviour [Temizer et al., 2014].

The 10th arborization field (AF-10) receives about 95% of the projections from RGC's. This region is the most complex layered brain structure in the fish and is called the Optic Tectum (OT) (see figure IV.13). The optic tectum is the homologous structure of the superior colliculus in mammals, which plays a prominent role in the

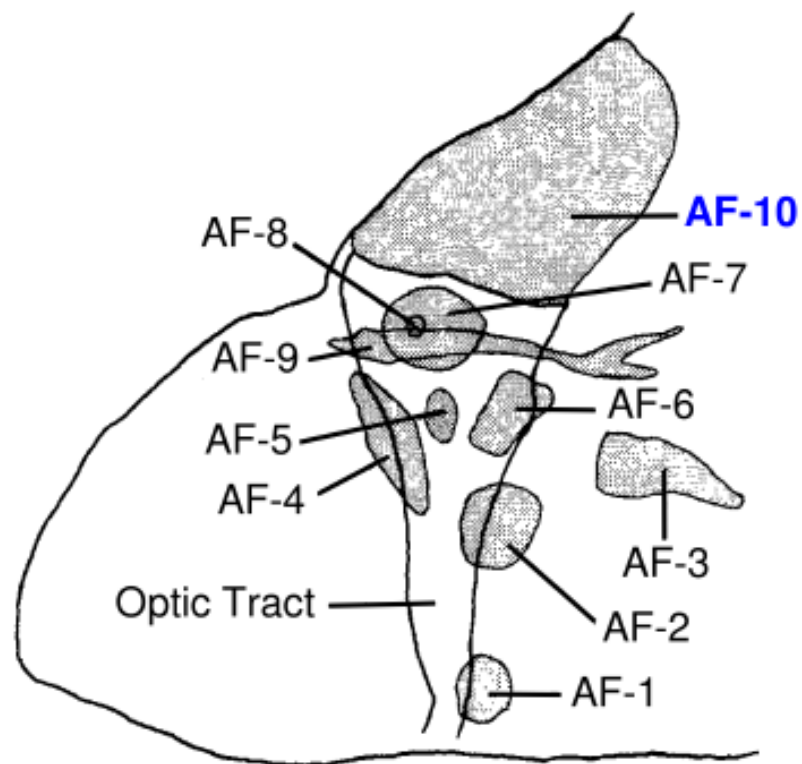


Figure IV.13: **Projections of the RGCs to the 10 arborization fields in a 6-7 day post fertilization larva.** A schematic diagram of the retinofugal Arborization fields (AFs) in a 6-7 dpf larva. The Optic Tectum (AF10) receives about 95 % of the projections. AF-7 and AF-9 correspond to the pretectum. Taken from [Burrill and SS Easter, 1994].

control of eye and head orienting movements. The zebrafish optic tectum is innervated by multiple RGC types [Robles et al., 2013] and is innervated by all sensory organs, either directly or indirectly. Each tectal hemisphere projects directly to the opposite tectal hemisphere and indirectly through the nucleus isthmi [Meek, 1983], to the hind brain motor centers [Sato et al., 2007], and indirectly to the spinal cord [Gahtan et al., 2005]. The tectal neurons form a retinotopic map of the contralateral visual field as evidenced by the RGC projections [Romano et al., 2015]. The dorso-ventral axis maps the contralateral dorsal and ventral visual hemifields whereas the rostro-caudal tectal axis maps the nasal and temporal hemifields. The neurons in the OT are mainly gabaergic interneurons, apart from glutamatergic and cholinergic neurons [Nevin et al., 2010].

Several functional roles have been attributed to the zebrafish OT. It is known to filter visual inputs sizes to capture prey [Del Bene et al., 2010] [Preuss et al., 2014] and is essential for visually guided prey capture [Gahtan et al., 2005]. It is involved in generating escape responses to looming stimuli [Temizer et al., 2015]. It is also involved in computing direction and orientation of inputs [Hunter et al., 2013]. Tectal cells show direction-selectivity as early as 12 hours post onset of visually evoked responses (78 hours post fertilization) [Niell and Smith, 2005] [Ramdya and Engert, 2008]. Studies show that the mechanism behind direction selectivity arises from both direction selective (DS) excitatory inputs and inhibitory inputs selective to the null directions [Ramdya and Engert, 2012] [Gabriel et al., 2012] [Hunter et al., 2013].

IV.7 MAE in the zebrafish larva

In this section, we outline the MAE in the zebrafish larva very briefly. A detailed version can be found in the next chapter, where we include the article about MAE and its neuronal correlates in the zebrafish larva.

Taking advantage of the optokinetic response, we showed that the zebrafish larva does perceive the MAE. In the absence of any moving stimuli, the zebrafish larva generates stereotypical saccade movements (duration ≈ 0.1 s) followed by either a fixation period or centripetal drifts (duration 20 ± 10 s) and a second saccade in the opposite direction. We, then, showed to the larva large-field coherent moving stimuli (a black and white grid, conditioning stimulus) at three different speeds (17, 26 and 59 degrees/s) and for different durations of 50, 100, 200, 250, 400 and 500 seconds. In the presence of the conditioning stimulus (CS), the larva exhibits the optokinetic response (OKR). Following the end of the conditioning stimulus, they presented either of the three stationary patterns: 1) the same grating used for the adapting stimulus, 2) stationary noise with the same average luminosity as for the conditioning stimulus, 3) a black screen. In contrast to the stereotypic spontaneous eye movements observed in the absence of a moving stimulus, following the end of the conditioning stimulus, and in the presence of either of the three stationary patterns, eye rotation movements corresponding to pursuits in the opposite direction of the conditioning stimulus were observed for ~ 250 seconds. After ~ 250 seconds, these pursuits decay and eye movements as observed for periods of spontaneous motor behavior begin to appear.

Moreover, we demonstrated via ablation studies that the optic tectum, the highest

visual center in the larva's brain, is involved in MAE. Upon single cell neuronal recording in the optic tectum of non-anesthetized and non-paralyzed larvae using 2Photon microscopy, we can identify three populations: non-direction-selective neurons, direction selective neurons in the direction of the CS, and direction-selective neurons in the opposite direction (MAE direction). During the CS period, we observe habituation in the direction selective neurons in the direction of CS and during the MAE period, we observe rhythmic synchronous activities mostly in the direction selective cells sensitive to the MAE direction. Furthermore, by correlating the population activity of the tectal direction-selective neurons with the eye-rotation kinematics, we find two classes of neurons: (1) direction-selective neurons that did not show spontaneous activity associated with optokinetic MAE-like behavior and (2) direction-selective neurons that showed correlated activity with optokinetic MAE-like behavior during the post-CS period (eyemotion-selective neurons).

MAE could be the result of the competition between two directional selective neuronal populations. During the presentation of the CS, the CS direction selective neurons are more active than those in the opposite direction. Due to CS-induced habituation, during the post-CS control period, CS direction-selective neurons are less spontaneously active than MAE direction-selective neurons. A comparison between these two populations could qualitatively explain the MAE-like effect that we observed. Therefore, the MAE-like behavior could emerge from a tectal sub-circuit that compares the activities of both direction-selective neuronal groups and generates adequate directional motor commands. These findings can be summarized with a model shown in figure IV.14. The model is based on a comparator tectal sub-circuit consisting of two cross-inhibiting neuronal populations: a CS comparator and a MAE comparator, each of them receiving excitatory inputs from the corresponding group of direction-selective neurons. These comparator populations represent the sub-groups of MAE direction-selective neurons displaying synchronous rhythmic activity associated with optokinetic MAE-like behavior. The comparator circuit computes the difference between the activities of the two groups of direction-selective neurons: each rhythmic stimulation produces a winner-takes-all dynamic in which one of the two comparator populations dominates the other in an input-dependent manner. In the model, the rhythmicity is implemented by a periodic input of similar magnitude on the two comparator populations. This periodic stimulus could originate from an intrinsic rhythmic tectal activity, a rhythmic tectal afferent, or a proprioceptive input associated with the eye saccades. We found that paralyzed larvae incapable of moving their eyes did not show, following the cessation of the CS, spontaneous rhythmic activity among MAE direction-selective neurons.

Using two-photon calcium imaging, it has been shown that the pretectum (AF-7 and AF-9) and the superficial layers of the optic tectum respond to large-field coherent visual motion presented to the contralateral eye [Portugues et al., 2014]. Similarly, unilateral stimulation of the pretectal area induced eye movements that resemble the optokinetic response (OKR; [Kubo et al., 2014]). As previously shown by the ablation of the RGC terminals in the optic tectum neuropil [Roeser and Baier, 2003a], ablation of a large portion of the tectal neurons did not abolish OKR, suggesting that the tectum does not play a major role in its generation. However, we show that the tectum seems to be necessary for the initial strong behavioral response to novel stimuli

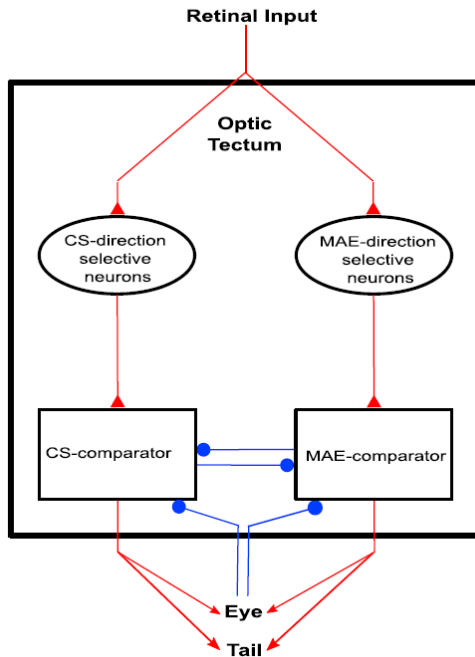


Figure IV.14: **An empirical model of MAE.** The model comprises four populations of neurons: CS direction-selective (CS-DS), MAE direction-selective (MAE-DS), and two comparator populations (CPs), one for each direction (CS-CP and MAE-CP). The DS populations receive retinal inputs, whereas the CPs' cells receive rhythmic input. The CPs receive excitatory input from the corresponding DS population and inhibitory input from the other DS population, and they cross-inhibit each other.

and for CS-induced behavioral habituation (decrease in the OKR gain). Similarly, the strong novelty response and habituation effect were present in the CS-induced neuronal responses in the optic tectum but absent in the retina. The lack of CS-induced behavioral habituation could explain the observed reduction of MAE in ablated larvae. We therefore suggest that MAE could emerge as a consequence of tectal adaptation to the CS.

IV.8 Laing Chow model

To model the MAE in the zebrafish, we take inspiration from the Laing and Chow model [Laing and Chow, 2002]. Laing and Chow developed a population rate model from a network of two populations of Hodgkin-Huxley type neurons with recurrent excitation, cross-inhibition, adaptation and synaptic depression to describe binocular rivalry. Binocular rivalry is the phenomenon of alternation in perception when the two eyes are presented with drastically different images. The subject, in this case, cannot fixate on both the images simultaneously but alternates between the two stimuli. The neurophysiological correlate of this alternation is the alternation between the activity of two populations of neurons, each coding for one image. The switching between the two populations is induced by a slow process such as spike frequency adaptation or synaptic depression [Abbott et al., 1997]. A calcium-dependent potassium current is used to model the spike frequency adaptation in the HH model [Huguenard and McCormick, 1992] [McCormick and Huguenard, 1992]. We will briefly present the population rate model and adapt it to our case of the phenomenon of motion after effect that we observe in the optic tectum. The equations used in their model are as follows:

$$\frac{du_1}{dt} = -u_1 + f(\alpha u_1 g_1 - \beta u_2 g_2 - a_1 + I_1), \quad (\text{IV.8.1})$$

$$\frac{du_2}{dt} = -u_2 + f(\alpha u_2 g_2 - \beta u_1 g_1 - a_2 + I_2), \quad (\text{IV.8.2})$$

$$\tau_a \frac{da_1}{dt} = -u_2 + \phi_a f(\alpha u_1 g_1 - \beta u_2 g_2 - a_1 + I_1), \quad (\text{IV.8.3})$$

$$\tau_a \frac{da_2}{dt} = -u_1 + \phi_a f(\alpha u_2 g_2 - \beta u_1 g_1 - a_2 + I_2), \quad (\text{IV.8.4})$$

$$\tau_d \frac{dg_1}{dt} = 1 - g_1 - g_1 \phi_d f(\alpha u_1 g_1 - \beta u_2 g_2 - a_1 + I_1), \quad (\text{IV.8.5})$$

$$\tau_d \frac{dg_2}{dt} = 1 - g_2 - g_2 \phi_d f(\alpha u_2 g_2 - \beta u_1 g_1 - a_2 + I_2), \quad (\text{IV.8.6})$$

where u_i represents the net excitatory activity of each population, a_i and g_i are the population adaptation and synaptic depression variables, respectively. The gain function f is taken to be the Heaviside step function i.e., $f(x) = 1$ for $x \geq 0$ and $f(x) = 0$ for $x < 0$. The time constants of adaptation and synaptic depression i.e. τ_a and τ_d are both assumed to be much larger than 1.

To simplify the dynamics of the above equations, we can separate the time-scales between the population activities that are the fast variables and the slow variables. The system either oscillates or goes to a steady state depending on the parameters. The different possible steady states of the system are

- a) when either both activities are zero (both off) or
- b) when either both activities are at 1 (both on), or
- c) one at 1 and the other at zero (one on) and vice versa.

To find the stability of these steady states, we can perturb the system and look at the resulting dynamics.

a) When only adaptation variables are active (i.e., $g_1 = g_2 = 1$), the both-off steady state i.e. $(u_1, u_2, a_1, a_2) = (0, 0, 0, 0)$ is steady when the total current entering through the gain function is below threshold, i.e., $I_1 < 0$ and $I_2 < 0$.

b) The both-on steady state i.e. $(u_1, u_2, a_1, a_2) = (1, 1, \phi_a, \phi_a)$ is steady when the input current is greater than threshold i.e. $\alpha - \beta - \phi_a + I_1 > 0$ and $\alpha - \beta - \phi_a + I_2 > 0$ i.e. strong inputs or strong excitation is required for the both-on state.

c) The one-on case, say, $(u_1, u_2, a_1, a_2) = (1, 0, \phi_a, 0)$ requires $\alpha - \phi_a + I_1 > 0$ and $-\beta + I_2 < 0$ i.e. it needs strong excitation and inhibition compared to the inputs.

When none of the fixed-state conditions are satisfied, then the system oscillates as shown in figure IV.15 for parameter values of $\alpha = 0.2$, $\beta = 0.4$, $\phi_a = 0.4$, $\tau_a = 20$, $I_1 = 0.43$, $I_2 = 0.5$. In this case, when the adaptation of one population variable has sufficiently decreased compared to the other, it becomes active. This is the regime of bistability that Laing and Chow had wished to model [Laing and Chow, 2002]. We will consider ourselves in this regime and model the MAE in the zebrafish using this model. We will, therefore, consider two cross-inhibiting populations with adaptation variables to model the comparator populations. We set the synaptic depression variables to 1 so that they don't play a role. These cross inhibiting populations receive a rhythmic input and the winner of the two populations determines the next movement of the

eye. We add two directional selective populations which receive input from the retina and excite the corresponding comparator populations. The details of the model are presented in the next section.

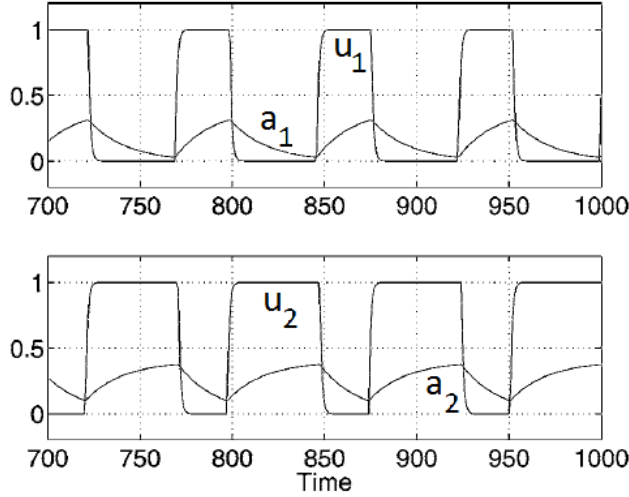


Figure IV.15: **Alternation of the two populations in the Laing-Chow model.** Solution of the reduced model with only adaptation variables. u_1 and a_1 are shown in the top plot and u_2 and a_2 are shown in the bottom plot for parameter values specified in the text. Image taken from [Laing and Chow, 2002].

IV.9 MAE model in the zebrafish tectum

The model schematically described in Figure IV.14 is mathematically implemented in this section using a rate model description for the different neuronal populations, as described below. The rate model for the two populations ($j = 1, 2$) of direction selective cells is defined by

$$\tau \frac{dv_j}{dt} = -v_j + f[I_j - a_{f,j} - a_{s,j}] \quad (\text{IV.9.1})$$

$$\tau_f \frac{da_{f,j}}{dt} = -a_{f,j} + \phi_f v_j, \quad (\text{IV.9.2})$$

$$\tau_s \frac{da_{s,j}}{dt} = -a_{s,j} + \phi_s v_j, \quad (\text{IV.9.3})$$

where, for simplicity, the f-I curve f is taken to be a saturating threshold linear function with $f(v) = 0, v < 0$, $f(v) = v, v \geq 0$ and $f(v) = v_m, v \geq v_m$. The variables v_j represents the mean discharge rates of the population 1 and 2, population 1 being assumed to be selective for the conditioning stimulus direction. The variables $a_{f,j}$ and $a_{s,j}$ represents slow habituation currents intrinsic to the cell population j . Two habituation time scales τ_f and τ_s are introduced to represent the double exponential decay of the DS cells observed in the experiments and τ is the membrane time constant of

the DS cell population. The variables ϕ_f and ϕ_s model the dynamics of the habitation currents induced for a given firing rate of the DS cell population. The current I_j models the retinal inputs with $I_j = I_{sp}$, the input current during sponatenous activity in absence of CS. During the CS, of duration T_{cs} , the current is increased to I_{cs} on the CS-selective population, i.e. $I_1 = I_{cs}$.

IV.9.1 Comparator cells

The two comparator cell populations are modelled in a similar manner. The variables u_j represent the mean firing rate of the j^{th} comparator cell population. We assume that each comparator cell population receives inputs from one of the two direction selective cells population with a coupling strength J_d and that the two comparator cell populations cross-inhibit each other with the inhibiting strength J_c . In addition, we suppose that they are endowed with an adaptation current b_j ($j=1,2$), similar to the direction selective cell population, which for simplicity we describe with a single exponential relaxation,

$$\tau \frac{du_1}{dt} = -u_1 + f[I_1^{(r)} - b_1 - J_c u_2 + J_d v_1], \quad (\text{IV.9.4})$$

$$\tau_b \frac{db_1}{dt} = -b_1 + \phi_b u_1, \quad (\text{IV.9.5})$$

$$\tau \frac{du_2}{dt} = -u_2 + f[I_2^{(r)} - b_2 - J_c u_1 + J_d v_2], \quad (\text{IV.9.6})$$

$$\tau_b \frac{db_2}{dt} = -b_2 + \phi_b u_2, \quad (\text{IV.9.7})$$

The variable ϕ_b models the dynamics of the habitation currents induced for a given comparator cell firing rate. We assume that the interaction, not modelled here, of these comparator neurons with neuronal populations outside the tectum (e.g. proprioceptive inputs) leads to the generation of the rhythmic depolarizing current $I_j^{(r)}$ in the comparator cells. In the performed simulation this rhythmic current was assumed to be periodic with a period T^r with during each period an ON-time with a value $I_{on,j}^{(r)}$ during a time T_{on}^r and a value $I_{off,j}^{(r)}$ during the complementary OFF-time T_{off}^r (i.e. $T^r = T_{on}^r + T_{off}^r$). In order to account for the imperfect alternation of the spontaneous activity, the ON-current was taken to take on average the same value $I_{on}^{(r)}$ on each comparator cell population but to fluctuate around this mean independently on the two populations and from period to period,

$$I_{on,j}^{(r)} = I_{on}^{(r)} + \xi_{j,p}. \quad (\text{IV.9.8})$$

These fluctuations are represented by $\xi_{j,p}$, a random gaussian current $\xi_{j,p}$ of standard deviation σ , $\langle \xi_{j,p} \xi_{j',p'} \rangle = \sigma^2 \delta_{j,j'} \delta_{p,p'}$, with j the population index and p the period index ($\delta_{a,b}$ denotes the kronecker δ -function, $\delta_{a,b} = 1$ if a is identical to b , $\delta_{a,b} = 0$ otherwise).

IV.10 Conclusion

In this chapter, we looked at the phenomenon of adaptation in sensory systems. We described the phenomenon of adaptation and used the zebrafish larva as an experimen-

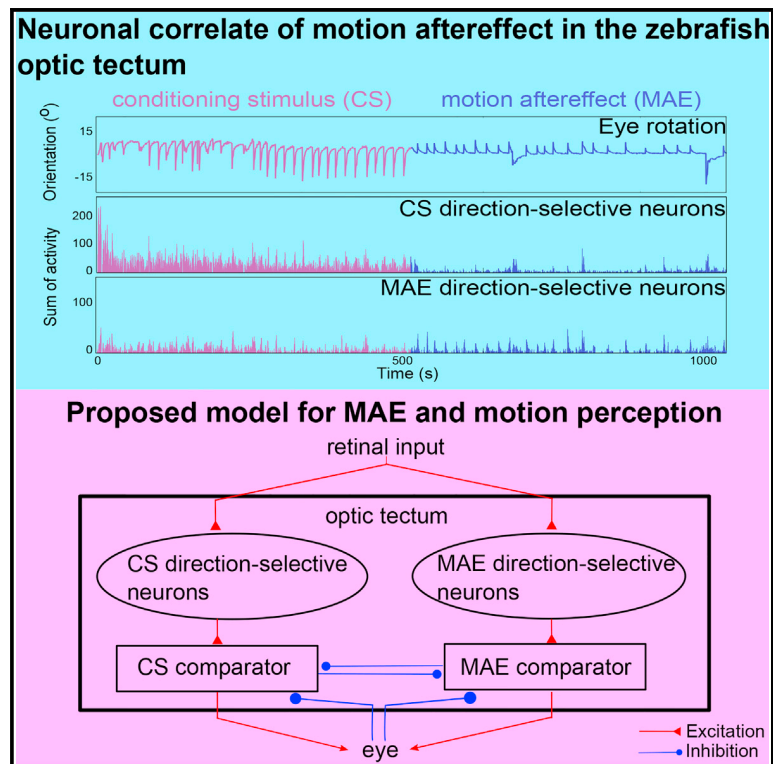
tal model to study the illusion of motion after effect, which is a result of adaptation. We recorded behavioural and neuronal activity in the highest visual center of the larva, the optic tectum and used rate models to model this phenomenon. The next chapter includes the manuscript which describes all the methods in detail.

Chapter V

Sustained Rhythmic Brain Activity Underlies Visual Motion Perception in Zebrafish

Sustained Rhythmic Brain Activity Underlies Visual Motion Perception in Zebrafish

Graphical Abstract



Authors

Verónica Pérez-Schuster, Anirudh Kulkarni, Morgane Nouvian, ..., Jonathan Boulanger-Weill, Vincent Hakim, Germán Sumbre

Correspondence

sumbre@biologie.ens.fr

In Brief

Pérez-Schuster et al. use two-photon functional imaging to follow behaving GCaMP zebrafish larvae while perceiving the motion aftereffect. Analysis of the in vivo dynamics of large neuronal populations and development of empirical models shed light on the circuit processes that govern visual motion perception.

Highlights

- Zebrafish larvae perceive the motion aftereffect (MAE)
- Ablation studies demonstrate that the optic tectum is involved in MAE
- Specific habituation of tectal direction-selective (DS) neurons is associated with MAE
- An empirical competition model of opposite DS neuronal populations reproduces MAE



Sustained Rhythmic Brain Activity Underlies Visual Motion Perception in Zebrafish

Verónica Pérez-Schuster,^{1,4,5} Anirudh Kulkarni,² Morgane Nouvian,¹ Sebastián A. Romano,^{1,3} Konstantinos Lygdas,¹ Adrien Jouary,¹ Mario Dippopa,¹ Thomas Pietri,¹ Mathieu Haudrechy,¹ Virginie Candat,¹ Jonathan Boulanger-Weill,¹ Vincent Hakim,² and Germán Sumbre^{1,6,*}

¹Ecole Normale Supérieure, PSL Research University, CNRS, Inserm, Institut de Biologie de l'ENS, IBENS, 75005 Paris, France

²Laboratoire de Physique Statistique, Ecole Normale Supérieure, PSL Research University, Université Pierre et Marie Curie, CNRS, 75005 Paris, France

³Present address: Instituto de Investigación en Biomedicina de Buenos Aires, CONICET, Partner Institute of the Max Planck Society, C1425FQD Buenos Aires, Argentina

⁴Present address: Laboratorio de Neurobiología de la Memoria, Departamento Fisiología, Biología Molecular y Celular, FCEyN, UBA and IFIBYNE-CONICET, Ciudad Universitaria, C1428EHA Buenos Aires, Argentina

⁵Present address: Departamento de Física, FCEyN, UBA and IFIBA-CONICET, Pabellón 1, Ciudad Universitaria, C1428EHA Buenos Aires, Argentina

⁶Lead Contact

*Correspondence: sumbre@biologie.ens.fr
<http://dx.doi.org/10.1016/j.celrep.2016.09.065>

SUMMARY

Following moving visual stimuli (conditioning stimuli, CS), many organisms perceive, in the absence of physical stimuli, illusory motion in the opposite direction. This phenomenon is known as the motion aftereffect (MAE). Here, we use MAE as a tool to study the neuronal basis of visual motion perception in zebrafish larvae. Using zebrafish eye movements as an indicator of visual motion perception, we find that larvae perceive MAE. Blocking eye movements using optogenetics during CS presentation did not affect MAE, but tectal ablation significantly weakened it. Using two-photon calcium imaging of behaving GCaMP3 larvae, we find post-stimulation sustained rhythmic activity among direction-selective tectal neurons associated with the perception of MAE. In addition, tectal neurons tuned to the CS direction habituated, but neurons in the retina did not. Finally, a model based on competition between direction-selective neurons reproduced MAE, suggesting a neuronal circuit capable of generating perception of visual motion.

INTRODUCTION

Visual aftereffects are often considered the by-products of neuronal adaptation processes for the optimization of sensory perception. Typical examples are calibration between movement perception and self-produced locomotion, decorrelation to increase efficiency of sensory coding, and gain control of sensory stimuli to extend the dynamic range of detection (Thompson and Burr, 2009). Therefore, they are useful tools to study the neuronal mechanisms underlying visual perception.

A particular example of visual aftereffects is the motion aftereffect (MAE), in which exposure to continuous, coherent, moving visual stimuli induces, following the cessation of the moving stimulus, the illusory perception of motion in the opposite direction. MAE was first described in ~330 BC by Aristotle in his book *Parva Naturalia* (trans. Biehl, 1898). Since then, many studies have described different psychophysical aspects of the phenomenon (Chaudhuri, 1990; Masland, 1969; Mather et al., 1998; Wohlgenuth, 1911). In addition to perceptual MAE, continuous, coherent, moving visual stimuli can induce oculomotor MAE (Braun et al., 2006; Chen et al., 2014; Watamaniuk and Heinen, 2007). Despite the vast literature on MAE, only a handful of studies have examined the underlying neuronal mechanisms. MAE was found to be associated with either a decrease or an increase in the response of direction-selective neurons. Direction-selective neurons are specialized for detecting motion along specific axes of the visual field, and they respond to visual stimulus moving in a given direction (the preferred direction) but do not respond or respond less to those moving in the opposite direction (the null direction). Using single-neuron recordings, MAE-associated adaptations have been described in different brain regions of different animal species: the rabbit's retina (Barlow and Hill, 1963), the owl monkey's medial temporal lobe (Petersen et al., 1985), the cat's primary visual cortex (Giaschi et al., 1993), the pigeon's nucleus lentiformis mesencephali (Niu et al., 2006), and the fly's lobula plate (Srinivasan, 1993).

Despite these advances, we lack a comprehensive explanation of the underlying mechanisms and the neuronal correlates of MAE at the circuit level. To that end, and to shed light on the potential mechanisms underlying visual motion perception, we used transgenic zebrafish larvae expressing the genetically encoded calcium indicator GCaMP3. We monitored the dynamics of large neuronal circuits from different brain regions using two-photon microscopy in an intact, non-anesthetized, behaving vertebrate model.

In zebrafish, the retinal ganglion cells (RGCs) project to at least ten arborization fields, with the optic tectum (OT) being the largest (Burrill and Easter, 1994; Nevin et al., 2010). The optic tectum is the zebrafish's most complex layered brain structure, and it is essential for visually guided prey detection and capture (Gahtan et al., 2005; Romano et al., 2015). Direction-selective neurons are found in both the retina (Nikolaou et al., 2012) and the optic tectum (Gabriel et al., 2012; Gebhardt et al., 2013; Grama and Engert, 2012; Hunter et al., 2013; Romano et al., 2015).

Using two-photon calcium imaging, it has been shown that the pretectum and the superficial layers of the optic tectum respond to large-field coherent visual motion presented to the contralateral eye (Portugues et al., 2014). Similarly, unilateral stimulation of the pretectal area induced eye movements resembling the optokinetic response (OKR; Kubo et al., 2014).

Here, we show that following the presentation of a coherently moving visual pattern (conditioning stimulus, CS) capable of inducing OKR, zebrafish larvae generated, in the absence of sensory stimuli, optokinetic movements in the direction opposite that induced by the CS. Reminiscent of MAE, these results suggest that following the CS, the larvae experienced perception of visual motion in the opposite direction. Using optogenetics to transiently block eye movements during the presentation of the CS, we show that neither muscular fatigue nor eye proprioception feedback plays a role in the generation of optokinetic MAE-like behavior. Moreover, two-photon laser ablation of the optic tectum significantly reduced MAE-like behavior. Using two-photon calcium imaging of transgenic zebrafish larva expressing GCaMP3, we monitored the neuronal activities of the larva's two main visual centers (retina and optic tectum). We found that following stimulus cessation, direction-selective neurons tuned to the direction of the CS displayed strong habituation in the optic tectum but not in the retina. Furthermore, we observed sustained rhythmic neuronal activity associated with the optokinetic MAE-like behavior among a specific group of direction-selective tectal neurons, thus arguing for a neuronal correlate of the MAE-like behavior. Finally, an empirical mathematical model based on the competition between direction-selective tectal neurons related to their activity could reproduce the OKR, the optokinetic MAE-like behavior, and the unconditioned spontaneous eye movements observed in the absence of moving visual stimulation. Overall, our results propose a functional neuronal circuit in the zebrafish optic tectum that is capable of generating perception of visual motion.

RESULTS

The Zebrafish Larva Shows MAE-like Behavior

To test whether the zebrafish larva is capable of perceiving MAE, we took advantage of the larva's OKR. OKR is a serial combination of smooth pursuits and rapid saccade eye movements generated upon the presentation of a moving visual stimulus. During OKR, the smooth pursuits follow the stimulus direction to stabilize the moving external world on the retina, while the saccades reset the eye's position (Huang and Neuhauss, 2008). This pursuit-saccade eye-movement pattern repetitively persists throughout the period of stimulation (Figure 1D). In the absence

of large-field coherent visual motion, the larva performs spontaneous eye rotations composed of a rapid saccade followed by an eye fixation period and a second saccade in the opposite direction (Easter and Nicola, 1997; Miri et al., 2011). Therefore, it is possible to infer whether the larva is perceiving motion and in which direction by looking at the eye-rotation kinematics (Orger et al., 2000, 2008; Orger and Baier, 2005; Qian et al., 2005; Rinner et al., 2005; Roeser and Baier, 2003). To test the hypothesis that zebrafish larvae can experience MAE, we embedded zebrafish larvae in low-melting agarose. When the agarose jellified, we transferred the larvae to an elevated stage within the center of a circular chamber. The chamber was then filled with fish embryo medium and the agarose around the eyes was removed to allow movement. Under these conditions, we monitored the eye movements of 7–9 days post-fertilization (DPF) larvae (Figures 1A and 1B) while projecting on a screen around the larva static, large-field, black-and-white, square-wave gratings for a period of 500 s (pre-CS control period). Then, we presented the CS (unidirectionally drifting square-wave grating) at different speeds ($17^\circ/\text{s}$, $26^\circ/\text{s}$, or $59^\circ/\text{s}$) and for different durations (50, 100, 200, 250, 400, or 500 s), and in both directions (toward the left or right). Following the cessation of the CS, the moving grating was stopped and kept stationary for a duration of 500 s (post-CS control). For clarity, we defined the CS direction as the direction of the CS despite its direction (leftward or rightward) and the MAE direction as the opposite one (the direction expected if MAE was generated).

During the pre-CS-control period, zebrafish larvae generated spontaneous eye movements (average duration of saccades, 0.12 ± 0.04 s; average duration of fixations, 20 ± 10 s). In some cases, the eye fixations slowly drifted in a centripetal direction (Figure 1C). In contrast to this stereotypic spontaneous eye behavior, the presentation of a coherent motion stimulus (the CS) induced a robust OKR (Figure 1D). Following the cessation of the CS (post-CS control period), we observed repetitive, unidirectional eye-rotation pursuit-saccade-like movements in the direction opposite that induced by the CS (MAE direction; violet curve in Figure 1D; Movie S1). Similar eye-pursuit movements have been observed in humans during MAE (Braun et al., 2006). We thus interpret these pursuit-saccade movements as an indication that the larva was experiencing visual movement in the opposite direction of the CS, reminiscent of MAE, and called these conditioned eye rotations optokinetic MAE-like behavior. Like humans, who perceive MAE with lower velocity and smaller displacement than the CS (Masland, 1969; Wohlgenuth, 1911), the zebrafish larva optokinetic MAE-like behavior was composed of eye pursuits of lower rotation speeds and smaller amplitudes than those observed during the CS (Figure 1D; Supplemental Experimental Procedures). To quantify the optokinetic MAE-like behavior, we defined the MAE index (Figures 1E and 1F; Supplemental Experimental Procedures). This index represents the ratio of the difference between the average number of pursuits in the CS and MAE directions and the total average number of eye movements. The MAE index will be equal to 1 if only pursuits in the MAE direction are observed. It will be equal to -1 if only pursuits in the CS direction are registered and around 0 for spontaneous eye movements (scanning eye movements or an equal number of pursuits in

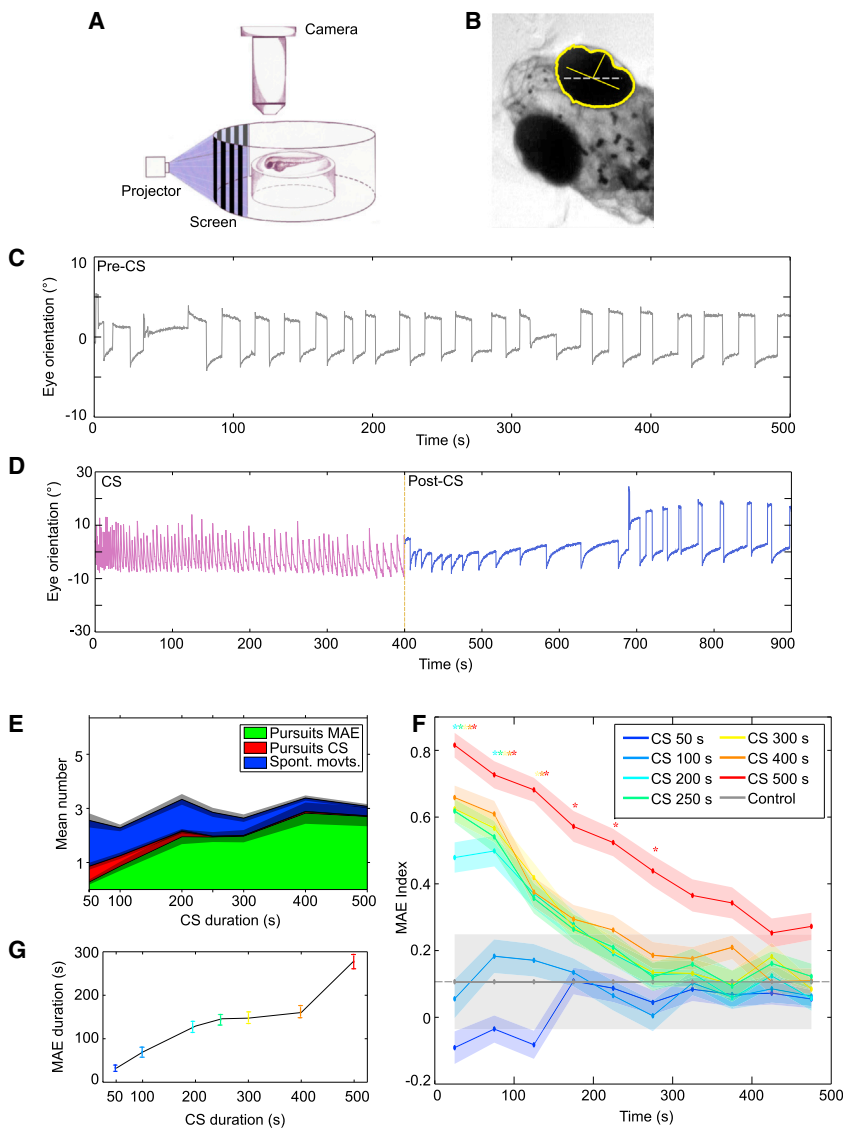


Figure 1. Zebrafish Larvae Perceive the MAE

(A) Experimental setup. Stimuli were projected on a screen around the larva immobilized in agarose. The agarose was then removed around the eyes, and their rotations were recorded from above using an objective, a tube lens, and a video camera.

(B) Detection of eye orientation. The original image was thresholded and converted to binary to detect the eyes. Yellow, the eye outline and the long and short axes of the fitted ellipse; gray dashed line, external axis. The orientation of the eyes was calculated with respect to the external horizontal axis.

(C) Stereotypic spontaneous eye rotations in the absence of visual stimuli. Saccades in one direction are followed by a fixation period and a saccade in the opposite direction.

(D) Eye rotations during CS and during the post-CS control period. Note the pursuit movements induced by the CS (magenta) and the pursuits in the opposite direction during the post-CS control period (blue), reminiscent of optokinetic MAE-like behavior. The latter gradually decreased in frequency until the stereotypical spontaneous eye movements were restored around 250 s. Mean eye velocity during the last 200 s of CS was $1.50^{\circ}/s \pm 0.03^{\circ}/s$, and eye velocity during optokinetic MAE-like behavior was $0.8^{\circ}/s \pm 0.03^{\circ}/s$ ($p = 1.6 \times 10^{-54}$, Wilcoxon rank sum test). Eye amplitude during CS was $13.7^{\circ} \pm 0.2^{\circ}$, and eye amplitude during optokinetic MAE-like behavior was $7.0^{\circ} \pm 0.1^{\circ}$ ($p = 1.03 \times 10^{-4}$, Wilcoxon rank sum test; $n = 40$ trials from 11 larvae for CS durations 500 s).

(E) Ratio of the different types of movements during the first 50 s of the post-CS control period as a function of the CS duration ($n = 36, 36, 39, 34, 36, 34,$ and 40 trials from 10, 9, 10, 10, 10, 9, and 11 larvae for CS durations of 50, 100, 200, 250, 300, 400, and 500 s, respectively). In all cases, the CS velocity was $26^{\circ}/s$. Green, pursuits in the MAE direction; red, pursuits in the CS direction; blue, spontaneous eye movements; gray shade, SE.

(F) Mean MAE index as a function of time during the post-CS control period. The curves are color coded according to the CS durations (top right legend). The gray dash line represents the control index. The asterisk indicates significantly different from control ($p < 0.01$, Kruskal-Wallis), color coded according to the corresponding colors. Error bars, SE.

(G) The average duration of optokinetic MAE-like behavior as a function of CS duration. The colors depict the duration of the CS as in (F). For (F) and (G), $n = 120, 104, 117, 110, 114, 112,$ and 97 trials from 20, 19, 20, 19, 19, 19, and 17 larvae for CS durations of 50, 100, 200, 250, 300, 400, and 500 s, respectively. Control is $n = 14$ trials from 14 larvae. Error bars, SE.

the CS and MAE directions). The MAE index was computed during the post-CS control for consecutive periods of 50 s and for a total of 500 s. For statistical purposes, we defined the control index as the MAE index during the pre-CS control period.

By comparing the statistically significant difference between the MAE index and the control index for experiments in which we presented CS of different durations, we observed that the induction and duration of optokinetic MAE-like behavior depended on the CS duration (Figure 1F). For CS durations of 50 and 100 s, the MAE index was not significantly different from the control index ($p > 0.05$ for all intervals, Kruskal-Wallis). For CS lasting 200 and 250 s, we observed a significant difference for the first 100 s

of the post-CS control period. For CS lasting 300 and 400 s, we observed a significant difference for the first 150 s ($p < 0.05$, Kruskal-Wallis). For a CS of 500 s, the MAE index was significantly higher than the control index for the first 300 s following the end of the CS ($p < 0.01$, Kruskal-Wallis), and it was significantly higher than those induced by the CS of 200–400 s ($p < 0.01$, Kruskal-Wallis). Therefore, to induce the optokinetic MAE-like behavior, the larva needs to be stimulated with a CS of at least 100 s. The duration of the MAE-like behavior depended on the further increase in the CS duration (Figures 1F and 1G). The optokinetic MAE-like behavior was observed in 85% of the experiments in which we used a CS of 500 s

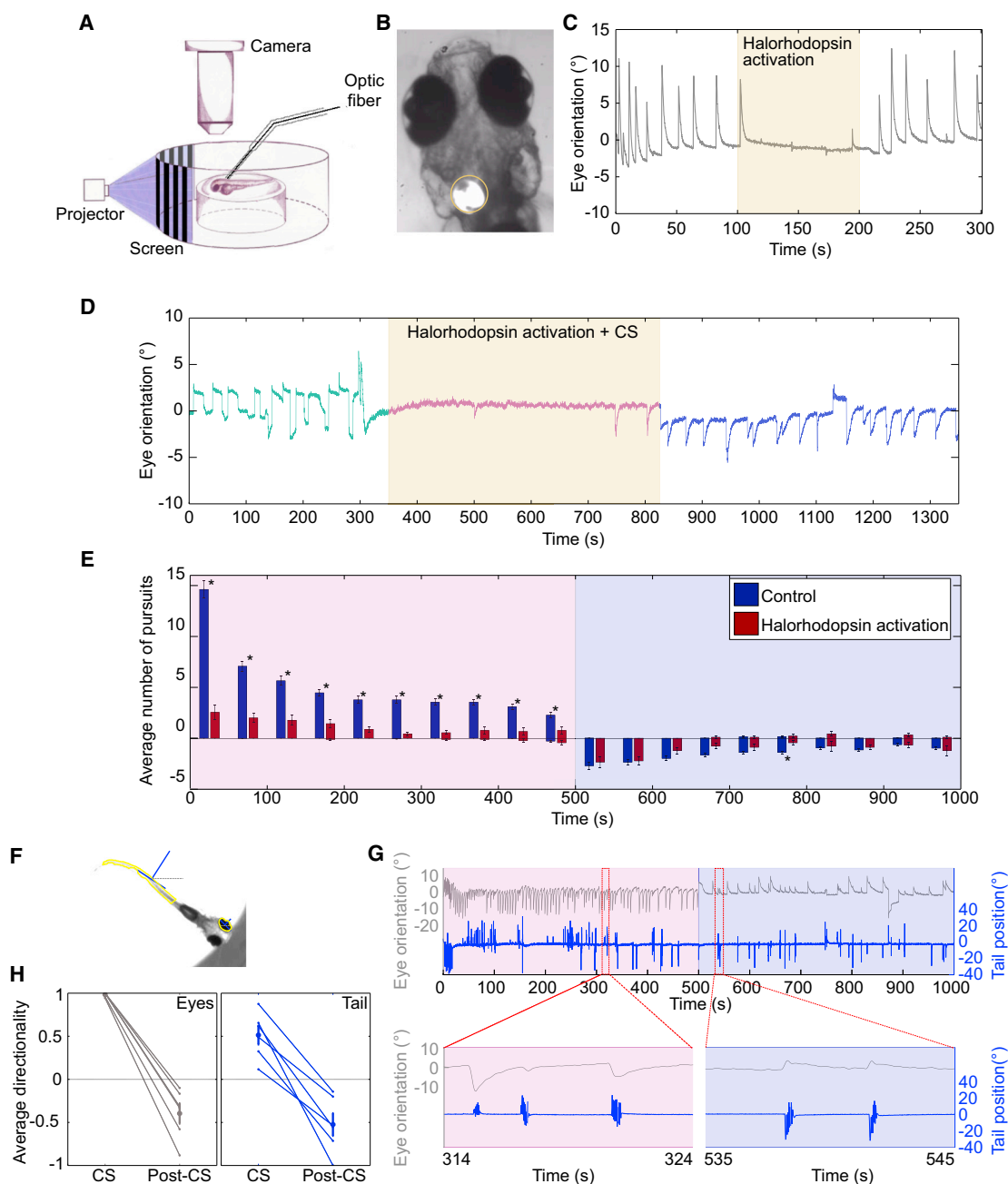


Figure 2. MAE Is Generated in a Sensory Brain Region

(A) Experimental setup used to block eye movements during the presentation of MAE. Eye movements were recorded as in Figure 1A. To inhibit eye movements, we used transgenic larvae pan-neuronally expressing NpHR and a 105 μm optic fiber coupled to a 565 nm LED mounted on a micromanipulator. (B) Image of larva obtained using the setup in (A). In all experiments, the fiber was positioned orthogonally and unilaterally above rhombomere 5. The yellow circle shows the illuminated zone. (C) Example of optogenetic inhibition of OKR during the presentation of MAE, with eye orientation as a function of time. The CS was presented during the entire 300 s period. The yellow patch represents the illumination period. Note the drastic and rapid inhibition of the eye movement upon halorhodopsin activation. (D) Example showing that optogenetic inhibition of eye movements during the presentation of CS did not perturb MAE; eye orientation as a function of time during CS. Green curve, pre-CS; pink curve, CS; blue curve, post-CS; yellow patch, NpHR activation period. (E) The average number of pursuits during the CS and the post-CS periods, summarizing all experiments as in (D). Pink background, CS period; violet background, post-CS control period; blue bars, control (LED off during CS); red bars, LED on during CS; positive values, pursuits in the direction of the CS; negative values, pursuits in the MAE direction. Asterisks mark significant differences ($p < 0.01$, Kruskal-Wallis; $n = 9$ trials from 9 larvae). Error bars, SE.

(legend continued on next page)

(the presence of optokinetic MAE-like behavior was defined as a MAE index larger than 95% of the control index for at least the first 50 s of the post-CS control period). Along the same lines, we found that the length of MAE was positively correlated with the level of habituation of the number of pursuits during the CS (Figure S1D).

We then tested the effect of the CS velocity (17°/s, 26°/s, and 59°/s) on the induction of optokinetic MAE-like behavior. Although we observed a tendency for a larger MAE index at CS velocities of 26°/s, we found few significant differences in the MAE index during the 500 s of the post-CS control periods for the three velocities tested ($p > 0.05$, Kruskal-Wallis); however, they did not follow the same tendency. These results suggest that CS velocity, within the range of 17°/s–59°/s, does not play a major role in modulating optokinetic MAE-like behavior (Figure S1A).

We also studied the effect of different patterns of static visual stimuli during the post-CS control period. We tested three conditions: (1) a static version of the grating presented during the CS (white-black square grating); (2) a stationary noise pattern, built by shuffling the pixel positions of the first condition; and (3) a black screen (Supplemental Experimental Procedures). Quantification of optokinetic MAE-like behavior, by means of the MAE index, did not show any significant difference among the three conditions ($p > 0.05$, Kruskal-Wallis; Figure S1B). We thus suggest that visual feedback during the post-CS control period is not necessary for the generation of optokinetic MAE-like behavior. In contrast to results obtained using other animal models, in which a static visual pattern is necessary to perceive MAE (Anstis et al., 1998; Mather et al., 2008), zebrafish larvae are capable of perceiving MAE in complete darkness. Because no visual feedback is necessary to drive MAE in zebrafish, MAE represents a case in which perception emerges in the absence of visual stimuli; therefore, it is a useful tool to study the neuronal dynamics underlying visual motion perception in zebrafish.

Blocking Eye Movements Using Optogenetics

To investigate the mechanism underlying MAE, we first asked whether eye muscular fatigue or eye proprioception during the CS is required for the generation of optokinetic MAE-like behavior. For this purpose, we blocked eye movements exclusively during the CS by means of optogenetics. Following the cessation of the CS, we released this suppression to assess the induction level of optokinetic MAE-like behavior.

To block eye movements via optogenetics, we used transgenic larvae expressing halorhodopsin in their entire nervous system (HuC:Gal4;UAS:NpHR (halorhodopsin)-mCherry line; Supple-

mental Experimental Procedures; Arrenberg et al., 2009). Halorhodopsin was locally activated via a 565 nm light-emitting diode (LED) coupled to a 100 μm optic fiber (Figure 2A; Supplemental Experimental Procedures) that was positioned unilaterally roughly above rhombomere 5, which was previously found to affect directional saccade generation in zebrafish when optogenetically inhibited (Schoonheim et al., 2010). This location likely corresponds to the nucleus abducens (Ma et al., 2014).

To assess the effect of halorhodopsin activation on eye movements during CS, we presented to the larva a visual stimulus consisting of a grating moving at 26°/s for 300 s. The 565 nm LED was turned on after the first 100 s for a period of 100 s. Upon halorhodopsin activation, OKR was robustly suppressed, and it almost immediately recovered when the stimulating LED was switched off. Because the optic fiber covered rhombomere 5 unilaterally, the eye-movement-suppression effect was unidirectional. It fully blocked OKR toward the ipsilateral direction from the optic fiber positioning, including both the saccades and the pursuits (the OKR direction toward the side on which the fiber was positioned; Figure 2C; Movie S2).

Once we were able to effectively prevent OKR using optogenetics, we tested the effect of CS-induced eye movements on the generation of optokinetic MAE-like behavior. We monitored spontaneous eye movements for 350 s (pre-CS control period). Then, we visually stimulated the larva with the CS for 500 s while simultaneously activating halorhodopsin. When the CS ceased, halorhodopsin activation was stopped and eye movements were monitored for an additional period of 500 s (post-CS control; Figure 2D). Using this paradigm, we were able to abolish or significantly reduce OKR ($p < 0.01$, Kruskal-Wallis; Figures 2D and 2E). Despite the significant reduction in the number of eye movements during the CS, we still observed optokinetic MAE-like behavior. The number of optokinetic MAE-like pursuits was not significantly different from the experiments in which halorhodopsin was not activated ($p > 0.05$, Kruskal-Wallis; Figure 2E). These results suggest that neither eye muscular fatigue nor eye proprioception during the CS plays an essential role in the generation of optokinetic MAE-like behavior.

MAE Is Reflected at the Level of Tail Movements

To further study the involvement of sensory and motor systems in the generation of the MAE-like behavior, we took advantage of another robust behavior of the larva, the optomotor response (OMR). During OMR, larvae swim by performing directional tail deflections in the direction of a unidirectional coherent motion visual stimulus (Portugues and Engert, 2009). Like OKR, OMR stabilizes a moving external world on the retina. In contrast to

(F) Detection of eye and tail orientation. The image of the larva superimposed with the automatic detection of the tail and eyes. The orientations were calculated with respect to the external horizontal axis (gray dashed lines).

(G) Optomotor MAE-like behavior. Top: eye and tail orientations during CS (pink background) and post-CS (magenta background). Bottom: expanded timescale of the indicated regions above (red dashed rectangles). Note the inversion of the directionality of both eye and tail movements during the post-CS period with respect to the CS period.

(H) Summary of all experiments as in (G). The average directionality of the eye pursuits (gray) and tail bouts (blue) during CS and post-CS periods ($n = 6$ trials from 6 larvae). To compute the directionality, we classified each pursuit and each tail bout as moving in the direction of the CS or in the opposite one. Movements performed in the direction of the CS were given the value 1, and movements in the opposite direction were given the value -1 . For each experiment, we calculated the average across movements. Large gray dots represent the population average. Error bars, SE. For all experiments, average directionality of both eye pursuits and tail bouts was inverted.

OKR, OMR involves reorienting tail movements rather than eye rotations. Although OKR and OMR share the same behavioral goal, the motor centers controlling both behaviors are different. Thus, observing MAE-like behavior at the level of OMR would suggest that MAE is generated within an upstream brain region common to both eye and tail motor centers, most likely the larva's sensory visual system.

To test this hypothesis, we presented to the larvae the following experimental paradigm: CS (moving grating at $26^\circ/\text{s}$ for 500 s) followed by a post-CS control period (stationary grating for 500 s). In this experiment, we removed the agarose around the eyes and around the tail so that the larvae could perform both OKR and OMR behaviors (Figures 2F and 2G). During the CS, the larvae performed both OKR and tail movements. However, tail movements were less frequent than eye movements (only $39\% \pm 16\%$ of eye movements were associated with a tail movement). During this period, $74\% \pm 13\%$ of the CS-induced tail deflections were performed in the direction of the CS (Figures 2G and 2H). During post-CS control, we observed the expected optokinetic MAE-like behavior, which was associated with tail flips ($68\% \pm 37\%$ of pursuits had an associated tail flip during post-CS control). The tail-flip direction was accordingly reversed ($73\% \pm 13\%$ of tail deflections were performed in the opposite direction of the CS; Figures 2G and 2H). These results suggest that a sensory brain region, rather than the eye's motor circuitry, is involved in the generation of the zebrafish MAE-like behavior.

Ablation of the Optic Tectum Affects MAE

The optic tectum is the highest visual center in the larva's brain. Therefore, to test whether the optic tectum is involved in the generation of MAE-like behavior, we studied the induction of MAE in larvae whose tecta were ablated. To perform the ablations, we scanned the entire periventricular layer of the optic tectum of HuC:GCaMP5 larvae using a two-photon microscope (Supplemental Experimental Procedures). The ablations induced massive tectal apoptosis (Dunn et al., 2016). As a first sign of cell damage, we observed a large relative increase in GCaMP5 fluorescence, especially in the nucleus (Movie S3). To test for apoptosis of the tectal neurons, we labeled the larvae with acridine orange, a marker of apoptosis (Paquet et al., 2009). The labeling was performed either immediately after the ablations or 24 hr after the ablations. In both cases, acridine orange labeled almost the entire tectum, confirming tectal ablation (Figures 3A and 3B; Movie S3; Supplemental Experimental Procedures).

After a 24 hr recovery period, we tested the capacity of inducing the MAE-like behavior in tectum-ablated larvae (Figure 3; Supplemental Experimental Procedures). To quantify the effect of the tectal ablation on the CS-induced eye movements and the optokinetic MAE-like behavior, we calculated the mean of the difference between the number of pursuits in the CS direction and those in the MAE direction (Supplemental Experimental Procedures).

Intact larvae showed OKR with a gradual reduction in the number of performed pursuits along the CS. This number of pursuits decreased according to two time constants: 12 and 195 s (Figure S5A). In contrast, fitting the number of pursuits in tectum-ablated larvae with just one time constant or two time

constants gave similar results (the coefficient of the second exponential was negligible with respect to the first; ratio = 0.2). Moreover, the observed average number of pursuits in the direction of the moving stimulus was significantly lower in tectum-ablated larvae than in intact ones during the first and the last 50 s of the CS (intact, 14.06; ablated, 8.62; $p < 0.01$, Kruskal-Wallis; Figure 3C). During the first 100 s, following the cessation of the CS (post-CS period), tectum-ablated larvae showed a significant lower average number of optokinetic MAE-like pursuits (intact, 5.11; ablated, 2.44; $p < 0.01$, Kruskal-Wallis; Figure 3C), indicating a reduction in the optokinetic MAE-like behavior ($n = 26$ trials from 4 larvae). Tectal ablations damaged around 85% of the tectal neurons. Thus, the decrease in rather than the full blockage of MAE could be explained the inability to ablate the optic tectum.

As a control experiment, we ablated the interpeduncular nucleus (IPN), a non-sensory processing region that projects to modulatory brain regions such as the ventral tegmental area (VTA) and raphe nucleus. In zebrafish, the IPN controls social aggressive behaviors (Chou et al., 2016; Okamoto et al., 2012). IPN ablations did not affect the two habituation time constants during OKR (16 and 218 s) and did not affect MAE. However, we observed a general increase in the number of pursuits during OKR (Figure S1C). A potential hypothesis is that ablation of the IPN increased arousal or alertness and therefore elicited a stronger OKR response.

As previously shown by the ablation of the RGC terminals in the optic tectum neuropil (Roeser and Baier, 2003), ablation of a large portion of the tectal neurons did not abolish OKR, suggesting that the tectum does not play a major role in its generation. However, the tectum seems to be necessary for the initial strong behavioral response to novel stimuli and for CS-induced behavioral habituation (decrease in the OKR gain). Similarly, the strong novelty response and habituation effect were present in the CS-induced neuronal responses in the optic tectum but absent in the retina (Figures S2E and S2F). The lack of CS-induced behavioral habituation could explain the observed reduction of MAE in ablated larvae. We therefore suggest that MAE could emerge as a consequence of tectal adaptation to the CS.

CS Induces Habituation of Direction-Selective Neurons in the Optic Tectum

To test whether the CS induces adaptation of specific tectal neurons, we monitored the activity of the larva's two main visual centers: the retina and the optic tectum. For this purpose, we performed two-photon calcium imaging of zebrafish larvae expressing the genetically encoded Ca^{2+} indicator GCaMP3. We first immobilized the larvae in low-melting agarose and paralyzed them (0.3 mg/mL pancuronium bromide; Tocris Bioscience) to avoid any possible rotation of the eyes. To test for potential adaptations of the CS-induced responses of direction-selective neurons in both the retina and the optic tectum (Figures S2E and S2F), we used the following paradigm, consisting of three steps: (1) sequential presentation to the larva of light-moving bars in two directions (CS and MAE directions, presented every 10 s); (2) presentation of the CS, consisting of a continuous series of moving bars in the same direction for 500 s; and (3) post-CS

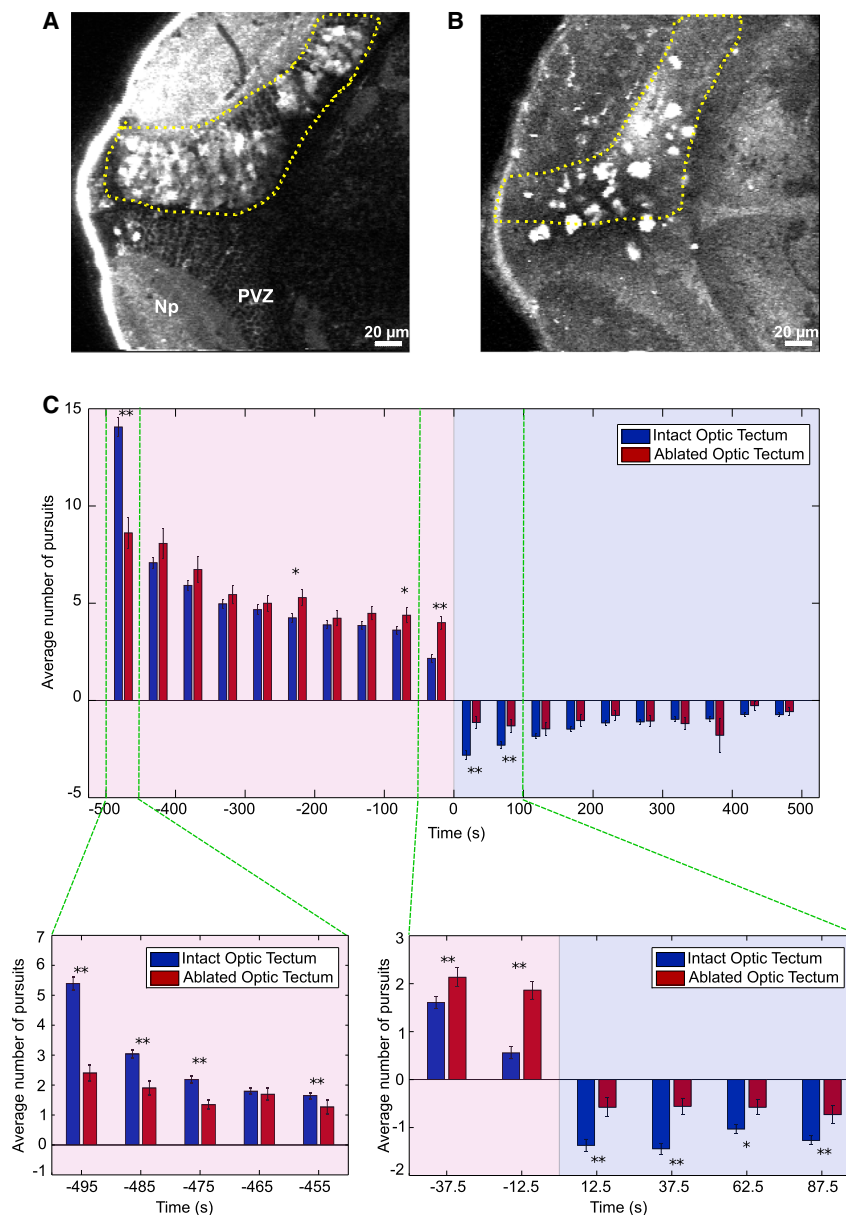


Figure 3. Ablation of the Optic Tectum Impairs the Generation of MAE

(A) An optical plane of the HuC:GCaMP5 zebrafish tectum after two-photon laser ablation. For visualization purposes, ablation of a single tectal hemisphere is shown. For the experiments, both hemispheres were ablated. Note the large increase in fluorescence of the ablated neurons with respect to the intact hemisphere.

(B) As in (A), but after labeling with acridine orange to label apoptotic neurons. The labeling was performed immediately after the behavioral experiments (1 day after the ablation).

(C) Top: summary of the behavioral experiments after tectal ablations. The chart shows the average number of pursuits during the CS and the post-CS periods. Pink background, CS period; violet background, post-CS control period; blue bars, control (intact optic tectum); red bars, ablated optic tectum; positive values, pursuits in the direction of the CS; negative values, pursuits in the MAE direction. Asterisks mark significant differences (* $p < 0.05$, ** $p < 0.01$, Kruskal-Wallis; $n = 26$ trials from 4 larvae). Error bars, SE. Bottom: expanded timescale of the indicated regions above (green dashed lines). Note the weak initial behavioral response to the CS in ablated larvae and the much weaker optokinetic MAE-like behavior in ablated larvae compared to intact larvae.

at the tectal neuropil. Because cellular resolution is not possible under these conditions, we segmented the tectal neuropil using a grid of square regions of interest (SROIs; Nikolaou et al., 2012; Supplemental Experimental Procedures).

To quantify a possible modulation of the SROI directional responses following the presentation of CS, we defined an adaptation index (Supplemental Experimental Procedures). To calculate this index, we first calculated the ratio between the population responses of direction-selective SROIs to the moving bars in the CS direction before and after the presentation of CS. This value was then divided by a similar ratio computed for responses to moving bars in the MAE direction. This index ranges from -1 to 1 . Negative values indicate habituation for the CS direction-selective SROIs. Positive values indicate habituation for the MAE direction-selective SROIs. Zero indicates equal directional responses before and after CS presentation. Using the adaptation index, we observed that CS direction-selective RGCs were slightly habituated with respect to zero ($p < 0.01$, Wilcoxon signed rank; Figures 4A and 4B; Figure S2E) for only 20 s following the CS. However, the dynamics of the habituation did not match the temporal scale of the optokinetic MAE-like behavior (150–200 s; Figure 4B; Figure S2D).

To test whether direction-selective neuronal responses in the optic tectum were modulated by CS, we used a similar

control, in which we presented light-moving bars in alternate directions every 10 s for a period of 500 s (Supplemental Experimental Procedures).

The first step determined the direction selectivity of neurons (CS or MAE directions) and served as a control for the amplitude of their Ca^{2+} responses before the presentation of the CS. The amplitudes were then compared to those induced by the moving bars presented during the post-CS control period. This comparison enabled us to test for a potential adaptation of direction-selective neurons following the CS.

We initially focused on the larva's retina. To that end, we used the *ath5:Gal4;UAS:GCaMP3* transgenic line expressing GCaMP3 almost exclusively in the retina (Supplemental Experimental Procedures). This line enabled monitoring of the RGC terminal activity

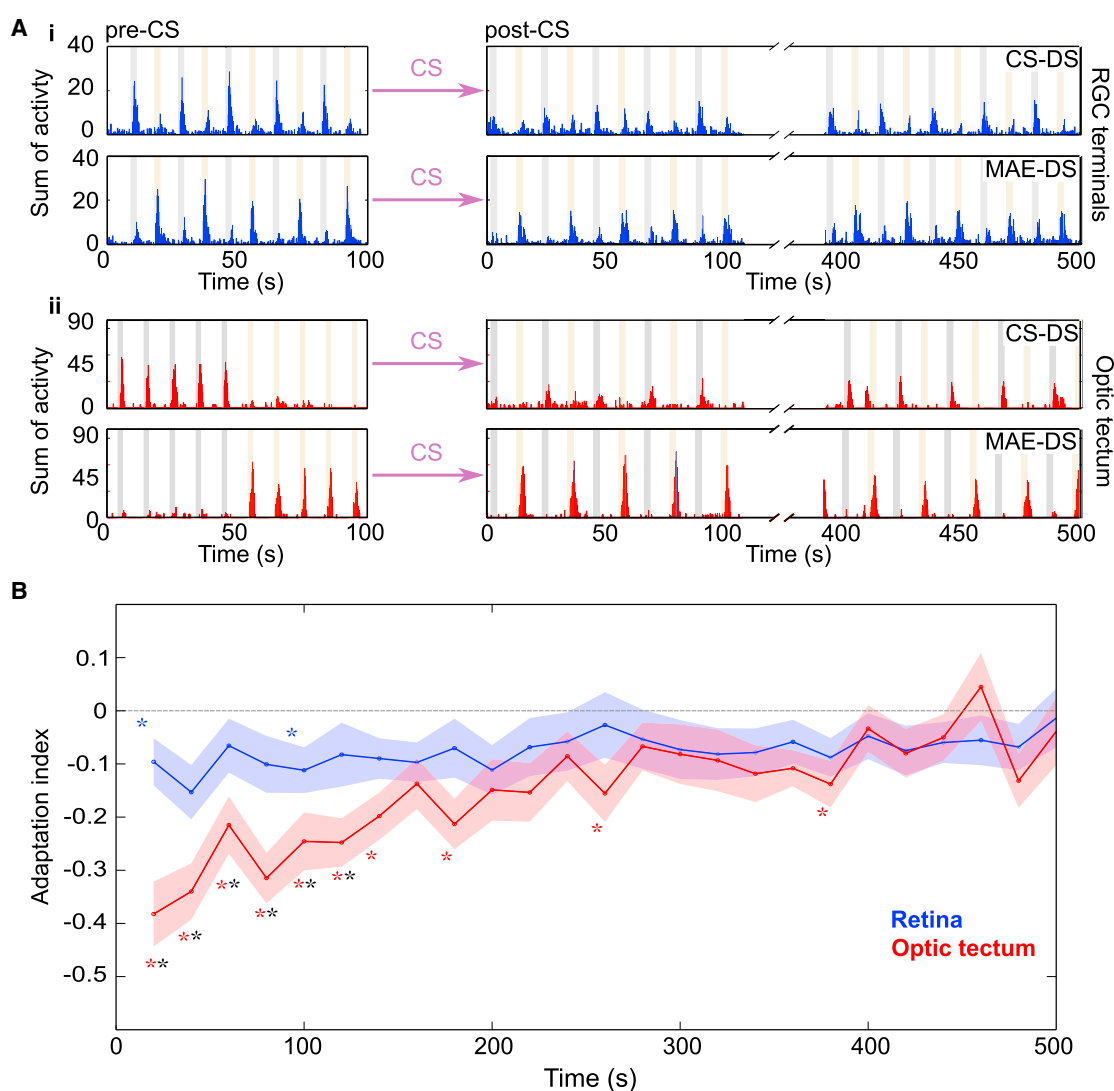


Figure 4. Habituation of Direction-Selective Neurons in the Optic Tectum

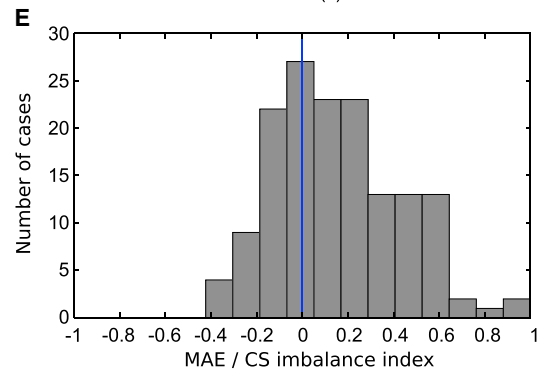
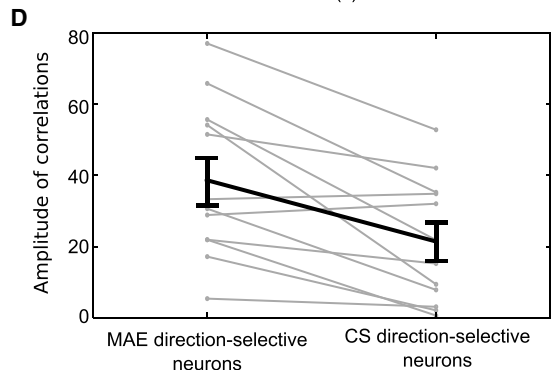
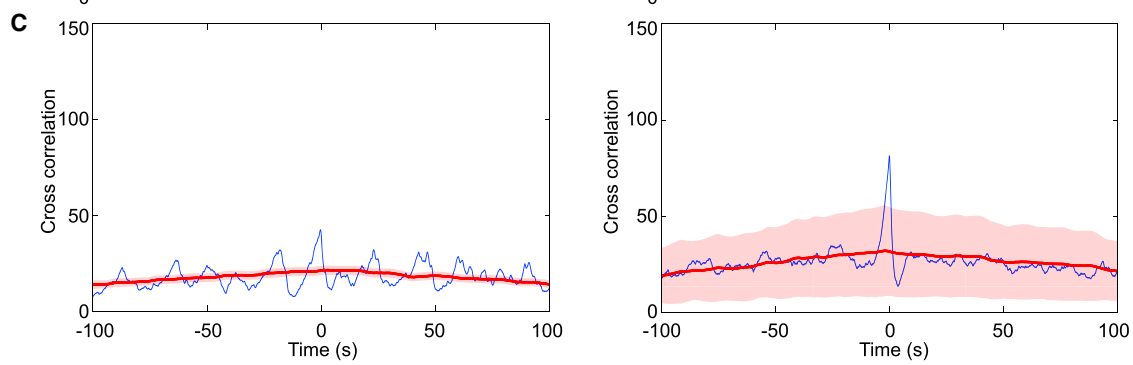
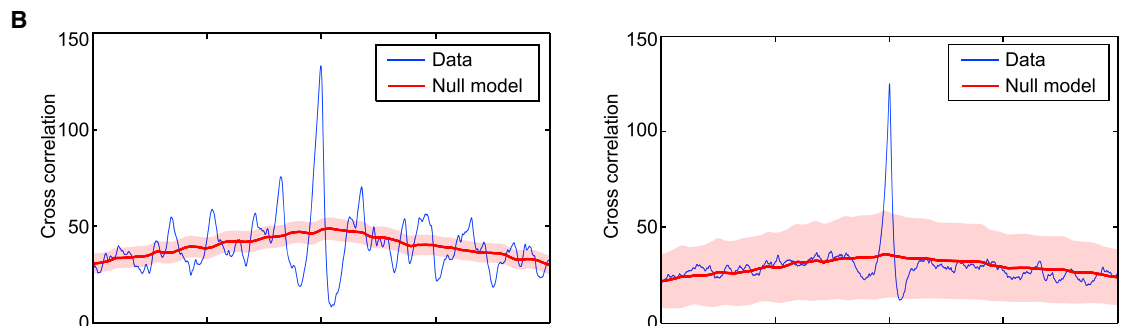
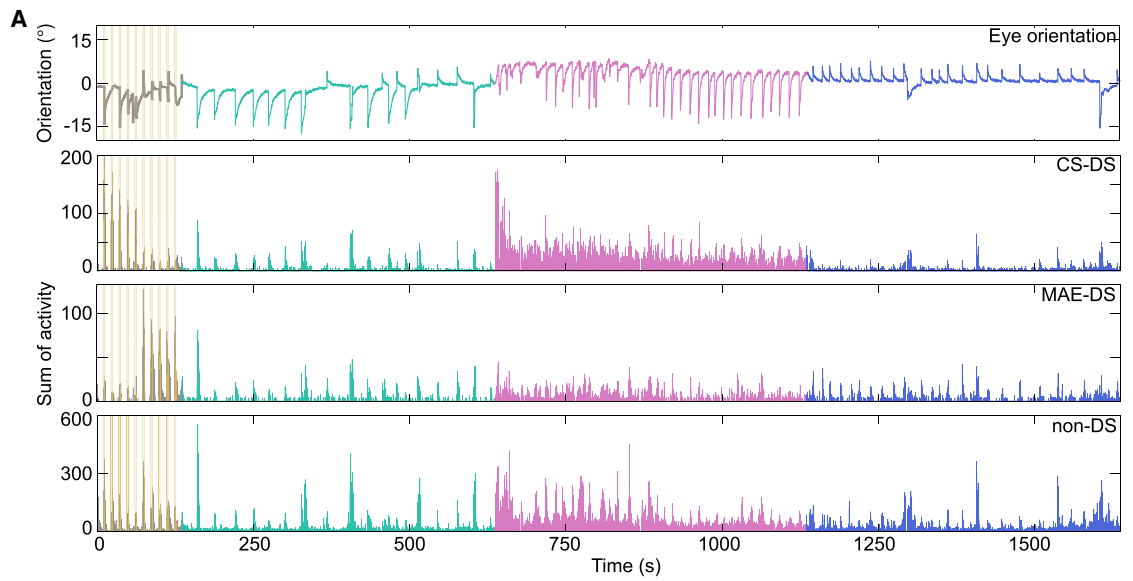
(A) Sum of the activity of direction-selective (DS) neuronal groups (CS-DS, top, and MAE-DS, bottom). (Ai) RGC projections (Aii) Tectal neurons. Blue bars, RGC responses during pre-CS and post-CS control periods; red bars, tectal responses during pre-CS and post-CS control periods; pink arrow, CS presentation; gray patches, time of presentation of the moving-bar stimulus in the CS direction; yellow patches, moving-bar stimulus in the MAE direction. Note the habituation of the response in the optic tectum during the first 100 s of the post-CS period.

(B) Adaptation index (AI) as a function of time during the post-CS period. Each dot represents the AI calculated in bins of 20 s. Blue, RGC terminals; red, tectal neurons. Blue and red asterisks denote significant differences of the AI values from zero (no habituation; $p < 0.01$, Wilcoxon signed rank test). Black asterisks denote significant differences between AIs (RGC and optic tectum; $p < 0.01$, Wilcoxon rank sum test). For RGC, 741 SROIs from $n = 18$ trials from 4 larvae. For optic tectum, 688 neurons from $n = 24$ trials from 6 larvae. Error bars, SE.

experimental design in zebrafish larvae expressing GCaMP3 under a pan-neuronal promoter (HuC; [Supplemental Experimental Procedures](#)). This transgenic line of zebrafish enabled monitoring, with single-neuron resolution, of a large and significant part of the periventricular layer of the optic tectum (839 ± 38 neurons per optical plane). Direction-selective neurons represented around 14% of the monitored neurons (59 ± 8 and 55 ± 7 neurons per optical plane for the CS and the MAE directions, respectively). In contrast to the RGCs, direction-selective tectal neurons showed an adaptation index of significantly larger negative values ($p < 0.01$, Wil-

coxon signed rank; [Figures 4A and 4B](#); [Figure S2F](#)) for a period that better matched the timescale of the optokinetic MAE-like behavior (~ 150 – 200 s; [Figure 4B](#); [Figure S2D](#)).

Moreover, this habituation observed among direction-selective neurons in the optic tectum was significantly larger than the habituation observed in the direction-selective RGCs ($p < 0.01$, Wilcoxon rank sum; [Figure 4B](#)). Therefore, we suggest that the zebrafish larva optokinetic MAE-like behavior mainly reflects habituation of direction-selective tectal neurons in the direction of the CS.



(legend on next page)

Neuronal Correlate of MAE in the Optic Tectum

Because the ablation of the optic tectum affected the generation of MAE-like behavior, and MAE-like-related neuronal habituation was observed in the larva's optic tectum rather than in the retina, we then investigated the tectal neuronal dynamics associated with optokinetic MAE-like behavior. To that end, we imaged tectal activity while simultaneously monitoring eye rotations in non-anesthetized and non-paralyzed larvae using the following experimental procedure. First, we determined direction-selective neurons by sequentially presenting to the larva light-moving bars in two directions. From the responses to these stimuli, we classified the imaged neuronal population into three groups: non-direction-selective neurons, direction-selective neurons in the direction of the CS, and direction-selective neurons in the opposite direction (MAE direction). Second, during a pre-CS control period, we allowed 500 s of spontaneous eye movements and tectal neuronal activity in the absence of visual feedback (black screen). Third, during the CS period, a continuous moving bar (in either the CS or the MAE direction) was presented for a duration of 500 s. Lastly, during a post-CS control, larvae were placed under the same conditions as for the pre-CS control period (Supplemental Experimental Procedures).

During the post-CS control period, we observed robust optokinetic MAE-like behavior (Figure S2D). During the same period, tectal dynamics showed rhythmic synchronous neuronal population activities. These synchronous activities were mainly observed among direction-selective neurons sensitive to the MAE direction (Figure 5A). To test whether the synchronous activities of the MAE direction-selective neurons were associated with the optokinetic MAE-like behavior, we cross-correlated this activity with the kinematics of the eye rotations during the post-CS period (Figure 5B). To compare the correlations across different experiments, we normalized the eye rotations according to the 95 percentile value, and then we calculated the mean of the total neuronal activity of the MAE direction-selective cells (Supplemental Experimental Procedures). Next, to test for the significance of the correlations, we generated a null model for the neuronal activity. We observed that the MAE direction-selective neurons were significantly more correlated with the eye pursuits in the MAE direction than those of the null model ($p < 0.01$, Kruskal-Wallis; Figure 5B). A similar phenomenon was observed for the CS direction-selective neurons ($p < 0.01$, Kruskal-Wallis; Figure 5C). Although not significantly different, the correlations of MAE direction-selective neurons tended to be higher than those of CS direction-selective neurons

($p = 0.06$, Kruskal-Wallis; Figure 5D). To quantify the difference in the correlation levels, we subtracted the peak of the correlations from 2 SD above the mean of correlations of the null models (Figure 5D).

Finally, the distribution of the ratios between the activity of MAE and that of CS neurons at the time of each eye movement in the MAE direction, during the post-CS period, was largely skewed to positive values (for the ratio values above 0.06 and below -0.06 , 72% were positive and 28% were negative and the average ratios were 30.1 and 6.4, respectively). Thus, we suggest that an imbalance between the activity of the MAE and that of the CS direction-selective neuronal population drives the direction of the eye movements. During MAE, this imbalance is biased toward MAE direction-selective neurons (positive values; Figure 5E).

We took advantage of the rhythmic nature of optokinetic MAE-like behavior and the population neuronal events during the post-CS period to perform spectral analysis. The normalized power spectrum of optokinetic MAE-like movements showed significant peaks at a fundamental frequency (0.048 ± 0.008 Hz) and its harmonics ($n = 9$ trials from 8 larvae; Figure 6A; Supplemental Experimental Procedures). We then performed the same type of spectral analysis on the population activity of the three neuronal groups: non-direction-selective, CS direction-selective, and MAE direction-selective neurons. During the post-CS control period, the MAE direction-selective group exhibited a normalized power-spectrum profile that closely matched that of the optokinetic MAE-like behavior, with significant large power values around the optokinetic MAE-like fundamental frequency and its harmonics. In contrast, the CS direction-selective and non-direction-selective neuronal groups showed a more uniformed normalized power spectrum without preference for any particular frequency (Figure 6A).

To quantify the level of association between the synchronous activities of the MAE direction-selective, CS direction-selective, and non-direction-selective neuronal groups with that of the optokinetic MAE-like behavior, we measured for each neuronal group the normalized power spectrum of their activities during the post-CS control period (Figure 6A). We then calculated the normalized power for the frequency bands significantly associated with the MAE-like OKR for each of the three neuronal groups (Figure 6B; Supplemental Experimental Procedures). To compare across different experiments, the power of the frequencies was normalized by the mean power of all neurons across the significant frequencies. This method enabled us to compare the relative power of the three direction-selective

Figure 5. Neuronal Correlate of MAE in the Optic Tectum

(A) Top: eye direction along the course of the experiment. Bottom: the sum of the activity of the different groups of tectal neurons in the following descending order: CS direction-selective (CS-DS), MAE direction-selective (MAE-DS), and non-direction-selective (non-DS). Plots are color coded according to the period of stimulation. Gray, period corresponding to the presentation of moving bars for the determination of the direction selectivity of the neurons; green, pre-CS control period; pink, presentation of CS; violet, post-CS control period.

(B) Left: correlation (blue) between the eye pursuits in the MAE direction and the neuronal activity of DS neurons in the MAE direction during the first 300 s following the post-CS period for the experiment in (A). Null model (red). Error bars, SE. Right: as in the left graph but representing the average across all experiments.

(C) As for (B), but for correlations between the eye pursuits in the MAE direction and the neuronal activity of DS neurons in the CS direction.

(D) Graph showing the peaks (gray) of the correlations of each trial (as in B and C) subtracted by 2 SD of the respective null models, for the MAE-DS and CS-DS neurons. Black bars, mean and SE.

(E) Histogram of the MAE-CS imbalance index for eye pursuits in the MAE direction during the first 300 s following the post-CS period.

For the population analysis, $n = 12$ trials from 9 larvae.

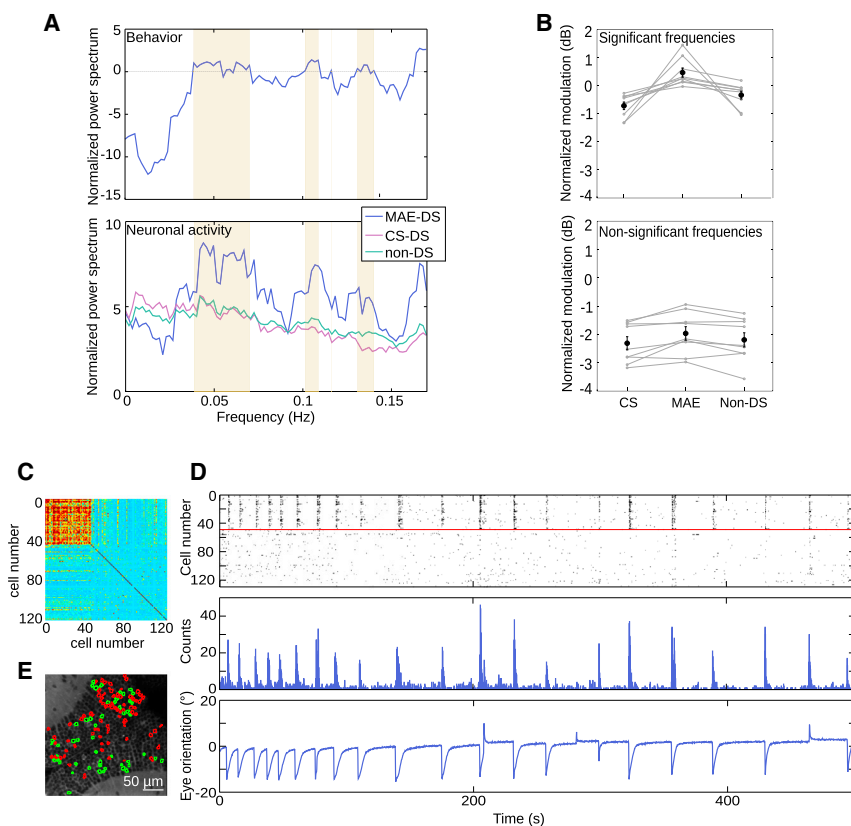


Figure 6. Frequency Analysis and Topography of MAE-Associated Neurons

(A) Top: normalized power spectrum of eye movements during MAE-like behavior. Bottom: normalized power spectrum of neuronal data during MAE-like behavior. Violet, MAE direction-selective neurons; pink, CS direction-selective neurons; green, non-direction-selective neurons; yellow patches, significant behavioral frequencies (normalized power spectrum exceeds a threshold set at zero, dashed gray line).

(B) Top: normalized averaged frequency power of behaviorally relevant significant frequencies, during post-CS control period. Gray lines, the individual experiments for the CS, MAE, and non-direction-selective neurons; black line, the mean power value. CS direction-selective modulation = -0.71 ± 0.13 dB, MAE direction-selective modulation = 0.15 ± 0.16 dB, and non-direction-selective modulation = -0.11 ± 0.14 dB ($p = 4.1 \times 10^{-5}$ for CS and MAE direction-selective neurons, $p = 2.9 \times 10^{-4}$ for non-direction-selective and MAE direction-selective neurons, $p = 0.04$ for CS and non-direction-selective neurons, Wilcoxon rank sum test). Bottom: as for top, but for non-significant non-behaviorally relevant frequencies. CS direction-selective modulation = -2.3 ± 0.7 dB, MAE direction-selective modulation = -1.96 ± 0.72 dB, and non-direction-selective modulation = -2.19 ± 0.75 dB ($p = 0.34$ for CS and MAE direction-selective neurons, $p = 0.49$ for non-direction-selective and MAE direction-selective neurons, $p = 0.6$ for CS and non-direction-selective neurons, Wilcoxon rank sum test). In both cases, error bars, SE. $n = 9$ trials from 8 larvae.

(C) Pairwise correlation matrix of MAE direction-selective neuronal activity during the post-CS period. The matrix was ordered according to k-means clustering. The color-scale bar shows the level of correlation.

(D) Top: raster plot of MAE direction-selective neurons during the post-CS control period ordered according to (A). Middle: sum of calcium activity. Bottom: eye orientation. About 30% of the neurons show synchronous Ca^{2+} transients associated with all eye pursuits in the MAE direction.

(E) Topography of the MAE direction-selective neurons. Green, neurons correlated with the pursuits in the direction of MAE; red, non-correlated neurons.

neuronal groups specifically within the frame of optokinetic MAE-like behavior. We observed that in all experiments, MAE direction-selective neurons showed significantly higher power than that of CS direction-selective and non-direction-selective neurons. As a control, we performed the same analysis, but for frequency bands not significantly associated with optokinetic MAE-like behavior (Figure 6B; Supplemental Experimental Procedures). We observed that none of the neuronal groups showed significantly different power levels.

During the MAE-like period, the rate of Ca^{2+} events for all three neuronal groups was similar (CS direction-selective neurons, 0.08 ± 0.03 ; MAE direction-selective neurons, 0.08 ± 0.04 ; non-direction-selective neurons, 0.07 ± 0.03). Therefore, the difference in power among the different neuronal groups during the optokinetic MAE-like behavior was specific to frequencies associated with MAE-like behavior, rather than being a direct consequence of an overall increase in the activity of MAE direction-selective neurons.

By correlating the population activity of the tectal direction-selective neurons with the eye-rotation kinematics (Supplemental Experimental Procedures), we found two classes of neurons: (1) direction-selective neurons that did not show spontaneous

activity associated with optokinetic MAE-like behavior and (2) direction-selective neurons that showed correlated activity with optokinetic MAE-like behavior during the post-CS period (eye-motion-selective neurons). These direction-selective and eye-motion-selective neurons represented $26\% \pm 0.06\%$ of the total population of direction-selective neurons (Figure S3B).

Finally, we observed that the synchronous Ca^{2+} events associated with the MAE-like behavior emerged mainly from the activity of single neurons among the eye-motion-selective neuronal population. Their rhythmic activity was highly correlated and phase locked to the synchronous population events (Figures 6C and 6D). These rhythmic neurons were sparsely dispersed within the tectal network, without showing clear topography (Figure 6E).

Overall, these results represent the first example of sustained rhythmic activity as a neuronal correlate of MAE.

An Empirical Cross-Inhibiting Mathematical Model Reproduces the Main Features of MAE-like Behavior

The competition between two directional-selective neuronal populations has long been thought to underlie MAE, but this has never been experimentally demonstrated. Our results

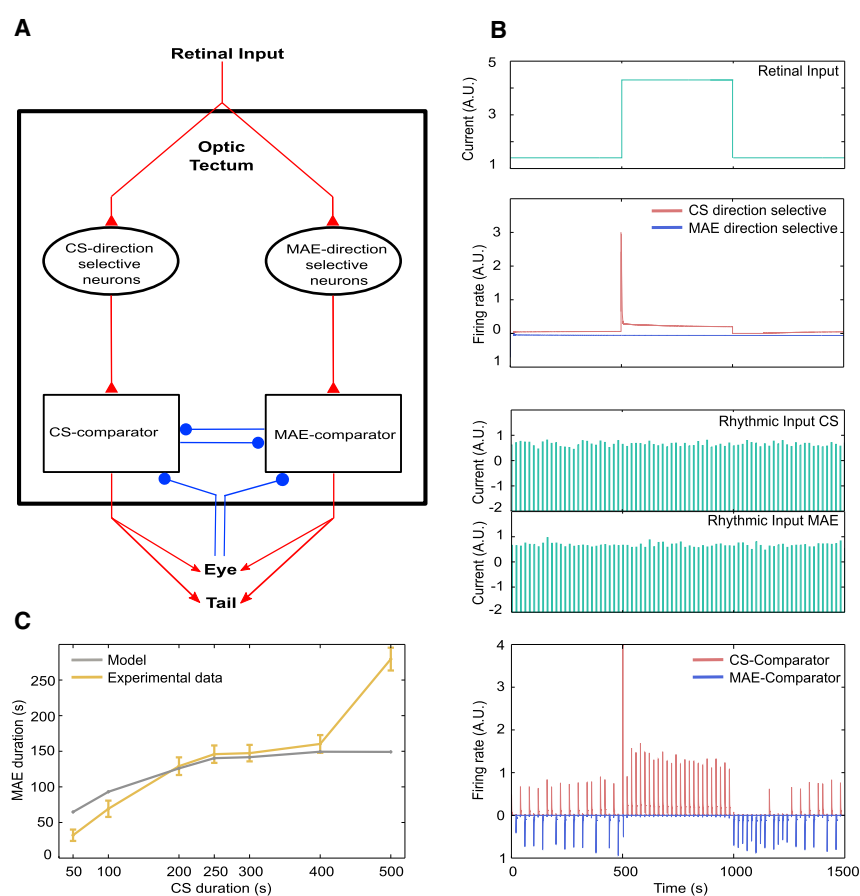


Figure 7. Empirical Mathematical Model of the MAE

(A) The model comprises four populations of neurons: CS direction-selective (CS-DS), MAE direction-selective (MAE-DS), and two comparator populations (CPs), one for each direction (CS-CP and MAE-CP). The DS populations receive retinal inputs, whereas the CPs' cells receive rhythmic input. The CPs receive excitatory input from the corresponding DS population and inhibitory input from the other DS population, and they cross-inhibit each other.

(B) The input currents and firing rates of the four populations in one representative computer simulation. A CS-retinal input is received by the CS-DS cell during the time interval 300–800 s. The firing rate of the CS-DS population increases and displays strong adaptation during the duration of the CS. At the end of the CS, however, the firing rate of the CS-DS population is smaller than it is during the spontaneous activity. As a result, despite the comparable rhythmic input received by the two CPs, the CS-CP fires predominantly during the CS, whereas the MAE-CP fires more during the MAE.

(C) The MAE duration model as a function of the duration of the CS. The MAE duration is defined as the period in which the MAE index is significantly greater than the control index (Figure S5F). For comparison, the yellow curve shows the values obtained for the behavioral data (Figure 1F).

show that during the presentation of the CS, the CS direction-selective neurons are more active than those in the opposite direction. Due to CS-induced habituation, during the post-CS control period, CS direction-selective neurons are less spontaneously active than MAE direction-selective neurons (Figure 5A; Figure S3A). A comparison between these two populations could qualitatively explain the MAE-like effect that we observed. Therefore, the MAE-like behavior could emerge from a tectal sub-circuit that compares the activities of both direction-selective neuronal groups and generates adequate directional motor commands. This hypothesis is supported by the identification of direction-selective and eye-motion-selective neuronal groups.

To consider whether our findings could be explained within the framework of this hypothesis, we developed an empirical mathematical model. This model was based on a comparator tectal sub-circuit consisting of two cross-inhibiting neuronal populations: a CS comparator and a MAE comparator, each of them receiving excitatory inputs from the corresponding group of direction-selective neurons (Figure 7A; Supplemental Experimental Procedures). These comparator populations represent the sub-groups of MAE direction-selective neurons displaying synchronous rhythmic activity associated with optokinetic MAE-like behavior (Figures 5A and 6A). The comparator circuit computes the difference between the activities of the two

groups of direction-selective neurons: each rhythmic stimulation produces a winner-takes-all dynamic in which one of

the two comparator populations dominates the other in an input-dependent manner. In the model, the rhythmicity was implemented by a periodic input of similar magnitude on the two comparator populations. This periodic stimulus could originate from an intrinsic rhythmic tectal activity, a rhythmic tectal afferent, or a proprioceptive input associated with the eye saccades. We found that paralyzed larvae incapable of moving their eyes did not show, following the cessation of the CS, spontaneous rhythmic activity among MAE direction-selective neurons (Figure S4). Thus, we suggest that the neuronal rhythmicity is generated by the closed loop between the neuronal command to move the eyes and the eyes' proprioception induced by the physical movement of the eye.

Simulations of the model resembled the experimental results (Figures 7B and 7C; Figures S5C–S5F). Before the CS, the two comparator populations received similar inputs; thus, each population won in an alternative manner (Laing and Chow, 2002). Fluctuations in the modeled rhythmic inputs made this alternation imperfect. During the CS, inputs from the CS direction-selective neurons biased the competition in favor of the CS comparator neurons. Following the cessation of the CS, spontaneous inputs from the non-habituated MAE direction-selective neurons were slightly larger than those from the habituated CS direction-selective ones. Thus, they generated a bias in favor of the MAE comparator. The habituation slowly decreased until

it reached control values, bringing the model back to the pre-CS regime. Using parameters obtained from experimental data (behavioral and neuronal adaptation time constants and the mean and peaks of spontaneous activity frequency of CS direction-selective neurons; [Supplemental Experimental Procedures](#)), the model was capable of reproducing the temporal dynamics of the neuronal and MAE-like behavior and the spontaneous scanning-like eye movements. The dependence of the MAE duration on the duration of the CS was also reproduced relatively well ([Figure 7C](#); [Figures S5C–S5F](#)). These results suggest that our experimental findings are sufficient for the generation of several features associated with larva's MAE-like behavior. We thus believe that the tectal circuit underlying the comparison between the activity of the CS direction-selective neurons and that of the MAE direction-selective neurons constitutes a plausible explanation for the observed MAE-like behavior.

DISCUSSION

Previous studies have found MAE or MAE-like behaviors in a variety of organisms ([Barlow and Hill, 1963](#); [Giaschi et al., 1993](#); [Mather et al., 1998](#); [Niu et al., 2006](#); [Petersen et al., 1985](#); [Srinivasan, 1993](#); [Wohlgemuth, 1911](#)). Here, we report for the first time that zebrafish perceive MAE during early larval development. Thus, the ability to induce MAE in developing neuronal circuits supports the hypothesis that MAE is generated as an unavoidable consequence of the brain's basic computational principles for visual motion detection.

In contrast to humans, zebrafish larvae are capable of perceiving MAE in the absence of any visual feedback (in darkness), suggesting that MAE reflects exclusively visual motion perception without the involvement of visual detection and that visual motion perception can emerge solely from the neuronal circuits' spontaneous dynamics. This difference could emerge from MAE-associated additional adaptations in cortical areas (e.g., V1 and middle temporal area [MT]; [Kohn and Movshon, 2003](#); [Watamaniuk and Heinen, 2007](#)). These cortical circuits could have evolved to reduce undesirable motion perception or afternystagmus following sustained visual motion.

Similar to previous studies ([Kubo et al., 2014](#); [Roesser and Baier, 2003](#)), we observed that the optic tectum was not necessary for the generation of OKR. However, tectal ablations prevented the behavioral habituation to the CS (as demonstrated by the habituation of OKR) and influenced the generation of the MAE-like behavior. Also, given that eye movements were not necessary for the generation of MAE and that optokinetic MAE-like behavior was observed within the frame of OMR, we hypothesized that the generation of MAE was probably linked to sensory brain regions rather than motor centers.

Using two-photon calcium imaging of GCaMP3 larvae, we observed that MAE-like behavior was associated with the habituation of tectal neurons sensitive to the direction of the CS, a habituation that was not relayed from the retina. Thus, we suggest that the optic tectum is not necessary for the generation of the OKR but is indispensable for the initial strong novelty response and its subsequent habituation. Tectal modulation of OKR could be achieved via recurrent projections between the

optic tectum and the pretectum ([Vanegas et al., 1984](#)). The latter has been shown to be necessary and sufficient for the generation of OKR ([Kubo et al., 2014](#)). Furthermore, by simultaneously monitoring eye movements and the optic tectum neuronal dynamics in awake intact larvae, we observed a specific subgroup of MAE direction-selective neurons whose synchronous rhythmic activities were associated with optokinetic MAE-like behavior.

We created an empirical mathematical model in which habituation of the tectal direction-selective neurons generates an imbalance between the spontaneous activity of the MAE direction-selective and that of the CS direction-selective neuronal circuits. This imbalance is then computed by a tectal circuit comparator, which generates the directional eye and tail motor commands. The model was capable of reproducing both behavioral and neuronal-circuit-dynamic aspects of MAE, as well as spontaneous eye-movement kinematics.

This model proposes a simple functional neuronal circuit capable of generating perception of visual motion in zebrafish. More specifically, we suggest that motion perception, at least within the context of MAE, emerges from the ability of the direction-selective tectal neurons to drive a tectal comparator circuit.

Finally, neuronal sustained activity has been traditionally associated with working memory processes lasting for tens of seconds ([Quintana and Fuster, 1999](#); [Romo et al., 1999](#); [Sumbre et al., 2008](#)). Here, we observed that visually induced sustained rhythmic activities could also underlie perceptual neuronal processes, such as visual motion perception lasting for an unprecedented extent (hundreds of seconds). Our empirical model sheds light on a potential circuit mechanism for the generation of these sustained activities underlying the perception of MAE.

EXPERIMENTAL PROCEDURES

Zebrafish Preparation and Transgenic Lines

Zebrafish embryos were collected and raised at 28.5°C in 0.5× E3 embryo medium (E3 in mM: 5 NaCl, 0.17 KCl, 0.33 CaCl₂, 0.33 MgCl₂ pH 7.2; [Westerfield, 1995](#)). Larvae were kept under 14/10 hours on/off light cycles and fed starting at 6 dpf. All experiments were approved by Le Comité d'Éthique pour l'Expérimentation Animale Charles Darwin (03839.03).

Visual Stimuli

The visual stimulus consisted of a square-wave moving grating (conditioning stimulus [CS]) covering the entire stimulation field (~90° × 90°, azimuth × height, of the larva's field of view). In order to minimize projection distortions due to the curvature of the screen, we calibrated the projection pattern according to the chamber's radius. Visual stimulation was generated with Psychophysics Toolbox extensions ([Brainard, 1997](#); [Pelli, 1997](#)) for Matlab (The MathWorks).

Two-Photon Calcium Imaging

We used a custom-made two-photon microscope. The setup was based on a MOM system (Sutter) with a 25× NA 1.05 Olympus objective and a Mai-Tai DeepSee Ti:sapphire laser tuned at 920 nm. The output power at the focal plane was less than 3 mW. The filters consisted of an FF705 dichroic filter (objective dichroic), an AFF01-680 short-path filter (IR Blocker), and an FF01 520/70 band-pass filter, all from Semrock. The photomultiplier (PMT) was an H1070 (gallium arsenide phosphide [GaAsP]) from Hamamatsu. The emission signal was pre-amplified with an SR-570 (Stanford Research Systems) and acquired using ScanImage ([Pologruto et al., 2003](#)) at 3.91 Hz, with 256 × 256 pixels resolution.

Detection of Significant Ca²⁺ Events

In order to infer the Ca²⁺-related fluorescence events associated with neuronal activity, we calculated the statistical significance of single-neuron calcium dynamics in an adaptive and unsupervised manner. We considered that any event in the fluorescence time series data belonged to either a neuronal activity process, A, or an underlying noisy baseline, B. In order to discriminate, with a desired degree of confidence, between these two sources, we built a data-driven model of B. Moreover, we took into account the biophysical constraints of the fluorescent calcium indicator (GCaMP3 fluorescence decay time constant). Then, we applied a Bayesian odds ratio estimation framework. Non-significant portions of the DF/F traces were then set equal to 0 in all subsequent analysis (for more details, see Romano et al., 2015).

SUPPLEMENTAL INFORMATION

Supplemental Information includes Supplemental Experimental Procedures, five figures, one table, and three movies and can be found with this article online at <http://dx.doi.org/10.1016/j.celrep.2016.09.065>.

AUTHOR CONTRIBUTIONS

V.P.-S. carried out the behavior and imaging experiments and analyzed the data. M.N. carried out and analyzed behavioral experiments. A.K. and V.H. implemented the model and contributed to writing the manuscript. A.K. analyzed data and performed the ablation experiments and the imaging experiments in paralyzed larvae. K.L. carried out optogenetics essays and built the optogenetic setup. S.A.R. participated in discussions about the data, developed imaging analysis, wrote software, and built the setup. A.J. participated in discussions and developed tools for tail behavior data analysis. M.D. performed initial behavioral experiments and data analysis. T.P. generated the elav3:GCaMP3 and Tg(UAS:GCaMP3) transgenic lines. M.H. performed tail-behavior experiments. V.C. participated in the tectal ablation experiments. J.B.-W. generated the elav3:GCaMP5 transgenic line. V.P.-S. and G.S. conceived the experiments and the model, built the setup, and wrote the manuscript.

ACKNOWLEDGMENTS

We thank P. Mamassian, H. Baier, F. Kubo, and P. Gongal for comments on the manuscript and B. Gutkin and M.S. Murmu for helpful discussions. This work was supported by ERC STG 243106, IRG 239512, and Ville de Paris 2009 grants to G.S.; Ministère de l'Enseignement Supérieur et de la Recherche fellowships to V.P.-S. and M.D.; and a Fondation pour la Recherche Médicale fellowship to V.P.-S., ANR-10-LABX-54 MEMO LIFE and ANR-11-IDEX-0001-02, PSL Research University.

Received: June 13, 2016

Revised: August 22, 2016

Accepted: September 20, 2016

Published: October 18, 2016

REFERENCES

- Anstis, S., Verstraten, F.A.J., and Mather, G. (1998). The motion aftereffect. *Trends Cogn. Sci.* *2*, 111–117.
- Arrenberg, A.B., Del Bene, F., and Baier, H. (2009). Optical control of zebrafish behavior with halorhodopsin. *Proc. Natl. Acad. Sci. USA* *106*, 17968–17973.
- Barlow, H.B., and Hill, R.M. (1963). Evidence for a physiological explanation of the waterfall phenomenon and figural after-effects. *Nature* *200*, 1345–1347.
- Biehl, W. (1898). *Aristotelis Parva Naturalia* (B.G. Teubner).
- Brainard, D.H. (1997). The psychophysics toolbox. *Spat. Vis.* *10*, 433–436.
- Braun, D.I., Pracejus, L., and Gegenfurtner, K.R. (2006). Motion aftereffect elicits smooth pursuit eye movements. *J. Vis.* *6*, 671–684.
- Burrill, J.D., and Easter, S.S., Jr. (1994). Development of the retinofugal projections in the embryonic and larval zebrafish (*Brachydanio rerio*). *J. Comp. Neurol.* *346*, 583–600.
- Chaudhuri, A. (1990). Modulation of the motion aftereffect by selective attention. *Nature* *344*, 60–62.
- Chen, C.-C., Huang, M.Y.-Y., Weber, K.P., Straumann, D., and Bockisch, C.J. (2014). Afternystagmus in darkness after suppression of optokinetic nystagmus: an interaction of motion aftereffect and retinal afterimages. *Exp. Brain Res.* *232*, 2891–2898.
- Chou, M.-Y., Amo, R., Kinoshita, M., Cherng, B.-W., Shimazaki, H., Agetsuma, M., Shiraki, T., Aoki, T., Takahoko, M., Yamazaki, M., et al. (2016). Social conflict resolution regulated by two dorsal habenular subregions in zebrafish. *Science* *352*, 87–90.
- Dunn, T.W., Gebhardt, C., Naumann, E.A., Riegler, C., Ahrens, M.B., Engert, F., and Del Bene, F. (2016). Neural circuits underlying visually evoked escapes in larval zebrafish. *Neuron* *89*, 613–628.
- Easter, S.S., Jr., and Nicola, G.N. (1997). The development of eye movements in the zebrafish (*Danio rerio*). *Dev. Psychobiol.* *31*, 267–276.
- Gabriel, J.P., Trivedi, C.A., Maurer, C.M., Ryu, S., and Bollmann, J.H. (2012). Layer-specific targeting of direction-selective neurons in the zebrafish optic tectum. *Neuron* *76*, 1147–1160.
- Gahtan, E., Tanger, P., and Baier, H. (2005). Visual prey capture in larval zebrafish is controlled by identified reticulospinal neurons downstream of the tectum. *J. Neurosci.* *25*, 9294–9303.
- Gebhardt, C., Baier, H., and Del Bene, F. (2013). Direction selectivity in the visual system of the zebrafish larva. *Front. Neural Circuits* *7*, 111.
- Giaschi, D., Douglas, R., Marlin, S., and Cynader, M. (1993). The time course of direction-selective adaptation in simple and complex cells in cat striate cortex. *J. Neurophysiol.* *70*, 2024–2034.
- Grama, A., and Engert, F. (2012). Direction selectivity in the larval zebrafish tectum is mediated by asymmetric inhibition. *Front. Neural Circuits* *6*, 59.
- Huang, Y.-Y., and Neuhauss, S.C.F. (2008). The optokinetic response in zebrafish and its applications. *Front. Biosci.* *13*, 1899–1916.
- Hunter, P.R., Lowe, A.S., Thompson, I.D., and Meyer, M.P. (2013). Emergent properties of the optic tectum revealed by population analysis of direction and orientation selectivity. *J. Neurosci.* *33*, 13940–13945.
- Kohn, A., and Movshon, J.A. (2003). Neuronal adaptation to visual motion in area MT of the macaque. *Neuron* *39*, 681–691.
- Kubo, F., Hablitzel, B., Dal Maschio, M., Driever, W., Baier, H., and Arrenberg, A.B. (2014). Functional architecture of an optic flow-responsive area that drives horizontal eye movements in zebrafish. *Neuron* *81*, 1344–1359.
- Laing, C.R., and Chow, C.C. (2002). A spiking neuron model for binocular rivalry. *J. Comput. Neurosci.* *12*, 39–53.
- Ma, L.-H., Grove, C.L., and Baker, R. (2014). Development of oculomotor circuitry independent of hox3 genes. *Nat. Commun.* *5*, 4221.
- Masland, R.H. (1969). Visual motion perception: experimental modification. *Science* *165*, 819–821.
- Mather, G., Verstraten, F., and Anstis, S.M., eds. (1998). *The Motion Aftereffect: A Modern Perspective* (MIT Press).
- Mather, G., Pavan, A., Campana, G., and Casco, C. (2008). The motion aftereffect reloaded. *Trends Cogn. Sci.* *12*, 481–487.
- Miri, A., Daie, K., Arrenberg, A.B., Baier, H., Aksay, E., and Tank, D.W. (2011). Spatial gradients and multidimensional dynamics in a neural integrator circuit. *Nat. Neurosci.* *14*, 1150–1159.
- Nevin, L.M., Robles, E., Baier, H., and Scott, E.K. (2010). Focusing on optic tectum circuitry through the lens of genetics. *BMC Biol.* *8*, 126.
- Nikolaou, N., Lowe, A.S.S., Walker, A.S.S., Abbas, F., Hunter, P.R.R., Thompson, I.D.D., and Meyer, M.P.P. (2012). Parametric functional maps of visual inputs to the tectum. *Neuron* *76*, 317–324.
- Niu, Y.-Q., Xiao, Q., Liu, R.-F., Wu, L.-Q., and Wang, S.-R. (2006). Response characteristics of the pigeon's pretectal neurons to illusory contours and motion. *J. Physiol.* *577*, 805–813.

- Okamoto, H., Agetsuma, M., and Aizawa, H. (2012). Genetic dissection of the zebrafish habenula, a possible switching board for selection of behavioral strategy to cope with fear and anxiety. *Dev. Neurobiol.* *72*, 386–394.
- Orger, M.B., and Baier, H. (2005). Channeling of red and green cone inputs to the zebrafish optomotor response. *Vis. Neurosci.* *22*, 275–281.
- Orger, M.B., Smear, M.C., Anstis, S.M., and Baier, H. (2000). Perception of Fourier and non-Fourier motion by larval zebrafish. *Nat. Neurosci.* *3*, 1128–1133.
- Orger, M.B., Kampff, A.R., Severi, K.E., Bollmann, J.H., and Engert, F. (2008). Control of visually guided behavior by distinct populations of spinal projection neurons. *Nat. Neurosci.* *11*, 327–333.
- Paquet, D., Bhat, R., Sydow, A., Mandelkow, E.-M., Berg, S., Hellberg, S., Fältling, J., Distel, M., Köster, R.W., Schmid, B., and Haass, C. (2009). A zebrafish model of tauopathy allows in vivo imaging of neuronal cell death and drug evaluation. *J. Clin. Invest.* *119*, 1382–1395.
- Pelli, D.G. (1997). The VideoToolbox software for visual psychophysics: transforming numbers into movies. *Spat. Vis.* *10*, 437–442.
- Petersen, S.E., Baker, J.F., and Allman, J.M. (1985). Direction-specific adaptation in area MT of the owl monkey. *Brain Res.* *346*, 146–150.
- Pologruto, T.A., Sabatini, B.L., and Svoboda, K. (2003). ScanImage: flexible software for operating laser scanning microscopes. *Biomed. Eng. Online* *2*, 13.
- Portugues, R., and Engert, F. (2009). The neural basis of visual behaviors in the larval zebrafish. *Curr. Opin. Neurobiol.* *19*, 644–647.
- Portugues, R., Feierstein, C.E., Engert, F., and Orger, M.B. (2014). Whole-brain activity maps reveal stereotyped, distributed networks for visuomotor behavior. *Neuron* *81*, 1328–1343.
- Qian, H., Zhu, Y., Ramsey, D.J., Chappell, R.L., Dowling, J.E., and Ripps, H. (2005). Directional asymmetries in the optokinetic response of larval zebrafish (*Danio rerio*). *Zebrafish* *2*, 189–196.
- Quintana, J., and Fuster, J.M. (1999). From perception to action: temporal integrative functions of prefrontal and parietal neurons. *Cereb. Cortex* *9*, 213–221.
- Rinner, O., Rick, J.M., and Neuhauss, S.C.F. (2005). Contrast sensitivity, spatial and temporal tuning of the larval zebrafish optokinetic response. *Invest. Ophthalmol. Vis. Sci.* *46*, 137–142.
- Roeser, T., and Baier, H. (2003). Visuomotor behaviors in larval zebrafish after GFP-guided laser ablation of the optic tectum. *J. Neurosci.* *23*, 3726–3734.
- Romano, S.A.A., Pietri, T., Pérez-Schuster, V., Jouary, A., Haudrechy, M., and Sumbre, G. (2015). Spontaneous neuronal network dynamics reveal circuit's functional adaptations for behavior. *Neuron* *85*, 1070–1085.
- Romo, R., Brody, C.D., Hernández, A., and Lemus, L. (1999). Neuronal correlates of parametric working memory in the prefrontal cortex. *Nature* *399*, 470–473.
- Schoonheim, P.J., Arrenberg, A.B., Del Bene, F., and Baier, H. (2010). Optogenetic localization and genetic perturbation of saccade-generating neurons in zebrafish. *J. Neurosci.* *30*, 7111–7120.
- Srinivasan, M.V. (1993). Even insects experience visual illusions. *Curr. Sci.* *64*, 649–655.
- Sumbre, G., Muto, A., Baier, H., and Poo, M.M. (2008). Entrained rhythmic activities of neuronal ensembles as perceptual memory of time interval. *Nature* *456*, 102–106.
- Thompson, P., and Burr, D. (2009). Visual aftereffects. *Curr. Biol.* *19*, R11–R14.
- Vanegas, H., Ebbesson, S.O., and Laufer, M. (1984). Morphological aspects of the teleostean optic tectum. In *Comparative Neurology of the Optic Tectum*, H. Vanegas, ed. (Plenum Press), pp. 93–120.
- Watamaniuk, S.N.J.S., and Heinen, S.J. (2007). Storage of an oculomotor motion aftereffect. *Vision Res.* *47*, 466–473.
- Westerfield, M. (1995). *The Zebrafish Book: A Guide for the Laboratory Use of Zebrafish (Danio rerio)* (University of Oregon Press).
- Wohlgemuth, A. (1911). On the affect-effect of seen movement. *Br. J. Psychol.* *1*, 1–115.

Cell Reports, Volume 17

Supplemental Information

Sustained Rhythmic Brain Activity Underlies

Visual Motion Perception in Zebrafish

Verónica Pérez-Schuster, Anirudh Kulkarni, Morgane Nouvian, Sebastián A. Romano, Konstantinos Lygdas, Adrien Jouary, Mario Dippopa, Thomas Pietri, Mathieu Haudrechy, Virginie Candat, Jonathan Boulanger-Weill, Vincent Hakim, and Germán Sumbre

Supplemental Experimental Procedures

Zebrafish preparation and transgenic lines

For all experiments we used wild type or nacre (Lister et al., 1999) (*mitfa*^{-/-}) zebrafish between 7 and 9 days post-fertilization (dpf). In addition, several transgenic lines were also generated.

To monitor the optic tectum activity we created a *Huc:GCaMP3* Nacre transgenic zebrafish line (Panier et al., 2013). The *tol2* *Huc:GCaMP3* vector was built by successive ligations of a 3.2 kb fragment of the zebrafish *HuC* (*elav3*) promoter (Park et al., 2000) (gift from HC Park, Kyungpook National University, Korea.), then *GCaMP3* calcium probe (Tian et al., 2009) (gift from L. Looger, Howard Hughes Medical Institute, Ashburn, Virginia, USA) into *pT2KXIG* in (from K. Kawakami, National Institute of Genetics, Shizuoka, Japan). The *HuC* promoter drives the expression of a RNA-binding protein and has been involved in neuronal differentiation. In zebrafish, the 3.2 kb proximal region encompassing the translation start site from 2771 base pairs of the 5'- upstream sequence up to +383/+385, has been shown to be sufficient to target specifically and efficiently all differentiated neurons (Park et al., 2000). One-cell stage Nacre zebrafish embryos were injected with 20 ng of the DNA plasmid and 25 ng of transposase RNA (generated from *pCS-TP* plasmid, K. Kawakami). Injected embryos were raised to adulthood and crossed individually with Nacre fish to obtain F1 embryos. These embryos were then screened and selected according to their level of transgene expression. The embryos with the strongest expression were raised to adulthood and incrossed to obtain the homozygous *HuC:GCaMP3^{GS5}* line (*ens100Tg* at ZFIN).

To record the activity of retinal ganglion neurons we used transgenic zebrafish expressing *GCaMP3* under the *ath5* promoter through the *UAS/Gal4* genetic system (Halpern et al., 2008). The *ath5* (*atoh7*) gene is expressed almost exclusively in the retina and predominantly in RGCs. We thus created the

Tg(UAS:GCaMP3)^{GS10} Nacre zebrafish line, where the calcium probe was placed under the control of 6 repetitions of the UAS (Upstream Activating Sequence).

The lines Tg(atoh7:Gal4)s1992t;Tg(UAS:Kaede)1999t (E. Baier) and Et(-1.5hsp70l:Gal4-VP16)s1113t;Tg(UAS:GCaMP3)^{GS10} were then intercrossed them and the progeny was selected accordingly to the expected pattern of expression of the Tg(atoh7:Gal4)s1992t transgene, and then raised to adulthood. To eliminate the Tg(UAS:Kaede)1999t transgene, DNA extracted from fin-clips was submitted to PCR to specifically amplify a fragment of the Kaede gene. This double selection allowed us to generate a Tg(atoh7:Gal4)s1992t;Tg(UAS:GCaMP3)^{GS10} line (referred as ath5:Gal4;UAS:GCaMP3).

To inhibit eye movements during OKR using optogenetics and spatially selected illumination via an optic fiber (Arrenberg et al., 2009; Schoonheim et al., 2010) we used the Tg(HuC:Gal4);Tg(UAS:eNpHR-mCherry)s1988t (E. Baier) zebrafish line, referred as to the HuC:Gal4;UAS:eNpHR-mCherry line.

To generate the HuC:GCaMP5G line, a tol2 HuC:GCaMP5G vector was built by insertion of a 3.2 kb fragment of the zebrafish HuC (elav3) pan-neuronal promoter (Park et al., 2000), then the genetically encoded Ca²⁺ indicator GCaMP5G (Akerboom et al., 2012) was inserted into pT2KXIG (from K. Kawakami). One-cell-stage nacre zebrafish embryos were injected with 10 ng of the plasmid DNA and 25 ng of transposase RNA (generated from pCS-TP plasmid, K. Kawakami). Injected embryos were raised to adulthood and crossed individually with nacre fish to obtain F1 embryos. These embryos were then screened and selected according to their level of transgene expression. The embryos with the highest expression were raised to adulthood and incrossed to obtain the homozygous HuC:GCaMP5G^{GS16} line.

In all cases, embryos were collected and raised at 28.5 °C in 0.5x E3 embryo medium (E3 in mM: 5 NaCl, 0.17 KCl, 0.33 CaCl₂, 0.33 MgCl₂ pH 7.2, (Westerfield, 1995). Larvae were kept under 14/10

hours on/off light cycles and fed starting at 6 dpf. All experiments were approved by Le Comité d'Éthique pour l'Expérimentation Animale Charles Darwin (03839.03).

Visual stimuli

The visual stimulus consisted of a square-wave moving grating (conditioning stimulus, CS) covering the entire stimulation field ($\sim 90^\circ \times 90^\circ$, azimuth x height, of the larva's field of view). The stimulus was presented at three different velocities, 17, 26 and 59 °/s, with angular sizes of 13.75° or 27.5°. CS durations were: 50, 100, 200, 250, 300, 400 and 500 s. The CS was presented in both directions, rightward and leftward. In order to minimize projection distortions due to the curvature of the screen, we calibrated the projection pattern according to the chamber's radius.

Visual stimulation were generated with Psychophysics Toolbox extensions (Brainard, 1997; Pelli, 1997) for Matlab (The MathWorks, Inc)).

Zebrafish larva motor behavior

Behavioral experiments were performed at 7 to 9 dpf, either using wild-type or nacre larvae. Larvae were immobilized in low-melting agarose (Invitrogen, concentration varying between 1.8% and 2%) and placed on an elevated stage within a cylindrical chamber filled with 0.5x E3 embryo medium. The agarose around the eyes or the tail was removed with an insect pin so that the eyes or the tail could freely move. Visual stimuli were projected on a screen (#216 White Diffusion, Rosco Cinegel) placed around the surface of the cylinder chamber using a pico-projector (refresh rate: 60 Hz., ADPP-305, Adapt mobile, **Figure 1A**). Eye rotations or tail movements were recorded from the larva's dorsal side using an objective, a tube lens, and a video camera (DMK 22BUC03, The Imaging Source). Videos were acquired using IC capture (The Imaging Source) at 60 Hz for eye rotations and 76 Hz for tail movements. Larvae were illuminated with an infra-red LED (920nm). To synchronize the video

recordings with the stimuli we used an I/O TTL board (ActiveWire, inc) controlled by Matlab (The MathWorks, Inc). Eye and tail movements were then analyzed offline using custom-written programs in Matlab (The MathWorks, Inc).

Calculation of the eye's orientation

To compute the eye rotations we thresholded the images for each single frame. Then morphological dilatation and erosion algorithms were applied to obtain only two objects representing each of the eyes. Once the eyes were detected, their orientation was calculated as the angle between the longest axis of an ellipse fitted to the objects representing the eyes (the elliptic eye perimeter), and the external (camera) X axis (**Figure 1B**). Since the angle value is arbitrary and it depends on the orientation in which we placed the larva with respect to the camera, for visualization purposes, the mean rotation for each eye was subtracted to obtain a zero baseline. All calculations were performed in Matlab (The MathWorks, Inc).

Eye angular velocity was calculated as $V = \frac{\Delta h}{\Delta t}$ where Δh is the amplitude of the eye movement (the eye's total displacement) and Δt the duration.

Classification of eye movements

Once eye orientations were calculated, a semi-automatic custom-made program was used to detect each type of eye movements (left or right saccade, left or right smooth pursuit and stereotypical spontaneous eye movements). We first calculated the eye rotation velocity. Thresholding this data enabled us to identify fast movements corresponding to saccades (fast eye movements). Slow movements between two saccades were defined as smooth pursuits if the direction of the subsequent saccade was opposite to that of the slow movement. We defined the unit 'pursuit-saccade movement' when the direction of

the fast movement was inverted with respect to the smooth pursuit movement. We defined eye fixations or drift movements as slow movements between two saccades in opposite directions. Accordingly, the spontaneous eye movement unit was defined as a slow movement followed by a saccade. Finally, potential detection mistakes were manually curated for all analyzed data.

Calculation of the tail's orientation

To calculate the tail's orientation, we thresholded the tail image for each video frame by applying a filter and binarization. Once the tail's morphology was recognized, we calculated its orientation as the angle between the longest axis of the elliptic perimeter of the body and the external X axis (camera, **Figure 2F**). As for the eye's detection where the angle value is arbitrary and it depends on the position that the zebrafish larva with respect to the camera, the mean of the tail's angle was subtracted for normalization purposes. All calculations were performed by custom-made functions written in Matlab (The MathWorks, Inc).

Behavior and optogenetics

For local spatial stimulation of eNpHR expressed pan-neuronally (HuC:Gal4;UAS:eNpHR-mCherry), we used a 105 μm optic fiber (AFS105/125Y 0.22 NA, Thorlabs), coupled to a 565 nm light emitting diode (LED, M565F1, Thorlabs). To enable precise positioning of the fiber above different brain areas, we mounted it via a bended glass pipette, on a micromanipulator (Model FX-117, Electron Microscopy Sciences, **Figures 2A and 2B**). For all the experiments the fiber was positioned above a unilateral region of the hindbrain, most likely including rhombomere 5, in an orthogonal orientation with respect to the dorsal surface of the larva. The output intensity was measured with a power meter to be in the order of 1.8 mW/mm².

Behavior under the two-photon microscope

In order to simultaneously monitor neuronal network Ca^{2+} dynamics and motor behavior we added to the two-photon imaging system a mini-microscope (DZ 1/L.75-5, The Imaging Source) connected to a video camera (DMK 21BF04, The Imaging Source). The larva's behavior was recorded from below (larva's ventral side, **Figures S2C and S2F**). To avoid image saturation by the infrared laser we used a FF01-842 Semrock short-pass filter. An infra-red LED (820nm) was used for illumination purposes. To synchronize the video recordings with the visual stimuli and the two-photon imaging acquisition, we used an I/O TTL board (ActiveWire, inc).

Visual stimulation under the two-photon microscope

As for the behavioral experiments, visual stimuli were presented on a curved screen (#216 White Diffusion, Rosco Cinegel) around the perimeter of the cylinder chamber using a pico-projector (refresh rate: 60 Hz, ADPP-305, Adapt mobile). Stimulation protocols were written using the Psychophysics Toolbox extensions (Brainard, 1997; Pelli, 1997) for MATLAB (The MathWorks, Inc.). To avoid interference with the GCaMP3 emission signal (peaking at 547 nm and filtered using a 520/70 band-pass filter), only the projector's red (620 nm) LED was used, and a BLP01-561 Semrock long-pass filter was placed in the front of the projector. In addition, we also reduced the size of the conditioning stimulus by using repetitive single-light-moving bars instead of a whole-field moving grating (**Figures S2E and 2F**). Bars were 4° wide moved at $45^\circ/\text{s}$. The repetitive moving-bars stimulus was as efficient as the whole-field moving grid in inducing MAE (**Figure S2D**).

Quantification of the optokinetic MAE-like behavior

To quantify the MAE-like behavior in zebrafish larvae, we calculated the difference between the mean number of pursuits in the direction of the CS and the mean number of pursuits in the MAE direction,

with respect to the total number of the three different types of eye movements (pursuits in the MAE and CS directions, and the spontaneous eye movements). This ratio was defined as the *MAE Index*.

Mathematically, we defined the *MAE index* as:

$$MAE\ index = \frac{\#\ pursuit_{MAE\ dir} - \#\ pursuit_{CS\ dir}}{\#\ pursuit_{MAE\ dir} + \#\ pursuit_{CS\ dir} + \#\ spontaneous} \quad (1)$$

For statistical purposes, we defined the control index as the *MAE index* during spontaneous eye movements before the presentation of a CS (stationary grating for 500 s). We thus claimed that the zebrafish larvae generate an optokinetic MAE-like behavior when we observed a significance difference between the *MAE index* and the *control index*.

The duration of MAE was computed as the first time bin (bins of 50 s) in which the *MAE index* was significantly larger than the control index.

Two-photon ablations

For the ablations we used a two-photon laser (920 nm and ~10 mW after the objective) to scan each optical plane for 1-3 min (the duration gradually increased as we scanned more ventral layers). For the tectal ablations, the optical planes were separated by 10-12 μm . For the interpeduncular nucleus, the optical planes were separated by 6 μm .

To quantify the effect of the ablations on the CS-induced eye movements (OKR), and the optokinetic MAE-like behavior, we calculated for each experiment, the difference in the number of pursuits in the CS direction and in the MAE direction for time bins of 50 s. We then computed the mean of this difference for all experiments (n=26, 4 fishes). We estimate that the tectal ablations induced apoptosis

in around 85% of the tectal neurons, what could explain why tectal ablations significantly reduced but did not completely prevent MAE.

Unfortunately, due to technical reasons (tectal specificity of tested transgenic lines and high-power illumination), optogenetic or genetic silencing of the optic tectum was not possible.

Labeling apoptotic neurons with Acridine

To test whether the tectal laser ablations induced neuronal death, we use the apoptosis marker Acridine. For this purpose, we submerged the larvae in a 3 % Acridine in embryo medium, for 30 min in the dark. Then, the larvae were rinsed twice with fresh embryo medium. After 5 min the larvae were immobilized in low-melting agarose within the recording chamber, and imaged using a two-photon microscope tuned to 970 nm, or a confocal microscope and a 488 nm CW laser.

Two-photon calcium imaging

We used a custom-made two-photon microscope. The set-up was based on a MOM system (Sutter) with a 25x NA 1.05 Olympus objective and a Mai-Tai DeepSee Ti:sapphire laser tuned at 920 nm. The output power at the focal plane was less than 3 mW. The filters consisted of a FF705 dichroic (objective dichroic), a AFF01-680 short path (IR Blocker) and a FF01 520/70 band-pass filter, all from Semrock. The PMT was a H1070 (GaAsP) from Hamamatsu. The emission signal was pre-amplified with a SR-570 (Stanford Research Systems) and acquired using ScanImage (Pologruto et al., 2003) at 3.91 Hz, with 256×256 pixels resolution.

To restrain the larvae under the two-photon microscope, we embedded them within a drop of 2 % low-melting agarose (Invitrogen) in 0.5x E3 embryo medium, on an elevated stage in the center of a cylindrical chamber filled with 0.5x E3 embryo medium. This chamber permitted the larva to have an

unobstructed vision of the visual stimuli on the projection screen. Larvae were left to rest and adapt to the dark for at least 30 min before the beginning of the experiments.

To study neuronal network dynamics in the optic tectum, we used the HuC:GCaMP3^{GS5}. For the experiments, we sequentially imaged different tectal planes. We started at a plane 30 μm below the skin's surface of the larva's dorsal side, and ended at 100 μm below.

To image the dynamics of the RGCs (retina output), we used the ath5:Gal4; UAS:GCaMP3 line, which enabled monitoring the activity of the RGC terminals at the tectal neuropil.

The experiments in which we measured the habituation of direction-selective tectal and retinal neurons were performed under the action of a paralyzer to prevent eye movements during the visual stimulation. For this purpose, the low-melting agarose solution used to immobilized the larva contained 0.3 mg/ml of Pancuronium bromide (TOCRIS, bioscience), a curare-derivative competitive acetylcholine antagonist of neuromuscular junctions, thus blocking neuromuscular transmission. In addition, the agarose around the eyes was not removed.

Two-photon calcium imaging data processing

Registration

The series of images during a given experiment were saved as TIFF stacks. To compensate for possible slow drifts in the XY plane, we registered the stacks using the Image J plugin Template Matching (Tseng et al., 2012), in combination with a custom-made algorithm (Matlab, The MathWorks, Inc) to further smooth the registration. We discarded videos with drifts in the ventro-dorsal direction (out-of-plane displacements).

Movement artifacts

Movement artifacts were detected according to large deviations in the cross-correlation between successive frames. All frames with large deviations (z-score smaller than -3) were then manually inspected. Due to the agarose elasticity, the imaging plane almost invariantly returned to its original position, after observing movement artifacts. If this was not the case, the complete experiment was discarded. Artifact episodes rarely exceeded 5 consecutive frames in non-paralyzed larvae and 1 in paralyzed larvae. For the subsequent data analysis, we did not include frames showing moving artifacts. In average, we detected 100 frames with moving artifacts out of 12000 in non-paralyzed larvae and 10 in paralyzed larvae.

Segmentation of the optic tectum

Regions of interest (ROIs) corresponding to the imaged neurons were semi-automatically detected on a morphological basis by the analysis of time-averaged pictures of the imaged tectal region. We implemented a series of digital imaging processing techniques (Gonzalez et al., 2004) in a custom-made program, that produced putative ROIs layouts that were afterwards manually curated. GCaMP3 is mainly localized in the cytosol with minimal penetration to the cellular nuclei. The algorithm first identified neuronal ROIs that corresponded to individual nuclei. The latter were detected by local fluorescence intensity wells. In order to flatten non-relevant intensity fluctuations in these minima, the eroded version of the imaged region was morphologically reconstructed under the mask given by same image. Local minima were detected by applying a user-defined threshold to the extended-minima transform of the resulting image. Finally, to obtain the ROIs perimeters we took advantage of the high density of the tectal stratum periventriculare (SPV) neurons. We calculated the euclidean distance transform of the local-minima image and performed a watershed segmentation to obtain the boundaries between neurons. The obtained ROIs were manually inspected and corrected when needed. ROIs

typically included the neuronal nuclei and the thin cytosolic surrounding ring, conservatively excluding the outermost cytosolic perimeter that could potentially be subject of cross-neuron fluorescence contamination due to the high neuronal density (**Figure S2A**). This procedure gave similar results to fully-manual ROI selection, accelerated the process by ~5-fold and minimized human subjectivity (Romano et al., 2015).

We then computed the changes in calcium associated to the activity of each imaged neuron by averaging the fluorescence of all pixels within the ROIs, across time.

In few cases, we observed high-frequency non-Gaussian noise, most probably originated at the PMT (GaAsP, H1070 from Hamamatsu). This non-Gaussian noise was very rare and was observed, even when the laser was turned off. This noise implicated only single frames and single pixels. To filter out this noise, we first calculated, for all the imaging frames, the inter-frame fluorescence change coefficient of variation (CV) among the ROI pixels. For frames with $CV > 1$, we calculated the average fluorescence across pixels by leaving out the outlier pixel (i.e., pixels whose fluorescence change, z-scored across ROI pixels, was bigger than 1.5, (Romano et al., 2015)).

Segmentation of RGCs in the tectal neuropil

Since we recorded the RGCs calcium transients at their terminals situated in the tectal neuropil, we had no clear anatomical structure to compute ROIs corresponding to single terminals. In consequence, we implemented an algorithm where square regions of interest (SROIs) were calculated using a manual mask corresponding to the tectal neuropil perimeter. From this mask, we generated a grid based on SROIs of 4x4 pixels (1.12 pixels per μm). The 16 pixels corresponding to each SROI were averaged across time. SROIs with mean intensities below a threshold (threshold=0.0007 fluorescence intensity arbitrary units) were discarded. As a control, we also tested the adaptation results using smaller (2x2) and larger (6x6) SROIs. We observed no significant differences between the adaptation indexes of the

two controls and the SROIs of 4x4 pixels, for the 500 s after the cessation of CS ($p > 0.19$, Wilcoxon signed rank test).

Detection of significant Ca^{2+} events

In order to infer the Ca^{2+} related fluorescence events associated with neuronal activity, we calculated the statistical significance of single-neuron calcium dynamics in an adaptive and unsupervised manner. We considered that any event in the fluorescence time series data belongs to either a neuronal activity process, A, or to an underlying noisy baseline, B. In order to discriminate, with a desired degree of confidence, between these two sources, we built a data-driven model of B. Moreover, we took into account the biophysical constraints of the fluorescent calcium indicator (GCaMP3 fluorescence decay time constant). Then, we applied a Bayesian odds ratio estimation framework. Non-significant portions of the DF/F traces were then set equal to 0 in all subsequent analysis (for more details see (Romano et al., 2015)).

Detection of RGC terminals calcium activities

To detect calcium events associated with neuronal activity, we estimated the $\Delta F/F$ time series of each SROI as described for tectal neurons.

Calcium transients were considered as activity events when they surpassed a simple linear threshold equivalent to 2 standard deviations above the baseline (**Figure S2B**).

Calculation of direction selectivity

To compute the direction selectivity of each imaged neuron or each neuropil's SROI, we presented to the larvae moving light bars towards the left or towards the right, across the entire stimulation field. The direction selectivity was calculated from the average response to 5 moving light bars presented in

the same direction. Calcium events were considered as neuronal responses to the moving light bars if they occurred within a 2 s time window after the stimulus onset. Since the amplitude response of each neuron is different and we had to compare between all the neurons, we z-scored these responses across neurons (subtraction of the mean and divided by the s.d.). We considered a neuron as consistently responsive to a stimulus if it had an average response z-score bigger than -1 and responded to at least 3 out of 5 bars towards one given direction.

For each responding neuron, we calculated their left-right selectivity as the difference of their average neuronal responses to light bars moving in opposite directions (left or right), divided by their sum. When this value was bigger/smaller than 0.3/-0.3, the neuron was considered as left/right directionally selective, respectively.

Calculation of neuronal response adaptation

We quantified the responses to moving bars during the post-CS period as the sum of all the directional responses for each of the presented bars (CS direction-selective ROIs to moving bars in CS direction and MAE direction-selective ROIs to moving bars in the MAE direction). We called this value *SDSR* (*Sum of Direction Selective Responses*). Based on the *SDSR* value, we then defined the *Adaptation Index (AI)* as follows:

$$AI_i = \frac{SDSR_{CS}^i / SDSR_{CS}^{control} - SDSR_{MAE}^i / SDSR_{MAE}^{control}}{SDSR_{CS}^i / SDSR_{CS}^{control} + SDSR_{MAE}^i / SDSR_{MAE}^{control}} \quad (2)$$

where i is the i -th bar and $SDSR^{control}$ is the mean *Sum of Direction Selective Responses* during the pre-CS control period in the corresponding direction (CS/MAE).

The numerator in equation (2) allowed us to compare responses in both directions during post-CS control period. Both responses were normalized with respect to their control period. The denominator forces the *Adaptation index*, to have values ranging from -1 to 1. Since the index is a relative value, it is both, independent of the stimulus direction and the variability across experiments.

In the extreme cases, the index will have a value of -1 if responses of CS direction-selective neurons to moving bars in the CS direction are negligible compared to the responses in the control period. Such a value will indicate a very strong habituation of groups of neurons responding to the CS direction. An index of 0 will mean that both direction selective groups respond as during the control period. A value of 1 will indicate that group responding to the direction of MAE were habituated with respect to the responses in the CS direction. Since the *Adaptation index* is a relative ratio between the responses to the two directions, before and after the presentation of the CS, positive or negative values could also represent an increase in the response to the null direction (non-preferred direction) rather than a habituation of the preferred direction. However, more detailed analysis showed that the latter was never the case.

Cross-correlation between neuronal activity and eye kinematics

In order to compare the cross correlation between the activity of MAE direction-selective neurons and the eye pursuits in the MAE direction across different experiments, we processed the two signals in each experiment as follows. We first compensated for the small drifts in the eye rotations signal by subtracting the baseline. The latter was calculated using a running average (time window of 800 frames). We then rectified the eye rotations signal and normalized it. Finally, we divided it by the 95 percentile value of the signal. For the neurons selective to the MAE direction, we calculated the mean neuronal activity of the MAE direction-selective neurons. To test whether the correlations were significant, we generated a null model for the neuronal activity. To that end, we shuffled the spike times

of each neuron during the first 300 s of the MAE duration while preserving the inter-spike interval distributions. The shuffling procedure was repeated 1000 times and the mean correlation of the null model datasets was obtained.

The MAE / CS imbalance index was calculated as the ratio of the difference of the maximum of the mean activity of the MAE direction-selective neurons and the maximum of the mean activity of the CS direction-selective neurons to their sum for each eye pursuit in the MAE direction. The imbalance index was taken into account only when either of these two values (the maximum of the mean activity of the MAE direction-selective neurons and the maximum of the mean activity of the CS direction-selective neurons), was larger than one s.d. above the mean activity of the respective neurons, during the first 300 s of MAE.

Classification of tectal neurons as direction selective or comparators

To discriminate between direction-selective neurons which show rhythmic activity associated with the eye pursuits in the CS direction, the eye pursuits in the MAE direction, or none, we computed the cross correlation between the eye rotations and the neuronal activity of individual MAE direction-selective neurons, throughout the entire experiment. The eye rotations were separated into two signals: the eye rotations in the CS direction and eye rotations in the MAE direction. These signals were normalized according to the 95 percentile to preserve the information of the relative amplitudes. To compare the resulting cross correlations across the different experiments, and to classify the different neurons as CS eye motion selective, MAE eye motion selective neurons, or none, we used a threshold representing 90 % of the sum of the mean correlations of all the neurons in both directions. The same threshold was used to compare the cross correlations of the neurons with the eye rotations in both directions. When the cross correlation of a neuron was greater than this threshold in either the direction of eye pursuits in the CS/MAE direction, we considered it as a CS/MAE eye-motion selective neuron, respectively.

Within the framework of the model, we refer to these neurons as the “comparator” neurons. All the other direction-selective neurons which had their cross correlation either greater than the threshold in both the directions or less than the threshold in the two directions were classified as direction-selective neurons.

Frequency analysis

The rhythmic conditioning stimulus induced both rhythmic eye movements and rhythmic neuronal tectal responses. Therefore, we performed frequency-domain analysis to infer the level of association between the optokinetic MAE-like behavior and the post-CS tectal activities. For this purpose, we considered eye movements and neuronal activities as point processes (binary events, (“<http://www.chronux.org/>,” 2013; Mitra and Bokil, 2008)).

The estimation of the frequency spectrum in noisy data segments of finite duration suffers from bias and variance problems that distort the underlying features in the signal. The bias consists in different frequency components being mixed together and “blurred”. However, even if the data length had been infinite, the spectral estimate obtained through the Fourier transformation is sensitive to data noise, producing inconsistent results (i.e. the variance problem). We therefore used an approach based on the multi-taper spectral estimation method (Thomson, 1982). Here, the data, $V(t)$, is multiplied by the k -th Slepian taper, $w_k(t)$, and Fourier-transformed in order to obtain the tapered spectral estimate $S_k(f)$

$$S_k(f) = \sum_{t=1}^T e^{-i2\pi ft} w_k(t) V(t) \quad (3)$$

Using multi-taper spectral estimation, we could produce several spectral estimates by using several orthogonal tapers and averaging across estimates. Using data tapers we reduced the influence of distant

frequencies at the expense of blurring the spectrum over nearby frequencies. The result is an increase in narrow-band bias and a reduction in broad-band bias. This practice is justified under the assumption that the true spectrum is locally constant and approximately the same for nearby frequencies. In this way we effectively reduced the bias of the estimates. Variance is usually addressed by averaging overlapping segments of the time series and by averaging across several tapered spectral estimates.

Here, we chose as tapers the discrete prolate spheroidal sequences (Slepian functions) (Slepian and Pollak, 1961), that had optimal spectral concentration properties for these taper functions. The Slepian functions formed an orthogonal basis set for sequences of length, T , and could be characterized by the half-bandwidth parameter, W . The usual strategy was to set T as the time length of the data and to select W to be a small multiple of the Raleigh's frequency $1/T$, and then to take the $2WT - 1$ leading Slepian functions as data tapers in the multi-taper analysis. The remaining functions showed progressively worsening spectral concentration properties. By setting W , we defined local frequency windows over which we calculated running averages that smoothed the spectral estimate, reducing its variance (Pesaran, 2008; Prechtel et al., 1997; Thomson, 1982).

Thus, for a given time series, denoted $V(t)$, the power spectrum was obtained by a direct multi-taper estimate given by:

$$s(f) = \frac{1}{K} \sum_{k=1}^K |S_k(f)|^2 \quad (4)$$

where $S_k(f)$ is the discrete Fourier transform of (3).

The bandwidth W was chosen to smooth the data while preserving its relevant spectral structure.

Calculation of power spectrum modulation

Normalized power spectrum (NPS) was defined as :

$$NPS = 10 * \log_{10}(spectrum / R) \quad (5)$$

Where R was the saccade rate in the case of behavioral data and firing rate in the case of neuronal data.

To compare the power of the different neuronal populations across the different experiments, we divided the spectrum by the mean power of all the neurons at the significant frequencies.

We defined significant frequencies in the behavioral normalized power spectrum as frequencies above a threshold (zero, **Figure 6A**, top panel) and below a frequency threshold of 0.15 Hz. Non-significant frequencies were defined as frequencies with behavioral normalized power spectrum lower than -1 and frequencies higher than 0.06Hz.

Finally, we averaged the modulation of significant and non-significant frequencies, for the different periods of the experiment.

Mathematical model

The model schematically described in Figure 7A was mathematically implemented using a rate model description for the different neuronal populations, as described below.

Direction-selective neurons definition

The rate model for the two populations ($j = 1, 2$) of direction selective neurons is defined by:

$$\tau \frac{dv_j}{dt} = -v_j + f[I_j - a_{f,j} - a_{s,j}] \quad (6)$$

$$\tau_f \frac{da_{f,j}}{dt} = -a_{f,j} + \phi_f v_j \quad (7)$$

$$\tau_s \frac{da_{s,j}}{dt} = -a_{s,j} + \phi_s v_j \quad (8)$$

where, for simplicity, the f-I curve f is taken to be a saturating threshold linear function with $f(v) = 0, v < 0, f(v) = v, 0 \leq v < v_m$ and $f(v) = v_m, v \geq v_m$. The variable v_j represents the mean discharge rates of the population 1 and 2, population 1 being assumed to be selective for the CS direction. The variables $a_{f,j}$ and $a_{s,j}$ represent slow habituation currents intrinsic to the cell population j, j being 1 or 2. Two habituation time scales are introduced to represent the double exponential decay of the direction-selective neurons observed experimentally.

The current I_j models the retinal inputs with $I_j = I_{sp}, j = 1, 2$ in the absence of CS. During the CS, of duration T_{cs} , the current is increased to I_{cs} on the CS-direction-selective population, i.e. $I_1 = I_{cs}$.

Comparator neurons definition

The two comparator neuronal populations are modelled similarly. We assume that each comparator cell population receives inputs from one of the two direction-selective neuronal populations and that the two comparator neuronal populations cross-inhibit each other. In addition, we suppose that they are endowed with an adaptation current, similarly to the direction-selective neuronal population, which for simplicity we describe with a single exponential relaxation:

$$\tau \frac{du_1}{dt} = -u_1 + f[I_1^{(r)} - b_1 - J_c u_2 + J_d v_1] \quad (9)$$

$$\tau_b \frac{db_1}{dt} = -b_1 + \phi_b u_1 \quad (10)$$

$$\tau \frac{du_2}{dt} = -u_2 + f[I_2^{(r)} - b_2 - J_c u_1 + J_d v_2] \quad (11)$$

$$\tau_b \frac{db_2}{dt} = -b_2 + \phi_b u_2 \quad (12)$$

We assume that the interaction, not modelled here, of these comparator neurons with neuronal populations outside the tectum (e.g. eye proprioceptive inputs) leads to the generation of the rhythmic depolarizing current $I_j^{(r)}$ in the comparator neurons. In the performed simulation, this rhythmic current was assumed to be periodic with a period T^r with during each period an ON-time with a value $I_{\text{on},j}^{(r)}$ during a time T_{on}^r and a value $I_{\text{off},j}^{(r)}$ during the complementary OFF-time T_{off}^r (i.e. $T^r = T_{\text{on}}^r + T_{\text{off}}^r$). In order to account for the imperfect alternation of the spontaneous activity, the ON-current was taken to take on average the same value $I_{\text{on}}^{(r)}$, on each comparator neuronal population but to fluctuate around this mean independently in the two populations and from period to period,

$$I_{\text{on},j}^{(r)} = I_{\text{on}}^{(r)} + \xi_{j,p} \quad (13)$$

These fluctuations are represented by $\xi_{j,p}$, a random Gaussian current $\xi_{j,p}$ of amplitude $\langle \xi_{j,p} \xi_{j',p'} \rangle = \sigma^2 \delta_{j,j'} \delta_{p,p'} \sigma$, with j the population index and p the period index ($\delta_{a,b}$ denotes the Kronecker δ -function, $\delta_{a,b} = 1$ if a is identical to b , $\delta_{a,b} = 0$ otherwise). The rhythmic currents on the two neuronal populations in a typical simulation are plotted in **Figure 7B**.

The values of the parameters used in the simulations are given in **Table 1**. They were obtained by the fitting procedure described below in section ‘‘Determination of the model parameters’’.

Definitions and computation of the model MAE *index* and MAE duration

The model MAE *index* and MAE duration in the model were computed as follows. First, the successive periods between two rhythmic inputs were defined as 'spontaneous movements' and 'pursuits' by comparing the successive burst of activities induced by the rhythmic input in the CS and MAE comparator neuronal populations. When activities of the two populations alternated, the time period was classified as 'spontaneous activity'. If, instead, the CS-comparator neurons were active consecutively, the time period was classified as CS-pursuit and likewise. If the MAE-comparator neurons were active consecutively, it was classified as a MAE pursuit. The MAE *index* (defined as equation 1) was computed over three consecutive periods (time bins of 60 s), after the cessation of the CS. The first eye movement after the cessation of the CS was always in the MAE direction. This movement was not taken into account in the calculation of the MAE *index* in the experimental data.

Therefore, for the model simulations, we also exclude the first value of the MAE *index* during MAE. For each CS duration (Figure 7C), the results were obtained by averaging over 400 simulations of the model. The duration of MAE was computed as the mean of the post-CS duration for which MAE *index* was greater than the control *index* of the 400 simulations of the model (Figure S5F).

Mathematical analysis

The model is sufficiently simple to lend itself to a full mathematical analysis. This allows determining the role and importance of the different parameters and their extraction from the experimental data. We first describe our analysis of the direction-selective neuron populations (Direction-selective neurons section below) during their three different dynamical phases in the three subsections *Spontaneous activity*, *CS phase* and *MAE phase*. We then present a similar analysis for the comparator neuronal populations (Comparator neurons section), and analyzed the dynamics of the two types of tectal populations in turn. We finally describe how these mathematical results were used to determine the model parameters (Determination of model parameters section).

Direction-selective neurons

Spontaneous activity

During ongoing spontaneous activity, the activity v_j , as well as the adaptation variables $a_{f,j}$ and $a_{s,j}$, take their steady-state values v^{sp} , a_f^{sp} and a_s^{sp} ,

$$v^{sp} = \frac{I_{sp}}{1 + \phi_f + \phi_s}, \quad a_f^{sp} = \phi_f v^{sp}, \quad a_s^{sp} = \phi_s v^{sp} \quad (14)$$

CS phase

When the CS is turned on, the CS-selective population dynamics can be decomposed according to the different scales of the reaction times of the activity (τ) and of the adaptation variables (τ_f and τ_s). Three different phases of the dynamics follow in succession.

On the very short time scale τ , the activity v_1 adapts to the value prescribed by the CS and the current value of the adaptation variables:

$$v_1 = I_{cs} - a_{f,1} - a_{s,1} \quad (15)$$

After the onset of the CS, the activity v_1 attains its peak value on this short time scale, before any significant adaptation has the time to evolve:

$$v_{\text{peak}} = I_{cs} - a_{f,sp} - a_{s,sp} \quad (16)$$

Then, the fast adaptation variable relaxes according to equation (7) with the slow variable $a_{s,1}$ still at its spontaneous value $a_{s,sp}$. Thus, the dynamics of $a_{f,1}$ obeys:

$$\tau_f \frac{da_{f,1}}{dt} = -(1 + \phi_f)a_{f,1} + \phi_f[I_{cs} - a_s^{sp}] \quad (17)$$

In this phase, driven by the increase of $a_{f,1}$, v_1 decreases with the characteristic time of $\tau_f / ((1 + \phi_f))$,

$$a_{f,1}(t) = \frac{\phi_f}{1 + \phi_f} [I_{cs} - a_s^{sp} + (I_{sp} - I_{cs} + a_s^{sp}) \exp[-t(1 + \phi_f)/\tau_f]] \quad (18)$$

$$v_1(t) = I_{cs} - \frac{I_{cs} - a_s^{sp}}{1 + \phi_f}(t) - a_s^{sp} \quad (19)$$

where the origin of time is taken to be the CS onset. At the end of this phase of fast decrease, v_1 is equal to the intermediate value v_I with:

$$v_I = \frac{I_{cs} - a_s^{sp}}{1 + \phi_f} \quad (20)$$

Finally, a phase with slowly decreasing activity sets in, driven by the increase of $a_{s,1}(t)$. In this final part of the CS-phase, the evolution of both v_1 and $a_{f,1}$ are driven by the evolution of $a_{s,1}$,

$$a_{f,1} = \phi_f v_1 \quad (21)$$

$$v_1 = \frac{I_{cs} - a_{s,1}}{1 + \phi_f} \quad (22)$$

With the conditions (21, 22), the dynamics of $a_{s,1}$ (equation (8)) obeys,

$$\tau_s \frac{da_{s,1}}{dt} = -\frac{1 + \phi_f + \phi_s}{1 + \phi_f} a_{s,1} + \frac{\phi_s}{1 + \phi_f} I_{cs} \quad (23)$$

In this last phase, $a_{s,1}$ slowly increases, on the time scale $\tau_s(1 + \phi_f)/(1 + \phi_f + \phi_s)$ as:

$$a_{s,1} = \frac{\phi_s}{1 + \phi_f + \phi_s} \left[I_{cs} + (I_{sp} - I_{cs}) \exp\left(-\frac{1 + \phi_f + \phi_s}{1 + \phi_f} \frac{t}{\tau_s}\right) \right] \quad (24)$$

Correlatively, v_1 decreases as (using Equation (22)),

$$v_1 = v_{cs} - \frac{\phi_s(I_{sp} - I_{cs})}{(1 + \phi_f)(1 + \phi_f + \phi_s)} \exp\left(-\frac{1 + \phi_f + \phi_s}{1 + \phi_f} \frac{t}{\tau_s}\right) \quad (25)$$

where the asymptotic value v_{cs} is given by:

$$v_{cs} = \frac{I_{cs}}{1 + \phi_f + \phi_s} \quad (26)$$

MAE phase

The direction-selective neuronal activity can be analyzed along similar lines after the CS cessation at $t = T_{cs}$, with a very short first phase on the time scale τ , then a second short phase of duration of order $\tau_f/(1 + \phi_f)$ and finally a slow phase. This phase is described in more details since it is important for the dynamics of the comparator neurons during the MAE period.

As in our previous description (Equations (21,22)), after the two short phases, the dynamics of both v_1 and $a_{f,1}$ are determined by the slow adaptation variable $a_{s,1}$

$$a_{f,1} = \phi_f v_1 \quad (27)$$

$$v_1 = \frac{I_{sp} - a_{s,1}}{1 + \phi_f} \quad (28)$$

The dynamics of $a_{f,1}$ obey, similarly to Equation (29):

$$\tau_s \frac{da_{s,1}}{dt} = -\frac{1 + \phi_f + \phi_s}{1 + \phi_f} a_{s,1} + \frac{\phi_s}{1 + \phi_f} I_{sp} \quad (29)$$

In this last phase, $a_{s,1}$ slowly returns, on the time scale $\tau_s(1 + \phi_f)/(1 + \phi_f + \phi_s)$, to its value during spontaneous activity as:

$$a_{s,1} = \frac{\phi_s}{1 + \phi_f + \phi_s} \left\{ I_{sp} + (I_{cs} - I_{sp}) \left[\exp\left(\frac{1 + \phi_f + \phi_s}{1 + \phi_f} \frac{T_{cs}}{\tau_s}\right) - 1 \right] \exp\left(-\frac{1 + \phi_f + \phi_s}{1 + \phi_f} \frac{t}{\tau_s}\right) \right\} \quad (30)$$

Correlatively, v_1 increases as (using Equation (28)),

$$v_1 = v_{sp} - \frac{\phi_s(I_{cs} - I_{sp})}{(1 + \phi_f)(1 + \phi_f + \phi_s)} \left[\exp\left(\frac{1 + \phi_f + \phi_s}{1 + \phi_f} \frac{T_{cs}}{\tau_s}\right) - 1 \right] \exp\left(-\frac{1 + \phi_f + \phi_s}{1 + \phi_f} \frac{t}{\tau_s}\right) \quad (31)$$

where the origin of time is taken as the beginning of the CS.

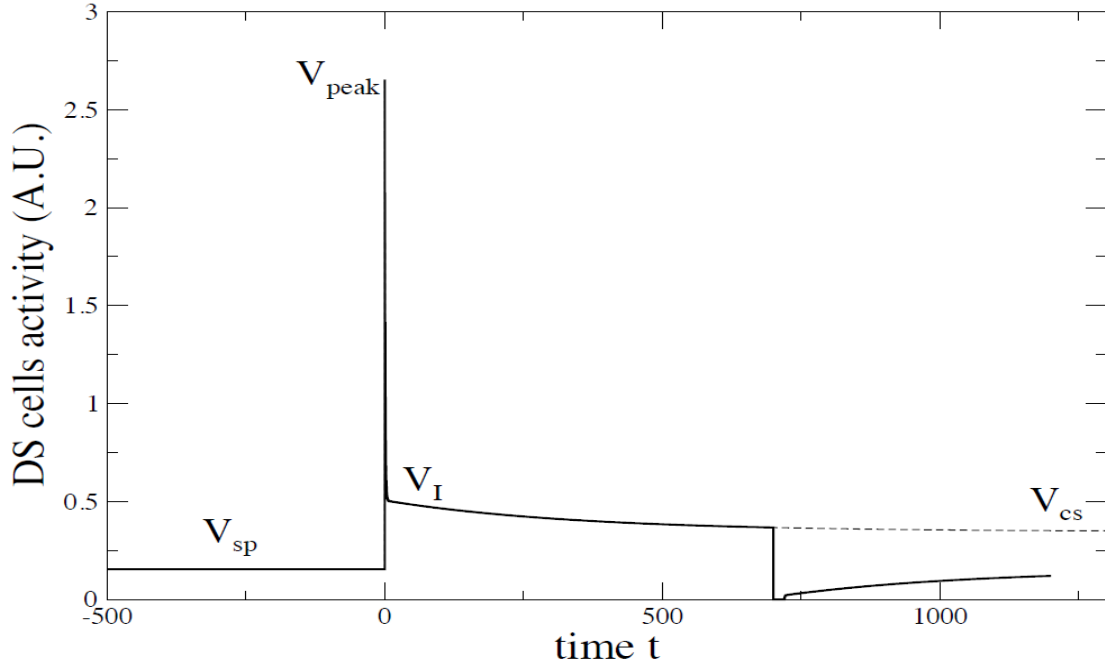


Figure: Activity of the direction-selective neurons: The CS is turned on at $t = 0$. As explained in the text, the constants of the model for the direction-selective neurons can be determined by measuring the neuronal activity v_{sp} , v_{peak} , v_I and v_{cs}

Comparator neurons

Rhythmically driven dynamics

The comparator neurons receive an inhibitory current $I_{\text{off}}^{(r)}$ except during repeated intervals of duration T_{on}^r when they are relieved from inhibition. During these intervals they receive the current $I_{\text{on},j}^{(r)}$ which produce a burst of activity in the CS-direction-selective neurons.

Just before the burst start, the adaptation variables have the value $b_1^{(n)}$ and $b_2^{(n)}$. As for the direction-selective neurons, the dynamics of the comparator neurons can be decomposed on different time scales. On the shortest time scale determined by τ , the adaptation variables do not change significantly and the CS-direction-selective activity obeys:

$$\tau \frac{du_1}{dt} = -u_1 - J_c u_2 + I_1^{(n)} \quad (32)$$

$$\tau \frac{du_2}{dt} = -u_2 - J_c u_1 + I_2^{(n)} \quad (33)$$

where $I_1^{(n)} = I_{\text{on},1}^{(r)} - b_1^{(n)} + J_d v_1$, $I_2^{(n)} = I_{\text{on},2}^{(r)} - b_2^{(n)} + J_d v_2$ are evaluated at the onset of the rhythmic current and are assumed to be constant. The dynamics is the superposition of a symmetric mode $u_s = (u_1 + u_2)/2$ and an antisymmetric mode $u_a = (u_2 - u_1)/2$ with

$$u_s = \frac{(I_1^{(n)} + I_2^{(n)})}{2(1 + J_c)} [1 - \exp(-t(1 + J_c)/\tau)] \quad (34)$$

$$u_a = \frac{(I_2^{(n)} - I_1^{(n)})}{2(J_c - 1)} [\exp(t(J_c - 1)/\tau) - 1] \quad (35)$$

At the rhythmic input onset, which we take as the time origin ($t = 0$), the two modes grow as $u_s \sim (I_1^{(n)} + I_2^{(n)})t/(2\tau)$ and $u_a \sim (I_1^{(n)} - I_2^{(n)})t/(2\tau)$. Since $I_1^{(n)}$ and $I_2^{(n)}$ are of similar magnitude, the symmetric mode dominates at first and both u_1 and u_2 grow (i.e. the two comparator populations become active). However, when $J_c > 1$, the antisymmetric mode grows exponentially and the comparator neuronal population with the largest input soon dominates. That is, for $J_c > 1$ the CS network with cross-inhibition indeed functions as a comparator which leads us to focus on this parameter regime. For definiteness, we consider that $I_2^{(n)} > I_1^{(n)}$. In this case, the growth of the antisymmetric mode leads u_1 to vanish and u_2 to reach I_2 in a period of the order of τ . Then u_2 follows adiabatically $I_2 - b_2$:

$$b_2 = \frac{\phi_b I_2}{1 + \phi_b} + \left(b_2^{(n)} - \frac{\phi_b I_2}{1 + \phi_b} \right) \exp[-t(1 + \phi_b)/\tau_b] \quad (36)$$

$$u_2 = \frac{I_2}{1 + \phi_b} + \left(\frac{\phi_b I_2}{1 + \phi_b} - b_2^{(n)} \right) \exp[-t(1 + \phi_b)/\tau_b] \quad (37)$$

where $I_2 = I_2^{(r)} + J_d v_2$ and where, for simplicity, we have supposed that τ_b is much shorter than the time τ_s which governs the evolution of v_1 and v_2 . When the rhythmic input disappears u_2 quickly returns to zero on the fast time scale τ , while b_2 decays on the slower time scale τ_b ¹. Therefore, at the onset of the next rhythmic input, the habituation current magnitude is:

$$b_2^{(n+1)} = \left\{ \frac{\phi_b I_2}{1 + \phi_b} + \left(b_2^{(n)} - \frac{\phi_b I_2}{1 + \phi_b} \right) \exp[-T_{\text{on}}^r (1 + \phi_b) / \tau_b] \right\} \exp[-T_{\text{off}}^r / \tau_b] \quad (38)$$

Spontaneous activity

As explained above, the comparator dynamics (32,33) are designed to compare the inputs $I_1^{(n)}$ and $I_2^{(n)}$ and to select the population with the largest input to be the active population in a “winner-takes-all” manner. During spontaneous activity, there are no specific inputs on directional neurons, and the difference of inputs reduces to:

$$I_1^{(n)} - I_2^{(n)} = b_2^{(n)} - b_1^{(n)} + \xi_{1,n} - \xi_{2,n} \quad (39)$$

where we have used the expression (13) for the rhythmic current. The comparator neuronal population 1 wins and is the active one when $(I_1^{(n)} - I_2^{(n)}) > 0$, population 2 is selected when the reverse inequality holds. Without noise ($\sigma = 0$), this leads to a strict alternation in the dominance of neuronal population 1 and 2 in the spontaneous steady-state activity, since the population that fired last has a stronger adaptation current b at the start of the next rhythmic current pulse. The situation is less simple in the presence of noise since noise sometime induces the same comparator population to be active at successive times.

Population 1 dominates when $\xi_{1,n} - \xi_{2,n} > b_1^{(n)} - b_2^{(n)}$. Since $(\xi_{1,n} - \xi_{2,n})$ is a Gaussian variable of variance $2\sigma^2$, this gives the probability that population one is selected:

¹ This is strictly true only when b_2 does not become large enough during the “on” period so that $I_2 - b_2$ becomes smaller than $I_1 - b_1 - J_c u_2$; otherwise u_1 would be released from inhibition and the u_1 -population would fire before the end of the “on” period (Laing and Chow, 2002).

$$p_1 = \frac{1}{2} \left[1 - \operatorname{erf} \left(\frac{b_1^{(n)} - b_2^{(n)}}{2\sigma} \right) \right] \quad (40)$$

where $\operatorname{erf}(x)$ is the error function

$$\operatorname{erf}(x) = \frac{2}{\sqrt{\pi}} \int_0^x du \exp(-u^2) \quad (41)$$

It is worth noting that $\operatorname{erf}(x) \simeq x$ with about a 10 percent precision for $0 \leq x \leq .9$.

We consider the regime where the adaptation variable $b_i^{(n)}$ is mostly determined by the last time the population i fired. We first determine the probability of dominance of each population after the two comparator populations have been active in alternation. For definiteness, we suppose that population 1 was the last active and obtain from :

$$b_1^{(n)} = \frac{\phi_b I_{\text{on}}^{(r)}}{1 + \phi_b} \{1 - \exp[-T_{\text{on}}^r (1 + \phi_b) / \tau_b]\} \exp[-T_{\text{off}}^r / \tau_b] \quad (42)$$

$$b_2^{(n)} = b_1^{(n)} \exp[-T^{(r)} / \tau_b] \quad (43)$$

These formulas together with (40) determine the probability p_1 that population 1 is again dominant after having fire last.

Finally, we consider the pair of consecutive firings and determine the fraction f_a where the firing populations are different (i.e alternating pairs) and the complementary fraction f_s where the population are identical. These are used to identify the ‘‘alternating stereotypical eye movements’’ and the ‘‘pursuit-saccade-like movements’’ in the model. Denoting the probability by $P_{n_1, n}^a$ (resp. $P_{n_1, n}^s$) that the pair $(n - 1, n)$ is alternating (resp. non-alternating), we have the recurrence relation (since p_1 depends only on the previous two firings):

$$P_{n, n+1}^a = (1 - p_1) P_{n_1, n}^a + P_{n_1, n}^s \quad (44)$$

$$P_{n, n+1}^s = p_1 P_{n_1, n}^a \quad (45)$$

where we have supposed that the same population never fires 3 times in succession (which is quite accurate in the case considered here when noise is not too strong). In the steady state, when the probability is the same for all consecutive pairs, both equations are reduced to $P^s = p_1 P^a$. This gives for the respective fractions:

$$f_a = \frac{1}{1 + p_1}, \quad f_s = \frac{p_1}{1 + p_1} \quad (46)$$

MAE phase

The neuronal population selective to the direction of the CS is chosen to be population 1. We consider the dynamics of the comparator neurons in the case when there are no fluctuations in the rhythmic current ($\sigma = 0$). We assume that the magnitude of the habituation currents as well as the input from the CS-direction-selective neurons are small as compared to the rhythmic current. In a first-order approximation, we can thus estimate $b_2(n)$ by approximating I_2 by $I_{\text{on}}^{(r)}$ in Equation (38). Thus, $b_2(n)$ relaxes exponentially with the burst number to $b^{(MAE)}$:

$$b^{(MAE)} = \frac{\phi_b I_{\text{on}}^{(r)}}{1 + \phi_b} \frac{\exp[T_{\text{on}}^r / \tau_b] - \exp[-T_{\text{on}}^r \phi_b / \tau_b]}{\exp[T^r / \tau_b] - \exp[-T_{\text{on}}^r \phi_b / \tau_b]} \quad (47)$$

Which of the two comparator populations fires during a rhythmic stimulation depends on which one has the greater stimulating current at the rhythmic onset. MAE lasts as long as population 2 fires (after a CS activating the direction-selective population 1), as long as:

$$I_2 - I_1 = J_d(v_2 - v_1) + b_1 - b_2 > 0 \quad (48)$$

Approximating b_2 and b_1 by their asymptotic values ($b_1 \simeq 0, b_2 \simeq b^{(MAE)}$) give for the MAE duration T_{MAE} with the help of Equation (31):

$$T_{MAE} = \tau_s \frac{1 + \phi_f}{1 + \phi_f + \phi_s} \ln \left\{ \frac{\phi_s(I_{cs} - I_{sp})}{(1 + \phi_f)(1 + \phi_f + \phi_s)I_{MAE}} \left[1 - \exp \left(- \frac{1 + \phi_f + \phi_s}{1 + \phi_f} \frac{T_{cs}}{\tau_s} \right) \right] \right\} \quad (49)$$

where we have denoted by $I_{MAE} = b^{(MAE)}/J_d$ the single quantity that characterizes the dynamics of the comparator neurons. From Equation (49), one sees that for long CS, the MAE duration is bounded and approaches the maximal duration T_{MAE}^{max} ,

$$T_{MAE}^{max} = \tau_s \frac{1 + \phi_f}{1 + \phi_f + \phi_s} \ln \left[\frac{\phi_s(I_{cs} - I_{sp})}{(1 + \phi_f)(1 + \phi_f + \phi_s)I_{MAE}} \right] \quad (50)$$

This comes about because for long CS the activity of the activated direction-selective neurons relaxes to a definite value (v_{cs}). Similarly, since T_{MAE} should be positive in Equation (49), there is a minimum duration of the CS, T_{cs}^{min} , necessary to induce MAE:

$$T_{cs}^{min} = \tau_s \frac{1 + \phi_f}{1 + \phi_f + \phi_s} \ln \left[\frac{\phi_s(I_{cs} - I_{sp})}{\phi_s(I_{cs} - I_{sp}) - (1 + \phi_f + \phi_s)I_{MAE}} \right] \quad (51)$$

$$\simeq \tau_s \frac{(1 + \phi_f)^2}{\phi_s} \frac{I_{MAE}}{I_{cs} - I_{sp}} \quad (52)$$

where the second equation (52) holds when the argument of the logarithm in equation (51) is close to 1 (a necessary condition to have $T_{cs}^{min} \ll T_{MAE}^{max}$ as observed in the experiments). One can note that Equations (49-52) are quite constraining since once the parameters of the direction-selective neurons are determined, the single remaining parameter is I_{MAE} . In particular, the time $\tau_s(1 + \phi_f)/(1 + \phi_f + \phi_s)$ is directly the long habituation time constant of the direction-selective neurons' activity and it governs both the scale of T_{MAE}^{max} and T_{cs}^{min} and the scale of the CS duration on which the MAE duration varies (e.g. the time scale of the exponential in Equation (49)).

Determination of the model parameters

Determination of the direction-selective neuron's parameters

The different constants governing the dynamics of direction-selective neurons can all, in principle, be obtained from the experimental data v_j . The actual scale of activity is arbitrary and can be fixed by the choice of I_{sp} . Therefore, it is necessary to determine I_{cs} , the time scales τ_s and τ_f , and the coupling constants ϕ_f and ϕ_s . This can be done from the measure of the spontaneous activity v_{sp} as well as from the neural activity during the CS, and specially from measuring the values v_{peak} , v_I and v_{cs} (see the **Figure** above).

The previous equations give:

$$I_{cs} = I_{sp} \frac{v_{cs}}{v_{sp}} \quad (53)$$

$$v_{peak} - v_{sp} = I_{cs} - I_{sp} = (1 + \phi_f + \phi_s)(v_{cs} - v_{sp}) \quad (54)$$

$$v_I - v_{sp} = \frac{1 + \phi_f + \phi_s}{1 + \phi_f} (v_{cs} - v_{sp}) \quad (55)$$

Equation (53) directly gives I_{cs} while Equations (54) and (55) determine ϕ_f and ϕ_s as

$$\phi_f = \frac{v_{peak} - v_I}{v_I - v_{sp}} \quad (56)$$

$$\phi_s = \frac{v_{peak} - v_{cs}}{v_{cs} - v_{sp}} - \phi_f \quad (57)$$

In practice, the above procedure was performed by fitting the average activity $A(t)$ during the CS as measured from the calcium signal as:

$$A(t) = A_0 + A_1 \exp(-t/t_1) + A_2 \exp(-t/t_2), \quad t_2 > t_1 \quad (58)$$

While t_1 was well determined by this fitting procedure, the slow time t_2 turned out to be rather very weakly constrained. We therefore chose to obtain it from a fit of the analytical curve (49) to the MAE duration vs. CS duration experimental data (omitting the experimental point for the longest 500 s which seems to involve supplementary phenomena). This provides the value of $t_2 = \tau_s(1 + \phi_f)/(1 + \phi_s + \phi_f)$. Using this value of t_2 , the other constants A_0, A_1, A_2, t_1 could be reliably determined by fitting the neural activity. The average activity during spontaneous activity A_{sp} was also fitted. From these, the direction-selective neuronal parameters were determined with the help of the above equations. The fit of the CS activity decrease provides the values, $v_{peak}/v_{sp}, v_i/v_{sp}, v_{cs}/v_{sp}$ (e.g. $v_{cs}/v_{sp} = A_0/A_{sp}$) and the time $t_1 = \tau_f/(1 + \phi_f)$. The values of ϕ_f and ϕ_s can be determined from these ratios with the help of the above equations. After ϕ_f and ϕ_s have been determined, the adaptation times τ_f and τ_s can be recovered from t_1 , and the previously determined t_2 . The short time τ could in principle also be measured from the rise of the neural activity when the CS is turned on, but it is too short to be reliably extracted from calcium signals. However, the exact value of τ does not play a role in the analysis, as long as it is small, as compared to the other times.

Determination of the comparator model and the rhythmic current parameters

Some constants of the comparator neurons can also be obtained from recordings of the neuronal activity. The rhythmic current $I_{on}^{(r)}$ was fitted from the peaks of the neuronal activity during the spontaneous phase. This activity phase served also to choose the period and duration of the rhythmic current. They were also chosen so as to reproduce the neuronal activity, which lasts about $T_{on}^{(r)} = 4$ s and occurs about once in every $T_{off}^{(r)} = 20$ s. The current $I_{off}^{(r)}$ was chosen to be of negative value so that the two comparator populations were silent in the absence of the rhythmic current $I_{on}^{(r)}$.

The comparator neurons parameters were chosen to reproduce the MAE duration curve as well as the MAE index curves taking into account other constraints, namely that only one comparator population fired during each rhythmic episode (this imposes in particular $J_c > 1$ as explained above) and that the MAE comparator population was never active during the CS. The noise σ was adjusted to reproduce the fraction $f_a \simeq 85\%$ (see above) of alternations between the comparator population during the spontaneous activity.

Table 1: Model parameters

Parameters	Values
f-I curve	
v_m (A.U.)	4
DS-cell parameters	
τ (ms)	200
τ_f (s)	24
τ_s (s)	294
ϕ_f (A.U.)	6
ϕ_s (A.U.)	9.4
CS-cell parameters	
τ (ms)	200
τ_b (s)	10
ϕ_b (A.U.)	11
J_c (A.U.)	15
J_d (A.U.)	7.5
Retinal input	
I_{sp} (A.U.)	1.15
I_{cs} (A.U.)	3.1
Rhythmic input	
T_{on}^r (s)	4
T_{off}^r (s)	16
$I_{on}^{(r)}$ (A.U.)	0.64
$I_{off}^{(r)}$ (A.U.)	-2
σ (A. U.)	0.11

References

- Akerboom, J., Chen, T.-W., Wardill, T.J., Tian, L., Marvin, J.S., Mutlu, S., Calderón, N.C., Esposti, F., Borghuis, B.G., Sun, X.R., Gordus, A., Orger, M.B., Portugues, R., Engert, F., Macklin, J.J., Filosa, A., Aggarwal, A., Kerr, R.A., Takagi, R., Kracun, S., Shigetomi, E., Khakh, B.S., Baier, H., Lagnado, L., Wang, S.S.-H., Bargmann, C.I., Kimmel, B.E., Jayaraman, V., Svoboda, K., Kim, D.S., Schreiter, E.R., Looger, L.L., 2012. Optimization of a GCaMP calcium indicator for neural activity imaging. *J. Neurosci.* 32, 13819–40. doi:10.1523/JNEUROSCI.2601-12.2012
- Arrenberg, A.B., Del Bene, F., Baier, H., 2009. Optical control of zebrafish behavior with halorhodopsin. *Proc. Natl. Acad. Sci. U. S. A.* 106, 17968–73. doi:10.1073/pnas.0906252106
- Brainard, D.H., 1997. The Psychophysics Toolbox. *Spat. Vis.* 10, 433–436. doi:10.1163/156856897X00357
- Gonzalez, R., Woods, R., Eddins, S., 2004. Digital image processing using MATLAB.
- Halpern, M.E., Rhee, J., Goll, M.G., Akitake, C.M., Parsons, M., Leach, S.D., 2008. Gal4/UAS transgenic tools and their application to zebrafish. *Zebrafish* 5, 97–110. doi:10.1089/zeb.2008.0530
- <http://www.chronux.org/> [WWW Document], 2013.
- Laing, C.R., Chow, C.C., 2002. A spiking neuron model for binocular rivalry. *J. Comput. Neurosci.* 12, 39–53. doi:10.1023/A:1014942129705
- Lister, J.A., Robertson, C.P., Lepage, T., Johnson, S.L., Raible, D.W., 1999. nacre encodes a zebrafish microphthalmia-related protein that regulates neural-crest-derived pigment cell fate. *Development* 126, 3757–67.
- Mitra, P., Bokil, H., 2008. *Observed Brain Dynamics, Convergence*. Oxford University Press, USA. doi:10.1093/acprof:oso/9780195178081.001.0001
- Panier, T., Romano, S.A., Olive, R., Pietri, T., Sumbre, G., Candelier, R., Debrégeas, G., 2013. Fast functional imaging of multiple brain regions in intact zebrafish larvae using selective plane illumination microscopy. *Front. Neural Circuits* 7, 65. doi:10.3389/fncir.2013.00065
- Park, H.C., Kim, C.H., Bae, Y.K., Yeo, S.Y., Kim, S.H., Hong, S.K., Shin, J., Yoo, K.W., Hibi, M., Hirano, T., Miki, N., Chitnis, a B., Huh, T.L., 2000. Analysis of upstream elements in the HuC promoter leads to the establishment of transgenic zebrafish with fluorescent neurons. *Dev. Biol.* 227, 279–93. doi:10.1006/dbio.2000.9898
- Pelli, D.G., 1997. The VideoToolbox software for visual psychophysics: transforming numbers into movies. *Spat. Vis.* 10, 437–442. doi:10.1163/156856897X00366
- Pesaran, B., 2008. Spectral Analysis for Neural Signals, in: Mitra, P. (Ed.), *Short Course III*. Society for Neuroscience, Washintong, DC, p. 1.

- Pologruto, T.A., Sabatini, B.L., Svoboda, K., 2003. ScanImage: flexible software for operating laser scanning microscopes. *Biomed. Eng. Online* 2, 13. doi:10.1186/1475-925X-2-13
- Prechtl, J.C., Cohen, L.B., Pesaran, B., Mitra, P.P., Kleinfeld, D., 1997. Visual stimuli induce waves of electrical activity in turtle cortex. *Proc. Natl. Acad. Sci. U. S. A.* 94, 7621–7626.
- Romano, S.A.A., Pietri, T., Pérez-Schuster, V., Jouary, A., Haudrechy, M., Sumbre, G., 2015. Spontaneous Neuronal Network Dynamics Reveal Circuit's Functional Adaptations for Behavior. *Neuron* 85, 1070–85. doi:10.1016/j.neuron.2015.01.027
- Schoonheim, P.J., Arrenberg, A.B., Del Bene, F., Baier, H., 2010. Optogenetic localization and genetic perturbation of saccade-generating neurons in zebrafish. *J. Neurosci.* 30, 7111–20. doi:10.1523/JNEUROSCI.5193-09.2010
- Slepian, D., Pollak, H.O., 1961. Prolate spheroidal wave function and fourier and uncertainty.pdf. I. *Bell Syst. Tech J.* 40, 43–63.
- Thomson, D.J., 1982. Spectrum estimation and harmonic analysis. *Proc. IEEE.* doi:10.1109/PROC.1982.12433
- Tian, L., Hires, S.A., Mao, T., Huber, D., Chiappe, M.E., Chalasani, S.H., Petreanu, L., Akerboom, J., McKinney, S. a, Schreiter, E.R., Bargmann, C.I., Jayaraman, V., Svoboda, K., Looger, L.L., 2009. Imaging neural activity in worms, flies and mice with improved GCaMP calcium indicators. *Nat. Methods* 6, 875–81. doi:10.1038/nmeth.1398
- Tseng, Q., Duchemin-Pelletier, E., Deshiere, A., Balland, M., Guillou, H., Filhol, O., Théry, M., 2012. Spatial organization of the extracellular matrix regulates cell-cell junction positioning. *Proc. Natl. Acad. Sci. U. S. A.* 109, 1506–11. doi:10.1073/pnas.1106377109
- Westerfield, M., 1995. *The zebrafish book: a guide for the laboratory use of zebrafish (Danio rerio)*. University of Oregon Press.

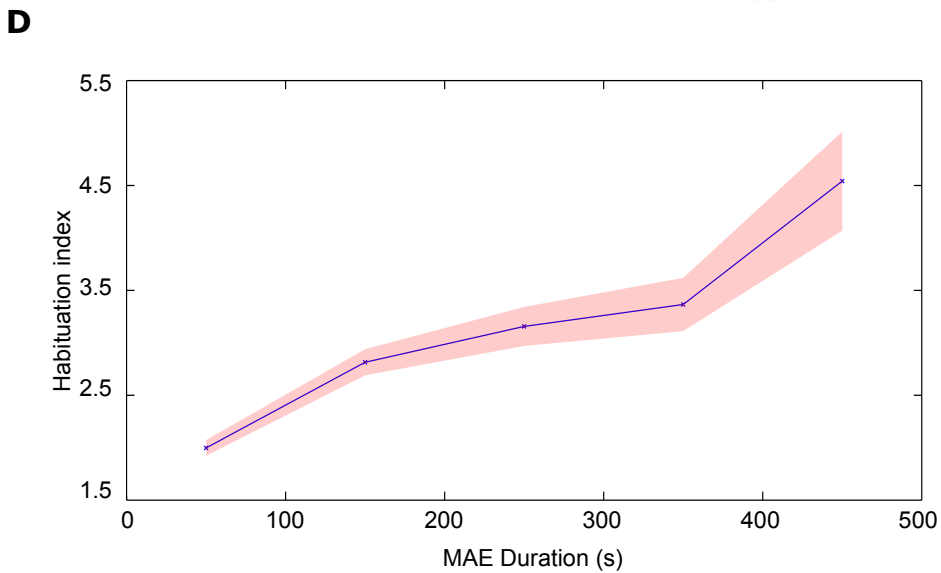
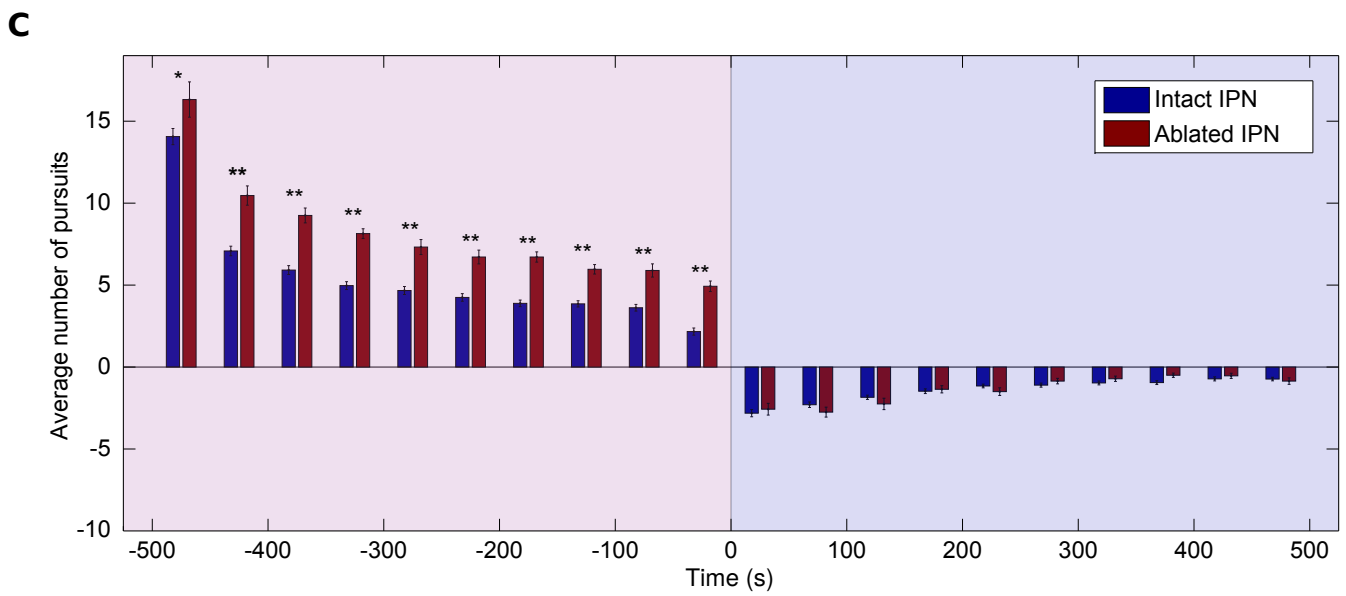
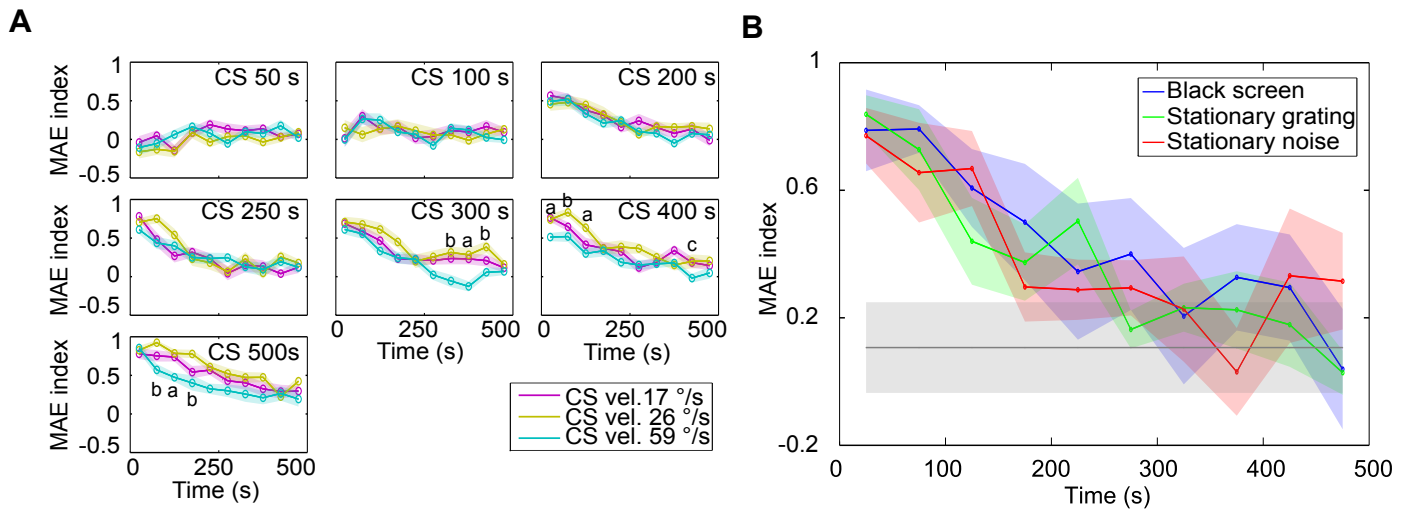


Figure S1. The effect of CS duration, CS velocity and stationary stimulus on MAE (related to Figure 1 and 3).

(A) *MAE index* as a function of time. Each panel represents a different duration of the CS. Each curve represents a different velocity of the CS. Magenta for 17 °/s, yellow for 26 °/s and cyan for 59 °/s. Error bars represent s.e. a: marks the intervals where 59 °/s was significantly different from 17 °/s and 26 °/s. b: marks the intervals where 59 °/s was significantly different from 26 °/s. c: depicts the intervals where 59 °/s was significantly different from 17 °/s. For CS velocity of 17 °/s, n= 48, 34, 40, 36, 38, 40, and 34 (trials), from 12, 11, 11, 10,11, 10 and 12 larvae for CS durations of 50, 100, 200, 250, 300, 400, 500 s, respectively. For CS velocity of 26 °/s n= 36, 36, 39, 34, 36, 34, and 40 (trials), from 10, 9, 10, 10, 10, 9, and 11 larvae for CS durations of 50, 100, 200, 250, 300, 400, 500 s, respectively. For CS velocity of 59 °/s n= 36, 34, 38, 40, 40, 38, and 22 (trials), from 11, 11, 10, 10, 10, 10, and 9 larvae for CS durations of 50, 100, 200, 250, 300, 400, 500 s, respectively.

(B) *MAE index* as a function of time after CS of 500 s when using as a stationary stimulus: 1) a black screen (blue), 2) stationary grating (green), 3) stationary noise (red). Gray line depicts the control index. For all cases, n=8, from 4 larvae. Error bars represent s.e., non-significant differences were found between the different stationary stimuli.

(C) Summary of the behavioral experiments after IPN ablations. The average number of pursuits during the CS and MAE periods. Pink background: CS period. Violet background: post-CS control period. Blue bars: intact IPN (control). Red bars: ablated IPN. Positive values: pursuits in the direction of the CS. Negative values: pursuits in the MAE direction. Asterisk marks significant differences (*: $p < 0.05$, **: $p < 0.01$, Kruskal-Wallis, $n=14$, 4 larvae). Error bars: s.e.

(D) The correlation between the OKR habituation *index* (the number of pursuits during the first 50 s divided by the number of pursuits during the last 50 s of the CS) and the length of MAE. Each black dot represents the mean of the habituation index for bins of 100 s except for the last bin (200 s including MAE durations of 400, 450 and 500 s). Error bars: s.e. Note the increase in MAE duration with the increase in the habituation *index*.

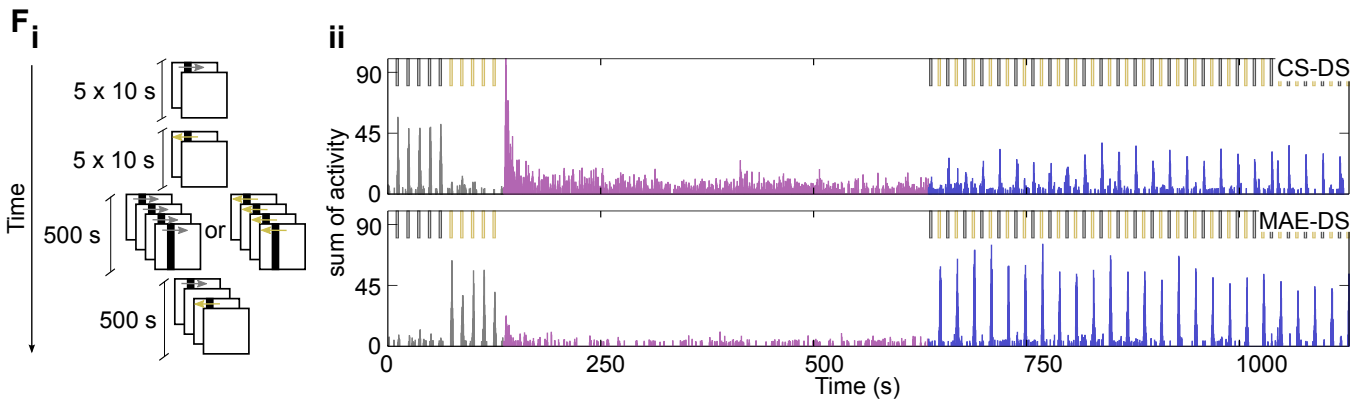
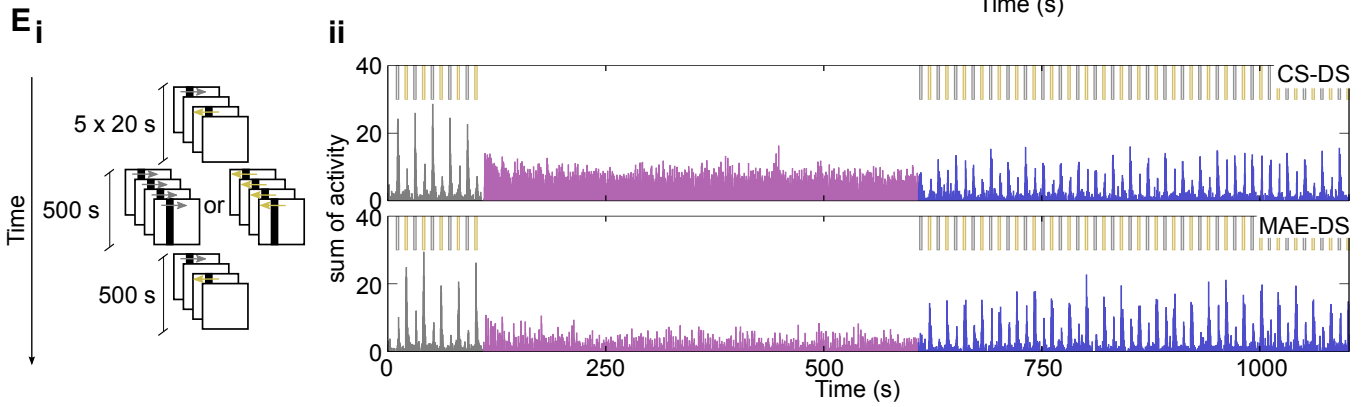
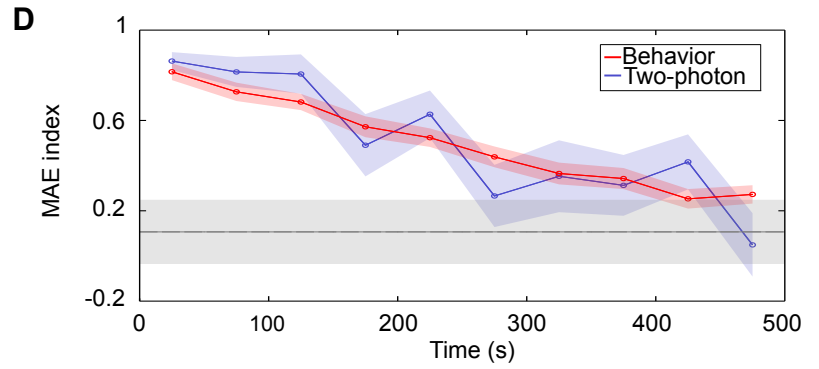
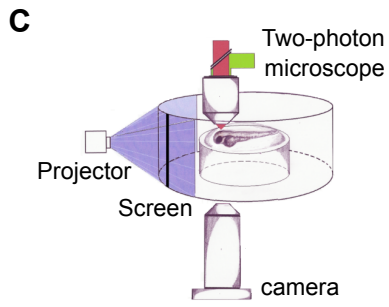
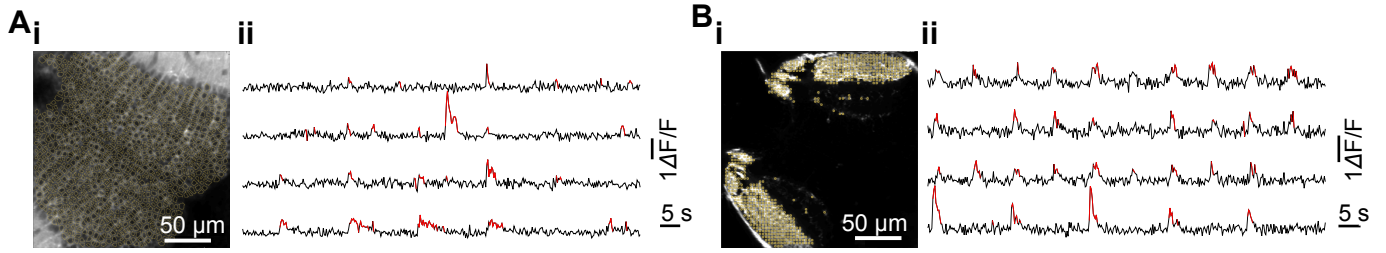


Figure S2. Calcium-imaging-data-processing methods and experimental protocols (related to Figure 4).

(A) **i.** An optical section of the zebrafish larva's optic tectum superimposed with the ROIs corresponding to each single neurons (yellow patches). **ii.** Examples of typical single-neuron $\Delta F/F$ traces (black) with significant fluorescence transients highlighted in red. Breaks in the traces depict discarded frames due to movement artifacts.

(B) **i.** An optical section of the optic tectum of an *ath5:GCaMP3* zebrafish larva, where the tectal neuropil can be clearly observed. The SROIs are superimposed to the image (yellow patches). **ii.** Examples of typical single-SROIs $\Delta F/F$ traces (black) with significant fluorescence transients highlighted in red. Breaks in the traces depict discarded frames due to movement artifacts.

(C) Experimental setup: Scheme of the two-photon system for simultaneously monitoring eye movements and presenting visual stimuli.

(D) *MAE index* as a function of time after CS under the two photon microscope. Blue curve: *MAE index* as a function of time under a two-photon microscope. CS consisted in repetitive moving bars for 500 s. Red curve: *MAE index* as a function of time as showed in **Fig. 1F**. CS consisted in whole field grating for 500 s. Gray line represents the control index for the two-photon experiments. Non-significant differences were found between the two conditions. Error bars: s.e. For repetitive moving bars, n=20 (trials), from 10 larvae. For whole field grating, n=15 (trials), from 15 larvae.

(E) **i.** Experimental paradigm for monitoring adaptation of RGC projections in paralyzed larvae. **ii.** The sum of the relative change in fluorescence intensity ($\Delta F/F$) of direction selective SROIs as a function of time. Top panel, CS direction selective SROIs. Bottom panel, MAE direction selective SROIs. The color bars represent the different stimulation blocks of the experimental paradigm: gray for pre-CS control, magenta for CS and blue post-CS control period. Top bars: depict the presentation period of each moving bar (gray: CS direction, yellow: MAE direction).

(F) As in E, but for tectal neuron recordings.

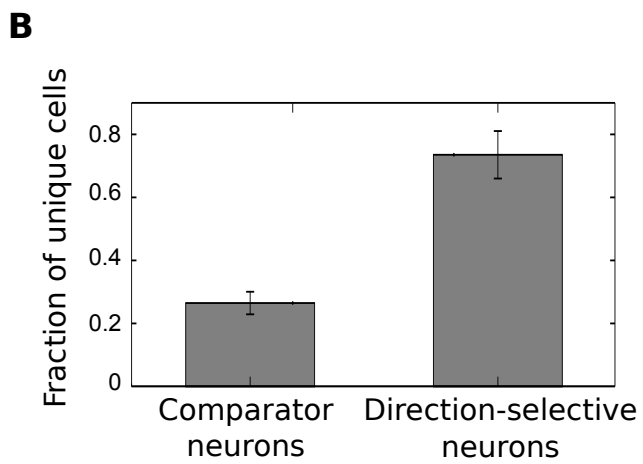
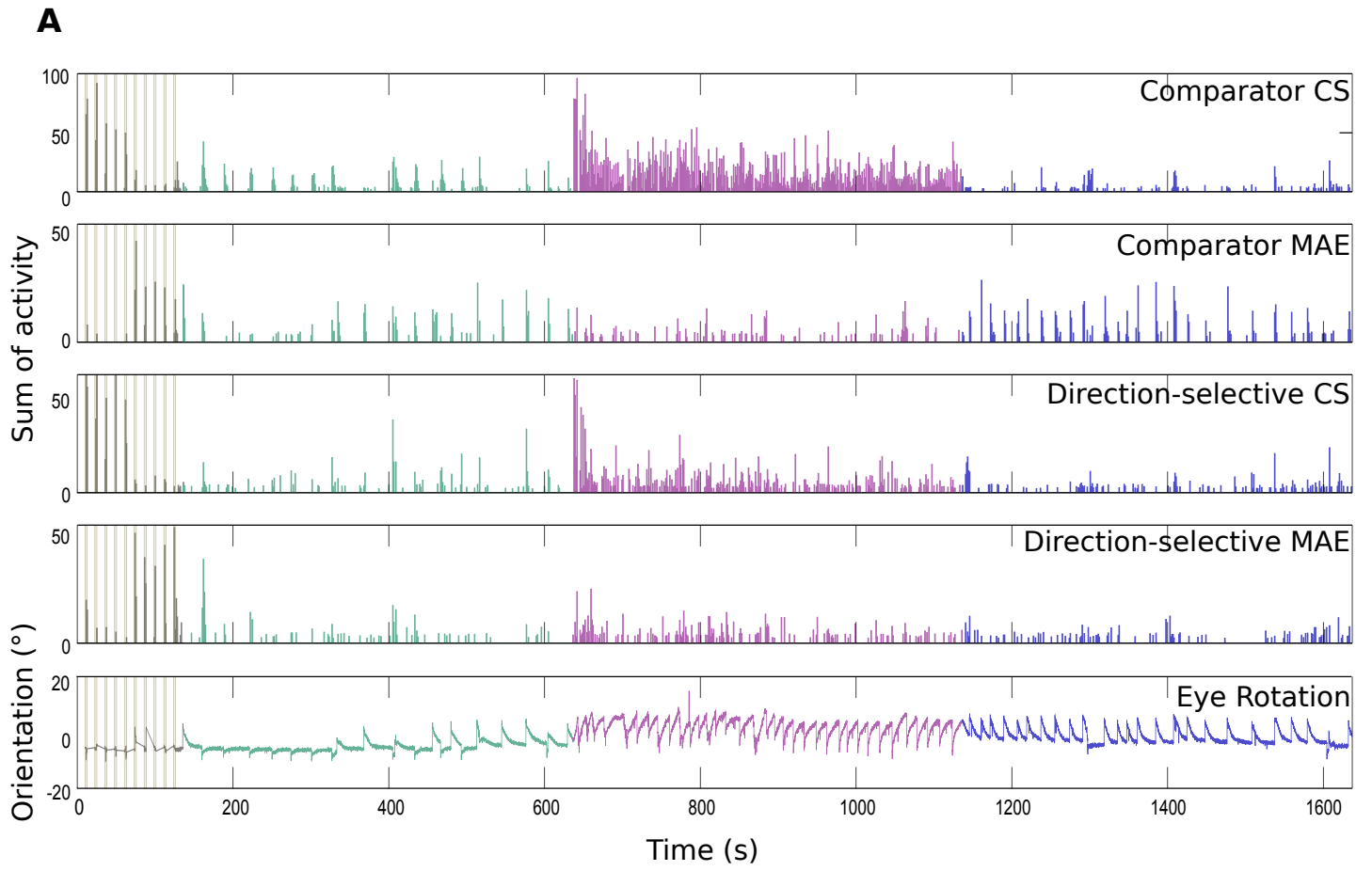
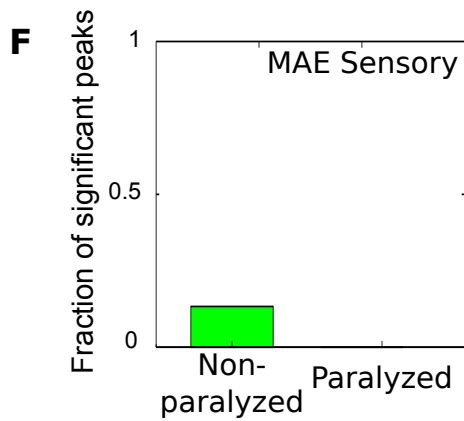
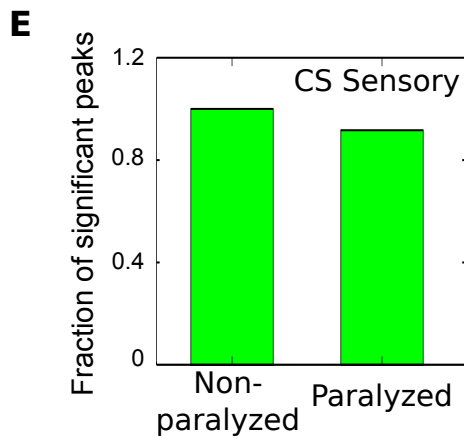
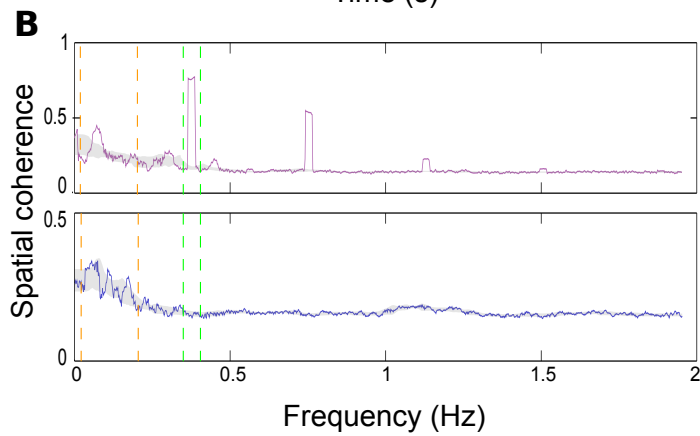
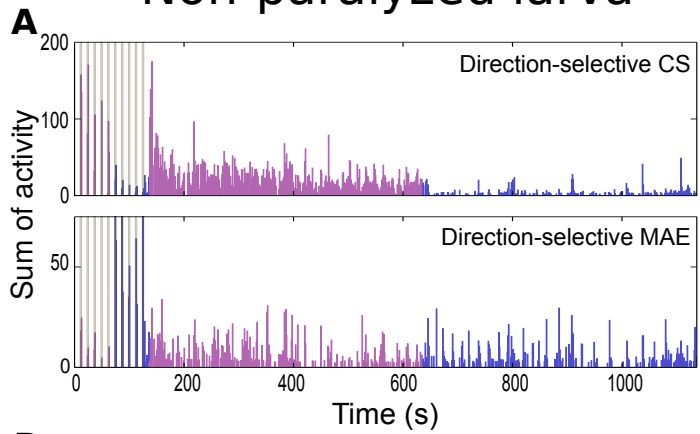


Figure S3. Determination comparator and direction selective neurons and estimation of their number (related to Figure 5).

(A) Top two panels: the sum of the activity of comparator tectal neurons (top, Comparator CS; bottom, Comparator MAE). Third and fourth panels: CS and MAE direction selective tectal neurons respectively as function of time. Bottom: eye direction as a function of time. Plots are color coded according to the period of stimulation, gray for pre-CS control, green for spontaneous activity, magenta for CS, and blue for post-CS control period.

(B) Mean fraction of unique comparator neurons and direction-selective neurons. Error bars, s.e. (n=12 (trials), from 9 larvae).

Non-paralyzed larva



Paralyzed larva

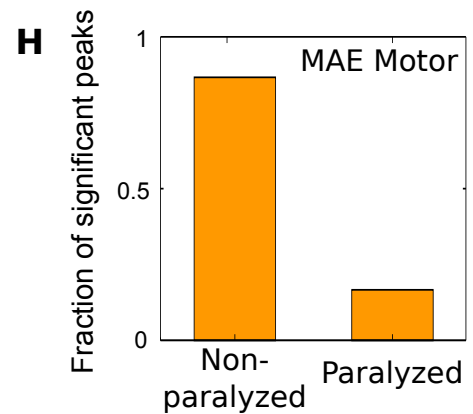
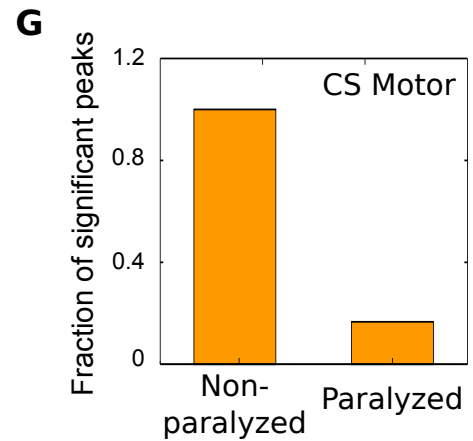
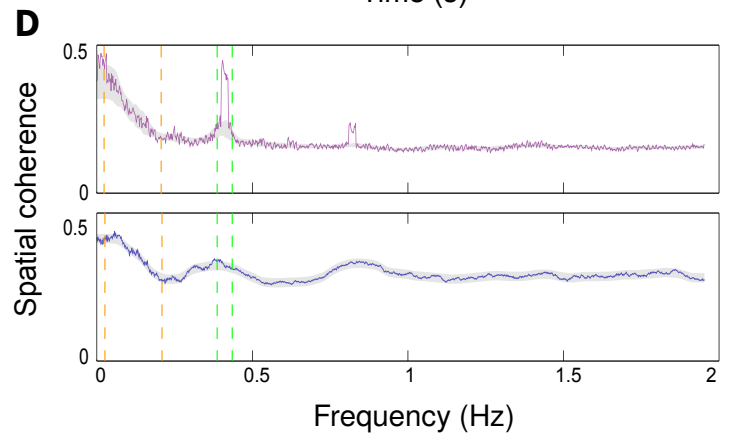
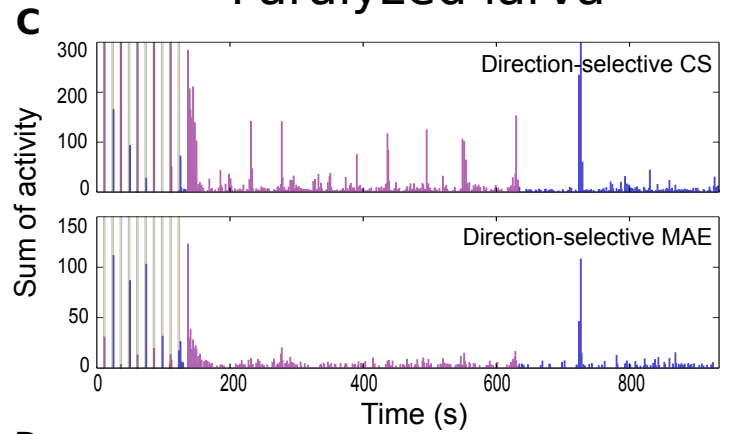


Figure S4. The rhythmicity of the MAE-associated tectal activity is generated through a neuro-muscular loop (related to Figure 7).

(A) Top: the sum of the Ca^{2+} transients of CS-direction-selective tectal neurons during the experimental paradigm for a representative non-paralyzed larva. Bottom: the sum of the activity of MAE-direction-selective tectal neurons. The panels are color coded according the different parts of the experimental paradigm. Magenta for CS, and blue for post-CS control period.

(B) Spatial coherence for the CS-direction-selective and MAE-direction-selective cells as a function of frequency for example in A. Orange dashed lines depict the frequency band associated with CS-induced eyes rotations. Green dashed lines represent the frequency band associated with tectal responses to the CS. Error bars: s.e.

(C and D) As for A and B, respectively, but for a representative paralyzed larva.

(E) Fraction of significant peaks in the sensory frequency band for non-paralyzed with respect to paralyzed larvae during the CS period.

(F) Fraction of significant peaks in the sensory frequency band for non-paralyzed with respect to paralyzed larvae during the MAE period.

(G) Fraction of significant peaks in the motor frequency band for non-paralyzed with respect to paralyzed larvae during the CS period.

(H) Fraction of significant peaks in the motor frequency band for non-paralyzed vs. paralyzed larvae during the MAE period. For (E-G) $n=12$ (trials), from 6 larvae.

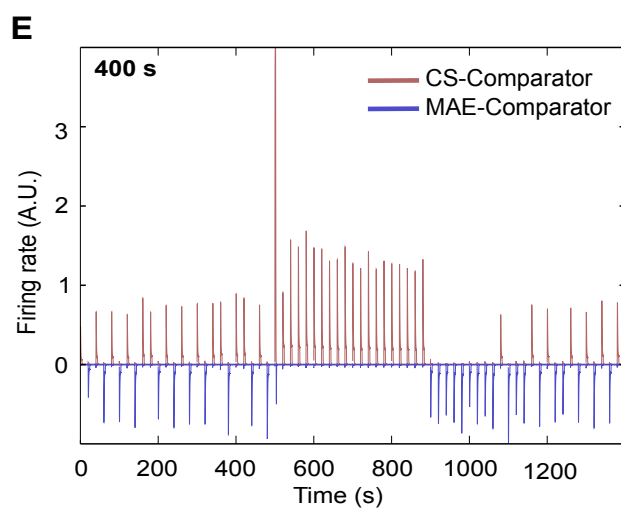
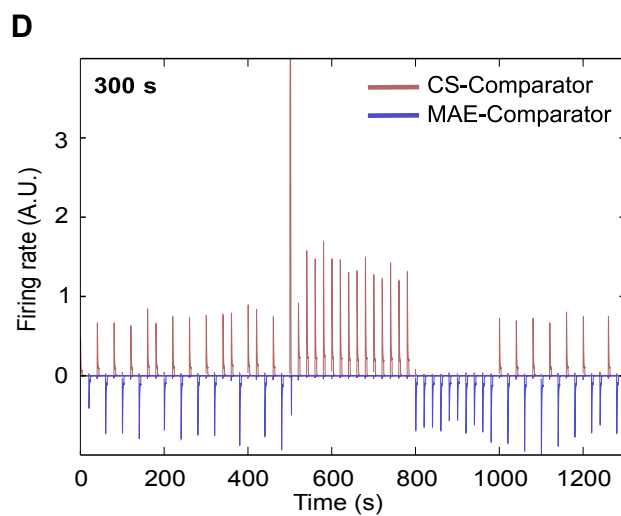
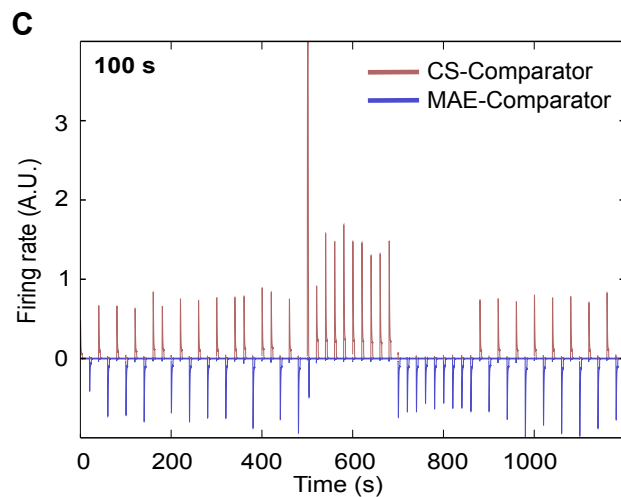
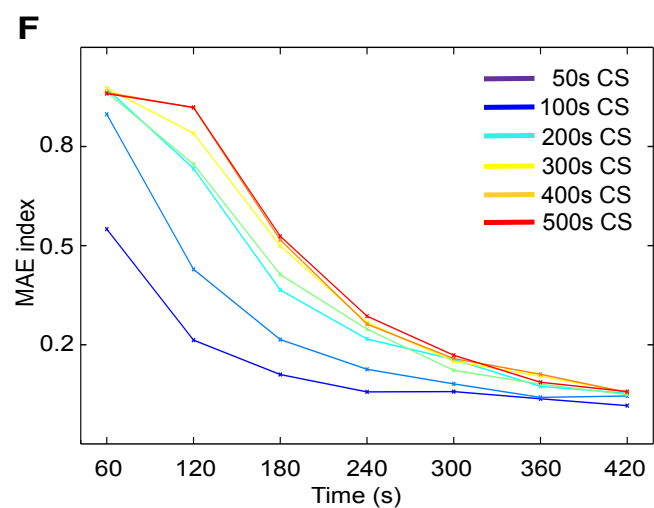
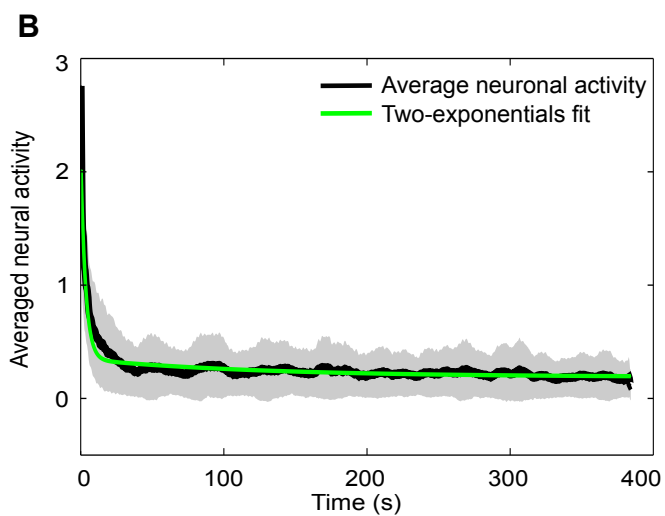
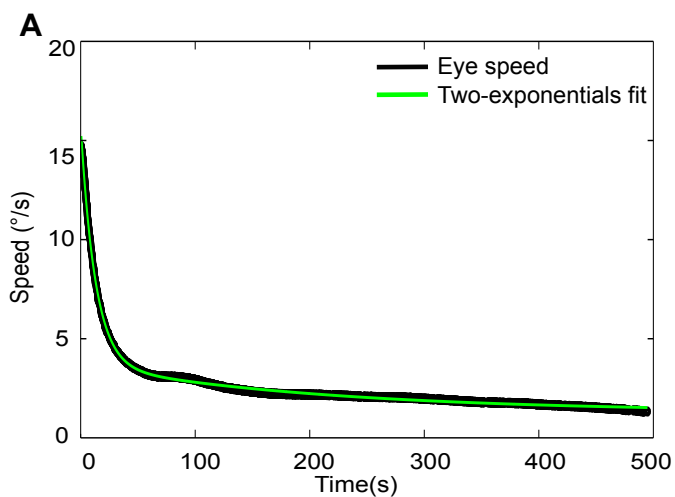


Figure S5. The empirical mathematical model reproduces the correlation between the CS duration and the extent of MAE (related to Figure 7).

(A) The pursuit velocity of the eyes induced by the CS (black) is best fitted by two exponentials (green, $t=12$ s. and 195 s). The CS velocity was 26 °/s.

(B) The averaged neuronal activity of the direction-selective population induced by the CS (black) can be fitted by two exponentials (green, $t=7$ s. and 650 s). The average neuronal activity of the direction-selective population was smoothed using a Gaussian kernel. These timescales were then used as the adaptation variables in the numerical model.

(C) Firing rates of the CS comparator populations and MAE comparator populations for a CS duration of 100 s, starting at 500 s.

(D and E) As for C, for CS durations of 300 and 400 s.

(F) The model *MAE duration* as a function of the duration of the CS. The MAE duration is defined as the time period where the MAE index is significantly greater than the control index, Fig. 7C). For comparison, the yellow curve shows the values obtained for the behavioral data (Fig. 1F).

Supplemental Video Legends

Video S1 (related to Figure 1) The video shows the CS, the larva's eyes outlined in yellow, and the eye position during the last 30 s of the CS and during the first 30 s of the optokinetic MAE-like behavior. Note the change in the pursuits' direction following the end of the conditioning stimulus (magenta vertical line).

Video S2 (related to Figure 2) The video shows the larva's eyes outlined in yellow during the presentation of the conditioning stimulus for 300 s, and the position of the eyes. During 100-200 s, Halorhodopsin was activated via a fiber optic (565 nm) to block eye movement (yellow patch). Note how the CS-induced pursuits are instantly blocked and rapidly recover at the onset and offset of the optogenetic stimulation.

Video S3 (related to Figure 3) The video shows different optical planes across the larva's optic tectum, in which the right hemisphere was ablated using a two-photon laser. The larva expressed GCaMP5 pan-neuronally. Note the large difference in basal fluorescence between both tecta, and the presence of GCaMP5 in the nucleus of neurons within the ablated hemisphere.

Chapter VI

Conclusion and Future perspectives

Rate models, even though they do not describe entirely the biophysical details of a network of neurons, help us to capture the various phenomena observed in the brain. In the first three chapters of this thesis, we have described a simple model of two groups of excitatory-inhibitory neurons and we have seen how they can help us study dynamical regimes of interaction of oscillations in the beta and low-gamma range. We found several regions in the phase diagram of this simple model: the phase oscillations of the neuron groups either synchronize or not depending on the coupling between the two groups. The alternating and modulating regimes are reported here for EI networks for the first time. This description of the two groups of EI networks can be extended to a chain of coupled and spatially extended EI networks. Such a description could help us understand the propagation of beta waves that was observed in the motor cortex of the monkey during motor preparation [Rubino et al., 2006]. Future work would be to compare the data obtained in the adaptive rate and the network simulations of the spatially extended chain to the exact experimental data and to assess how much of the experimental data can be reproduced by our models. These models also suggest experiments to observe if the system goes from synchrony to desynchrony upon the reduction of excitatory coupling between two areas, perhaps in a mutant species which lacks these long range connections. Moreover, recent studies in mice show that somatostatin (SOM) interneurons are required for long-distance coherence of gamma waves in the visual cortex [Veit et al., 2017]. This hypothesis could be tested in our model to see if the system goes from a desynchronized regime to a synchronized regime upon the addition of long-range E-I coupling. It also suggests to study refined models with different types of interneurons instead of clamping them into a single cell group as we have done here for simplicity.

In the second half of the thesis i.e. chapter 4 and chapter 5, we have used rate models to study the phenomenon of sensory adaptation, particularly that of the motion after effect in the zebrafish larva. With our simple model whose parameters were extracted from the experimental data, we were able to capture a lot of the features of the MAE phenomenon. The model, however, assumes the presence of a rhythmic input that generates the periodic eye movement. Future perspectives include finding the region in the zebrafish larva where this input is generated and integrating it in the framework of this model to build a more integrated description of the eye movements in the zebrafish larva. The study of other visual illusions such as bistable perception

seems also very promising and it is a line of work that we hope to pursue.

Bibliography

- [nne, 2016] (2016). Focus on neural computation and theory. *Nature Neuroscience*, 19.
- [neu, 2017] (2017). How does the brain work? *Neuron*, 94.
- [Abbott and Regehr, 2004] Abbott, L. and Regehr, W. (2004). Synaptic computation. *Nature*, 431:796-803.
- [Abbott et al., 1997] Abbott, L., Varela, J., Sen, K., and Nelson, S. (1997). Synaptic depression and cortical gain control. *Science*, 275:220-224.
- [Abbott and van Vreeswijk, 1993] Abbott, L. F. and van Vreeswijk, C. (1993). Asynchronous states in a network of pulse-coupled oscillators. *Phys Rev E*, 48, 1483–1490.
- [Achermann and Borbely, 1997] Achermann, P. and Borbely, A. A. (1997). Low-frequency (1 Hz) oscillations in the human sleep electroencephalogram. *Neuroscience*, 81: 213-222.
- [Adrian, 1935] Adrian, E. (1935). Discharge frequencies in the cerebral and cerebellar cortex. *Proc Phys Soc*, 83: 32-33.
- [Adrian, 1942] Adrian, E. (1942). Olfactory reactions in the brain of the hedgehog. *J Physiol*, 100: 459-473.
- [Adrian and Zotterman, 1926a] Adrian, E. D. and Zotterman, Y. (1926a). The impulses produced by sensory nerve endings: Part 3 impulses set up by touch and pressure. *J Physiol*, 61:465-483.
- [Adrian and Zotterman, 1926b] Adrian, E. D. and Zotterman, Y. (1926b). The impulses produced by sensory nerve-endings: Part ii. the response of a single end-organ. *J Physiol*, 61:151-171.
- [Ahrens et al., 2012] Ahrens, M., Li, J., Orger, M., Robson, D. N., Schier, A., Engert, F., and Portugues, R. (2012). Brain-wide neuronal dynamics during motor adaptation in zebrafish. *Nature*, 485, no. 7399 :471-7.
- [Ahrens and Engert, 2015] Ahrens, M. B. and Engert, F. (2015). Large-scale imaging in small brains. *Current opinion in neurobiology*, 32:78-86.

- [Ahrens et al., 2013] Ahrens, M. B., Orger, M. B., Robson, D. N., Li, J. M., and Keller, P. J. (2013). Whole-brain functional imaging at cellular resolution using light-sheet microscopy. *Nature methods*, 10(5):413–20.
- [Akerboom et al., 2012] Akerboom, J., Chen, T. W., Looger, L. L., et al. (2012). Optimization of a gcamp calcium indicator for neural activity imaging. *J Neurosci.*, 32(40):13819-40.
- [Aladjalova, 1957] Aladjalova, N. A. (1957). Infra-slow oscillations of the steady potential of the cerebral cortex. *Nature*, 179.
- [Alle et al., 2009] Alle, H., Roth, A., and Geiger, J. R. P. (2009). Energy-efficient action potentials in hippocampal mossy fibers. *Science*, 325.
- [Amari, 1977] Amari, S. (1977). Dynamics of pattern formation in lateral-inhibition type neural fields. *Biol Cybern*, 27, 77–87.
- [Amit and Brunel, 1997] Amit, D. J. and Brunel, N. (1997). Model of global spontaneous activity and local structured activity during delay periods in the cerebral cortex. *Cerebral Cortex*, 7, 237–252.
- [Amit and Tsodyks, 1991] Amit, D. J. and Tsodyks, M. (1991). Quantitative study of attractor neural network retrieving at low spike rates i: Substrate—spikes, rates and neuronal gain. *Network*, 2, 259–274.
- [Andersen and Andersson, 1968] Andersen, P. and Andersson, S. A. (1968). *Physiological Basis of the Alpha-Rhythm*. New York: Appleton-Century-Crofts.
- [Andersen and Eccles, 1962] Andersen, P. and Eccles, J. (1962). Inhibitory phasing of neuronal discharge. *Nature*, 196: 645-647.
- [Andersen et al., 2006] Andersen, P., Morris, R., Amaral, D., Bliss, T., and O’Keefe, J. (2006). *The Hippocampus Book*. Oxford Neuroscience Series.
- [Anstis et al., 1998] Anstis, S., Verstraten, F. A. J., and Mather, G. (1998). The motion aftereffect. *Trends in Cognitive Sciences*, 2(3).
- [Attneave, 1954] Attneave, F. (1954). Some informational aspects of visual perception. *Psychol Rev*, 61:183-193.
- [Augustin et al., 2016] Augustin, M., Ladenbauer, J., Baumann, F., and Obermayer, K. (2016). Low-dimensional spike rate models derived from networks of adaptive integrate-and-fire neurons: comparison and implementation. *arXiv*, 1611.07999.
- [Baccus and Meister, 2002] Baccus, S. and Meister, M. (2002). Fast and slow contrast adaptation in retinal circuitry. *Neuron*, 36:909-919.
- [Badel et al., 2008a] Badel, L., Lefort, S., Berger, T. K., Petersen, C., Gerstner, W., and Richardson, M. J. (2008a). Dynamic i-v curves are reliable predictors of naturalistic pyramidal-neuron voltage traces. *J Neurophysiol*, 99, 656–666.

- [Badel et al., 2008b] Badel, L., Lefort, S., Berger, T. K., Petersen, C., Gerstner, W., and Richardson, M. J. (2008b). Extracting non-linear integrate-and-fire models from experimental data using dynamic i-v curves. *Biol Cybern*, 99, 361–370.
- [Bai et al., 2006] Bai, L., Huang, X., Yang, Q., and Wu, J. Y. (2006). Spatiotemporal patterns of an evoked network oscillation in neocortical slices: coupled local oscillators. *J Neurophysiol*, 96: 2528-2538.
- [Baker et al., 1999] Baker, S. N., Kilner, J. M., Pinches, E. M., and Lemon, R. N. (1999). The role of synchrony and oscillations in the motor output. *Exp. brain Res.*, 128: 109.
- [Ball, 2005] Ball, C. (2005). Motion aftereffects in a self-organizing model of primary visual cortex. *Master's thesis, The University of Edinburgh*.
- [Barlow, 1990] Barlow, H. (1990). *A theory about the functional role and synaptic mechanism of visual aftereffects. In Visual Coding and Efficiency*. Cambridge University Press.
- [Barlow et al., 1976] Barlow, H., Macleod, D., and van Meeteren, A. (1976). Adaptation to gratings: no compensatory advantages found. *Vision Research*, 16:1043-5.
- [Barlow and Hill, 1963] Barlow, H. B. and Hill, R. M. (1963). Evidence for a physiological explanation of the waterfall phenomenon and figural after-effects. *Nature*, 200.
- [Bednar and Miikkulainen, 2000] Bednar, J. and Miikkulainen, R. (2000). Tilt after-effects in a self-organizing model of the primary visual cortex. *Neural Comput*, 12(7):1721-1740.
- [Berger, 1929] Berger, H. (1929). Über das elektrenkephalogramm des menschen. *Archiv für Psychiatrie und Nervenkrankheiten*, 87: 527-570.
- [Berridge et al., 2003] Berridge, M., Bootman, M., and Roderick, H. (2003). Calcium signalling: dynamics, homeostasis and remodelling. *Nat. Rev. Mol. Cell Biol.*, 4, 517–529.
- [Berridge et al., 2000] Berridge, M., Lipp, P., , and Bootman, M. (2000). The versatility and universality of calcium signalling. *Nat. Rev. Mol. Cell Biol.*, 1, 11–21.
- [Beurle, 1956] Beurle, R. L. (1956). Properties of a mass of cells capable of regenerating pulses. *Philos Trans Roy Soc London B*, 240, 5594.
- [Bi and Poo, 2001] Bi, G. and Poo, M. (2001). Synaptic modification by correlated activity. *Annual Review of Neuroscience*, 24 pp 139-66.
- [Binzegger et al., 2004] Binzegger, T., Douglas, R. J., and Martin, K. (2004). A quantitative map of the circuit of cat primary visual cortex. *J Neurosci*, 24.
- [Bland, 1986] Bland, B. (1986). The physiology and pharmacology of hippocampal formation theta rhythms. *Prog Neurobiol*, 26: 1-54.

- [Blankenship and Feller, 2010] Blankenship, A. G. and Feller, M. B. (2010). Mechanisms underlying spontaneous patterned activity in developing neural circuits. *Nat Rev Neurosci*, 11: 18-29.
- [Borgers and Kopell, 2003] Borgers, C. and Kopell, N. (2003). Synchronization in networks of excitatory and inhibitory neurons with sparse, random connectivity. *Neural Computation*, 15(3): 509-38.
- [Bouvier et al., 2016] Bouvier, G., Clopath, C., Bimbard, C., Nadal, J., Brunel, N., Hakim, V., and Barbour, B. (2016). Cerebellar learning using perturbations. *bioRxiv*.
- [Bouyer et al., 1981] Bouyer, J., Montaron, M., and Rougeul, A. (1981). Fast frontoparietal rhythms during combined focused attentive behaviour and immobility in cat: cortical and thalamic localizations. *Electroencephalogr Clin Neurophysiol*, 51: 244-252.
- [Bragin et al., 1995] Bragin, A., Jando, G., Nadasdy, Z., Hetke, J., Wise, K., and Buzsaki, G. (1995). Gamma (40-100 Hz) oscillation in the hippocampus of the behaving rat. *J Neurosci*, 15: 47-60.
- [Brenner et al., 2000] Brenner, N., Bialek, W., and de Ruyter van, S. R. (2000). Adaptive rescaling maximizes information transmission. *Neuron*, 26:695-702.
- [Brette, 2013] Brette, R. (2013). Sharpness of spike initiation in neurons explained by compartmentalization. *PLoS Comp Biol*, 9(12).
- [Brette et al., 2007] Brette, R., Rudolph, M., Carnevale, T., Hines, M., Beeman, D., Bower, J. M., Diesmann, M., et al. (2007). Simulation of networks of spiking neurons: A review of tools and strategies. *J Comput Neurosci*, 23, 349-398.
- [Brown et al., 1975] Brown, J., Cohen, L., De Weer, P., Pinto, L., Ross, W., and Salzberg, B. (1975). Rapid changes in intracellular free calcium concentration. detection by metallochromic indicator dyes in squid giant axon. *Biophys. J.*, 15, 1155-1160.
- [Brunel, 2000] Brunel, N. (2000). Dynamics of sparsely connected networks of excitatory and inhibitory spiking neurons. *J Comput Neurosci*, 8, 183-208.
- [Brunel, 2011] Brunel, N. (2011). *Principles of neural coding: chapter 25*. CRC Press.
- [Brunel and Hakim, 1999] Brunel, N. and Hakim, V. (1999). Fast global oscillations in networks of integrate-and-fire neurons with low firing rates. *Neural Comp*, 11, 1621-1671.
- [Brunel and Hansel, 2006] Brunel, N. and Hansel, D. (2006). How noise affects the synchronization properties of networks of inhibitory neurons. *Neural Comp*, 18, 1066-1110.
- [Bryant and Segundo, 1976] Bryant, H. and Segundo, J. (1976). Spike initiation by transmembrane current: a white-noise analysis. *Journal of Physiology*, 260:279-314.

- [Buonomano and Maass, 2009] Buonomano, D. and Maass, W. (2009). State-dependent computations: Spatiotemporal processing in cortical networks. *Nat Rev Neurosci*, 10:113-125.
- [Burrill and SS Easter, 1994] Burrill, J. and SS Easter, S. S. (1994). Development of the retinofugal projections in the embryonic and larval zebrafish (*brachydanio rerio*). *Journal of Comparative Neurology*, 600.
- [Buzsaki, 2006] Buzsaki, G. (2006). *Rhythms of the Brain*. New York: Oxford Univ. Press.
- [Buzsaki and Chrobak, 1995] Buzsaki, G. and Chrobak, J. (1995). Temporal structure in spatially organized neuronal ensembles: a role for interneuronal networks. *Curr Opin Neurobiol*, 5: 504-510.
- [Buzsaki and Draguhn, 2004] Buzsaki, G. and Draguhn, A. (2004). Neuronal oscillations in cortical networks. *Science*, 304: 1926-1929.
- [Buzsaki et al., 1983] Buzsaki, G., Leung, L. W., and Vanderwolf, C. H. (1983). Cellular bases of hippocampal eeg in the behaving rat. *Brain Res*, 287: 139-171.
- [Buzsaki et al., 1992] Buzsaki, G., Urioste, R., Hetke, J., and K., W. (1992). High frequency network oscillation in the hippocampus. *Science*, 256: 1025-1027.
- [Canolty et al., 2006] Canolty, R., Edwards, E., Dalal, S., Soltani, M., Nagarajan, S., Kirsch, H., Berger, M., Barbaro, N., and Knight, R. (2006). High gamma power is phase-locked to theta oscillations in human neocortex. *Science*, 313: 1626-1628.
- [Carandini and Ferster, 1997] Carandini, M. and Ferster, D. (1997). A tonic hyperpolarization underlying contrast adaptation in cat visual cortex. *Science*, 276:949-952.
- [Carpenter and Grossberg, 1981] Carpenter, G. and Grossberg, S. (1981). Adaptation and transmitter gating in vertebrate photoreceptors. *J Theoret Neurobiol*, 1: 1-42.
- [Chalasani et al., 2007] Chalasani, S., Chronis, N., Tsunozaki, M., Gray, J., Ramot, D., Goodman, M., and Bargmann, C. (2007). Dissecting a circuit for olfactory behaviour in *caenorhabditis elegans*. *Nature*, 450, 63-70.
- [Chander and Chichilnisky, 2001] Chander, D. and Chichilnisky, E. J. (2001). Adaptation to temporal contrast in primate and salamander retina. *J Neurosci*, 21:9904-9916.
- [Chichilnisky, 2001] Chichilnisky, E. J. (2001). A simple white noise analysis of neuronal light responses. *Network: Computation in Neural Systems*, 12:199-213.
- [Chopin and Mamassian, 2012] Chopin, A. and Mamassian, P. (2012). Predictive properties of visual adaptation. *Curr Bio*, 22:622-6.
- [Chung et al., 2002] Chung, S., Li, X., and Nelson, S. (2002). Short-term depression at thalamocortical synapses contributes to rapid adaptation of cortical sensory responses in vivo. *Neuron*, 34:437-446.

- [Cilluffo et al., 2004] Cilluffo, M., Matthews, H., Brockerhoff, S., and Fain, G. (2004). Light-induced ca release in the visible cones of the zebrafish. *Visual Neuroscience*, 21: 599-609.
- [Ciroux, 2005] Ciroux, J. (2005). Simulating the mccollough effect in a self-organizing model of the primary visual cortex. *Master's thesis, The University of Edinburgh*.
- [Clark et al., 2013] Clark, D., Benichou, R., Meister, M., and Azeredo da Silveira, R. (2013). Dynamical adaptation in photoreceptors. *PLoS Comput Biol*, 9(11): e1003289.
- [Clifford et al., 2007] Clifford, C., Webster, M., and Stanley, G. (2007). Visual adaptation: neural, psychological and computational aspects. *Vis Res*, 47:3125-3131.
- [Contreras and Llinas, 2001] Contreras, D. and Llinas, R. (2001). Voltage-sensitive dye imaging of neocortical spatiotemporal dynamics to afferent activation frequency. *J Neurosci*, 21: 9403-9413.
- [Cover and Thomas, 2005] Cover, T. M. and Thomas, J. A. (2005). *Elements of Information Theory*. Wiley-Interscience.
- [Dahmen et al., 2010] Dahmen, J., Keating, P., Nodal, F., Schulz, A., and King, A. (2010). Adaptation to stimulus statistics in the perception and neural representation of auditory space. *Neuron*, 66:937-948.
- [Dayan and Abbott, 2001] Dayan, P. and Abbott, L. (2001). *Theoretical Neuroscience*. Cambridge University Press.
- [Dean et al., 2005] Dean, I., Harper, N., and McAlpine, D. (2005). Neural population coding of sound level adapts to stimulus statistics. *NatNeurosci*, 8:1684-1689.
- [Deco and Thiele, 2009] Deco, G. and Thiele, A. (2009). Attention: oscillations and neuropharmacology. *Eur J Neurosci*, 30: 347-354.
- [Del Bene et al., 2010] Del Bene, F., Wyart, C., Robles, E., Tran, A., Looger, L., Scott, E. K., Isacoff, E. Y., and Baier, H. (2010). Filtering of visual information in the tectum by an identified neural circuit. *Science*, 330(6004):669-673.
- [Denk et al., 1990] Denk, W., Strickler, J. H., and Webb, W. W. (1990). Two-photon laser scanning fluorescence microscopy. *Science*, 248, pages 73-76.
- [Deo and MacRae, 2011] Deo, R. and MacRae, C. (2011). The zebrafish: scalable in vivo modeling for systems biology. *Wiley Interdiscip Rev Syst Biol Med.*, 3(3):335-46.
- [Destexhe and Sejnowski, 2009] Destexhe, A. and Sejnowski, T. J. (2009). The wilson-cowan model, 36 years later. *Biol Cybern*, 101:1-2.
- [Dombeck et al., 2010] Dombeck, D., Harvey, C., Tian, L., Looger, L., and Tank, D. (2010). Functional imaging of hippocampal place cells at cellular resolution during virtual navigation. *Nat. Neurosci.*, 13, 1433-1440.

- [Dougherty et al., 2005] Dougherty, D., Wright, G., and Yew, A. (2005). Computational model of the camp-mediated sensory response and calcium-dependent adaptation in vertebrate olfactory receptor neurons. *Proc Natl Acad Sci U S A*, 102(30): 10415-10420.
- [Douglas and Martin, 2007] Douglas, R. J. and Martin, K. A. C. (2007). Recurrent neuronal circuits in the neocortex. *Current Biology*, 17 No 13.
- [Douglass et al., 2008] Douglass, A. D., Kraves, S., Deisseroth, K., Schier, A. F., and Engert, F. (2008). Escape behavior elicited by single, channelrhodopsin-2-evoked spikes in zebrafish somatosensory neurons. *Current biology*, 18, no. 15:1133-7.
- [Doya et al., 2007] Doya, K., Ishii, S., Pouget, A., and Rao, R. (2007). *Bayesian brain: probabilistic approaches to neural coding*. MIT Press, Cambridge.
- [Dragoi et al., 2000] Dragoi, V., Sharma, J., and M., S. (2000). Adaptation-induced plasticity of orientation tuning in adult visual cortex. *Neuron*, 28:287-298.
- [Drew and Abbott, 2006] Drew, P. and Abbott, L. (2006). Models and properties of power-law adaptation in neural systems. *J Neurophysiol*, 96:826-833.
- [Dulhunty, 2006] Dulhunty, A. (2006). Excitation-contraction coupling from the 1950s into the new millennium. *Clin. Exp. Pharmacol. Physiol.*, 33, 763–772.
- [Easter and Nicola, 1996] Easter, S. and Nicola, G. (1996). The development of vision in the zebrafish (danio rerio). *Developmental biology*, 180, no. 2:646-663.
- [Easter and Nicola, 1997] Easter, S. and Nicola, G. (1997). The development of eye movements in the zebrafish (danio rerio). *Developmental biology*, 31, no. 4:267-276.
- [Eckhorn et al., 1988] Eckhorn, R., Bauer, R., Jordan, W., Brosch, M., Kruse, W., Munk, M., and Reitboeck, H. (1988). Coherent oscillations: a mechanism of feature linking in the visual cortex? multiple electrode and correlation analyses in the cat. *Biol Cybern*, 60: 121-130.
- [Eeckman and Freeman, 1978] Eeckman, F. H. and Freeman, W. J. (1978). Spatial properties of an eeg event in the olfactory bulb and cortex. *Electroencephalogr Clin Neurophysiol*, 44: 586-605.
- [Eeckman and Freeman, 1990] Eeckman, F. H. and Freeman, W. J. (1990). Correlations between unit firing and eeg in the rat olfactory system. *Brain Res*, 528: 238-244.
- [Eilers et al., 1995] Eilers, J., Augustine, G., and Konnerth, A. (1995). Subthreshold synaptic ca²⁺ signalling in fine dendrites and spines of cerebellar purkinje neurons. *Nature*, 373, 155–158.
- [Ermentrout, 1994] Ermentrout, G. B. (1994). Reduction of conductance based models with slow synapses to neural nets. *Neural Comput*, 6, 679–695.

- [Ermentrout, 1996] Ermentrout, G. B. (1996). Type i membranes, phase resetting curves, and synchrony. *Neural Comput*, 8, 979–1001.
- [Ermentrout and Kopell, 1986] Ermentrout, G. B. and Kopell, N. (1986). Parabolic bursting in an excitable system coupled with a slow oscillation. *SIAM J Appl Math*, 46, 233–253.
- [Fain et al., 2001] Fain, G., Matthews, H., Cornwall, M., and Koutalos, Y. (2001). Adaptation in vertebrate photoreceptors. *Physiological Reviews*, 81: 117-151.
- [Fairhall et al., 2001] Fairhall, A., Lewen, G., Bialek, W., and deRuyter, R. (2001). Efficiency and ambiguity in an adaptive neural code. *Nature*, 412.
- [Fioravante and Regehr, 2011] Fioravante, D. and Regehr, W. (2011). Short-term forms of presynaptic plasticity. *Curr Opin Neurobiol*, 21:269-274.
- [Fletcher et al., 2009] Fletcher, M., Masurkar, A., Xing, J., Imamura, F., Xiong, W., Nagayama, S., Mutoh, H., Greer, C., Knopfel, T., and Chen, W. (2009). Optical imaging of postsynaptic odor representation in the glomerular layer of the mouse olfactory bulb. *J. Neurophysiol.*, 102, 817–830.
- [Foster, 2011] Foster, D. H. (2011). Color constancy. *Vision Res*, 51:674-700.
- [Fourcaud and Brunel, 2002] Fourcaud, N. and Brunel, N. (2002). Dynamics of the firing probability of noisy integrate-and-fire neurons. *Neural Comput*, 14(9), 2057–2110.
- [Fourcaud-Trocmé et al., 2003] Fourcaud-Trocmé, N., Hansel, D., van Vreeswijk, C., and Brunel, N. (2003). How spike generation mechanisms determine the neuronal response to fluctuating inputs. *J Neurosci*, 23, 11628–11640.
- [Frazor and Geisler, 2006] Frazor, R. and Geisler, W. (2006). Local luminance and contrast in natural images. *Vis Res*, 46:1585-1598.
- [Freeman, 1968] Freeman, W. (1968). Relations between unit activity and evoked potentials in prepyriform cortex of cats. *J Neurophysiol*, 31: 337-348.
- [Freeman, 1975] Freeman, W. J. (1975). *Mass Action in the Nervous System*. New York: Academic.
- [Friedlander and Brenner, 2009] Friedlander, T. and Brenner, N. (2009). Adaptive response by state-dependent inactivation. *Proc Nat Ac Sci*, 106: 22558-22563.
- [Friedrich et al., 2010a] Friedrich, R., Jacobson, G. A., and Zhu, P. (2010a). Dhodh modulates transcriptional elongation in the neural crest and melanoma. *Current Biology*, 20, no. 8:R371-R381.
- [Friedrich et al., 2010b] Friedrich, R. W., Jacobson, G. A., and Zhu, P. (2010b). Circuit neuroscience in zebrafish. *Current Biology*, 20 no.80.
- [Fries et al., 2007] Fries, P., Nikolic, D., and Singer, W. (2007). The gamma cycle. *Trends Neurosci*, 30: 309-316.

- [Frolov and Medvedev, 1986] Frolov, A. and Medvedev, A. (1986). Substantiation of the “point approximation” for describing the total electrical activity of the brain with the use of a simulation model. *Biophysics*, 31: 304-308.
- [Fuhrmann et al., 2002] Fuhrmann, G., Markram, H., and Tsodyks, M. (2002). Spike frequency adaptation and neocortical rhythms. *J Neurophysiol*, 88, 761–770.
- [Gabriel et al., 2012] Gabriel, J. P., Trivedi, C. A., Maurer, C. M., Ryu, S., , and Bollmann, J. H. (2012). Layer-specific targeting of direction-selective neurons in the zebrafish optic tectum. *Neuron*, 76(6):1147-1160.
- [Gahtan et al., 2005] Gahtan, E., Tanger, P., and Baier, H. (2005). Visual prey capture in larval zebrafish is controlled by identified reticulospinal neurons downstream of the tectum. *The Journal of neuroscience*, 25.
- [Geisler et al., 2007] Geisler, C., Robbe, D., Zugaro, M., Sirota, A., and Buzski, G. (2007). Hippocampal place cell assemblies are speed-controlled oscillators. *Proc Natl Acad Sci USA*, 104: 8149-8154.
- [Gerstner and Kistler, 2002] Gerstner, W. and Kistler, W. (2002). *Spiking neuron models*. Cambridge University Press.
- [Ghazanfar et al., 2008] Ghazanfar, A., Chandrasekaran, C., and Logothetis, N. (2008). Interactions between the superior temporal sulcus and auditory cortex mediate dynamic face/voice integration in rhesus monkeys. *J Neurosci*, 28: 4457-4469.
- [Giaschi et al., 1993] Giaschi, D., Douglas, R., Marlin, S., and Cynader, M. (1993). The time course of direction-selective adaptation in simple and complex cells in cat striate cortex. *Vision research*, 70, no. 5.
- [Gilbert, 1993] Gilbert, C. D. (1993). Circuitry, architecture, and functional dynamics of visual cortex. *Cereb Cortex*, 3: 373-386.
- [Goepfert-Mayer, 1931] Goepfert-Mayer, M. (1931). Uber elementarakte mit zwei quantensprünge. *Annals of Physics*, 9(3).
- [Gollisch and Meister, 2010] Gollisch, T. and Meister, M. (2010). Eye smarter than scientists believed: Neural computations in circuits of the retina. *Neuron*, 65:150-164.
- [Goodman and Brette, 2008] Goodman, D. F. M. and Brette, R. (2008). Brian: a simulator for spiking neural networks in python. *Frontiers in neuroinformatics*, 2.
- [Goodman and Brette, 2009] Goodman, D. F. M. and Brette, R. (2009). The brian simulator. *Front. Neurosci.*, 3.
- [Gray, 1994] Gray, C. M. (1994). Synchronous oscillations in neuronal systems: mechanisms and functions. *J Comput Neurosci*, 1: 11-38.
- [Gray-Keller and Detwiler, 1994] Gray-Keller, M. and Detwiler, P. (1994). The calcium feedback signal in the phototransduction cascade of vertebrate rods. *Neuron*, 13: 849-861.

- [Greenlee and Heitger, 1988] Greenlee, M. and Heitger, F. (1988). The functional role of contrast adaptation. *Vision Research*, 28:791-7.
- [Grienberger and Konnerth, 2012] Grienberger, C. and Konnerth, A. (2012). Imaging calcium in neurons. *Neuron*, 73.
- [Griffith, 1963] Griffith, J. S. (1963). A field theory of neural nets: I: Derivation of field equations. *Bull Math Biophys*, 25, 111–120.
- [Griffith, 1965] Griffith, J. S. (1965). A field theory of neural nets: Ii: Properties of field equations. *Bull Math Biophys*, 7, 187–195.
- [Grinvald and Hildesheim, 2004] Grinvald, A. and Hildesheim, R. (2004). VSDI: a new era in functional imaging of cortical dynamics. *Nature Reviews Neuroscience.*, 5: 874–85.
- [Gutkin and Ermentrout, 1998] Gutkin, B. and Ermentrout, G. (1998). Dynamics of membrane excitability determine interspike interval variability: A link between spike generation mechanisms and cortical spike train statistics. *Neural Comp*, 10, 1047–1065.
- [Hansel and Mato, 2003] Hansel, D. and Mato, G. (2003). Asynchronous states and the emergence of synchrony in large networks of interacting excitatory and inhibitory neurons. *Neural Comput*, 15: 1-56.
- [Harris et al., 2003] Harris, K. D., Csicsvari, J., Hirase, H., Dragoi, G., and Buzsáki, G. (2003). Organization of cell assemblies in the hippocampus. *Nature*, 424: 552-556.
- [Hasselmo, 2005] Hasselmo, M. E. (2005). What is the function of hippocampal theta rhythm? linking behavioral data to phasic properties of field potential and unit recording data. *Hippocampus*, 15: 936-949.
- [Hay et al., 2011] Hay, E., Hill, S., Schurmann, F., Markram, H., and Segev, I. (2011). Models of neocortical layer 5b pyramidal cells capturing a wide range of dendritic and perisomatic active properties. *Plos Comput Biol*, 7:e1002107.
- [Helmchen and Denk, 2005] Helmchen, F. and Denk, W. (2005). Deep tissue two-photon microscopy. *Nat. Methods*, 2, 932–940.
- [Hodgkin, 1975] Hodgkin, A. L. (1975). The optimum density of sodium channels in an unmyelinated nerve. *Philos. Trans. R. Soc. London Ser. B*, 270(908):297-300.
- [Hodgkin and Huxley, 1952] Hodgkin, A. L. and Huxley, A. F. (1952). A quantitative description of membrane current and its application to conduction and excitation in nerve. *Journal of Physiology*, 117 (4): 500–544.
- [Horowitz, 1972] Horowitz, J. M. (1972). Evoked activity of single units and neural populations in the hippocampus of the cat. *Electroencephalogr Clin Neurophysiol*, 32: 227-240.

- [Hosoya et al., 2005] Hosoya, T., Baccus, S. A., and Meister, M. (2005). Dynamic predictive coding by the retina. *Nature*, 436:71-77.
- [Howe et al., 2013] Howe, K., Clark, M. D., Stemple, D. L., et al. (2013). The zebrafish reference genome sequence and its relationship to the human genome. *Nature*, 496(7446):498-503.
- [Huber et al., 2004] Huber, R., Ghilardi, M. F., Massimini, M., and Tononi, G. (2004). Local sleep and learning. *Nature*, 430: 78-81.
- [Huguenard and McCormick, 1992] Huguenard, J. R. and McCormick, D. A. (1992). Simulation of the currents involved in rhythmic oscillations in thalamic relay neurons. *J. Neurophysiol.*, 68(4): 1373–1383.
- [Hunter et al., 2013] Hunter, P. R., Lowe, A. S., Thompson, I. D., and Meyer, M. P. (2013). Emergent properties of the optic tectum revealed by population analysis of direction and orientation selectivity. *The Journal of neuroscience*, 33(35):13940-5.
- [Izhikevich, 2001] Izhikevich, E. M. (2001). Resonate-and-fire neurons. *Neural Networks*, 14, 883–894.
- [Jaeger, 2015] Jaeger, D. (2015). *Encyclopedia of Computational Neuroscience*. Springer Science+Business Media New York.
- [Jasper and Penfield, 1949] Jasper, H. and Penfield, W. (1949). Electroconvulsions in man: effect of voluntary movement upon the electrical activity of the precentral gyrus. *Eur Arch Psychiatry Clin Neurosci*, 183: 163-174.
- [Kalatsky and Stryker, 2003] Kalatsky, V. and Stryker, M. (2003). New paradigm for optical imaging: temporally encoded maps of intrinsic signal. *Neuron*, 38(4):529-45.
- [Katz et al., 2006] Katz, Y., Heiss, J. E., and Lampl, I. (2006). Cross-whisker adaptation of neurons in the rat barrel cortex. *J Neurosci*, 26:13363-13372.
- [Kim and Rieke, 2001] Kim, K. J. and Rieke, F. (2001). Temporal contrast adaptation in the input and output signals of salamander retinal ganglion cells. *J Neurosci*, 21:287-299.
- [King et al., 2011] King, A., Dahmen, J., Keating, P., et al. (2011). Neural circuits underlying adaptation and learning in the perception of auditory space. *Neurosci Biobehav Rev*, 35:2129-2139.
- [Knight, 1972] Knight, B. W. (1972). Dynamics of encoding in a population of neurons. *J Gen Physiol*, 59, 734–766.
- [Kohn, 2007] Kohn, A. (2007). Visual adaptation: physiology, mechanisms, and functional benefits. *J Neurophysiol*, 97:3155-3164.
- [Kohn and Movshon, 2003] Kohn, A. and Movshon, J. (2003). Neuronal adaptation to visual motion in area mt of the macaque. *Neuron*, 39, 681-691.

- [Kubo et al., 2014] Kubo, F., Hablitzel, B., DalMaschio, M., Driever, W., Baier, H., and Arrenberg, A. B. (2014). Functional architecture of an optic flow-responsive area that drives horizontal eye movements in zebrafish. *Neuron*, 81(6):1344-1359.
- [Kuramoto, 1984] Kuramoto, Y. (1984). *Chemical Oscillations, Waves, and Turbulence*. Springer, Berlin.
- [Kvale and Schreiner, 2004] Kvale, M. and Schreiner, C. (2004). Short-term adaptation of auditory receptive fields to dynamic stimuli. *J Neurophysiol*, 91:604-612.
- [La Camera et al., 2006] La Camera, G., Rauch, A., Thurbon, D., Luscher, H. R., Senn, W., and Fusi, S. (2006). Multiple time scales of temporal response in pyramidal and fast spiking cortical neurons. *J Neurophysiol*, 96:3448-3464.
- [Laing and Chow, 2002] Laing, C. and Chow, C. (2002). A spiking neuron model for binocular rivalry. *Journal of Computational Neuroscience*, 12, 39-53.
- [Lapicque, 1907] Lapicque, L. (1907). Recherches quantitatives sur l'excitabilité électrique des nerfs traitée comme une polarisation. *J Physiol Pathol Gen*, 9, 620-635.
- [Latham et al., 2000] Latham, P. E., Richmond, B. J., Nelson, P., and Nirenberg, S. (2000). Intrinsic dynamics in neuronal networks. *J Neurophysiol*, 83, 808.
- [Laughlin, 1981] Laughlin, S. (1981). A simple coding procedure enhances a neuron's information capacity. *Z Naturforsch C*, 36:910-2.
- [Ledoux and Brunel, 2011] Ledoux, E. and Brunel, N. (2011). Dynamics of networks of excitatory and inhibitory neurons in response to time-dependent inputs. *Front Comput Neurosci*, 5, 25.
- [Leung, 1982] Leung, L. S. (1982). Nonlinear feedback model of neuronal populations in hippocampal cal region. *J Neurophysiol*, 47: 845-868.
- [Li and Hopfield, 1989] Li, Z. and Hopfield, J. J. (1989). Modeling the olfactory bulb and its neural oscillatory processings. *Biol Cybern*, 61: 379-392.
- [Llinas and Ribary, 1993] Llinas, R. and Ribary, U. (1993). Coherent 40-hz oscillation characterizes dream state in humans. *Proc Natl Acad Sci USA*, 90: 2078-2081.
- [Looger and Griesbeck, 2011] Looger, L. and Griesbeck, O. (2011). Genetically encoded neural activity indicators. *Curr. Opin. Neurobiol.*, 22(1).
- [Lu and Means, 1993] Lu, K. and Means, A. (1993). Regulation of the cell cycle by calcium and calmodulin. *Endocr. Rev.*, 14, 40-58.
- [Lundstrom and Fairhall, 2006] Lundstrom, B. N. and Fairhall, A. L. (2006). Decoding stimulus variance from a distributional neural code of interspike intervals. *J Neurosci*, 26:9030-9037.
- [Lundstrom et al., 2010] Lundstrom, B. N., Fairhall, A. L., and Maravall, M. (2010). Multiple timescale encoding of slowly varying whisker stimulus envelope in cortical and thalamic neurons in vivo. *J Neurosci*, 30:5071-5077.

- [Lundstrom et al., 2008] Lundstrom, B. N., Higgs, M. H., Spain, W. J., and Fairhall, A. L. (2008). Fractional differentiation by neocortical pyramidal neurons. *Nat Neurosci*, 11:1335-1342.
- [Lyons and West, 2011] Lyons, M. and West, A. (2011). Mechanisms of specificity in neuronal activity-regulated gene transcription. *Prog. Neurobiol.*, 94, 259–295.
- [Mainen et al., 1995] Mainen, Z. F., Joerges, J., Huguenard, J., and Sejnowski, T. J. (1995). A model of spike initiation in neocortical pyramidal neurons. *Neuron*, 15:1427–1439.
- [Mainen and Sejnowski, 1995] Mainen, Z. F. and Sejnowski, T. J. (1995). Reliability of spike timing in neocortical neurons. *Science*, 265:1503-1506.
- [Mante et al., 2005] Mante, V., Frazor, R. A., Bonin, V., Geisler, W. S., and Carandini, M. (2005). Independence of luminance and contrast in natural scenes and in the early visual system. *Nat Neurosci*, 8:1690-1697.
- [Maravall, 2011] Maravall, M. (2011). *Principles of neural coding: chapter 18*. CRC Press.
- [Maravall et al., 2007] Maravall, M., Petersen, R., Fairhall, A., et al. (2007). Shifts in coding properties and maintenance of information transmission during adaptation in barrel cortex. *PLoS Biol*, 5.
- [Markram et al., 1998] Markram, H., Gupta, A., Uziel, A., Wang, Y., and Tsodyks, M. (1998). Information processing with frequency-dependent synaptic connections. *Neurobiol Learn Mem*, 70:101-112.
- [Marom, 2010] Marom, S. (2010). Neural timescales or lack thereof. *Prog Neurobiol*, 90:16-28.
- [Marr, 1982] Marr, D. (1982). *Vision*. W.H. Freeman and Company.
- [Massimini et al., 2007] Massimini, M., Ferrarelli, F., Esser, S., Riedner, B., Huber, R., Murphy, M., Peterson, M., and Tononi, G. (2007). Triggering sleep slow waves by transcranial magnetic stimulation. *Proc Natl Acad Sci USA*, 104: 8496-8501.
- [Massimini et al., 2004] Massimini, M., Huber, R., Ferrarelli, F., Hill, S., and Tononi, G. (2004). The sleep slow oscillation as a traveling wave. *J Neurosci*, 24: 6862-6870.
- [Mather et al., 1988] Mather, G., Verstraten, F., and Anstis, S. (1988). *The Motion Aftereffect: A Modern Perspective*. MIT Press.
- [McCormick and Huguenard, 1992] McCormick, D. A. and Huguenard, J. R. (1992). A model of the electrophysiological properties of thalamocortical relay neurons. *J. Neurophysiol.*, 68(4): 1384–1400.
- [McCulloch and Pitts., 1943] McCulloch, W. S. and Pitts., W. A. (1943). A logical calculus of the ideas immanent in nervous activity. *Bull Math Biophys*, 5, 115–133.

- [Meek, 1983] Meek, J. (1983). Functional anatomy of the tectum mesencephali of the goldfish. an explorative analysis of the functional implications of the laminar structural organization of the tectum. *Brain research*, 297.
- [Meltzer et al., 2008] Meltzer, J., Zaveri, H., Goncharova, I., Distasio, M., Papademetris, X., Spencer, S., Spencer, D., and Constable, R. (2008). Effects of working memory load on oscillatory power in human intracranial eeg. *Cereb Cortex*, 18: 1843-1855.
- [Miyawaki et al., 1997] Miyawaki, A., Llopis, J., Heim, R., McCaffery, J., Adams, J., Ikura, M., and Tsien, R. (1997). Fluorescent indicators for ca²⁺ based on green fluorescent proteins and calmodulin. *Nature*, 388, 882–887.
- [Mongillo et al., 2005] Mongillo, G., Curti, E., Romani, R., and Amit, D. J. (2005). Learning in realistic networks of spiking neurons and spike-driven plastic synapses. *European Journal of Neuroscience*, 21, pp.3143-3160.
- [Monto et al., 2008] Monto, S., Palva, S., Voipio, J., and Palva, J. M. (2008). Very slow eeg fluctuations predict the dynamics of stimulus detection and oscillation amplitudes in humans. *Journal of Neuroscience*, 28(33).
- [Morgan et al., 2006] Morgan, M. et al. (2006). Predicting the motion after-effect from sensitivity loss. *Vision Res.*, 46, 2412-2420.
- [Murphy and Davidson, 2013] Murphy, D. B. and Davidson, M. W. (2013). *Fundamentals of Light Microscopy and Electronic Imaging*. Wiley-Blackwell.
- [Murphy et al., 2009] Murphy, M., Riedner, B. A., Huber, R., Massimini, M., Ferrarelli, F., and Tononi, G. (2009). Source modeling sleep slow waves. *Proc Natl Acad Sci USA*, 106: 1608-1613.
- [Murthy and Fetz, 1992] Murthy, V. and Fetz, E. (1992). Coherent 25- to 35-hz oscillations in the sensorimotor cortex of awake behaving monkeys. *Proc. Natl. Acad. Sci. USA*, 89, 5670-5674.
- [Nagel and Doupe, 2006] Nagel, K. and Doupe, A. (2006). Temporal processing and adaptation in the songbird auditory forebrain. *Neuron*, 51:845-859.
- [Nakai et al., 2001] Nakai, J., Ohkura, M., and Imoto, K. (2001). A high signal-to-noise ca⁽²⁺⁾ probe composed of a single green fluorescent protein. *Nat. Biotechnol.*, 19, 137–141.
- [Naundorf et al., 2006] Naundorf, B., Wolf, F., and Volgushev, M. (2006). Unique features of action potential initiation in cortical neurons. *Nature*, 440.
- [Neher and Sakaba, 2008] Neher, E. and Sakaba, T. (2008). Multiple roles of calcium ions in the regulation of neurotransmitter release. *Neuron*, 59, 861–872.
- [Neuhauss et al., 1999] Neuhauss, S., Biehlmaier, O., Seeliger, M., Das, T., Kohler, K., Harris, W. A., and Baier, H. (1999). Genetic disorders of vision revealed by a behavioral screen of 400 essential loci in zebrafish. *The Journal of neuroscience : the official journal of the Society for Neuroscience*, 19, no. 19: 8603-15.

- [Nevin et al., 2010] Nevin, L. M., Robles, E., Baier, H., and Scott, E. K. (2010). Focusing on optic tectum circuitry through the lens of genetics. *BMC biology*, 8.
- [Niell and Smith, 2005] Niell, C. M. M. and Smith, S. J. J. (2005). Functional imaging reveals rapid development of visual response properties in the zebrafish tectum. *Neuron*, 45.
- [Niu et al., 2006] Niu, Y., Xiao, Q., Liu, R., Wu, L., and Wang, S. (2006). Evidence for a physiological explanation of the waterfall phenomenon and figural after-effects. *The Journal of physiology*, 577.
- [Nordström and O'Carroll, 2009] Nordström, K. and O'Carroll, D. (2009). The motion aftereffect: local and global contributions to contrast sensitivity. *Proceedings. Biological sciences / The Royal Society*, 276,no. 1662.
- [Oheim et al., 2001] Oheim, M., Beaurepaire, E., Chaigneau, E., Mertz, J., and Charpak, S. (2001). Two-photon microscopy in brain tissue: parameters influencing the imaging depth. *J. Neurosci. Methods*, 111, 29–37.
- [Orbach and Cohen, 1983] Orbach, H. S. and Cohen, L. B. (1983). Optical monitoring of activity from many areas of the in vitro and in vivo salamander olfactory bulb: a new method for studying functional organization in the vertebrate central nervous system. *J Neurosci*, 3: 2251-2262.
- [Orrenius et al., 2003] Orrenius, S., Zhivotovsky, B., and Nicotera, P. (2003). Regulation of cell death: the calcium-apoptosis link. *Nat. Rev. Mol. Cell Biol.*, 4, 552–565.
- [Ostojic and Brunel, 2011] Ostojic, S. and Brunel, N. (2011). From spiking neuron models to linear-nonlinear models. *PLOS Comp Biol*, 17.
- [Paik et al., 2009] Paik, S. B., Kumar, T., and Glaser, D. A. (2009). Spontaneous local gamma oscillation selectively enhances neural network responsiveness. *PLoS Comput Biol*, 5: e1000342.
- [Panier et al., 2013] Panier, T., Romano, S., Olive, R., Pietri, T., Sumbre, G., Candelier, R., and Debrégeas, G. (2013). Fast functional imaging of multiple brain regions in intact zebrafish larvae using selective plane illumination microscopy. *Frontiers in neural circuits*, 7(April):65.
- [Paquet et al., 2009] Paquet, D., Bhat, R., Sydow, A., Mandelkow, E.-m., Berg, S., Hellberg, S., Fälting, J., Distel, M., Köster, R. W., Schmid, B., and Haass, C. (2009). Technical advance: A zebrafish model of tauopathy allows in vivo imaging of neuronal cell death and drug evaluation. *The Journal of Clinical Investigation*, 119(5):1382-1395.
- [Paredes et al., 2008] Paredes, R., Etzler, J., Watts, L., Zheng, W., and Lechleiter, J. (2008). Chemical calcium indicators. *Methods*, 46, 143–151.
- [Parichy, 2015] Parichy, D. M. (2015). Advancing biology through a deeper understanding of zebrafish ecology and evolution. *eLife*, 4:e05635.

- [Petersen and Sakmann, 2001] Petersen, C. and Sakmann, B. (2001). Functionally independent columns of rat somatosensory barrel cortex revealed with voltage-sensitive dye imaging. *J Neurosci*, 21: 8435-8446.
- [Petersen et al., 2009] Petersen, R., Panzeri, S., and Maravall, M. (2009). Neural coding and contextual influences in the whisker system. *Biol Cybern*, 100:427-446.
- [Petersen et al., 1997] Petersen, R. S., Panzeri, S., and Maravall, M. (1997). Neural coding and contextual influences in the whisker system. *Biol Cybern*, 100:427-446.
- [Petersen et al., 1985] Petersen, S., Baker, J., and Allman, J. (1985). Direction-specific adaptation in area mt of the owl monkey. *Brain research*, 346, no. 1.
- [Pietri et al., 2013] Pietri, T., Roman, A.-C., Guyon, N., Romano, S. A., Washbourne, P., Moens, C. B., de Polavieja, G. G., and Sumbre, G. (2013). The first mecp2-null zebrafish model shows altered motor behaviors. *Frontiers in neural circuits*, 7(July):118.
- [Pillow, 2007] Pillow, J. (2007). *Bayesian Brain: Probabilistic approaches to Neural coding*. MIT press.
- [Pillow et al., 2008] Pillow, J., Shlens, J., Paninski, L., Sher, A., Litke, A. M., Chichilnisky, E. M., and Simoncelli, E. P. (2008). Spatio-temporal correlations and visual signalling in a complete neuronal population. *Nature*, 454.
- [Poirazi et al., 2003] Poirazi, P., Brannon, T., and Mel, B. W. (2003). Pyramidal neuron as two-layer neural network. *Neuron*, 37:989-999.
- [Portugues and Engert, 2009] Portugues, R. and Engert, F. (2009). The neural basis of visual behaviors in the larval zebrafish. *Current Opinion in Neurobiology*, 19(6):644-647.
- [Portugues et al., 2014] Portugues, R., Feierstein, C., Engert, F., and Orger, M. (2014). Whole-brain activity maps reveal stereotyped, distributed networks for visuomotor behavior. *Neuron*, 81, 1328-1343.
- [Prechtl et al., 1997] Prechtl, J., Cohen, L., Pesaran, B., Mitra, P., and Kleinfeld, D. (1997). Visual stimuli induce waves of electrical activity in turtle cortex. *Proc Natl Acad Sci USA*, 94: 7621-7626.
- [Preuss et al., 2014] Preuss, S. and Trivedi, C., vom Berg Maurer, C., Ryu, S., and Bollmann, J. (2014). Classification of object size in retinotectal microcircuits. *Current Biology*, 24(20):2376-2385.
- [Qian et al., 2005] Qian, H., Zhu, Q., Ramsey, D., Chappell, R., Dowling, J., and Ripps, H. (2005). Directional asymmetries in the optokinetic response of larval zebrafish (*danio rerio*). *Zebrafish*, 2,no. 3:189-96.
- [Quiroga and Panzeri, 2009] Quiroga, Q. R. and Panzeri, S. (2009). Extracting information from neuronal populations: information theory and decoding approaches. *Nat Rev Neurosci*, 10: 173-185.

- [Ramdya and Engert, 2008] Ramdya, P. and Engert, F. (2008). Emergence of binocular functional properties in a monocular neural circuit. *Nature neuroscience*, 11(9):1083-1090.
- [Ramdya and Engert, 2012] Ramdya, P. and Engert, F. (2012). Direction selectivity in the larval zebrafish tectum is mediated by asymmetric inhibition. *Frontiers in Neural Circuits*, 6(September):1-9.
- [Ranganath and Rainer, 2003] Ranganath, C. and Rainer, G. (2003). Neural mechanisms for detecting and remembering novel events. *Nat Rev Neurosci*, 4:193-202.
- [Ribary et al., 1991] Ribary, U., Ioannides, A., Singh, K., Hasson, R., Bolton, J., Lado, F., Mogilner, A., and Llinas, R. (1991). Magnetic field tomography of coherent thalamocortical 40-hz oscillations in humans. *Proc Natl Acad Sci USA*, 88: 11037-11041.
- [Richardson et al., 2003] Richardson, M., Brunel, N., and Hakim, V. (2003). From subthreshold to firing-rate resonance. *J Neurophysiol*, 89, 2538–2554.
- [Richardson, 2007] Richardson, M. J. (2007). Firing-rate response of linear and non-linear integrate-and-fire neurons to modulated current-based and conductance-based synaptic drive. *Phys Rev E Stat Nonlin Soft Matter Phys*, 76, 021919.
- [Richardson and Swarbrick, 2010] Richardson, M. J. and Swarbrick, R. (2010). Firing-rate response of a neuron receiving excitatory and inhibitory synaptic shot noise. *Phys Rev Lett*, 105, 178102.
- [Rick et al., 2000] Rick, J., Horschke, I., and Neuhauss, S. C. (2000). Optokinetic behavior is reversed in achiasmatic mutant zebrafish larvae. *Current biology*, 10, no. 10: 595-8.
- [Rieke, 2001] Rieke, F. (2001). Temporal contrast adaptation in salamander bipolar cells. *J Neurosci*, 21:9445-9454.
- [Rieke et al., 1997] Rieke, F., Warland, D. K., de Ruyter van, S. R. R., and Bialek, W. (1997). *Spikes: Exploring the Neural Code*. Cambridge, MA: MIT Press.
- [Robles et al., 2013] Robles, E., Filosa, A., and Baier, H. (2013). Precise lamination of retinal axons generates multiple parallel input pathways in the tectum. *The Journal of Neuroscience*, 33.
- [Roeser and Baier, 2003a] Roeser, T. and Baier, H. (2003a). Visuomotor behaviors in larval zebrafish after gfp-guided laser ablation of the optic tectum. *The Journal of neuroscience : the official journal of the Society for Neuroscience*, 23, no. 9:3726-34.
- [Roeser and Baier, 2003b] Roeser, T. and Baier, H. (2003b). Visuomotor behaviors in larval zebrafish after gfp-guided laser ablation of the optic tectum. *The Journal of neuroscience*, 23.

- [Romano et al., 2015] Romano, S., Pietri, T., Pérez-Schuster, V., Jouary, A., Haudrechy, M., and Sumbre, G. (2015). Spontaneous neuronal network dynamics reveal circuit’s functional adaptations for behavior. *Neuron*, 85.
- [Rubino et al., 2006] Rubino, D., Robbins, K., and Hatsopoulos, N. (2006). Propagating waves mediate information transfer in the motor cortex. *Nat Neurosci*, 9: 1549-1557.
- [Rudolph and Destexhe, 2009] Rudolph, M. and Destexhe, A. (2009). How much can we trust neural simulation strategies?. *Neurocomputing*, 70.10: 1966-1969.
- [Sanchez-Vives et al., 2000] Sanchez-Vives, M., Nowak, L., and McCormick, D. (2000). Membrane mechanisms underlying contrast adaptation in cat area 17 in vivo. *J Neurosci*, 20:4267-4285.
- [Sato et al., 2007] Sato, T., Hamaoka, T., Aizawa, H., Hosoya, T., and Okamoto, H. (2007). Genetic single-cell mosaic analysis implicates ephrinb2 reverse signaling in projections from the posterior tectum to the hindbrain in zebrafish. *The Journal of neuroscience*, 27.
- [Schneider et al., 2009] Schneider, G., Havenith, M. N., and Nikoli, D. (2009). Spatiotemporal structure in large neuronal networks detected from cross-correlation. *Neural Comput*, 18: 2387-2413.
- [Schoonheim et al., 2010] Schoonheim, P., Arrenberg, A. B., Del Bene, F., and Baier, H. (2010). Optogenetic localization and genetic perturbation of saccade-generating neurons in zebrafish. *The Journal of neuroscience: the official journal of the Society for Neuroscience*, 30, no. 20:7111-20.
- [Shadlen and Newsome, 1998] Shadlen, M. N. and Newsome, W. T. (1998). The variable discharge of cortical neurons: implications for connectivity, computation, and information coding. *J Neurosci.*, 18(10):3870-3896.
- [Shimomura et al., 1962] Shimomura, O., Johnson, F., and Saiga, Y. (1962). Extraction, purification and properties of aequorin, a bioluminescent protein from the luminous hydromedusan, aequorea. *J. Cell. Comp. Physiol.*, 59, 223–239.
- [Shouval et al., 2002] Shouval, H. Z., Bear, M. F., and Cooper, L. N. (2002). A united model of nmda receptor-dependent bidirectional synaptic plasticity. *Proceedings of the National Academy of Sciences*, 99 no 16.
- [Sik et al., 1995] Sik, A., Penttonen, M., Ylinen, A., and Buzsaki, G. (1995). Hippocampal ca1 interneurons: an in vivo intracellular labeling study. *J Neurosci*, 15: 6651-6665.
- [Simoncelli and Olshausen, 2001] Simoncelli, E. and Olshausen, B. (2001). Natural image statistics and neural representation. *Annu Rev Neurosci*, 24:1193-216.
- [Srinivasan et al., 1982] Srinivasan, M., Laughlin, S., and Dubs, A. (1982). Predictive coding: a fresh view of inhibition in the retina. *Proc R Soc Lond B Biol Sci*, 216:427-59.

- [Stepanyants et al., 2007] Stepanyants, A., Hirsch, J. A., Martinez, L. M., Kisvarday, Z. F., Ferecsko, A. S., and Chklovskii, D. B. (2007). Local potential connectivity in cat primary visual cortex. *Cereb Cortex*, 18: 13-28.
- [Steriade, 2006] Steriade, M. (2006). Grouping of brain rhythms in corticothalamic systems. *Neuroscience*, 137: 1087-1106.
- [Stocker and Simoncelli, 2006] Stocker, A. and Simoncelli, E. (2006). *Sensory adaptation within a Bayesian framework for perception*. MIT Press, Cambridge.
- [Streisinger et al., 1981] Streisinger, G., Walker, C., Dower, N., Knauber, D., and Singer, F. (1981). Production of clones of homozygous diploid zebra fish (*brachydanio rerio*). *Nature*, 291(5813):293- 296.
- [Sumbre and de Polavieja, 2014] Sumbre, G. and de Polavieja, G. G. (2014). The world according to zebrafish: how neural circuits generate behavior. *Frontiers in neural circuits*, 8, article91.
- [Sumbre et al., 2008] Sumbre, G., Muto, A., Baier, H., and Poo, M. M. (2008). Entrained rhythmic activities of neuronal ensembles as perceptual memory of time interval. *Nature*, 456(7218) : 102-106.
- [Tabak et al., 2000] Tabak, J., Senn, W., O'Donovan, M. J., and Rinzel, J. (2000). Modeling of spontaneous activity in developing spinal cord using activity-dependent depression in an excitatory network. *J Neurosci*, 20, 3041–3056.
- [Tanifuji et al., 1994] Tanifuji, M., Sugiyama, T., and Murase, K. (1994). Horizontal propagation of excitation in rat visual cortical slices revealed by optical imaging. *Science*, 266: 1057-1059.
- [Temizer et al., 2014] Temizer, I., Donovan, J., Baier, H., and Semmelhack, J. (2014). A dedicated visual pathway for prey detection in larval zebrafish. *eLife*, 3:1-19.
- [Temizer et al., 2015] Temizer, I., Donovan, J., Baier, H., and Semmelhack, J. (2015). A visual pathway for looming-evoked escape in larval zebrafish. *Current Biology*, 25(14):1823-1834.
- [Tian et al., 2009] Tian, L., Hires, S., Schreiter, E., et al. (2009). Imaging neural activity in worms, flies and mice with improved gcamp calcium indicators. *Nat. Methods*, 6, 875–881.
- [Tiesinga et al., 2008] Tiesinga, P., Fellous, J., and Sejnowski, T. (2008). Regulation of spike timing in visual cortical circuits. *Nat Rev Neurosci*, 9: 97-107.
- [Tognoli and Kelso, 2009] Tognoli, E. and Kelso, J. A. (2009). Brain coordination dynamics: true and false faces of phase synchrony and metastability. *Prog Neurobiol*, 87: 31-40.
- [Tootell et al., 1995] Tootell, R. B., Reppas, J. B., Dale, A. M., Look, R. B., Sereno, M., Malach, R., Brady, T. J., and Rosen, B. R. (1995). Visual motion aftereffect in human cortical area mt revealed by functional magnetic resonance imaging. *Nature*, 375.

- [Touboul, 2008] Touboul, J. (2008). Bifurcation analysis of a general class of nonlinear integrate-and-fire neurons. *J Appl Math*, 68, 1045–1079.
- [Traub et al., 1996] Traub, R. D., Whittington, M. A., Collins, S. B., Buzsaki, G., and Jefferys, J. G. R. (1996). Analysis of gamma rhythms in the rat hippocampus in vitro and in vivo. *J Physiol*, 493: 471-484.
- [Truccolo et al., 2004] Truccolo, W., Eden, U., Fellows, M., Donoghue, J., and Brown, E. (2004). A point process framework for relating neural spiking activity to spiking history, neural ensemble and extrinsic covariate effects. *Journal of Neurophysiology*, 93(2):1074–1089.
- [Tsodyks et al., 1997] Tsodyks, M., Skaggs, W., Sejnowski, T., and McNaughton, B. (1997). Paradoxical effects of external modulation of inhibitory interneurons. *J Neurosci*, 17: 4382-4388.
- [Tsodyks et al., 2000] Tsodyks, M., Uziel, A., and Markram, H. (2000). Synchrony generation in recurrent networks with frequency dependent synapses. *J Neurosci*, 20.
- [Tsodyks and Markram, 1997] Tsodyks, M. V. and Markram, H. (1997). The neural code between neocortical pyramidal neurons depends on neurotransmitter release probability. *Proc Natl Acad Sci USA*, 94, 719–723.
- [Tsodyks et al., 1998] Tsodyks, M. V., Pawelzik, K., and Markram, H. (1998). Neural networks with dynamic synapses. *Neural Comput*, 10, 821–835.
- [Tuckwell, 1988] Tuckwell, H. C. (1988). *Introduction to Theoretical Neurobiology*. Cambridge: Cambridge University Press.
- [Van de Grind et al., 2003a] Van de Grind, W. et al. (2003a). Influence of viewing distance on aftereffects of moving random pixel arrays. *Vision Res*, 43, 2413-2426.
- [Van de Grind et al., 2003b] Van de Grind, W. et al. (2003b). Storage for free: a surprising property of a simple gain-control model of motion aftereffects. *Vision Res*, 44, 2269-2284.
- [Van Kampen, 1992] Van Kampen, N. G. (1992). *Stochastic processes in physics and chemistry*, volume 1. Elsevier.
- [Vanhatalo et al., 2004] Vanhatalo, S., Palva, J. M., Holmes, M. D., Miller, J. W., Voipio, J., and Kaila, K. (2004). Infraslow oscillations modulate excitability and interictal epileptic activity in the human cortex during sleep. *Proceedings of the National Academy of Sciences*, 101.
- [Veit et al., 2017] Veit, J., Hakim, R., Jadi, M. P., Sejnowski, T. J., and Adesnik, H. (2017). Cortical gamma band synchronization through somatostatin interneurons. *Nature Neuroscience*, 20:7.

- [Volgushev et al., 2008] Volgushev, M., Malyshev, A., Balaban, P., Chistiakova, M., Volgushev, S., and Wolf, F. (2008). Onset dynamics of action potentials in rat neocortical neurons and identified snail neurons: Quantification of the difference. *Plos ONE*, 3 Issue 4.
- [Wang et al., 2003] Wang, J., Wong, A., Flores, J., Vosshall, L., and Axel, R. (2003). Two-photon calcium imaging reveals an odor-evoked map of activity in the fly brain. *Cell*, 112, 271–282.
- [Wang, 1999] Wang, X. J. (1999). Fast burst firing and short-term synaptic plasticity: a model of neocortical chattering neurons. *Neuroscience*, 89: 347-362.
- [Wang, 2010] Wang, X. J. (2010). Neurophysiological and computational principles of cortical rhythms in cognition. *Physiol Rev*, 90.
- [Wang and Buzsaki, 1996] Wang, X. J. and Buzsaki, G. (1996). Gamma oscillation by synaptic inhibition in a hippocampal interneuronal network model. *J Neurosci*, 16: 6402-6413.
- [Wark et al., 2009] Wark, B., Fairhall, A., and Rieke, F. (2009). Timescales of inference in visual adaptation. *Neuron*, 61:750-761.
- [Wark et al., 2007] Wark, B., Lundstrom, B., and Fairhall, A. (2007). Sensory adaptation. *Curr Opin Neurobiol*, 17:423-9.
- [Watamaniuk and Heinen, 2007] Watamaniuk, S. and Heinen, S. (2007). Storage of an oculomotor motion aftereffect. *Vision research*, 47, no. 4.
- [Webster, 2012] Webster, M. (2012). Evolving concepts of sensory adaptation. *F1000 Biology Reports*, 4:21.
- [White et al., 2011] White, R. M., Cech, J., Zon, L. I., et al. (2011). Dhodh modulates transcriptional elongation in the neural crest and melanoma. *Nature*, 471(7339):518-522.
- [Whittington et al., 1995] Whittington, M. A., Traub, R. D., and Jefferys, J. G. R. (1995). Synchronized oscillations in interneuron networks driven by metabotropic glutamate receptor activation. *Nature*, 373: 612-615.
- [Whittington et al., 2000] Whittington, M. A., Traub, R. D., Kopell, N., Ermentrout, B., and Buhl, E. H. (2000). Inhibition-based rhythms: experimental and mathematical observations on network dynamics. *Int J Psychophysiol.*, 38: 315-336.
- [Wilson and Cowan, 1972] Wilson, H. R. and Cowan, J. D. (1972). Excitatory and inhibitory interactions in localized populations of model neurons. *Biophys J*, 12: 1-24.
- [Wilson and Cowan, 1973] Wilson, H. R. and Cowan, J. D. (1973). A mathematical theory of the functional dynamics of cortical and thalamic nervous tissue. *Kybernetik*, 13: 55-80.

- [Wohlgemuth, 1911] Wohlgemuth, A. (1911). On the after-effect of seen movement. *The British Journal of Psychology*.
- [Wu et al., 1999] Wu, J., Guan, L., and Tsau, Y. (1999). Propagating activation during oscillations and evoked responses in neocortical slices. *J. Neurosci.*, 19, 5005-5015.
- [Wu et al., 2008] Wu, J., Huang, X., and Zhang, C. (2008). Propagating waves of activity in the neocortex: what they are, what they do. *Neuroscientist*, 14: 487-502.
- [Xu et al., 2007] Xu, W., Huang, X., Takagaki, K., and Wu, J. (2007). Compression and reflection of visually evoked cortical waves. *Neuron*, 55: 119-129.
- [Yu et al., 2008] Yu, Y., Shu, Y., and McCormick, D. (2008). Cortical action potential backpropagation explains spike threshold variability and rapid-onset kinetics. *J Neurosci*, 28(29).
- [Zada et al., 2014] Zada, D., Tovin, A., Lerer-Goldshtein, T., Vatine, G. D., and Appelbaum, L. (2014). Altered behavioral performance and live imaging of circuit-specific neural deficiencies in a zebrafish model for psychomotor retardation. *PLoS Genetics*, 10 (9): e1004615.
- [Zhu et al., 2012] Zhu, P., Fajardo, O., Shum, J., Zhang Schärer, Y.-P., and Friedrich, R. W. (2012). Highresolution optical control of spatiotemporal neuronal activity patterns in zebrafish using a digital micromirror device. *Nature Protocols*, 7(7):1410-1425.
- [Zucker, 1999] Zucker, R. (1999). Calcium- and activity-dependent synaptic plasticity. *Curr. Opin. Neurobiol.*, 9, 305-313.
- [Zucker and Regehr, 2002] Zucker, R. S. and Regehr, W. G. (2002). Short-term synaptic plasticity. *Annu Rev Physiol*, 64:355-405.

Sujet : Dynamique des réseaux neuronaux.

Résumé : Dans cette thèse, nous étudions le vaste domaine des neurosciences à travers des outils théoriques, numériques et expérimentaux. Nous étudions comment les modèles à taux de décharge peuvent être utilisés pour capturer différents phénomènes observés dans le cerveau. Nous étudions les régimes dynamiques des réseaux couplés de neurones excitateurs (E) et inhibiteurs (I): Nous utilisons une description fournie par un modèle à taux de décharge et la comparons avec les simulations numériques des réseaux de neurones à potentiel d'action décrits par le modèle EIF. Nous nous concentrons sur le régime où le réseau EI présente des oscillations, puis nous couplons deux de ces réseaux oscillants pour étudier la dynamique résultante. La description des différents régimes pour le cas de deux populations est utile pour comprendre la synchronisation d'une chaîne de modules E-I et la propagation d'ondes observées dans le cerveau. Nous examinons également les modèles à taux de décharge pour décrire l'adaptation sensorielle: Nous proposons un modèle de ce type pour décrire l'illusion du mouvement consécutif («motion after effect», (MAE)) dans la larve du poisson zèbre. Nous comparons le modèle à taux de décharge avec des données neuronales et comportementales nouvelles.

Mots clés : Réseaux de neurones, modèles de taux, oscillations, poisson zèbre, adaptation, neurosciences computationnelles, physique statistique

Subject : Dynamics of Neuronal Networks

Abstract : In this thesis, we investigate the vast field of neuroscience through theoretical, numerical and experimental tools. We study how rate models can be used to capture various phenomena observed in the brain. We study the dynamical regimes of coupled networks of excitatory (E) and inhibitory neurons (I) using a rate model description and compare with numerical simulations of networks of neurons described by the EIF model. We focus on the regime where the EI network exhibits oscillations and then couple two of these oscillating networks to study the resulting dynamics. The description of the different regimes for the case of two populations is helpful to understand the synchronization of a chain of E-I modules and propagation of waves observed in the brain. We also look at rate models of sensory adaptation. We propose one such model to describe the illusion of motion after effect in the zebrafish larva. We compare this rate model with newly obtained behavioural and neuronal data in the zebrafish larva.

Keywords : networks of neurons, rate models, oscillations, zebrafish, adaptation, computational neuroscience, statistical physics